

UNIVERSITY OF OKLAHOMA
GRADUATE COLLEGE

FUNDAMENTAL INVESTIGATION OF PRE-EXISTING FRACTURE SLIP AND
PROPAGATION IN RESERVOIR STIMULATION

A DISSERTATION
SUBMITTED TO THE GRADUATE FACULTY
in partial fulfillment of the requirements for the
Degree of
DOCTOR OF PHILOSOPHY

By
ZHI YE
Norman, Oklahoma
2019

FUNDAMENTAL INVESTIGATION OF PRE-EXISTING FRACTURE SLIP AND
PROPAGATION IN RESERVOIR STIMULATION

A DISSERTATION APPROVED FOR THE
MEWBOURNE SCHOOL OF PETROLEUM AND GEOLOGICAL ENGINEERING

BY THE COMMITTEE CONSISTING OF

Dr. Ahmad Ghassemi, Chair

Dr. Jean-Claude Roegiers

Dr. Brett Carpenter

Dr. Xingru Wu

Dr. Mashhad Fahes

© Copyright by ZHI YE 2019
All Rights Reserved.

Dedicated to my wife, Shan, and the little Michelle.

“不积跬步，无以至千里；不积小流，无以成江海”

*No accumulation of steps, can't lead to thousand miles; no integration of streams, can't
result in seas and oceans.*

ACKNOWLEDGEMENTS

I would like to express my great appreciation to my advisor, Dr. Ahmad Ghassemi, who has provided me the best support and mentorship. His wisdom and willingness to explore scientific and engineering unknowns have influenced me deeply, and always motivated me to strive for the best. In addition, I am particularly thankful for the opportunities he offered me to present my works on many conferences including ARMA, URTeC, Stanford Geothermal Workshop, and SPE HFTC, which help me get more academic exposure and enhance the connections with professionals. He is not just a good advisor, but a great mentor. He has set a good example that I am willing to follow in my future career.

Dr. Jean-Claude Roegiers, Dr. Brett Carpenter, Dr. Xingru Wu, and Dr. Mashhad Fahes are gratefully acknowledged for serving as my Ph.D. dissertation committee. I do benefit a lot from their valuable suggestions and guidance during my dissertation research.

I thank our lab technician, Stephen Dwyer, for his technical assistance. I very much enjoyed and appreciated our collaboration efforts.

I also thank my colleagues and friends in Dr. Ghassemi's Reservoir Geomechanics and Seismicity Research Group: Michael Janis, Yawei Li, Lianbo Hu, Xuejun Zhou, Kai Huang, Varahanaresh Sesetty, Qinglu Chen, Qian Gao, Dharmendra Kumar, Amirhossein Kamali, Behzad Hemami, Weiqi Yu, Ziyuan Wang, and Lei Han. I have learned a lot from the cooperation with them.

I owe my deepest appreciation to my parents, Zhongchu Chen and Shiyi Ye, my wife, Shan Dai, for their unconditional love and support. Also, I thank my adorable daughter, Michelle J. Ye, for the true happiness she brings to my life.

ABSTRACT

The deformation behavior and transport properties of subsurface reservoir rock masses are highly influenced by the existence of natural fractures. Shear reactivation of pre-existing fractures by pressurized fluid injection has been recognized as an important mechanism of reservoir stimulation and induced seismicity for a long time. In order to fundamentally reveal the roles of pre-existing fractures in reservoir stimulation and induced seismicity, novel laboratory injection experiments were conducted for this dissertation.

First, the dissertation presents the injection-induced shear tests on both granite and shale fractures (either rough or smooth). The results show that significant shear-induced permeability enhancement can be achieved on rough rock fractures by injection. Also, the enhanced permeability can be retained in the sheared fractures after the fluid pressure is decreased, indicating that the permeability increase by fracture shearing may be permanent. Moreover, the various observations for rough and smooth fractures demonstrate that normal dilation and self-propping of a rough fracture during shearing is key to the success of shear stimulation.

Additionally, the propagation and coalescence of pre-existing fracture(s) by injection is explored for the first time using triaxial-injection experiments. It is observed that the pre-existing fracture(s) can be propagated as tensile, shear or mixed-mode at injection pressures below the minimum principal stress. As a result, interconnected fracture networks can be created through the coalescence of newly propagated cracks with the pre-existing fractures, resulting in a remarkable permeability enhancement. This indicates that in addition to commonly accepted dilatant shear slip, tensile or shear mode propagation, coalescence of pre-existing fractures is also significant in reservoir stimulation and could be viewed as

integrated mechanisms of permeability enhancement in low injection pressure shear stimulation.

At last, the fully coupled seismo-hydro-mechanical response of rock fractures (granite or shale) is probed through laboratory injection-induced fracture slip tests with concurrent acoustic emission monitoring. The tests reveal a transitional seismic response during fracture shear slip namely, aseismic (or creeping) slip to seismic slip during fluid injection. In the aseismic creep interval, the fracture sheared at a relatively low rate ($\sim 10^{-8}$ m/s), and very few or no acoustic emission events were triggered concomitant with a small decline of the shear stress and a slight enhancement of flow rate into the fracture. A significant number of acoustic emission events were detected in the seismic slip interval with a relatively high slip rate ($\sim 10^{-5}$ to $\sim 10^{-4}$ m/s). The shear failure of the fracture occurred in the seismic slip stage, and was accompanied by a large stress drop (up to 50 MPa) and a dramatic fluid flow rate increase. In granite fracture test, a large number of AE events were detected during the dynamic slip interval corresponding with a frictional weakening behavior. The spatio-temporal evolution of acoustic emission hypocenters demonstrates the existence of slip heterogeneity on the fracture plane having a heterogeneous roughness distribution. In the shale fracture test, the fracture reactivation occurs with a limited number of AE events, which is likely related to the friction strengthening response during shearing. The results also show that microseismicity, permeability, fracture slip correlate well with each other: more microseismic events possibly indicate a better production performance. This laboratory observation is consistent with some field measurements.

The research findings in this dissertation demonstrate the important role of pre-existing fractures in reservoir stimulation and induced seismicity. Observations and results

enhance the physical understanding of the mechanical deformation and fluid flow processes of crustal rocks (having natural fractures/discontinuities), and help engineer solutions for subsurface energy developments and management of induced seismicity, and potentially provide insights into crustal permeability dynamics.

TABLE OF CONTENTS

ACKNOWLEDGEMENTS	V
ABSTRACT	VI
TABLE OF CONTENTS	IX
LIST OF TABLES.....	XII
LIST OF FIGURES.....	XIII
CHAPTER 1: INTRODUCTION	1
1.1 BACKGROUND AND OBJECTIVES	1
1.2 DISSERTATION OVERVIEW.....	5
1.3 LIST OF PUBLICATIONS	7
1.3.1 Refereed Journal Papers.....	7
1.3.2 Conference Proceedings	7
1.3.3 Poster Presentations	9
CHAPTER 2: INJECTION-INDUCED SHEAR SLIP AND PERMEABILITY ENHANCEMENT IN GRANITE FRACTURES	11
2.1 ABSTRACT	11
2.2 INTRODUCTION	12
2.3 EXPERIMENTAL METHODS.....	17
2.3.1 Sample Preparation and Characterization.....	17
2.3.2 Boundary Conditions and Experimental Control	23
2.3.3 Experimental Setup and Procedure.....	27
2.3.4 Permeability Evaluation.....	29
2.4 EXPERIMENTAL RESULTS	31
2.5 DISCUSSION	38
2.5.1 Retainable Permeability Enhancement	38
2.5.2 Permeability Evolution with Mechanical Properties	39
2.5.3 Slip Characteristics and Stress Relaxation.....	43
2.5.4 Asperity Degradation During Injection-Induced Fracture Shearing.....	47
2.5.5 The Effect of Loading Frame Stiffness during Fracture Shear Failure	50
2.6 CHAPTER SUMMARY	53
CHAPTER 3: INJECTION-INDUCED SHEAR SLIP AND PERMEABILITY ENHANCEMENT IN SHALE FRACTURES	56
3.1 ABSTRACT	56
3.2 INTRODUCTION	57
3.3 EXPERIMENTAL METHODS.....	59
3.3.1 Sample Preparation and Characterization.....	59

3.3.2 Experimental Setup.....	62
3.3.3 Experimental Procedure.....	62
3.3.4 Fracture Deformation and Permeability	65
3.4 EXPERIMENTAL RESULTS	68
3.5 DISCUSSION	74
3.5.1 The Mechanisms of Permeability Enhancement by Fracture Shear Slip.....	74
3.5.2 Retainable Permeability Enhancement in Shale Fractures	77
3.5.3 Slip Characteristics and Stress Drop.....	78
3.5.4 Asperity Degradation and Gouge Production.....	79
3.6 CHAPTER SUMMARY	80
CHAPTER 4: INJECTION-INDUCED FRACTURE PROPAGATION AND COALESCENCE IN GRANITE	82
4.1 ABSTRACT	82
4.2 INTRODUCTION	83
4.3 EXPERIMENTAL METHODS.....	86
4.3.1 Sample Preparation	86
4.3.2 Experimental Control.....	89
4.3.3 Experimental Setup and Procedure.....	92
4.4 RESULTS AND DISCUSSIONS.....	94
4.4.1 Hydro-Mechanical Coupled Measurements	94
4.4.2 Crack Characteristics	102
4.4.3 Fluid Flow/Permeability Enhancement	109
4.4.4 Relation to Crustal Permeability and Induced Seismicity	110
4.5 CHAPTER SUMMARY	112
CHAPTER 5: INJECTION-INDUCED FRACTURE PROPAGATION AND COALESCENCE IN SHALE	114
5.1 ABSTRACT	114
5.2 INTRODUCTION	115
5.3 EXPERIMENTAL METHODS.....	117
5.3.1 Sample Materials	117
5.3.2 Sample Preparation	118
5.3.3 Experimental Setup and Procedure.....	120
5.4 EXPERIMENTAL RESULTS	122
5.4.1 Hydro-Mechanical Coupled Measurements	122
5.4.2 Crack Characteristics	125
5.4.3 Permeability Enhancement	129
5.5 CHAPTER SUMMARY	130
CHAPTER 6: INJECTION-INDUCED FRACTURE SLIP AND MICROSEISMICITY IN GRANITE	132
6.1 ABSTRACT	133

6.2 INTRODUCTION	134
6.3 EXPERIMENTAL METHODS.....	137
6.3.1 Sample Preparation and Characterization.....	137
6.3.2 Experimental Setup.....	139
6.3.3 Pencil Lead Break Test	141
6.3.4 Experimental Procedure.....	142
6.4 EXPERIMENTAL RESULTS	144
6.5 DISCUSSION	149
6.5.1 The Slip-Seismicity-Permeability Relationship.....	149
6.5.2 Acoustic Emission/Microseismic Signature	150
6.5.3 The Effect of Fracture Surface Roughness	153
6.6 CHAPTER SUMMARY	155
CHAPTER 7: INJECTION-INDUCED FRACTURE SLIP AND MICROSEISMICITY IN SHALE.....	158
7.1 ABSTRACT	158
7.2 INTRODUCTION	159
7.3 EXPERIMENTAL METHODS.....	162
7.3.1 Sample Preparation and Characterization.....	162
7.3.2 Experimental Setup and Procedure.....	164
7.4 EXPERIMENTAL RESULTS	167
7.4.1 Pencil Lead Break (PLB) Test.....	167
7.4.2 The Seismo-Hydro-Mechanical Measurements.....	168
7.5 DISCUSSION	173
7.5.1 Permeability Enhancement by Dilatant Fracture Slip.....	173
7.5.2 Stress Control on Fracture Slip and Microseismicity	174
7.5.3 The Slip-Seismicity-Permeability Relationship.....	178
7.5.4 Acoustic Emission/Microseismic Signature	180
7.6 CHAPTER SUMMARY	181
CHAPTER 8: CONCLUSIONS	183
8.1 CONCLUSIONS OF THE PRESENT WORK	183
8.2 ORIGINAL CONTRIBUTIONS.....	186
8.3 SUGGESTIONS FOR FUTURE RESEARCH.....	188
REFERENCES.....	190

LIST OF TABLES

Table 2.1: Sample dimension and fracture angle of granite samples.....	19
Table 2.2: Hydro-mechanical parameters under each hold stage with constant injection pressure.	34
Table 2.3: The values of slip rate and stress drop rate at slip period of each test.....	47
Table 3.1: Sample dimension and fracture angle of shale samples.....	62
Table 3.2: Hydro-mechanical measurements of the two injection-induced shear tests. ...	69
Table 3.3: The values of slip rate and stress drop rate at slip period of each test.....	79
Table 5.1: Some geomechanical parameters of the Eagle Ford shale.....	118
Table 5.2: Mineralogy composition of Eagle Ford shale.....	118

LIST OF FIGURES

Figure 2.1: The procedures of sample preparation: (a) a cylindrical granite sample containing a tensile fracture; (b) a cylindrical granite sample containing a saw-cut fracture.19

Figure 2.2: Laser scanning contours of the two fracture surfaces of each sample: (a) sample SW-T1; (b) sample SW-T2; (c) sample SW-S3; (d) sample SW-S4. Among the contours of each sample profile, the left contour represents the top fracture surface, while the right contour describes the bottom fracture surface. The laser scanning of the untested fractures were completed before drilling the boreholes, so the boreholes are not shown in the contours.21

Figure 2.3: The histogram and normal fitting of JRC distribution of the fractures: (a) sample SW-T1; (b) sample SW-T2; (c) sample SW-S3; (d) sample SW-S4.23

Figure 2.4: (a) The sketch of experimental setup; (b) granite fracture with boreholes for fluid flow; (c) the sketch of fracture deformation during triaxial shear tests.24

Figure 2.5: The evolution of normal and shear stress components on the fracture plane during triaxial-injection shear test (the confining pressure is held constant, and the slip is induced by increasing injection pressure). (a) Constant axial stress control: the shear stress is held constant, and a non-stop slip (red dot) will be induced on the fracture when shear stress reaches the critical shear strength. (b) Constant piston displacement control: both shear stress and effective normal stress decrease when fracture slip (red dot) is initiated by water injection, and thus the fracture will reach a stable state (green dot) at a lower stress level.25

Figure 2.6: (a) The elliptical surface of a saw-cut fracture in Sierra White granite. (b) Fluid flow region for fracture permeability evaluation: the ellipse is the actual fluid flow region, while the rectangular area delineated by blue dotted lines is the equivalent fluid flow region.31

Figure 2.7: The hydro-mechanical measurements of injection-induced shear tests: (a) sample SW-T1; (b) sample SW-T2; (c) sample SW-S3; (d) sample SW-S4.35

Figure 2.8: The retention of permeability enhancement during the loading-unloading cycle of injection pressure: (a) sample SW-T1; (b) sample SW-T2; (c) sample SW-S3; (d) sample SW-S4.39

Figure 2.9: Permeability evolution with effective normal stress: (a) samples SW-T1 and SW-T2; (c) samples SW-S3 and SW-S4. Permeability evolution with shear stress: (b) samples SW-T1 and SW-T2; (d) samples SW-S3 and SW-S4. In the plots, the black, red and green data points are for the *slick*, the *slip*, and the *unloading* periods, respectively. Rough fractures (SW-T1, SW-T2 and SW-S3) show a rapid stress relaxation in the *slip* period (including 2 red data points), while a gradual stress relaxation is observed for the smooth fracture (SW-S4).40

Figure 2.10: Permeability evolution with fracture’s normal dilation: (a) samples SW-T1 and SW-T2; (c) samples SW-S3 and SW-S4. Permeability evolution with fracture’s shear slip: (b) samples SW-T1 and SW-T2; (d) samples SW-S3 and SW-S4. In the plots, the back, red, and green data points represent the *slick*, the *slip*, and the *unloading* periods, respectively. Rough fractures (SW-T1, SW-T2 and SW-S3) show a rapid shear slip in the *slip* period (including 2 red data points), while a gradual shear slip with lower velocity is observed for the smooth fracture (SW-S4).42

Figure 2.11: Slip characteristics and stress relaxation in the rapid slip period of each injection test: (a) sample SW-T1; (b) sample SW-T2; (c) sample SW-S3; (d) sample SW-S4.....44

Figure 2.12: Shear-induced asperity degradation on rough tensile fractures: (a) the tested sample SW-T1; (b) the scanning contours of sample SW-T1 after testing (the left contour is for the top fracture surface; the right contour is for the bottom fracture surface); (c) the tested sample SW-T2; (d) the scanning contours of sample SW-T2 after testing (the left contour is for the top fracture surface; the right contour is for the bottom fracture surface); (e) and (f) are the JRC distribution of SW-T1 and SW-T2 after testing, respectively. Before scanning the fractures, the boreholes on fracture surfaces were filled with modeling clay carefully to avoid the influences of voids on the scanning results. Therefore, the boreholes were not located on the scanning contours.49

Figure 2.13: Injection-induced shear test on sample SW-T1. The energy release of rock sample during the 1800-s injection interval with fluid pressurization.....52

Figure 2.14: Injection-induced shear test on sample SW-T1. The energy release (purple), and the axial deformation (light-green) of the loading system during the 1800-s injection interval with fluid pressurization.....52

Figure 3.1: Sample preparation: (a) raw sample B-20V; (b) rough fracture created by splitting; (c) 3D laser scanning contour.61

Figure 3.2: Sample preparation: (a) raw sample P-20V; (b) rough fracture created by splitting; (c) 3D laser scanning contour.61

Figure 3.3: (a) The sketch of experimental setup; (b) shale fracture with boreholes for fluid flow.64

Figure 3.4: Deformation during injection-induced shear test under triaxial stress.....66

Figure 3.5: Fluid flow region for fracture permeability estimation: the ellipse is the actual fluid flow region, while the rectangular area delineated by blue dotted lines is the equivalent fluid flow region.....68

Figure 3.6: The hydro-mechanical measurements of injection-induced shear test in shale sample B-20V. The temporal evolution of the piston displacement (green), differential stress (teal), the injection pressure (blue), the production pressure (gray), the effective normal stress (black), the shear stress (golden), the normal dilation (purple), the shear slip (pink), the steady-state flow rate (dark-blue) and the fracture permeability (dark-green) during the

2500-s-long fluid injection are illustrated. The axial shortening of the sample is calculated from the measured axial displacement, since the sample length is larger than the actual gauge length (see Figure 3.3(a)).70

Figure 3.7: The hydro-mechanical measurements of injection-induced shear test in shale sample P-20V. The temporal evolution of the piston displacement (green), differential stress (teal), the injection pressure (blue), the production pressure (gray), the effective normal stress (black), the shear stress (golden), the normal dilation (purple), the shear slip (pink), the steady-state flow rate (dark-blue) and the fracture permeability (dark-green) during the 2700-s-long fluid injection are illustrated. The axial shortening of the sample is calculated from the measured axial displacement, since the sample length is larger than the actual gauge length (see Figure 3.3(a)).71

Figure 3.8: A new fracture plane was created during the shear slip of original fracture by injection in Sample B-20V. In the figure, the blue-dashed line indicates the original fracture plane, and the red-dashed line represents the newly created fracture.76

Figure 3.9: The retention of permeability enhancement during the pressurization-depressurization cycle of injection pressure in (a) sample B-20V and (b) sample P-20V. .77

Figure 3.10: Slip characteristics and stress drop in the rapid slip period of each injection test: (a) sample B-20V; (b) sample P-20V.....79

Figure 3.11: Gouge production on tested sample: (a) sample B-20V and (b) sample P-20V. In left figure, the blue-dashed line indicates the original fracture plane, and the red-dashed line represents the newly created fracture.80

Figure 4.1: Sample preparation: (a) geometry of sample SW-1 with a single pre-existing fracture; (b) details of the pre-existing fractures; (c) side-view of sample SW-1; (d) geometry of sample SW-2 containing two pre-existing fractures; (e) details of the two pre-existing fractures and the fracture ligament; (f) side-view of sample SW-2.88

Figure 4.2: The sketches of experimental setup: (a) sample SW-1 containing a single pre-existing fracture; (b) sample SW-2 having two pre-existing fractures. LVDT = linear variable differential transformer.93

Figure 4.3: Test results for sample SW-1 (having a single pre-existing fracture): (a) the full stress-strain curve, in which points A, B, C, D and E describe the multi-step experimental procedure; (b) the hydro-mechanical measurements over time during injection (corresponding with the interval from point D to point E in the stress-strain curve), in which the temporal evolution of the piston displacement (green), differential stress (black), the injection pressure (blue), the injection pump volume (brown), the axial shortening (red), the radial expansion (pink), and the injection flow rate (purple) during the 440 s long fluid injection are illustrated. The axial shortening of the sample is calculated from the measured axial displacement, since the sample length is larger than the actual gauge length (see Figure 4.2(a)).98

Figure 4.4: Test results for sample SW-2 (having two pre-existing fractures): (a) the full stress-strain curve, in which points A, B, C, D and E indicate the multi-step experimental procedure; (b) the hydro-mechanical measurements over time during the injection (corresponding with the interval from point D to point E in the stress-strain curve), in which the temporal evolution of the piston displacement (green), the differential stress (black), the injection pressure (blue), the injection pump volume (brown), the production pressure (gray), the production pump volume (teal), the axial shortening (red), the radial expansion (pink), the injection flow rate (purple), and the production flow rate (gold) during the 480 s long fluid injection are illustrated. Here, the axial shortening of the sample is calculated from the measured axial displacement, since the sample length is larger than the actual gauge length (see Figure 4.2(b)).102

Figure 4.5: Assemblage of SEM images from sample SW-1 (containing a single pre-existing fracture). Center: image of the entire induced cracks that propagated from the pre-existing fracture; the tensile wing cracks are indicated by purple brackets, and the secondary cracks are marked by green brackets. Left: the enlarged image of the secondary cracks from the lower tip of the fracture. Right: the enlarged image of the secondary cracks from the upper tip of the fracture. The crack paths in the enlarged images are indicated by the red dots. 104

Figure 4.6: SEM image assemblages of sample SW-2 (containing two pre-existing fracture). Center: image of the entire induced cracks that propagated from the two parallel pre-existing fractures; the tensile wing cracks are indicated by purple brackets, the secondary cracks are marked by green brackets, and the bridge crack is represented by the blue bracket. Left: the enlarged image of the secondary cracks from the outer tip of the lower fracture. Right: the bridge crack (bottom), and the secondary cracks from the outer tip of the upper fracture (top). The crack paths in the enlarged images are indicated by the red dots.105

Figure 5.1: Sample preparation of the double-flawed Eagle Ford shale: (a) the sketch of sample geometry; (b) the Eagle Ford shale with two pre-existing fractures; (c) injection/production wellbore on one sample end.119

Figure 5.2: Experimental setup of the injection-induced fracture propagation test on Eagle Ford sample.121

Figure 5.3: Hydro-mechanical measurements of the double-flawed Eagle Ford shale during injection-induced fracture propagation test.123

Figure 5.4: The propagation and coalescence of pre-existing fractures on Eagle Ford shale: (a) front view; (b) back view; (c) the view of the sample end (production); (d) the view of the sample end (injection).126

Figure 5.5: SEM images of the cracks propagated from the lower fracture: (a) the inner tip of the lower fracture; (b) the outer tip of the lower fracture. The left picture in each figure is with 1-mm scale, while the right picture is with 100- μ m scale.127

Figure 5.6: SEM images of the cracks propagated from the upper fracture: (a) the inner tip of the upper fracture; (b) the outer tip of the upper fracture. The left picture in each figure is with 1-mm scale, while the right picture is with 100- μ m scale.128

Figure 5.7: SEM images in (a) the ligament area and (b) the interaction area of the newly propagated crack and the calcite vein.129

Figure 6.1: Sample preparation: (a) cylindrical Sierra White granite (SW-A1) having a single rough fracture; (b) fracture surfaces, and one borehole was drilled on one part of the sample for water injection; (c) 3D surface scanning contour, the u (the long axis of the contour), v (the short axis of the contour) and w coordinates (the color scale of the contour) are the length, width and asperity height of fracture surface, respectively.....139

Figure 6.2: Experimental setup: (a) sketch of sample configuration; (b) projected sample surface showing the location of 8 piezoelectric crystal transducers for AE monitoring (the blue circles indicate the transducers). The red line in the left plot represents the fracture. AE=Acoustic Emission, LVDT= Linear Variable Differential Transformer.141

Figure 6.3: Waveforms of the 8 crystal sensors in a PLB test on the granite sample SW-A1. PLB=Pencil Lead Break.....142

Figure 6.4: The seismo-hydro-mechanical response of granite sample SW-A1 during injection-induced shear test: temporal evolution of the piston displacement (green), the differential stress (black), the shear stress (teal), the effective normal stress (dark-red), the injection pressure (blue), the pump volume (orange), the fracture shear slip (pink), the fracture normal dilation (red), the injection flow rate (light-blue), the cumulated AE hits (gold), and the cumulated AE events (purple) during the 700-s-long fluid injection.....146

Figure 6.5: The location of acoustic emission events in: (a) x - z plane; and (b) y - z plane. The black line in the x - z plane (left) and the black ellipse in y - z plane (right) are the projection of the pre-existing fracture onto the two planes, respectively. The pre-drilled borehole for fluid injection is represented by the light-gray pillar. In the two plots, the dots with different sizes indicate the AE events with different amplitudes (from 55 dB to 97 dB), while the color scheme is used to represent the elapsed time from 270 s to 530 s.151

Figure 6.6: The spatio-temporal evolution profiles of acoustic emission events in x - z plane (top) and y - z plane (bottom) at $t = 270, 290, 310, 370, 500,$ and 530 s. The black line in the x - z plane (top) and the black ellipse in y - z plane (bottom) are the projection sketches of the pre-existing fracture onto the two planes, respectively. The pre-drilled borehole for fluid injection is represented by the light-gray pillar. In the plots, the dots with different sizes indicate the AE events with different amplitudes (from 55 dB to 97 dB), while the color scheme is used to represent the elapsed time from 270 s to 530 s.153

Figure 6.7: The projection of AE hypocenter locations on the scanning contours of fracture surfaces (lefts is the bottom surface): (a) the distribution of AE location at $t=310$ s; (b) the distribution of AE location at $t=530$ s. In the scanning contour, the color scheme indicates the asperity height. The black circles indicate the AE hypocenters with different magnitudes from 55 dB to 97 dB.155

Figure 7.1: Anisotropy evaluation of P-wave velocity: the small velocity differences in three directions indicate that this Eagle Ford shale is without significant velocity anisotropy. In

the plot, D is the sample diameter, L is the sample length, and t represent the arrival time of P-Wave.163

Figure 7.2: Sample preparation: (a) Eagle Ford shale having an inclined groove; (b) fracture surfaces, and two boreholes were drilled for water injection/fluid flow; (c) 3D surface scanning contour, the x (the long axis of the contour), y (the short axis of the contour) and z coordinates (the color scale of the contour) are the length, width and asperity height of fracture surface, respectively164

Figure 7.3: Experimental setup: (a) sketch of sample configuration; (b) projected sample surface showing the location of 8 piezoelectric crystal transducers for AE monitoring (the blue circles indicate the transducers). The red line in the left plot represents the fracture. AE=Acoustic Emission, LVDT= Linear Variable Differential Transformer.165

Figure 7.4: Waveforms of the 8 crystal sensors in a PLB test on the shale sample EF #1. PLB=Pencil Lead Break. (check).....168

Figure 7.5: The seismo-hydro-mechanical response of sample EF #1 during injection-induced shear test: temporal evolution of the piston displacement (green), the effective normal stress (black), the shear stress (teal), the effective normal stress (dark-blue), the injection pressure (blue), the production pressure (orange), the fracture shear slip (pink), the fracture opening/normal dilation (red), the injection flow rate (dark-red), the production flow rate (light-blue), the cumulated AE hits (gold), and the cumulated AE events (purple) during the 500-s-long fluid injection.172

Figure 7.6: AE Location map: (a) before applying a AE amplitude filter; (b) after applying a AE amplitude filter. In the plots, the blue dots indicate the AE events (with different magnitudes), and the red line represents the pre-existing fracture. AE = Acoustic Emission.173

Figure 7.7: The temporal evolution plots of shear stress (teal), injection pressure (blue), fracture shear slip (pink), cumulated AE hits (gold), AE rates (orange) and the production flow rate (dark-green).175

Figure 7.8: Stress state on the fracture plane during injection: (a) pre-slip stage; (b) slip stage; (c) post-slip stage. In the figure, the black circle indicates the initial stress state, the blue circle indicates the stress state at pre-slip stage, the red circle indicates the stress state at slip stage, and the green circle indicates the stress state at post-slip stage.177

Figure 7.9: The relationships of fracture shear slip, cumulated AE hits, and production flow rate. (a) Cumulated AE hits vs. Fracture shear slip; (b) Production flow rate vs. Fracture shear slip; (c) Production flow rate vs. Cumulated AE hits. AE = Acoustic Emission.179

Figure 7.10: The evolution of friction coefficient with fracture shear slip in: (a) Eagle Ford shale having a rough tensile fracture (sample EF #1); (b) a Sierra White granite sample containing a rough tensile fracture.181

Chapter 1

Introduction

1.1 Background and Objectives

High grade geothermal resources and unconventional shale oil/gas stored in low permeability reservoir rocks frequently require permeability enhancement through hydraulic stimulation to reach economic flow rates. Most reservoir rocks contain abundant pre-existing discontinuities such as faults, fractures, foliation planes, and mineralization bands distributed at different scales (from the perspective of reservoir geomechanics, hereinafter the term *fracture* is used to represent a pre-existing discontinuity). The deformation and failure behavior and transport properties of subsurface rock masses are highly influenced by how these pre-existing fractures respond to injection during reservoir stimulation. In addition, it is widely observed that the induced microseismic or seismic events during hydraulic injection are mostly related to the shear failure of pre-existing fractures. Reactivation of pre-existing fractures by pressurized fluid injection has been considered as an important mechanism of reservoir stimulation and induced seismicity for a long time (Cornet & Yin, 1995; Ellsworth, 2013; Evans et al., 2005; Guglielmi et al., 2015; Kim, 2013; Majer et al., 2007; Pine & Batchelor, 1984; Willis-Richards et al., 1996; Ye & Ghassemi, 2018a; Zoback et al., 2012). This approach is often referred as *shear stimulation* or *hydroshearing*. In contrast to hydraulic fracturing in petroleum industry which involves massive high pressure injection and proppant use, shear stimulation is carried out at treatment pressures below the minimum principal stress and fracture self-propping by asperities is viewed as an effective means of permeability enhancement (Baria et al., 1999;

Cheng, Wang & Ghassemi, 2019; Evans et al., 2005; Pine & Batchelor, 1984; Rahman et al., 2002; Tester et al., 2006; Willis-Richards et al., 1996; Ye & Ghassemi, 2018). During shear stimulation, a small reduction of effective normal stress by direct injection or the leak-off from a hydraulic fracture can be sufficient to induce the dilatant shearing of optimally oriented pre-existing fractures. Although the dilatant shear slip of pre-existing fractures is theoretically well-understood and routinely modeled, the fundamental investigations through laboratory tests have been limited. Most laboratory shear-flow tests on fractures have focused on force-driven fracture slip using direct shear design (Esaki et al., 1999; Gutierrez et al., 2000; Li et al., 2008; Olsson & Brown, 1993; Park et al., 2013; Samuelson et al., 2009; Yeo et al., 1998) or have manually displaced the fractured specimen to represent fracture slip (Chen et al., 2000; Crawford et al., 2017; Durham & Bonner, 1994; Hofmann et al., 2016; Vogler et al., 2016). However, there have been no or very few laboratory experiments that directly inducing fracture shear slip by injection under realistic boundary and stress conditions, so that the evolution of permeability creation during fracture shear slip are still poorly understood. For Chapter 2 and Chapter 3, injection-induced shear tests are presented on both granite and shale fractures to probe the coupled hydro-mechanical responses and permeability evolution during fracture shearing. The results and observations reveal the role of fracture shear slip in the hydraulic stimulation of shale and geothermal reservoirs,

Less known is the fact that shear reactivation of pre-existing fractures can also lead to their propagation because of the stress intensity increase (Horii & Nemat-Nasser, 1986; Jung, 2013; Min et al., 2010; Rutledge et al., 2004; Ye & Ghassemi, 2018b; Ye, Ghassemi, & Riley, 2018). Injection-induced propagation and coalescence of pre-existing fractures can

help generate an interconnected fracture network and further enhance the permeability of naturally fractured reservoir. But, most studies of this phenomenon have limited to analytical and numerical modeling (Kamali & Ghassemi, 2018; Petit & Barquins, 1988; Rao et al., 2003) and some field data interpretation (Jung, 2013). Little or no laboratory experiments have been performed to physically probe the propagation and coalescence of pre-existing fractures at low injection pressure stimulation under realistic stress and boundary conditions. Over the past 70 years, extensive experimental studies have been carried out to investigate the development (the process of crack initiation, propagation and coalescence) of pre-existing fracture(s) in artificial or rock materials under uniaxial/biaxial compression (e.g. Brace & Bombolakis, 1963; Hoek & Bombolakis, 1965; Nemat-Nasser & Horii, 1982; Sobolev, 1986; Shen et al., 1995; Bobet & Einstein, 1998; Lee and Jeon, 2011; Wong and Einstein, 2009a, 2009b; Yin et al., 2014). In these previous laboratory works, the propagation and coalescence of pre-existing fractures were induced via elevating the mechanical load without confining stress (in uniaxial compression) or with a low confining stress (in biaxial compression). The observations in these experiments can benefit near-surface engineering practices such as tunnel design, rock slope stability, etc. However, the aforementioned experiments are not very representative of the rock behavior in deep geothermal and shale reservoirs or the crust in general, where high confining stresses prevail, and where fracture propagation is usually induced by a pressurized fluid (e.g., injection during hydraulic stimulation). For Chapter 4 and Chapter 5, novel triaxial-injection tests on cylindrical granite or shale samples each containing a single or two pre-existing fracture(s) are described. The goal is to examine the creation of an interconnected fracture network through the coalescence

of newly propagated cracks/fractures and the pre-existing fractures, and its influence on crustal/reservoir permeability evolution.

Microseismic or seismic events caused by fluid injection are frequently observed during reservoir development and disposal well operations. The microseismic events accompanying with reservoir stimulation can be caused by the creation of new fractures or the reactivation of pre-existing fractures. Often, the shear slip of pre-existing fractures is usually the dominant source mechanism of induced seismicity during hydraulic injection, since the typical microseismic events induced by the creation of new fractures (tensile-mode) are with low moment magnitudes (less than 0) and hard to be detected. Some field observations indicate that a large stimulated reservoir volume (mapped from the microseismic motoring) results in a better production performance (Fisher et al., 2004; Mayerhofer et al., 2010). However, the fundamental understanding on the relationships of fracture shear slip, induced microseismicity, and permeability are limited. In addition, the heterogeneity of fault/facture slip and seismicity distribution in the episodes of fault reactivation and earthquake rupture has been frequently discussed through field observations, geophysical inverse studies, and numerical models. These previous works have suggested that slip heterogeneity may be related to the heterogeneity of fault/fracture surface roughness (e.g., Resor & Meer, 2009; Tinti et al., 2016; Zielke et al., 2017). However, geophysical inverse studies and numerical models are usually with large uncertainties, while the direct observations on fault zone geometry are from exhumed fault zones but not from the seismic faults at depth. To date, there has no or few reliable evidences to directly link fracture surface roughness and slip heterogeneity. Moreover, the occurrence of aseismic and seismic slip and their relation to the fault constitutive behavior (slip weakening vs slip

strengthening) and the role of pore pressure and fracture surface heterogeneity are not well interpreted. For Chapter 6 and Chapter 7, injection-induced fracture slip tests with concurrent acoustic emission monitoring are presented (on granite and shale fractures). The seismo-hydro-mechanical measurements of rock fractures are used to explore several key issues in induced seismicity during reservoir stimulation, including microseismic signature, slip-seismicity-permeability, aseismic-seismic transition, and slip heterogeneity.

In this dissertation, the role of pre-existing fractures in reservoir stimulation and induced seismicity is fundamentally explored through novel laboratory injection experiments, and the implications to enhanced geothermal systems (EGS) and unconventional shale reservoirs are also demonstrated. The main objectives of this research are to improve fundamental understanding of the dominant effects of pre-existing fractures on mechanical behavior, transport properties, and seismic response of crustal rocks, to further help engineer subsurface energy development and manage the accompanying induced seismicity.

1.2 Dissertation Overview

This dissertation includes eight chapters: Chapter 1 provides a brief introduction of the dissertation; Chapters 2 to 7 present the main experimental works conducted on both granite and shale rocks; Chapter 8 summarizes the conclusions as a consequence of my dissertation research. An overview of each chapter is presented here:

- Chapter 1 briefly introduces the background and motivation of this research, and also summarizes the main accomplishments.
- Chapter 2 describes the results of injection-induced shear slip and permeability enhancement in granite fractures, and the effect of fracture roughness on dilatant

fracture shear slip. The work in this chapter is published in *Journal of Geophysical Research: Solid Earth*.

- Chapter 3 expands the role of fracture shear slip and its contribution to permeability creation in shale reservoir stimulation. This chapter will be submitted to *Unconventional Resources Technology Conference*, Austin, Texas, July 2020.
- Chapter 4 demonstrates the propagation and coalescence of pre-existing fractures in granite during pressurized fluid injection, and the generation of interconnected fracture network caused by the coalescence of newly propagated fractures and the pre-existing ones. The work in this chapter has been published in *Journal of Geophysical Research: Solid Earth*.
- Chapter 5 explores the propagation and coalescence of pre-existing fractures in shale and its potential contribution to permeability enhancement during reservoir stimulation. This chapter is published in *Unconventional Resources Technology Conference*, Houston, Texas, July 2018.
- Chapter 6 discusses the injection-induced fracture slip and microseismicity in granite, including the microseismic signature, slip heterogeneity and aseismic-seismic slip transition. A journal paper is under preparation based on this chapter.
- Chapter 7 probes the microseismic signature and the slip-seismicity-permeability evolution in a shale fracture experiencing a shear slip by pressurized fluid injection. This chapter is published in *Unconventional Resources Technology Conference*, Denver, Colorado, July 2019.

- Chapter 8 summarizes the concluding remarks of this research, the implications to the development of unconventional shale resources and enhanced geothermal systems.

1.3 List of Publications

Here I list all my publications (either published or in-preparation) during the course of my doctoral research, including 5 journal papers, 12 conference proceedings, and 4 poster presentations.

1.3.1 Refereed Journal Papers

- **Ye, Z., & Ghassemi, A.** (2019). Injection-Induced Fracture Slip and Seismicity: Aseismic-Seismic Transition and Heterogeneity. (In preparation)
- **Ye, Z., & Ghassemi, A.** (2019). Investigation of Micro-Seismicity and Permeability Evolution in Shale Fractures During Stimulation. (Submitted to *SPE Production & Operations*)
- **Ye, Z., & Ghassemi, A.** (2019). Injection-Induced Propagation and Coalescence of Pre-Existing Fractures in Granite Under Triaxial Stress. *Journal of Geophysical Research: Solid Earth*. <https://doi.org/10.1029/2019JB017400>
- **Ye, Z., & Ghassemi, A.** (2018). Injection-Induced Shear Slip and Permeability Enhancement in Granite Fractures. *Journal of Geophysical Research: Solid Earth*, 123 (10), 9009-9032. <https://doi.org/10.1029/2018JB016045>
- **Ye, Z., Sestety, V., & Ghassemi, A.** (2018). Experimental and Numerical Investigation of Shear Stimulation and Permeability Evolution in Shales. *Hydraulic Fracturing Journal*, 5(3), 28-41.

1.3.2 Conference Proceedings

- **Ye, Z., & Ghassemi, A. (2019).** *Investigation of micro-seismicity and permeability evolution in shale fractures during stimulation.* Paper presented at the Unconventional Resources Technology Conference (URTeC), Denver, Colorado, USA.
- **Ye, Z., Vachaparampil, A., Zhou, X., Ghassemi, A., and Kneafsey, T. (2019).** *Failure behavior of the Poorman Schist and its fractures from EGS Collab Stimulation Site.* Paper presented at the 44th Workshop on Geothermal Reservoir Engineering, Stanford, California, USA.
- **Ye, Z., Sesity, V., & Ghassemi, A. (2018).** *Experimental and Numerical Investigation of Shear Stimulation and Permeability Evolution in Shales.* Paper presented at the SPE Hydraulic Fracturing Technology Conference and Exhibition, Woodlands, TX, USA.
- **Ye, Z., & Ghassemi, A. (2018).** *Experimental Study on Injection-induced Fracture Propagation and Coalescence for EGS Stimulation.* Paper presented at the 43rd Workshop on Geothermal Reservoir Engineering, Stanford, CA, USA.
- **Ye, Z., & Ghassemi, A. (2018).** *Injection-induced Fracture Propagation and Coalescence Under Triaxial Loading.* Paper presented at the 52nd US Rock Mechanics / Geomechanics Symposium, Seattle, WA, USA.
- **Ye, Z., Ghassemi, A., & Riley, S. (2018).** *Stimulation Mechanisms in Unconventional Reservoirs.* Paper presented at the Unconventional Resources Technology Conference (URTeC), Houston, TX, USA.
- **Ye, Z., Janis, M., Ghassemi, A., & Bauer, S. (2017).** *Experimental Investigation of Injection-driven Shear Slip and Permeability Evolution in Granite for EGS*

Stimulation. Paper presented at the 42nd Workshop On Geothermal Reservoir Engineering, Stanford, CA.

- **Ye, Z.,** Janis, M., & Ghassemi, A. (2017). *Injection-driven Shear Slip and The Coupled Permeability Evolution of Granite Fractures for EGS Stimulation*. Paper presented at the 51st US Rock Mechanics / Geomechanics Symposium, San Francisco, CA, USA.
- **Ye, Z.,** Janis, M., Ghassemi, A., & Riley, S. (2017). *Laboratory Investigation of Fluid Flow and Permeability Evolution through Shale Fractures*. Paper presented at the Unconventional Resources Technology Conference (URTeC), Austin, Texas, USA.
- **Ye, Z.,** Janis, M., & Ghassemi, A. (2017). *Laboratory investigation of permeability evolution in shear stimulation of granite fractures for EGS*. Paper presented at the 41st GRC Annual Meeting & GEA GeoExpo+, Salt Lake City, UT, USA.
- **Ye, Z.,** & Ghassemi, A. (2016). *Deformation Properties of Saw-Cut Fractures in Barnett, Mancos and Pierre Shales*. Paper presented at the 50th US Rock Mechanics/Geomechanics Symposium, Houston, TX, USA.
- **Ye, Z.,** Ghassemi, A., & Riley, S. (2016). *Fracture properties characterization of shale rocks*. Paper presented at the Unconventional Resources Technology Conference (URTeC), San Antonio, Texas, USA.

1.3.3 Poster Presentations

- **Ye, Z.,** & Ghassemi, A. (2019). *The Role of Pre-existing Fractures in Permeability Creation during Shale Reservoir Stimulation*. Poster presented at

Houston Geological Survey Applied Geoscience Conference, Houston, TX, USA.

- **Ye, Z., & Ghassemi, A. (2018).** *Experimental Study on Injection-induced Fracture Slip and Permeability Enhancement in Crystalline Rocks.* Poster presented at Workshop on Drilling Investigation of Seismogenic Crust in Oklahoma (DISCO), OK, USA.
- **Ye, Z., & Ghassemi, A. (2017).** *Laboratory Investigation of Shear Stimulation and Permeability Evolution in Shale Fractures.* Poster presented at Houston Geological Survey Applied Geoscience Conference, Houston, TX, USA.
- **Ye, Z., & Ghassemi, A. (2017).** *Geomechanical Properties Characterization of Shale Fractures Undergoing Triaxial Loadings.* Poster presented at SPE OKC Oil & Gas Symposium, Oklahoma City, OK, USA.

Chapter 2

Injection-Induced Shear Slip and Permeability Enhancement in Granite Fractures

The shear slip of pre-existing fractures caused by increased pore pressure due to injection has been explored as an important mechanism for permeability enhancement in reservoir stimulation. During hydraulic injection, the effective normal stress (σ'_n) and the corresponding critical shear stress $\tau_c = \mu\sigma'_n$ (μ is the sliding friction coefficient) gradually decrease as the pore pressure is elevated. Fracture slip occurs when the critical shear stress (τ_c) is reduced to the shear stress (τ) along the fracture plane. Due to the existence of asperities on fracture surfaces, fractures can dilate in the normal direction by shear slip, resulting in the increase of fracture aperture/permeability. Also, shear slip can help break the seals in fractures, and further enhance fracture permeability. The stimulation approach to achieve economic flow rates by reactivating pre-existing fractures is often referred as *shear stimulation* or *hydro-shearing*. To reveal the mechanisms of permeability creation caused by the shear slip of pre-existing fractures during hydraulic stimulation of Enhanced Geothermal Systems (EGS), novel injection-induced shear slip tests conducted on granite fractures are presented in this chapter.

2.1 Abstract

Shear stimulation, so-called “hydroshearing”, is believed to reactivate critically or near critically stressed pre-existing fractures by pressurized fluid injection, causing them to slip and dilate for economic production from geothermal and unconventional petroleum reservoirs. However, little or no experiments have been conducted to directly probe the

coupled hydro-mechanical responses and permeability evolution during fracture shearing. In this paper, we present the results of novel injection-induced shear tests on cylindrical granite samples each containing a single tensile or saw-cut fracture. The shear test on rough fractures demonstrate that retainable permeability enhancement can be achieved through dilatant shear slip. The characteristic “stick-slip” behavior of the fracture during shearing is also observed. Fracture aperture controlled by effective normal stress dominates the fluid flow in “stick” state, while in “slip” state, the major contributor to production increase is the irreversible normal dilation caused by fracture shear slip. The experimental data show that depending on the fracture roughness, the fracture slip process includes two “quasi-static” slip intervals with a slip velocity of $\sim 10^{-9}$ to $\sim 10^{-6}$ m/s, and a “dynamic” slip interval with a slip velocity of $\sim 10^{-7}$ to $\sim 10^{-5}$ m/s. The fracture slip correlates well with the associated stress relaxation: a faster fracture slip induces a quicker stress relaxation, and vice versa. The influence of surface roughness on the hydro-mechanical responses during fracture shearing, and the shear-induced asperity degradation are also studied. The various experimental observations on rough and smooth fractures clearly indicate that the key component to shear stimulation is fracture self-propping by asperities.

2.2 Introduction

In an EGS project, an injection well is first drilled into the geothermal reservoir (typical host rocks are crystalline rocks) containing open and sealed pre-existing fractures. Next, water is injected at sufficient pressure to create a high conductivity fracture network by reactivating pre-existing fractures and inducing man-made fractures. Two or more production wells are further drilled into the stimulated fracture network to form flow paths for water circulation. As a result, the production of geothermal energy can be achieved by

injecting cold water into the stimulated EGS reservoir through the injection well and producing hot water/steam from the production wells. In contrast to hydraulic fracturing in the petroleum industry which involves massive high pressure injection and proppant use, some researchers argue that an EGS stimulation should be carried out at treatment pressures below the minimum principal stress and fracture self-propping by asperities is viewed as an effective means of flow rate retention (Baria et al., 1999; Cheng & Ghassemi, 2016; Evans et al., 2005; Nygren & Ghassemi, 2005; Pine & Batchelor, 1984; Rahman et al., 2002; Tester et al., 2006; Willis-Richards et al., 1996).

Although the aforementioned process of shear stimulation is theoretically well-understood and routinely modeled, the fundamental investigations through laboratory tests and field measurements have been limited. Guglielmi et al. completed two mesoscale reactivation tests by injecting high pressure fluid into a carbonate fault (Guglielmi, et al., 2015a) and a shale fault (Guglielmi, et al., 2015b), respectively. One of the insights achieved from these two in-situ reactivation tests is that aseismic/seismic shear slip by fluid injection definitely enhanced the fluid transport/conductivity of the faults. However, these two field tests were conducted into the faults at a relatively shallow depth (< 600 m), in rocks that are not geothermal reservoir rocks.

Most laboratory shear-flow tests on fractures have focused on force-driven fracture slip using direct shear design (Esaki et al., 1999; Gutierrez et al., 2000; Li et al., 2008; Olsson & Barton, 2001; Olsson & Brown, 1993; Park et al., 2013; Samuelson et al., 2009; Su & Ghoreychi, 1999; Yeo et al., 1998) or have manually displaced the fractured specimen to represent fracture slip (Chen et al., 2000; Crawford et al., 2017; Durham & Bonner, 1994; Fang et al., 2017; Hofmann et al., 2016; Ishibashi et al., 2016; Vogler et al., 2016; Zhang et

al., 2013). The observations in most of these tests have been used to prove that fracture self-propping and associated permeability increase can be obtained by fracture shearing. However, fracture slip in a direct shear test is induced by mechanical force rather than by fluid injection, and the use of a direct shear assembly has some disadvantages. For example, the fractures are sheared at very low effective normal stress, extremely low fluid injection pressures are used due to sealing issues, and the fluid flow in the test is usually a seepage flow with a low flow rate. The method of manually imposing shear offset can be widely adopted in direct shear test, or regular triaxial test, or core flooding test. However, the test cannot capture the hydro-mechanical coupled responses of fracture during shearing, and also overestimates the flow rate enhancements because it cannot realistically reflect the slip process with asperity degradation and gouge production. In short, the above two types of experiments do not reveal real injection-induced fracture slip, and cannot describe the slip characteristics and fluid flow behavior during the reactivation of faults/fractures by injection.

Another test design of fracture slip in a laboratory scale is triaxial shear test. In a triaxial shear test, the fracture slip can be induced by either mechanical force or fluid injection under triaxial loading on a cylindrical specimen containing a single fracture (e.g., a saw-cut fracture, a natural fracture, an induced fracture, or a healed fracture). Usually, the inclination angle of the fracture is 20° ~ 60° with respect to the long axis of the cylindrical sample. Triaxial shear test has been used to investigate the pore pressure change caused by fracture shearing (Lockner & Byerlee, 1994), to analyze the effects of pore fluid pressure on rock properties (e.g. Blanpied et al., 1995), to reactivate healed fracture by injection (Bakshi et al., 2016), and to explore the acoustic response during fracture shearing by adding acoustic emission detection (Bakshi et al., 2016; Goebel et al., 2012; Stanchits et al., 2006). Wu et al.

(2017) produced fracture slips on saw-cut fractures of Eagle Ford shale under triaxial loading by controlling slip velocity through axial loading increase, and quantified the permeability changes before and after fracture slip. However, in this test the fracture slip was still induced by mechanical force but not by fluid pressurization.

A few researchers have conducted triaxial-injection shear tests on saw-cut fractures (Bauer et al., 2016; French et al., 2016; Nemoto et al., 2008; Rutter & Hackson, 2017). French et al. (2016) conducted saw-cut fracture slip tests on dry or saturated sandstones (permeable Berea and Darley Dale sandstones) to investigate the effects of stress path and fluid pressurization rate on fracture slip characteristics (slip velocity, shear stress drop, etc.). Rutter & Hackson (2017) completed similar triaxial shear tests on permeable (Darley Dale sandstone) or impermeable (tight Pennant sandstone) saw-cut fractures to study friction change and shear failure of fractured rocks with or without gouge. The primary goal of the above two studies were not to address permeability/fluid flow evolution during fracture shearing. To our knowledge, the injection-induced shear slip tests on rock fractures for reservoir stimulation were started by Nemoto et al. (2008) and Bauer et al. (2016). Nemoto et al. (2008) generated fracture slip on a single saw-cut Iidate granite fracture by increasing the injection pressure under the experimental control of constant axial stress, and observed stepwise fracture slip and temporal increase of fluid flow. In this case, the flow rate was measured from the injection wellbore and not the production wellbore, so that production enhancement could not be characterized. In order to demonstrate the role of cooling effects and pore pressure change on fracture slip and flow rate increase in geothermal reservoir stimulation, Bauer et al. (2016) flowed cold water into a hot and stressed saw-cut Westerly granite fracture to induce fracture slip. This was done by decreasing the downstream/outlet

pressure under the boundary condition with a constant axial stress. The above-mentioned triaxial-injection shear tests have improved the understanding of the reactivation of fractures/faults. However, the fractures used in all these tests are saw-cut. In addition, the fluid flow observed in the above injection tests were in transient flow regime and not in steady-state flow regime, and the retention of flow rate/permeability increase after fracture shearing was not studied. Moreover, fracture slip in these triaxial-injection shear tests were induced by decreasing the confining pressure or by increasing the pore pressure under constant axial stress control. Because of this experimental control, these experiments were unable to capture the dynamic processes of *stick-slip* and associated stress relaxation which occurs on real faults and fractures during subsurface injection. The shear stress drop demonstrated by French et al. (2016) was achieved by manually decreasing the effective normal stress (in contrast to an evolving energy release during fracture shearing due to injection). In this paper, we focus on dilatant shear slip and permeability evolution of granite fractures during injection-induced fracture shearing using a constant piston displacement control mode to enable realistic shearing and stress drop variations during the test.

Four ~50 mm diameter, cylindrical granite samples, each containing a single tensile or saw-cut fracture (SW-T1 and SW-T2 are tensile fractures, while SW-S3 and SW-S4 are saw-cut fractures), were used to conduct the novel injection-induced shear tests under triaxial loading. This newly developed test method involves a stepwise injection strategy, and captures the stress relaxation associated with fracture slip, and allows the evaluation of fluid flow under a steady-state flow regime. During the tests, injection pressure was increased stepwise to induce fracture slip, and then it was decreased in the same manner using the same pressure increment after fracture shearing to examine the retainable behavior of

permeability enhancement. The mechanical properties (stress and displacement) and fluid flow parameters (flow rate and pressure) of the fractures with different surface roughness were all measured to examine the following key points: (1) the coupled hydro-mechanical responses during injection-induced fracture shearing; (2) the fundamental mechanisms of permeability enhancement in shear stimulation; (3) the retention of permeability enhancement in sheared fractures; (4) slip characteristics and stress relaxation (energy release) during fracture shearing by injection; (5) shear-induced asperity degradation, and the influence of surface roughness on the hydro-mechanical responses of fracture in shearing process.

2.3 Experimental Methods

2.3.1 Sample Preparation and Characterization

Rock samples used in the injection-induced shear tests are Sierra White granite acquired from a commercial outlet and delivered to the laboratory as cubic blocks (330mm×330mm×330mm). A series of regular uniaxial compression, triaxial compression and Brazilian tests were conducted to obtain relevant mechanical properties of this Sierra White granite: Young's modulus ($E=67$ GPa), Poisson's ratio ($\nu=0.32$), uniaxial compressive strength ($UCS=150$ MPa), internal friction angle ($\phi=46^\circ$) and tensile strength ($T=11$ MPa). In addition, the matrix permeability of the granite was determined as 5×10^{-19} m² to 1×10^{-18} m² using steady-state permeability tests on 25 mm diameter granite discs with 12.5 mm thickness. X-ray diffraction analysis shows the granite consists of mostly Quartz and Albite (43.5% and 46.1% weight fraction, respectively) with a few percentages of Sanidine (4.8%), Biotite (2.7%), Illite (2.0%) and Clinocllore (0.9%).

To create the cylindrical granite samples with a single rough fracture, a large cubic block of granite was first separated into smaller rectangular pieces with dimensions of 75mm×75mm×150mm. An inclined groove (5 mm in width and 5 mm in depth) was cut at a 30-degree angle with respect to the long axis of the rectangular granite piece, and then an MTS 810 frame fitted with a V-shaped blade was used to induce a tensile fracture by splitting the grooved granite block (Ye et al., 2017b). After that, a diamond coring system was used to obtain ~50 mm diameter cylindrical granite cores containing a single tensile fracture (Figure 2.1(a)). On the other hand, to prepare the cylindrical samples with a saw-cut fracture, we first cored several ~50 mm diameter granite plugs from the same Sierra White block. Next, a diamond saw was used to cut the granite plugs at a 30-degree angle with respect to the long axis of the plug to form a saw-cut fracture (Figure 2.1(b)). The end surfaces of all cylindrical samples were finely polished using a rock surface grinder (Brown & Sharpe 818 Micromaster Grinder) with a 200-grit grinding wheel according to ISRM standard (Kovari et al., 1983). Before testing, all fractured samples, especially the samples with a tensile fracture, were placed into an ultra-sonic bath in deionized water to remove any fines that might affect fluid flow in the fracture. The samples were then dried in a vacuum oven at a temperature of 60 °C for at least 24 hours.

Fracture roughness is considered to be an important factor influencing the deformation properties and fluid flow of rock fractures. In this study, we prepared four Sierra White granite fractures with various values of Joint Roughness Coefficient (JRC, Barton, 1973) to carry out injection-induced shear tests. Samples SW-T1 and SW-T2 are tensile fractures induced by the above-mentioned rock splitting method: samples were split with a steel wedge using a displacement loading rate of 0.01 mm/min. Samples SW-S3 and SW-S4

are saw-cut fractures: the only difference between the two saw-cut fractures is that the fracture surfaces of sample SW-S4 were polished by the rock surface grinder. This means that sample SW-S4 has the smoothest fracture surfaces among the four samples. The sample dimensions and fracture angle with respect to the long axis of the sample are listed in Table 2.1.

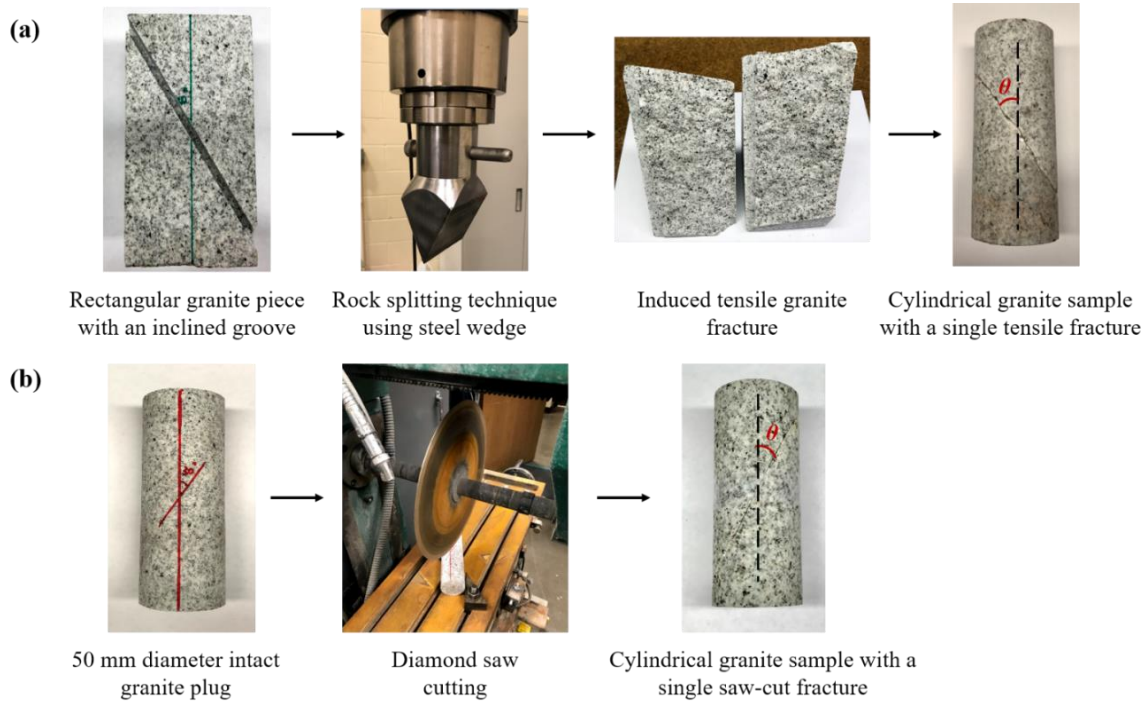


Figure 2.1: The procedures of sample preparation: (a) a cylindrical granite sample containing a tensile fracture; (b) a cylindrical granite sample containing a saw-cut fracture.

Table 2.1: Sample dimension and fracture angle of granite samples.

Sample No.	Fracture Type	Length (L), mm	Diameter (D), mm	Fracture angle* (θ), degree
SW-T1	tensile	128.80	50.52	32°
SW-T2	tensile	132.70	50.52	31°
SW-S3	saw-cut	123.40	50.53	29°
SW-S4	saw-cut	118.70	50.51	30°

* Angle measured from the long axis of sample to the fracture plane (see Figure 2.1).

A three-dimensional (3D) laser scanning system (model #CMDM88) made by B&H Machine Company, with a 2-micron resolution laser beam, was used to measure the

topography of the fracture surfaces. The 3D scanning contours of the two surfaces of each fracture are shown in Figure 2.2. The x (the long axis of the contour in Figure 2.2), y (the short axis of the contour in Figure 2.2) and z coordinates (the color scale of the contour in Figure 2.2) of the scanning contours are the length, width and asperity height of fracture surface, respectively. The color scale in the contour describes the values of asperity height with respect to the lowest point of the fracture surface (indicated by black color). The dark blue to light red zones represent asperity heights ranging from low to high values (with reference to the lowest point). The elliptical contours are cropped from the scanning results to avoid boundary effects. The real scanning area of the fracture surfaces are not perfectly elliptical and are a little larger than the contours shown in Figure 2.2. In the scanning profile of each sample in Figure 2.2, the left contour represents the top fracture surface of the sample, while the right contour indicates the bottom fracture surface of the sample. In addition, both the tensile fractures and the saw-cut fractures were prepared carefully with a high degree of fracture matching, therefore the Joint Matching Coefficient (JMC, see Zhao, 1997a, 1997b) of the fractures are close to 1.0 (tensile fractures) or are equal to 1.0 (saw-cut fractures). As a result, the color scales of the two contours of each sample profile are almost identical, so we only use one color scale for the two fracture surfaces of each sample in the scanning contours (as shown later, this is not the case for sheared fractures).

The Sierra White granite used in our experiments has mean crystal size around 0.5 mm. The tensile fracture created tends to propagate along the boundaries of the crystals which are significantly weaker than the constituent minerals (quartz, albite, etc.). In general, a fracture will have rough small-scale asperities controlled by grain/crystal size, and with broad wavelength disparities as in samples SW-T1 and SW-T2. In these two samples, the

maximum surface relief between the highest point (peak) and lowest point (valley) of the fracture surfaces are 6.43 mm and 5.86 mm, respectively. Samples SW-S3 and SW-S4 were saw cut to provide a control group for the tensile fractures. Sample SW-S4 was further polished to obtain an even smoother surface, sample SW-S3 was only saw cut. The maximum surface relief of sample SW-S4 is only 0.25 mm, while sample SW-S3 has a surface relief of just above 0.62 mm. This means that the polished saw-cut fracture SW-S4 is noticeably smoother than the unpolished saw-cut fracture SW-S3. The reason that sample SW-S3 has a relatively larger surface relief is most likely due to slight movement of the sample during cutting.

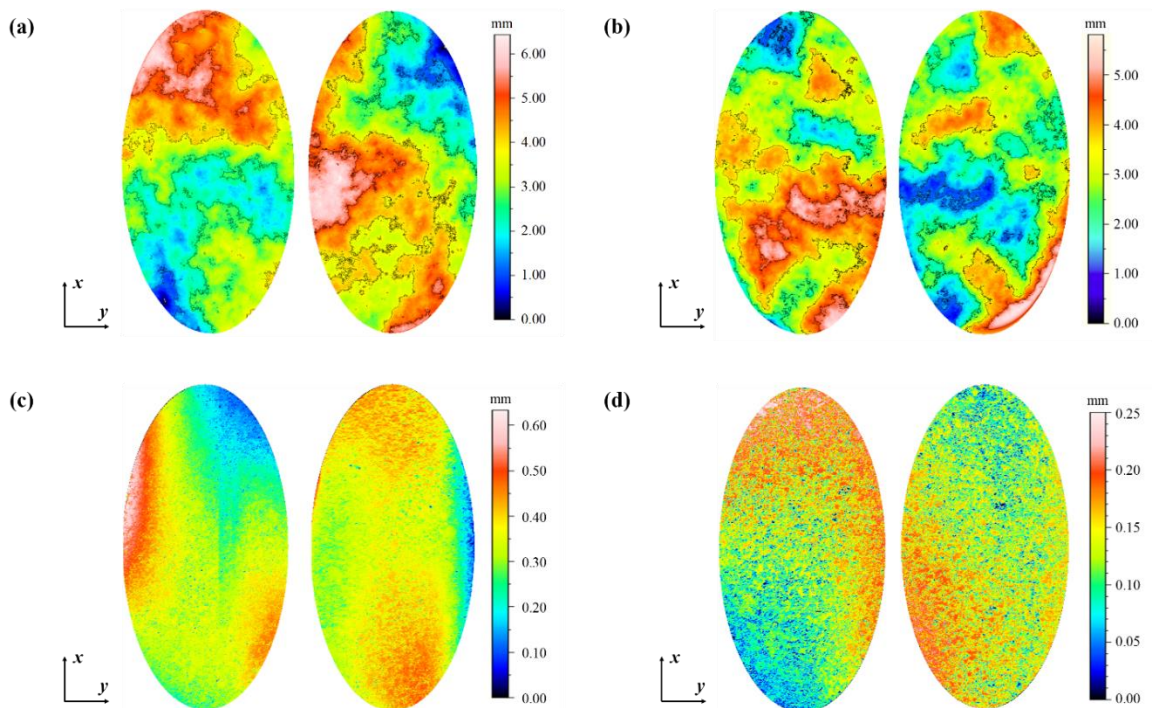


Figure 2.2: Laser scanning contours of the two fracture surfaces of each sample: (a) sample SW-T1; (b) sample SW-T2; (c) sample SW-S3; (d) sample SW-S4. Among the contours of each sample profile, the left contour represents the top fracture surface, while the right contour describes the bottom fracture surface. The laser scanning of the untested fractures were completed before drilling the boreholes, so the boreholes are not shown in the contours.

After the 3D scanning, the digitized data were exported in xyz file format to estimate the Joint Roughness Coefficient (JRC). The surface roughness parameter, Z_2 , the root mean

square of the slope of a 2D profile is widely used to correlate with JRC value (Jang et al., 2014; Tatone & Grasselli, 2012; Tse & Cruden, 1979; Yang et al., 2001; Yu & Vayssade, 1991). For a 2D profile, Z_2 is given by:

$$Z_2 = \left[\frac{1}{(n-1)(\Delta x)^2} \sum_{i=1}^{n-1} (z_{i+1} - z_i)^2 \right]^{0.5} \quad (2-1)$$

where, n is the number of data points along the 2D profile; Δx is the interval between the data points; and z_i is the value of the asperity height at point i .

Empirical correlations between Z_2 and JRC were proposed with different sampling spans such as 0.5 mm (Jang et al., 2014; Tatone & Grasselli, 2012; Yang et al., 2001; Yu & Vayssade, 1991), 1 mm (Tatone & Grasselli, 2012; Yu & Vayssade, 1991), and 1.27 mm (Tse & Cruden, 1979). The 3D profile of a fracture surface can be considered to be a combination of 2D profiles; here we used a 0.5 mm sampling span and calculated the Z_2 value for each 2D profile, and then estimated the JRC values of these 2D profiles. As shown in Figure 2.2, each fractured sample has two fracture surfaces, and therefore the JRC value of a fractured sample is calculated by averaging the JRC values of the two fracture surfaces. The empirical correlation used for JRC estimation is (Yu & Vayssade, 1991):

$$JRC = 61.79 \times Z_2 - 3.47 \quad (2-2)$$

where, JRC is joint roughness coefficient and Z_2 is the root mean square of the slope of a given 2D profile.

The histograms of JRC distribution are given in Figure 2.3. The average JRC values of the four fractures (SW-T1, SW-T2, SW-S3 and SW-S4) are 15.32, 14.63, 1.96 and 1.19, respectively. In Figure 2.3, the red curves fitted to the histograms show that JRC values of the 2D profiles on a fractured sample tend to have a normal distribution. The range of JRC values is from 0 to 20 (Barton, 1973), the tensile fractures (SW-T1 and SW-T2) have similar

JRC values, which are much higher than the JRC values of the two saw-cut fractures (SW-S3 and SW-S4). In addition, sample SW-S4 which has the smallest JRC value is used to represent an *ideally* smooth fracture. Considering the JRC values and the procedures of sample preparation, the tensile fractures SW-T1 and SW-T2 can be referred to as *very rough*, SW-S3 is considered a *rough* fracture, while SW-S4 is a *smooth* fracture.

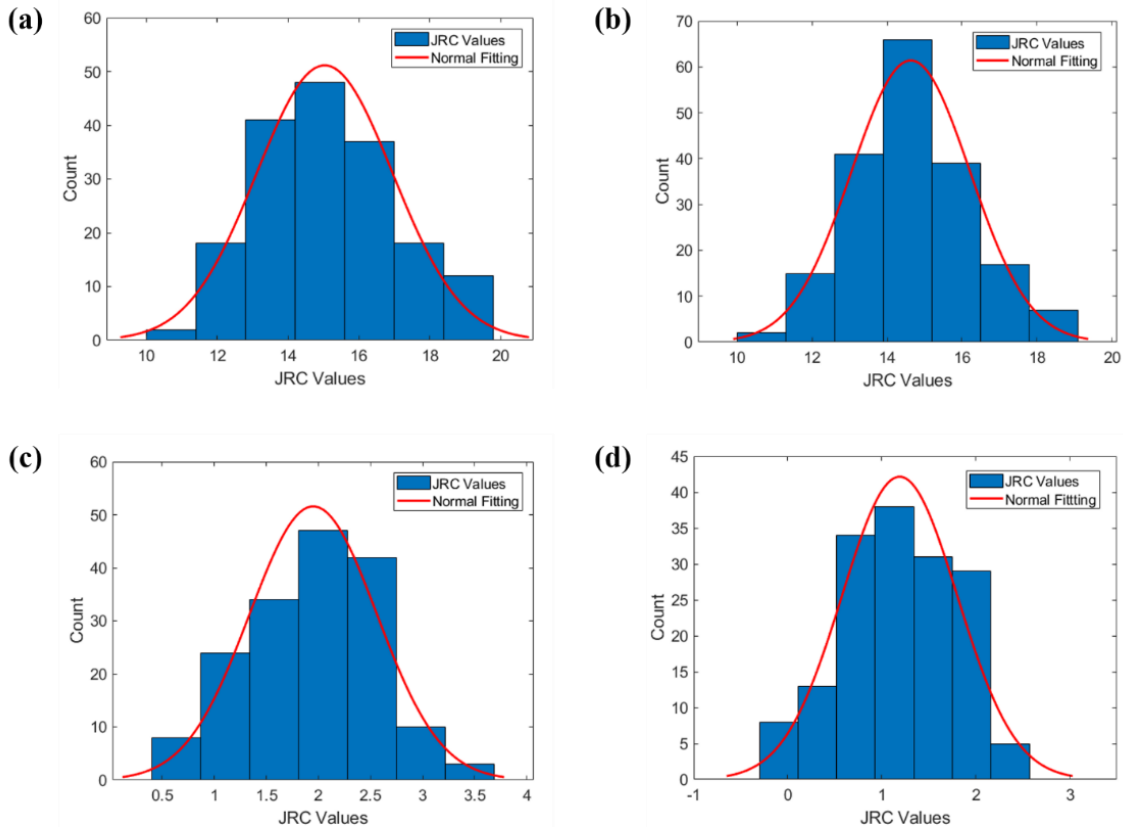


Figure 2.3: The histogram and normal fitting of JRC distribution of the fractures: (a) sample SW-T1; (b) sample SW-T2; (c) sample SW-S3; (d) sample SW-S4.

2.3.2 Boundary Conditions and Experimental Control

As shown in Figure 2.4(a), our triaxial shear test with injection is designed to improve the understanding of shear stimulation. The test involves a cylindrical sample containing a single inclined fracture, and the inclination angle of the fracture is θ degrees with respect to the vertical axis of the sample. Two 3.5 mm diameter vertical boreholes (see Figure 2.4(b)), 6 mm from the sidewall, are drilled (using a diamond drill bit) from each end

surface of the cylindrical sample to reach the fracture and to form a flow path. The flow path is illustrated by the red-arrowed lines in Figure 2.4(a). In the test, deionized water is injected into the fracture through the bottom borehole and is produced out from the top borehole.

As shown in Figure 2.4(c), the effective normal stress and shear stress on the local n - s coordinates of the fracture plane are:

$$\sigma'_n = (\sigma_3 - P_p) + (\sigma_1 - \sigma_3)\sin^2\theta \quad (2-3)$$

$$\tau = (\sigma_1 - \sigma_3)\sin\theta\cos\theta \quad (2-4)$$

where, σ'_n and τ are the effective normal stress and shear stress on the fracture plane, respectively; θ is the fracture inclination angle with respect to the vertical axis of the sample; σ_1 is axial stress; σ_3 is confining pressure; P_p is pore pressure which can be estimated as the average of the injection pressure (P_i) and the production pressure (P_o):

$$P_p = 0.5 \times (P_i + P_o) \quad (2-5)$$

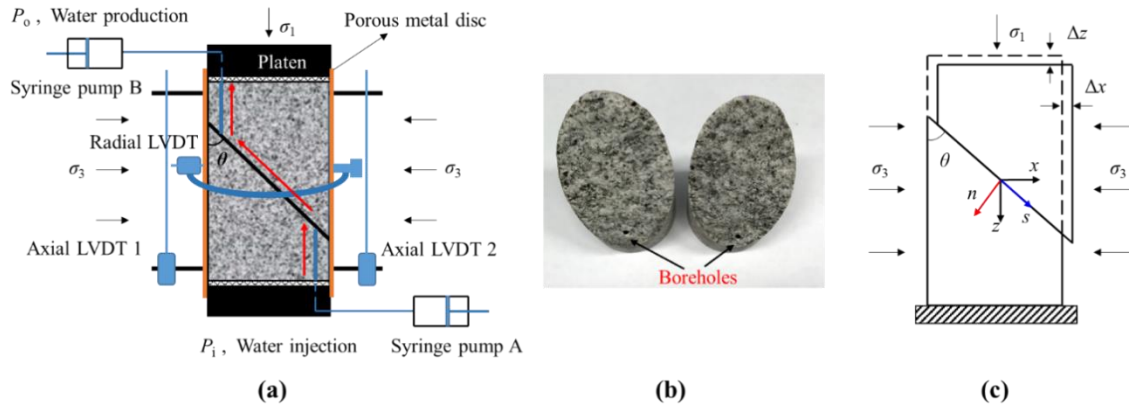


Figure 2.4: (a) The sketch of experimental setup; (b) granite fracture with boreholes for fluid flow; (c) the sketch of fracture deformation during triaxial shear tests.

For a given stress condition with a constant confining pressure (σ_3) and an initial axial stress (σ_1), constant axial stress (Bauer et al., 2016; Nemoto et al., 2008; Rutter & Hackson, 2017; Ye et al., 2017a, 2017b) and constant piston displacement (Ye et al., 2017a, 2017b) are two different experimental control modes that can be used to induce fracture slip

by increasing injection pressure. These two control modes provide two different boundary conditions when running a triaxial shear test. During a triaxial shear test with injection, the effective normal stress (σ'_n) and the corresponding critical shear stress $\tau_c = \mu\sigma'_n$ (μ is the sliding friction coefficient) gradually decrease as the pore pressure is elevated. Fracture slip occurs when the critical shear stress (τ_c) is reduced to the shear stress (τ) along the fracture plane. In a test using constant axial stress control, the initial axial stress (σ_1) on the sample is held constant. This means that the differential stress ($\sigma_d = \sigma_1 - \sigma_3$) does not change so that the shear stress (τ) remains constant (see Eq. (2-4)). As a result, the fracture slip does not stop when the shear stress along the fault touches the shear strength envelope (Figure 2.5(a)). In one injection test we conducted on a rough-walled granite fracture using the constant axial stress control (Ye et al., 2017a), a rapid, non-stop, and audible shear slip occurred. The relatively large shear slip (>2 mm) caused jacket failure and the test was terminated.

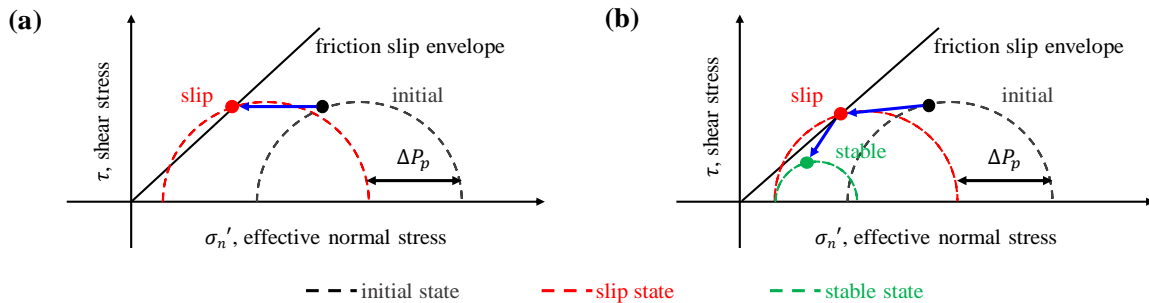


Figure 2.5: The evolution of normal and shear stress components on the fracture plane during triaxial-injection shear test (the confining pressure is held constant, and the slip is induced by increasing injection pressure). (a) Constant axial stress control: the shear stress is held constant, and a non-stop slip (red dot) will be induced on the fracture when shear stress reaches the critical shear strength. (b) Constant piston displacement control: both shear stress and effective normal stress decrease when fracture slip (red dot) is initiated by water injection, and thus the fracture will reach a stable state (green dot) at a lower stress level.

On the other hand, the loading piston does not move during injection and fracture slip under constant piston displacement control, by controlling the displacement of the loading piston on the MTS actuator and setting it to a constant. Once fracture slip is initiated,

the differential stress acting on the sample decreases significantly in response to the sample shortening with the gradual sliding of the fracture. As a result, the fracture slip slows down and finally terminates when the differential stress decreases to a lower level (Figure 2.5(b)). It is clear that an injection test performed under the experimental control of constant piston displacement is more realistic, and it captures stress relaxation and post-shear behavior of the fracture. All the four injection tests in this paper were conducted using the constant piston displacement control. To our knowledge, the tests reported herein are the first triaxial-injection tests using constant piston displacement control that can capture stress relaxation during fracture shearing.

As shown in Figure 2.4(c), the measurements of fracture deformation (stress and displacement) in the test are with respect to the x - z coordinates rather than the local n - s coordinates of the fracture plane. To probe the permeability evolution in response to fracture deformation on the local fracture plane, coordinate transformations are required. The effective normal stress and shear stress can be separately calculated using Eq. (2-3) and Eq. (2-4). In addition, the normal dilation and shear slip are calculated as:

$$d_n = \Delta z \sin\theta - \Delta x \cos\theta \quad (2-6)$$

$$d_s = \Delta z \cos\theta + \Delta x \sin\theta \quad (2-7)$$

where, d_n and d_s are the fracture's normal dilation and shear slip, respectively; Δz is the total specimen axial deformation minus that due to the compression of the rock matrix; and Δx is the total specimen radial deformation minus radial deformation of the rock matrix.

The deformation of the rock matrix was neglected since it is relatively small compared with fracture deformation. Estimating the matrix deformation of a fractured rock sample based on intact rock elastic moduli overestimates the deformation of the matrix in a

fractured sample (due to stress concentration on the fracture), resulting in an underestimation of the deformation of the fracture. In this study, Δz is the average axial displacement recorded by two axial LVDTs, and Δx equals the lateral displacement measured by a radial LVDT.

2.3.3 Experimental Setup and Procedure

The experiments are carried out using an MTS 816 frame, which has a maximum axial load capacity of 1000 kN and includes a triaxial cell with a limit of 138 MPa confining pressure. Control and data acquisition are performed using MTS Series 793TM Control software. In the test, as shown in Figure 2.4(a), the average axial displacement of the rock sample is measured by two Linear Variable Differential Transformer (LVDT) position sensors mounted on the sample. Another LVDT sensor attached on a radial ring is used to record the transverse displacement of the sample. The associated error of this type of LVDT is $\pm 0.05\%$. The applied axial force is measured by a load-cell located inside of the triaxial pressure vessel, with maximum 1 KN loading error. Two Teledyne ISCO 100DM syringe pumps (68.95 MPa pressure limit, 25 mL/min flowrate limit, and 103 mL volume capacity) are used to inject / produce water and to measure the parameters related to fluid flow (pressure, flow rate and pump volume). The ISCO pump has a $\pm 0.5\%$ pressure error and a $\pm 0.3\%$ flow rate error. In addition, two porous metal discs (50.8 mm diameter by 3.2 mm thickness) with a pore size of 60 microns are placed on each end of the sample to provide an even fluid flow distribution (see Figure 2.4(a)). The measurements of mechanical parameters (displacement and stress) and fluid flow parameters (pressure and flow rate) are used to characterize the hydro-mechanical coupled responses of the fracture in shearing process. The

recording rate of the mechanical parameters is 2 Hz, while the recording rate of the pump data is 1 Hz.

As illustrated in Figure 2.4(a), during the test, a 30 MPa confining pressure (σ_3) was first applied on the sample. After that, the production pressure of pump B (P_o) was fixed to a constant value of 5 MPa, and the injection pressure of pump A (P_i) was set to an initial value of 5 MPa and later was increased incrementally to induce fracture slip. The purpose of providing an initial production and injection pressure is to completely saturate the fracture and to reduce the time period required to reach a steady-state flow regime at later injection steps. To diminish the plastic deformation caused by the initial seating between fractures, porous metal discs and platens, five loading-unloading cycles of differential stress (to a relatively low differential stress level of 10~20 MPa) were performed on the sample assembly. Before starting to increase injection pressure, the sample was loaded to a near-critical differential stress level which was determined from the deflection/dilation of the stress-strain curves (Li et al., 2012; Ye & Ghassemi, 2016). This near-critical stress level should be large enough to cause fracture slip during injection, but not exceed the shear strength to induce fracture slip before injection starts. Next, the test was switched to the constant piston displacement control which keeps the loading piston displacement of the MTS 816 frame constant during injection and fracture slip. Subsequently, the injection pressure was increased stepwise at a rate of 0.03 MPa/s from 5 MPa to 28 MPa to induce fracture slip. During the entire injection test, the injection pressure was at least 2 MPa smaller than the 30 MPa confining pressure. This prevents the jacket from bursting during water injection, and ensures that the *treatment* pressure is lower than the minimum principal stress. The stepwise elevation of the injection pressure was employed to investigate the evolution

of steady-state flow rate during fracture shearing. Due to the pressure difference between the two pumps, water was circulated from pump A to pump B after starting injection. Each injection pressure step lasted 300-500 seconds including a pressure buildup stage which required 150-250 seconds and a constant pressure hold stage which lasted another 150-250 seconds. After a target injection pressure was achieved, the pressure was held constant for at least 100 seconds before recording the flow rate to ensure the flow rate measurement was in the steady-state flow regime. When the flow rate out of pump A was nearly identical to the flow rate into pump B (the difference of flow rates is less than 5%), we considered the fluid flow through the fracture to have reached a steady-state flow regime. The injection pressure was increase in the stepwise manner described to induce fracture slip, resulting in significant displacement change, stress-drop, and flow rate increase.

To address whether the flow rate increase is retained after the fracture slips, an unloading segment was subsequently performed in which the injection pressure was lowered stepwise from 28 MPa to 8 MPa using the same pressure increment. Similarly, the steady-state flow rate at each injection pressure step during unloading segment was also measured. In the test, the time evolutions of fracture deformation and fluid flow were all recorded during the so-called *loading-unloading* cycle of injection pressure.

2.3.4 Permeability Evaluation

According to the cubic law (Witherspoon et al., 1980; Zimmerman & Bodvarsson, 1996), the fracture (granite fracture or shale fracture) used in our injection test is assumed as a parallel-sided fracture with an equivalent hydraulic aperture (a_h). The fracture permeability (k) is further evaluated by:

$$k = \frac{a_h^2}{12} \quad (2-8)$$

where, k is the fracture permeability evaluated by the cubic law; a_h is the equivalent hydraulic aperture of the fracture.

Considering the matrix permeability of the Sierra White granite is very small ($<10^{-18} \text{ m}^2$) and the gravity effect is negligible, the steady-state flow rate (Q) is represented using Darcy's law:

$$Q = -\frac{W a_h^3}{12\mu} \cdot \frac{\Delta P}{L} \quad (2-9)$$

where, Q is the steady-state flow rate under the constant injection pressure hold stage; ΔP is the differential pressure; μ is the fluid viscosity ($1.002 \times 10^{-3} \text{ Pa}\cdot\text{s}$ at $20 \text{ }^\circ\text{C}$ for water); W and L are the fracture width and length, respectively.

Therefore, the equivalent hydraulic aperture (a_h) of the fracture is estimated using the measurements in steady-state flow regime:

$$a_h = \left(-\frac{12\mu L Q}{W \Delta P} \right)^{1/3} \quad (2-10)$$

The two surfaces of each fracture are elliptical or near elliptical, and each surface contains a borehole (Figure 2.6(a)). In order to simplify the evaluation of the fracture permeability, the fluid flow region is assumed as a *rectangle* covered by the blue dotted line in Figure 2.6(b). The rectangle is assigned the same area (A) as the ellipse. The length (L) of the rectangle is the distance between the two boreholes on fracture surface, and the width (W) of the rectangle is equal to the area (A) of the ellipse divided by the length (L) of the rectangle. The actual fluid flow is different from the above assumption, but this method provides a rapid estimate of the fracture permeability.

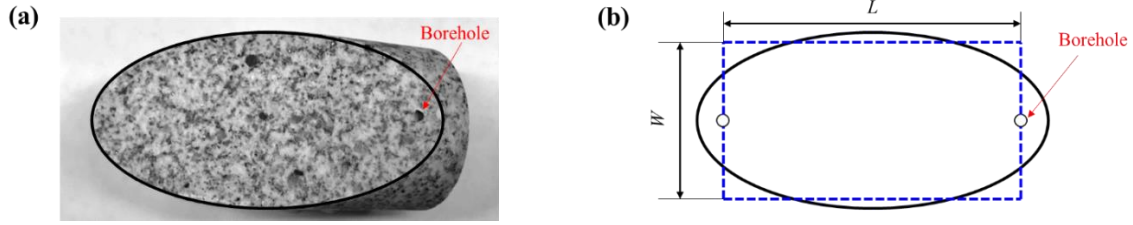


Figure 2.6: (a) The elliptical surface of a saw-cut fracture in Sierra White granite. (b) Fluid flow region for fracture permeability evaluation: the ellipse is the actual fluid flow region, while the rectangular area delineated by blue dotted lines is the equivalent fluid flow region.

2.4 Experimental Results

The test results of each injection test are shown in the time evolution plots of Figure 2.7(a)–2.7(d). The deformation properties and fluid flow parameters in the pre-injection stage (initial applications of confining pressure, axial loading, production pressure and injection pressure) are not shown. This means that the displacements and flow rates have been zeroed before injection. In the plots, the green curve represents the loading piston displacement of the MTS 816 frame, which was kept as constant under a constant piston displacement control. The blue curve is the injection pressure which was increased stepwise from 5 MPa to 28 MPa with six injection pressure steps ($P_i = 8, 12, 16, 20, 24$ and 28 MPa); after fracture shearing, the injection pressure was incrementally lowered to 8 MPa with the same step size of 4 MPa as in the loading path of injection pressure. The constant production pressure ($P_o = 5$ MPa) is represented by the gray curve. The cyan curve describes the differential stress history which shows a significant drop once fracture slip is initiated. The computed effective normal stress and shear stress (see Eq. (2-3) and Eq. (2-4)) on the fracture plane are separately illustrated by the black and dark-yellow curves. The purple and pink curves are the normal dilation and shear slip of the fracture calculated using Eq. (2-6) and Eq. (2-7), respectively. The steady-state flow rates measured at each injection pressure hold stage are shown as the dark-blue triangles linked with the dashed dark-blue curve. The

fracture permeability estimated from the steady-state flow rates (see Eq. (2-8) to Eq. (2-10)) are depicted by the dark-green dots connected by dashed dark-green curve. It is clear from the plots that the stresses, displacements, flow rates, and permeability values vary with the stepwise changes of injection pressure. Here, we used a rock mechanics sign convention: compression is positive. Therefore, fracture slip and dilation during water injection are demonstrated by a positive trend of shear slip and a negative trend of normal dilation, respectively. The experimental data in the injection pressure hold stages for each sample, including the steady-state flow rates (Q), the normal dilation (d_n) and shear slip (d_s), the effective normal stress (σ'_n) and shear stress (τ), as well as the hydraulic aperture (a_h) and fracture permeability (k), are listed in the Table 2.2.

Generally, as shown in Figure 2.7, the time evolution of the injection-induced fracture slip tests in this study have the same pattern and each test can be roughly divided into three stages: *stick* stage 1, *slip* stage 2, and *unloading* stage 3. Among these three stages, the stage 1 and stage 2 are from the loading path of injection pressure, while stage 3 illustrates the test during the unloading path of injection pressure. Major aspects of each stage and different hydro-mechanical responses of each test with characteristics related to the particular fracture surface roughness are discussed below:

- Stage 1: The injection pressure is less than 24 MPa (for samples SW-T1, SW-T2 and SW-S3) or less than 16 MPa (for sample SW-S4). In this stage, the fracture is in a *stick* state with almost negligible shear slip and dilation. Considering three decimal places in the displacement measurements, the fracture slip and dilation are zero or close to zero in this stage (see Table 2.2). The effective normal stress gradually decreased with the increase of pore pressure due to water injection, while the shear

stress declines slightly because of only minor decrease of the differential stress at this pre-shearing stage. This is to be expected because the shear stress only correlates with differential stress and the fracture angle but does not depend on the pore pressure (Eq. (2-4)). In this stage, relatively small enhancements of flow rate and fracture permeability are observed (the flow rate tends to linearly increase with the injection pressure). Hence, in this stage the major contributor to the increase of flow rate/permeability is the increase of fracture aperture in response to a decrease of the effective normal stress, with very little aperture increase caused by the dilatant shear slip of the fracture.

- Stage 2: In this stage, the injection pressure is continually increased stepwise to 28 MPa to induce fracture slip. In this *slip* stage, the fracture slip is accelerated due to the increasing injection pressure. As shown in the plots, the rapid increases of fracture slip and dilation occur at the highest injection pressure (from 24 MPa to 28 MPa) in the first three rough fracture tests (samples SW-T1, SW-T2 and SW-S3). Meanwhile, the flow rate and the corresponding permeability are also greatly enhanced due to the large aperture increase mainly caused by the dilatant shear slip of the fracture. The relaxation of the differential stress can be clearly observed, resulting in a dramatic decrease of both effective normal stress and shear stress on the fractures. The reduction of the effective normal stress also contributes to the increase of flow rate. However, the sudden and nonlinear *jump* in displacements (shear slip and normal dilation), differential stress, flow rate, and fracture permeability clearly demonstrate that the contribution of the fracture opening controlled by the effective normal stress should be much smaller than that of the self-

propping of asperities during and after the dilatant shear slip. Upon the rapid drop of the differential stress, the fracture slip rate decreases, and the slip appears

Table 2.2: Hydro-mechanical parameters under each hold stage with constant injection pressure.

Sample #	P_i (MPa)	Loading Segment						Unloading Segment				
		8	12	16	20	24	28	24	20	16	12	8
SW-T1	Q (mL/min)	0.053	0.114	0.190	0.280	0.389	6.220	4.270	2.870	1.900	1.120	0.462
	d_n (mm)	0.000	0.000	0.000	-0.001	-0.003	-0.157	-0.139	-0.130	-0.123	-0.118	-0.113
	d_s (mm)	0.000	0.000	0.001	0.002	0.008	0.532	0.539	0.534	0.529	0.525	0.521
	σ'_n (MPa)	65.47	63.35	61.27	59.14	56.94	31.79	33.45	35.35	37.29	39.22	41.14
	τ (MPa)	67.16	66.96	66.82	66.63	66.32	29.35	28.72	28.57	28.48	28.36	28.23
	a_h ($\times 10^{-6}$ m)	1.63	1.59	1.62	1.66	1.72	4.05	3.81	3.61	3.49	3.40	3.36
	k ($\times 10^{-12}$ m ²)	0.22	0.21	0.22	0.23	0.25	1.37	1.21	1.09	1.02	0.97	0.94
SW-T2	Q (mL/min)	0.115	0.276	0.450	0.750	1.505	11.100	7.200	5.150	3.540	2.160	0.910
	d_n (mm)	0.000	-0.001	-0.002	-0.003	-0.005	-0.142	-0.142	-0.139	-0.139	-0.133	-0.130
	d_s (mm)	0.000	0.001	0.003	0.007	0.015	0.571	0.572	0.566	0.565	0.557	0.552
	σ'_n (MPa)	66.74	64.53	62.37	60.19	57.88	29.36	31.26	33.23	35.23	37.18	39.14
	τ (MPa)	74.87	74.54	74.25	73.94	73.40	27.48	27.29	27.24	27.25	27.15	27.09
	a_h ($\times 10^{-6}$ m)	2.11	2.13	2.16	2.31	2.69	4.92	4.54	4.39	4.30	4.24	4.21
	k ($\times 10^{-12}$ m ²)	0.37	0.38	0.39	0.44	0.60	2.02	1.72	1.61	1.54	1.50	1.48
SW-S3	Q (mL/min)	0.022	0.050	0.078	0.121	0.150	0.860	0.460	0.310	0.210	0.130	0.054
	d_n (mm)	0.000	0.000	0.000	0.000	0.000	-0.044	-0.044	-0.044	-0.043	-0.042	-0.041
	d_s (mm)	0.000	0.000	0.000	0.001	0.001	0.071	0.072	0.072	0.073	0.073	0.073
	σ'_n (MPa)	31.65	29.58	27.53	25.48	23.42	15.25	17.27	19.14	21.01	22.86	24.79
	τ (MPa)	14.70	14.57	14.48	14.38	14.26	3.55	3.19	2.95	2.68	2.44	2.31
	a_h ($\times 10^{-6}$ m)	1.22	1.21	1.20	1.26	1.25	2.10	1.81	1.72	1.68	1.66	1.64
	k ($\times 10^{-13}$ m ²)	1.24	1.21	1.21	1.32	1.30	3.66	2.74	2.47	2.34	2.30	2.25
SW-S4	Q (mL/min)	0.005	0.012	0.022	0.035	0.056	0.113	0.064	0.037	0.024	0.013	0.005
	d_n (mm)	0.000	0.000	-0.001	-0.008	-0.021	-0.041	-0.038	-0.036	-0.034	-0.033	-0.032
	d_s (mm)	0.000	0.000	0.000	0.017	0.041	0.075	0.077	0.078	0.079	0.079	0.079
	σ'_n (MPa)	30.75	28.73	26.51	22.92	19.25	15.31	17.13	19.00	20.89	22.82	24.81
	τ (MPa)	12.56	12.53	12.14	9.38	6.48	3.12	2.82	2.59	2.41	2.28	2.27
	a_h ($\times 10^{-6}$ m)	0.74	0.75	0.79	0.83	0.90	1.07	0.94	0.85	0.81	0.77	0.74
	k ($\times 10^{-13}$ m ²)	0.46	0.47	0.52	0.58	0.67	0.95	0.74	0.60	0.55	0.49	0.46

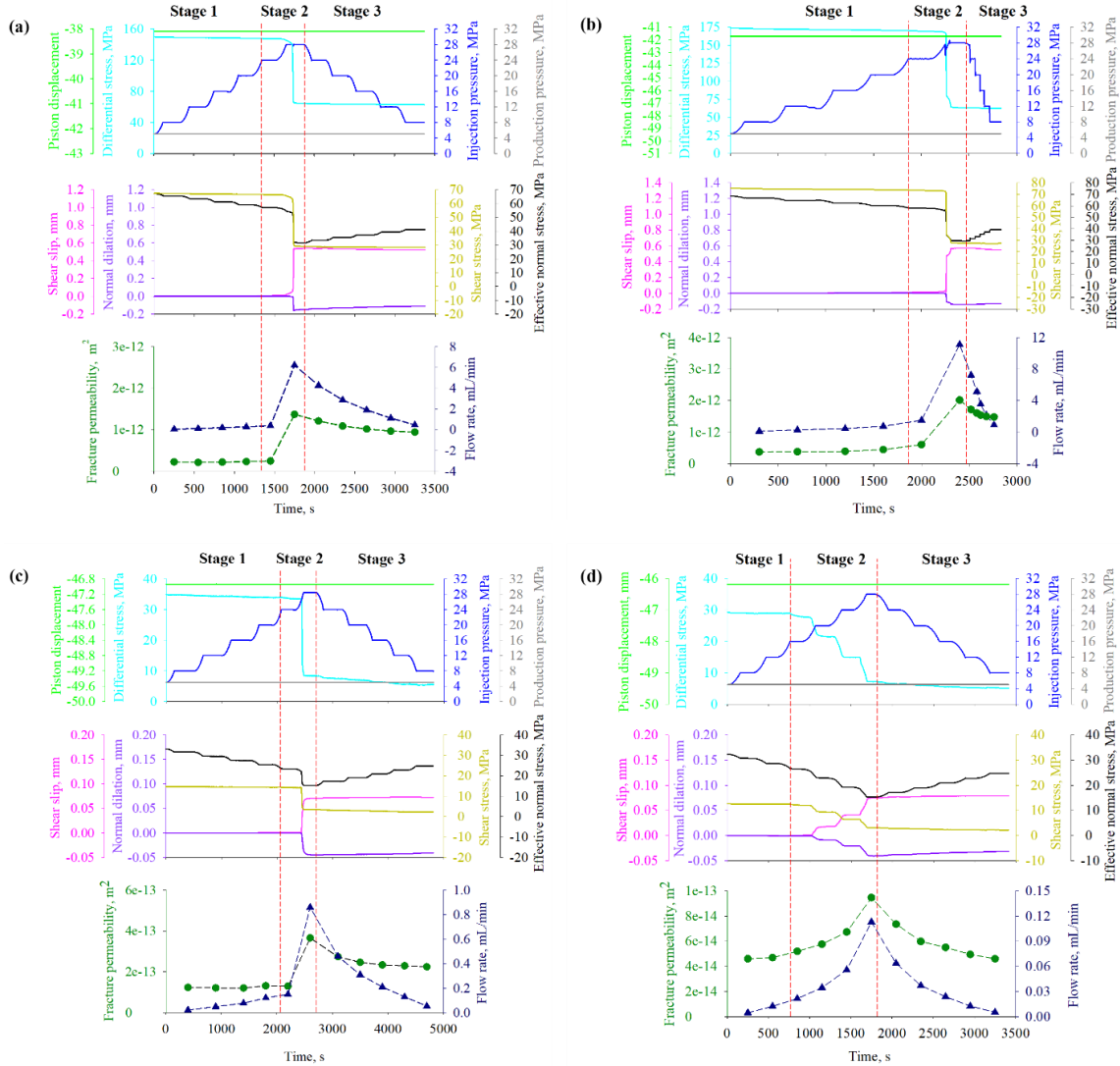


Figure 2.7: The hydro-mechanical measurements of injection-induced shear tests: (a) sample SW-T1; (b) sample SW-T2; (c) sample SW-S3; (d) sample SW-S4.

to terminate at some lower stress. On the other hand, the fracture slip in sample SW-S4 (the polished saw-cut fracture) occurred gradually after the pressure was increased above 16 MPa, resulting in a relatively small displacement change, stress-drop, and flow rate/permeability increase.

- Stage 3: The injection pressure is incrementally decreased from 28 MPa to 8 MPa with a step size of 4MPa after the shear slip of the fractures. During this *unloading* stage, the effective normal stress increases due to the decrease in pore pressure while

the shear stress shows no significant change (the differential stress shows no notable drop after termination of the rapid shear sliding). With continuous decline of pore pressure, the fracture closes due to the increase in effective normal stress, resulting in a flow rate/permeability decrease. In addition, the asperity degradation and gouge produced in the shearing process could block the flow pathways, further causing the flow rate/permeability to decrease.

For sample SW-T1, a shear slip of 0.532 mm and a normal dilation of 0.157 mm were induced during the period of high pressure injection (24 MPa to 28 MPa), leading to a ~117 times flow rate increase, from the base flow rate of 0.053 mL/min to 6.22 mL/min (the base flow rate was measured at the 8 MPa injection pressure stage before fracture shearing) while the differential stress dropped from 148 MPa to 64 MPa. During fracture shearing, the corresponding fracture permeability increased ~6 times; from the base permeability of $0.22 \times 10^{-12} \text{ m}^2$ to the enhanced permeability of $1.37 \times 10^{-12} \text{ m}^2$. For sample SW-T2, the flow rate increased rapidly from the base flow rate of 0.115 mL/min to a maximum steady-state flow rate of 11.10 mL/min (~97 times increase) in response to a shear slip of 0.571 mm and a normal dilation of 0.142 mm, and a differential stress drop of 107 MPa (from 170 MPa to 63 MPa). Also, by comparing the maximum permeability ($2.02 \times 10^{-12} \text{ m}^2$) and the base permeability ($0.37 \times 10^{-12} \text{ m}^2$), it is noticed that permeability has been increased by more than five times. As shown in Figure 2.7(b), the time period of each injection step during the unloading segment of the test on sample SW-T2 was only ~100 seconds, which was shorter than the 400 seconds duration of each injection step during the loading segment. Since the flow rate was high (11.10 mL/min) after the fracture was sheared, the limited pump volume (103 mL) mandated reducing the time of each step during the lowering of the injection

pressure to complete the test without refilling/bleeding pumps. However, even during a shorter time interval, the fluid flow quickly reached steady-state as evidenced by the rapid equilibration of the production and injection flow rates (fast fluid flow after fracture shearing).

In the third test on the unpolished saw-cut fracture, SW-S3, relatively smaller shear slip (0.071 mm) and normal dilation (0.044 mm) were observed in the fracture slip stage. However, the flow rate still was enhanced 39 times to 0.86 mL/min from the base flow rate of 0.022 mL/min while the relaxation of differential stress was 26 MPa (from 34 MPa to 8 MPa) during the fracture shearing. The enhanced permeability was calculated to be $3.66 \times 10^{-13} \text{ m}^2$, which is ~ 3 times larger than the base permeability of $1.24 \times 10^{-13} \text{ m}^2$. The last injection test was performed on the polished saw-cut fracture, SW-S4, which was used as a control sample to simulate injection-induced shear slip on an *ideally* smooth fracture. The slip on this sample was distinct from those in other samples. Sample SW-S4 displayed gradual fracture slip after the pressure was increased above 16 MPa. For the other samples with a rough fracture, rapid slip was induced in a short time (~ 10 seconds) once the injection pressure reached the critical condition. The enhanced flow rate for sample SW-S4 was 0.113 mL/min (~ 23 times larger than the based flow rate of 0.005 mL/min) corresponding to a shear slip of 0.075 mm, a normal dilation of 0.041 mm, and a differential stress drop of 20 MPa (from 27 MPa to 7 MPa). The fracture permeability of the sample SW-S4 increased ~ 2 times; from the base value of $0.46 \times 10^{-13} \text{ m}^2$ to $0.95 \times 10^{-13} \text{ m}^2$ with the elevation of the injection pressure. While the two saw-cut fractures experienced nearly the same magnitude of normal dilation during fracture shearing, the dilatant slip on the unpolished fracture promoted larger permeability enhancement than that in the polished fracture.

Overall, the results of the four tests indicate that rough fractures tend to experience much larger changes of fracture deformation, stress relaxation, flow rate, and permeability during fracture shearing by injection. Recognizing that it is possible to induce significant permeability enhancement on rough fractures, the notion of permeability increase related to fracture self-propping by asperities during reservoir stimulation by shearing is reasonable.

2.5 Discussion

2.5.1 Retainable Permeability Enhancement

To study whether the permeability enhancement due to fracture slip and dilation can be retained after the pore pressure (or reservoir pressure) is reduced, the injection pressure was incrementally decreased after fracture slip during the unloading stage (3rd stage) of each test. Figure 2.8(a) – 2.8(d) are plots of the permeability vs. injection pressure; an expected hysteresis of permeability during the loading-unloading cycle of injection pressure is observed in samples SW-T1, SW-T2 and SW-S3, while just a minor hysteresis of permeability is detected on the sample SW-S4. During the loading path (with increase of injection pressure), permeability tends to linearly increase with the elevation of injection pressure until fracture slip is initiated. The permeability enhancement then becomes nonlinear, increasing more rapidly. Here, the nonlinear behavior of fluid flow is not only related to the high-pressure injection (Javadi et al., 2014; Ranjith & Viete, 2011; Singh et al., 2015), but also to the dilatant fracture shearing. On the other hand, the fluid flow tends to change from nonlinear flow to linear flow as the decrease of injection pressure during the unloading segment of each test. Since there is no further fracture shearing during the unloading segment, the alteration of flow behavior should be dependent on the change of injection pressure in the fracture that has experienced shear-induced asperity degradation.

The ratio of the permeability at a given injection pressure step after fracture shearing and the permeability of a step at the same injection pressure but before fracture shearing (see the permeability data in Table 2.2), provides an indicator of permeability retention. The average retention ratios are separately 5, 4, and 2 for the first three tests on rough fractures, while the average retention ratio of sample SW-S4 is close to 1. This means that the permeability increase is negligible for an *ideally* smooth fracture with insufficient asperities. Considering the surface roughness characteristics of the fractured samples, a probable explanation for the retention of the permeability increase is that sufficient dilation of the rough fracture was caused by water injection, allowing the fracture to prop open due to the asperities.

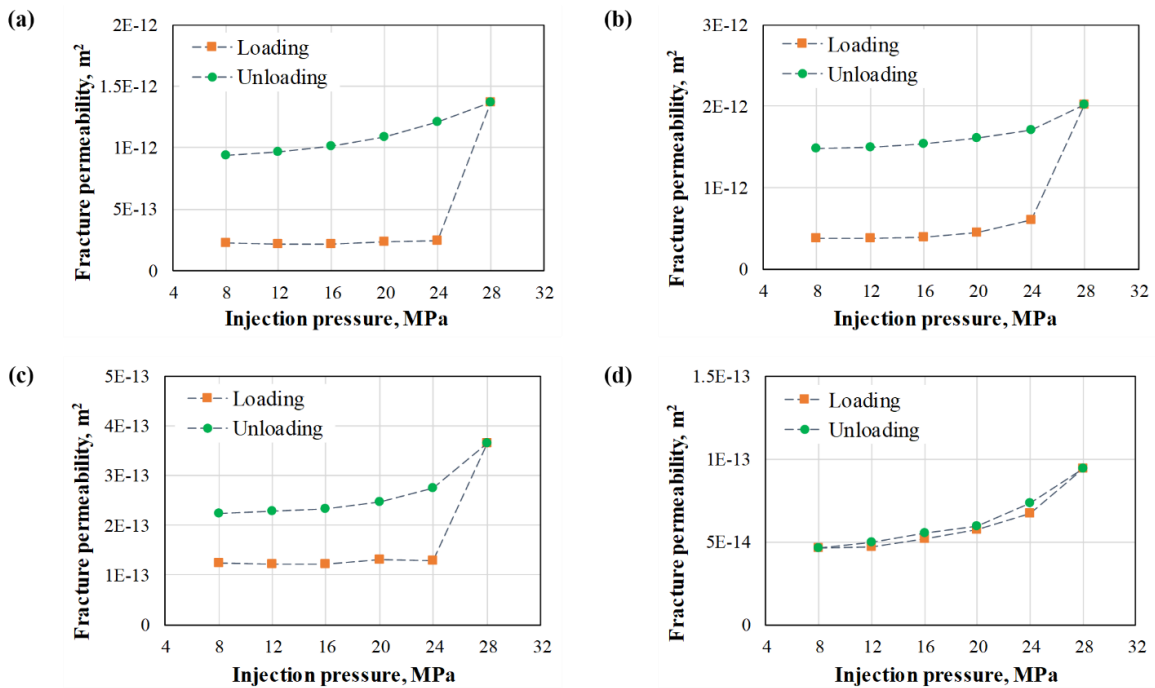


Figure 2.8: The retention of permeability enhancement during the loading-unloading cycle of injection pressure: (a) sample SW-T1; (b) sample SW-T2; (c) sample SW-S3; (d) sample SW-S4.

2.5.2 Permeability Evolution with Mechanical Properties

Another question that can be addressed from our experiments is how the mechanical properties (displacement and stress) influence fluid flow during fracture shearing. Using the data in Table 2.2, we plotted fracture permeability vs. effective normal and shear stresses

(Figure 2.9), and fracture permeability vs. normal and shear displacements (Figure 2.10) on the fracture plane to investigate permeability evolution with mechanical deformation. The hydro-mechanical coupled plots in Figure 2.9 and Figure 2.10 can be divided into three periods: *stick* period, *slip* period, and *unloading* period. It is clear that most changes of stress, displacement, and permeability occur in the *slip* period of the plots.

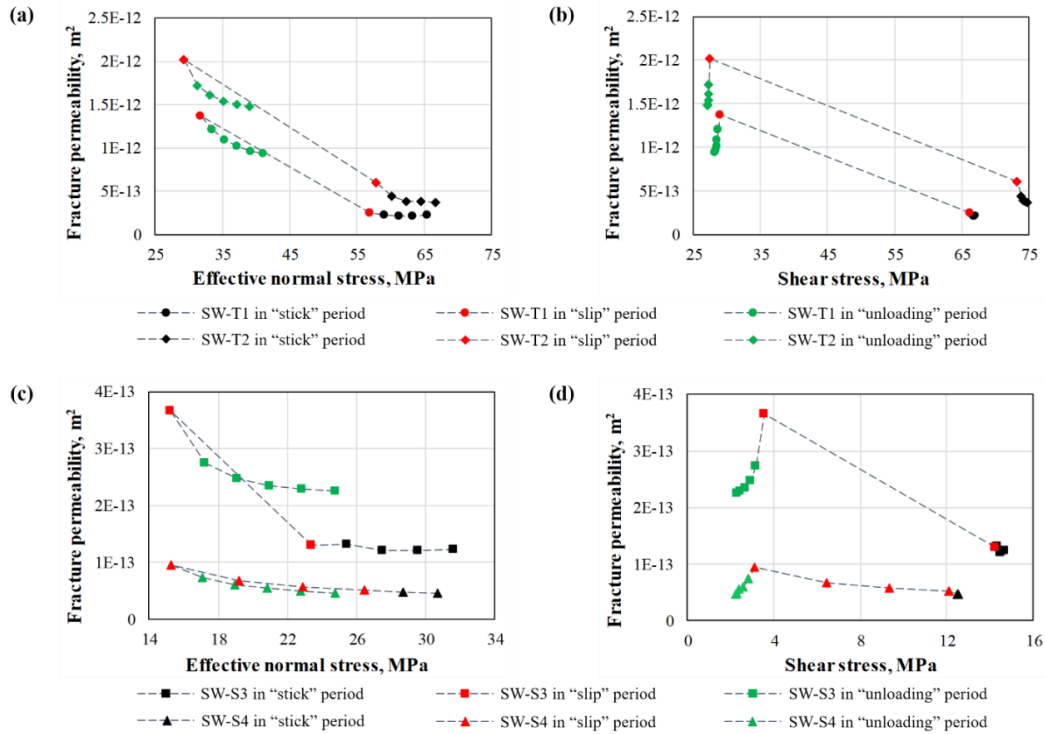


Figure 2.9: Permeability evolution with effective normal stress: (a) samples SW-T1 and SW-T2; (c) samples SW-S3 and SW-S4. Permeability evolution with shear stress: (b) samples SW-T1 and SW-T2; (d) samples SW-S3 and SW-S4. In the plots, the black, red and green data points are for the *stick*, the *slip*, and the *unloading* periods, respectively. Rough fractures (SW-T1, SW-T2 and SW-S3) show a rapid stress relaxation in the *slip* period (including 2 red data points), while a gradual stress relaxation is observed for the smooth fracture (SW-S4).

As can be seen in Figure 2.9, samples with a tensile fracture (SW-T1 and SW-T2) or an unpolished saw-cut fracture (SW-S3) experienced a rapid stress-drop and a significant permeability increase during the *slip* period, while the sample with a polished saw-cut fracture (SW-S4) shows a gradual change of stress and permeability during fracture shearing. In the rough fracture tests (SW-T1, SW-T2 and SW-T3), a relatively large decrease (8 to 9

MPa) of effective normal stress and a slight decrease (0.4 to 1.5 MPa) of shear stress are noticed in the *stick* period, demonstrating that the minor increase of permeability in this period is mainly caused by the decrease of effective normal stress due to the elevation of injection pressure. In the *slip* period, a considerable relaxation of both effective normal stress (25 to 28 MPa decrease in samples SW-T1 and SW-T2, and 8 MPa decrease in sample SW-S3) and shear stress (37 to 46 MPa drop in samples SW-T1 and SW-T2, and 11 MPa drop in sample SW-S3) are observed. The large stress relaxation and the high permeability increase in this *slip* period correlate well with the fast fracture slip. In the *unloading* period, the effective normal stress increased noticeably (9 to 10 MPa increase due to the incrementally decrease of injection pressure), while the shear stress decreased slightly (0.4 to 1.2 MPa). This means that the decline of permeability in this period (*unloading* period) is related to the increase of the effective normal stress. On the other hand, the *ideally* smooth fracture SW-S4 presents a gradual and slow stress change (see Figure 2.9(c) and Figure 2.9(d)), and shows a slight increase in the fracture permeability. Moreover, in the rough fracture tests, a fast and nonlinear decline of permeability is observed during the lowering of the injection pressure, even though the magnitude of the effective normal stress change in the *unloading* period is very close to that in the *stick* period. This indicates that in addition to the fracture closure caused by the increase in the effective normal stress, the shear-induced asperity degradation could also be a major factor in restricting the fluid flow after fracture shearing.

As shown in Figure 2.10, samples with a tensile fracture (SW-T1 and SW-T2), have similar values of fracture deformation (0.14 to 0.16 mm normal dilation, and 0.53 to 0.57 mm shear slip) during shearing. The fracture deformation caused by shearing of the two saw-

cut fractures are also close to each other (0.041 to 0.044 mm normal dilation, and 0.071 to 0.075 mm shear slip) and are relatively smaller than those of the tensile fractures. As a result, the permeability values of the tensile fractures are around one or two orders of magnitude higher than that in saw-cut fractures. During the injection tests, initially

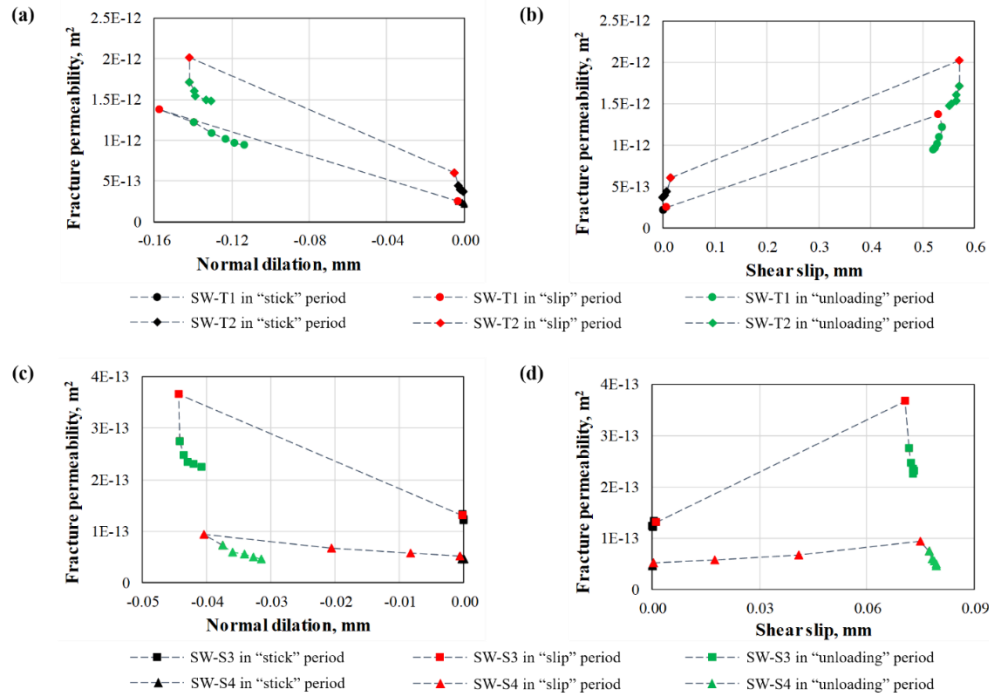


Figure 2.10: Permeability evolution with fracture’s normal dilation: (a) samples SW-T1 and SW-T2; (c) samples SW-S3 and SW-S4. Permeability evolution with fracture’s shear slip: (b) samples SW-T1 and SW-T2; (d) samples SW-S3 and SW-S4. In the plots, the back, red, and green data points represent the *stick*, the *slip*, and the *unloading* periods, respectively. Rough fractures (SW-T1, SW-T2 and SW-S3) show a rapid shear slip in the *slip* period (including 2 red data points), while a gradual shear slip with lower velocity is observed for the smooth fracture (SW-S4).

fractures tend to be in a *stick* period, showing slight changes of shear slip and normal dilation, and thus resulting in a small increase in fracture permeability. Once reaching the critical condition with increasing injection pressure, fractures start to slip and dilate: rough fractures tend to slip at a faster rate, while smooth fractures tend to slip at a moderate rate. Much higher permeability increase is observed in the *slip* period because of the larger normal dilation caused by shearing. During *unloading*, the normal dilation decreases because fractures tend to close under compression as the injection pressure declines. The shear slip

on the tensile fracture shows a minor decrease during unloading (see Figure 2.10(b)), which could be related to the increase in contact between asperities under lower injection pressure. In contrast, the shear slip of the saw-cut fracture shows a slight increasing trend with decreasing injection pressure (see Figure 2.10(d)). A possible reason is that a smooth fracture has less shear resistance, so it can slip a little even under low injection pressure. Moreover, the irreversible behaviors of shear slip and normal dilation can be clearly observed in the plots, implying that a fracture is propped open by asperities after fracture shearing. The smoothest fracture, SW-S4, starts to slip at a relatively lower injection pressure, and with a slow slip rate. In addition, the shear slip on SW-S4 only leads to a slight permeability increase, indicating that the permeability enhancement by shear stimulation is highly dependent on the roughness of fractures.

According to the aforementioned observations, it can be concluded that the evolution of the hydro-mechanical properties during fracture shearing experiments reflect the processes which occur during injection into the fractured subsurface rocks for saltwater disposal, and EGS, etc. In particular: (1) before the fracture is sheared (nonslip stage), the production from the sample shows only a limited increase in response to injection. This is mainly due to an effective normal stress reduction without propping; (2) with continued injection, the effective normal stress is further decreased and the fracture reaches a slip state, resulting in a significant permeability enhancement and thus production increase due to the irreversible normal dilation caused by a relatively large shear slip.

2.5.3 Slip Characteristics and Stress Relaxation

The shearing of faults/fractures and associated stress relaxation/drop are widely observed in the episodes of seismicity or micro-seismicity (Brenner et al., 2008; Gao &

Crampin, 2004; Kato et al., 1997; Yang & Toksöz, 1981). In order to probe the stress relaxation and its correlation with slip characteristics during fracture shearing by injection, the time evolution plots of shear slip, and differential stress in the slip period of each test are highlighted in Figure 2.11. The plots (in Figure 2.11(a) - 2.11(c)) correspond to the rapid slip period of the test on rough fractures (tensile fractures SW-T1 and SW-T2, and the unpolished saw-cut fracture SW-S3). On the other hand, the polished saw-cut fracture (SW-S4) displays a gradual fracture slip mode after the pressure was increased above 16 MPa, and contains three slip periods (see Figure 2.7(d)). Figure 2.11(d) shows the third slip period of SW-S4 with a relatively faster slip velocity under high pressure injection.

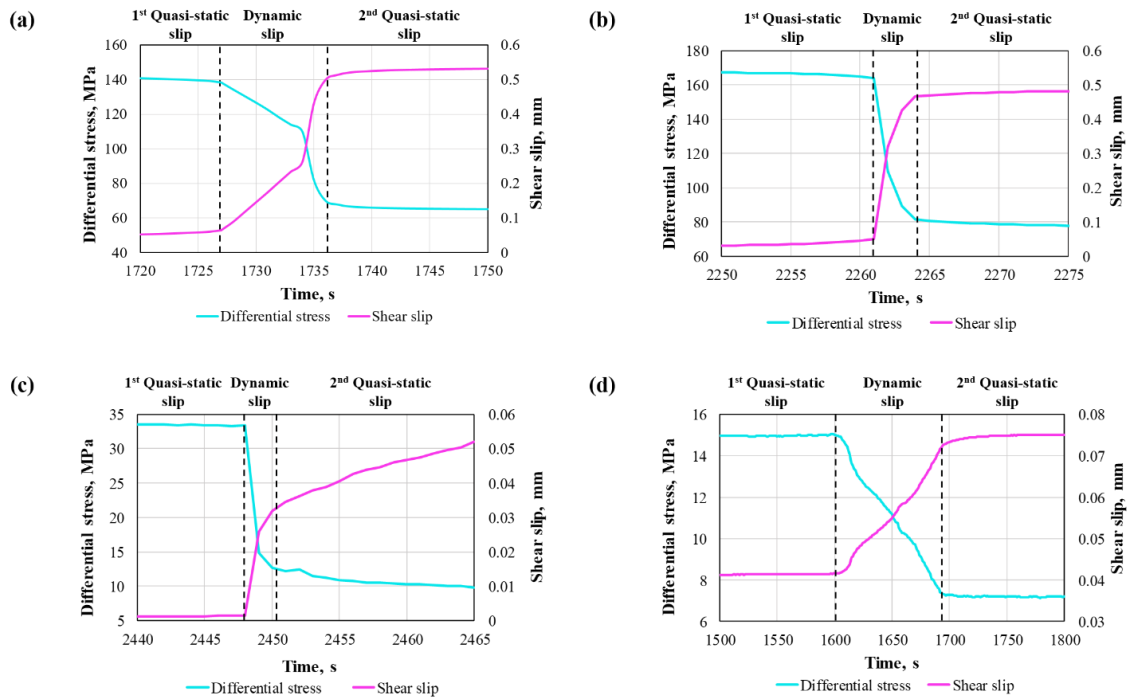


Figure 2.11: Slip characteristics and stress relaxation in the rapid slip period of each injection test: (a) sample SW-T1; (b) sample SW-T2; (c) sample SW-S3; (d) sample SW-S4.

Using injection-induced shear tests on saw-cut fractures, Nemoto et al. (2008) used the term *quasi-static* slip to represent fracture slip with a low velocity (less than 5×10^{-5} m/s), and used *dynamic* slip to indicate fracture slip with a fast velocity (higher than 5×10^{-5} m/s).

However, the corresponding stress drop during fracture slip was not characterized in their tests. In this paper, we use the same terminology for fracture shear slip to further analyze the slip characteristics and associated stress relaxation.

The plots in Figure 2.11 show that the curves of shear slip (d_s , pink curve), and differential stress (σ_d , cyan curve) are piecewise linear functions of elapsed time during fracture slip. As shown in Figure 2.11(a) to Figure 2.11 (c), the injection tests on rough fractures (samples SW-T1, SW-T2, and SW-S3) display similar shear slip characteristics during the shearing process. In the first part of the time evolution plot, fracture slips at a relatively slow rate which can be referred to as quasi-static slip interval. In this quasi-static slip interval, only a small stress relaxation is observed ($< 3\text{MPa}$ stress drop in all tests). As the injection continues, fracture slip rapidly, and a much higher flow rate is achieved. The duration of this dynamic slip interval is less than 10 seconds for the rough fracture tests. The associated stress drop is high with a fast decline rate (70 to 80 MPa stress drop in tensile fractures SW-T1 and SW-T2, and $\sim 20\text{MPa}$ stress drop for the unpolished saw-cut fracture SW-S3). Because of the large stress drop, the fracture slip tends to slow down and switches back to quasi-static slip state. It is reasonable to expect that the fracture slip will be eventually stop once the shear stress declines to a lower level (unless the stress re-accumulates by further loading). The test control sample (*ideally* smooth fracture SW-S4) also exhibits a piecewise linear behavior of shear slip, containing two quasi-static slip intervals and one dynamic slip interval. However, the slip duration of each interval in this sample lasts much longer (~ 100 seconds), and the fracture slips with a much lower velocity corresponding to a relatively small stress relaxation ($\sim 8\text{MPa}$ stress drop).

The slopes of the time evolution plots of shear slip (d_s) and differential stress (σ_d) are the shear slip rate ($\frac{dd_s}{dt}$) and the corresponding stress drop rate ($\frac{d\sigma_d}{dt}$, the negative sign means stress drop), respectively. The average values of slip rate and stress drop rate under each slip interval are listed in Table 2.3. For rough fractures (tensile fractures SW-T1 and SW-T2, and the unpolished saw-cut fracture SW-S3), the slip rate in the quasi-static slip interval is on the order of $\sim 10^{-8}$ to $\sim 10^{-6}$ m/s. While in the dynamic slip interval, the slip rate is on the order of $\sim 10^{-5}$ m/s. Guglielmi et al. (2015a) directly measured the shear slip on a real fault in carbonate rock during a field-scale injection test and observed $\sim 10^{-6}$ to $\sim 10^{-5}$ m/s slip rates at the onset of micro-seismicity. This means that the slip rate measurements in our lab-scale injection tests on rough fractures are in the same range as the field observations, except the slip rate of the unpolished saw-cut fracture (SW-S3) which had a relatively slower slip rate of 2.35×10^{-8} m/s in the first quasi-static slip interval. In addition, rapid stress drop rates of ~ 7 to ~ 20 MPa/s are observed in the dynamic slip intervals of rough fracture tests, indicating a large energy release in a short time during fracture shearing. The rates of stress relaxation under quasi-static slip intervals are one or two orders of magnitude smaller than the slip rates in the dynamic slip interval. For the polished saw-cut fracture (SW-S4), the slip rates in the quasi-static slip intervals are on the order of $\sim 10^{-9}$ to $\sim 10^{-8}$ m/s, while in the dynamic interval the slip rate is 3.22×10^{-7} m/s. The associated stress drop rate is also much smaller, and on the order of $\sim 10^{-4}$ to $\sim 10^{-2}$ MPa/s. Moreover, fracture slip correlates well with the associated stress relaxation: a faster fracture slip induces a quicker stress relaxation, and vice versa.

Table 2.3: The values of slip rate and stress drop rate at slip period of each test.

Sample #	Slip rate ($\frac{dd_s}{dt}$), m/s			Stress relaxation rate ($\frac{d\sigma_d}{dt}$), MPa/s		
	1 st quasi-static slip	dynamic slip	2 nd quasi-static slip	1 st quasi-static slip	dynamic slip	2 nd quasi-static slip
SW-T1	1.76×10^{-6}	4.89×10^{-5}	1.07×10^{-6}	-0.33	-7.69	-0.15
SW-T2	1.61×10^{-6}	9.81×10^{-5}	1.01×10^{-6}	-0.25	-19.51	0.20
SW-S3	2.35×10^{-8}	1.05×10^{-5}	1.21×10^{-6}	-0.03	-6.56	-0.16
SW-S4	2.38×10^{-9}	3.22×10^{-7}	1.47×10^{-8}	-5.14×10^{-4}	-0.08	-5.03×10^{-4}

2.5.4 Asperity Degradation During Injection-Induced Fracture Shearing

The degradation of fracture asperities and gouge production during fracture shearing processes have been recognized in many previous laboratory-scale tests (Homand et al., 2001; Huang et al., 1993; Hutson & Dowding, 1990; Lee et al., 2001; Vogler et al., 2016; Zhao et al., 2012). However, most of these tests have been used to study the asperity degradation controlled by normal stress or shear stress under different loading modes (single-stage loading or cyclic loading). The observations of asperity degradation, and gouge production during fracture shearing caused by injection are rare. After completion of the injection tests, we observed a few relatively large rock chips (maximum ~5 mm wide by ~10 mm long) and large amounts of small-sized gouge (0.1-1.0 mm) in the tensile fractures (SW-T1 and SW-T2). However, only minor surface damage and very fine gouges (<0.3 mm) were detected in the two saw-cut fractures (SW-S3 and SW-S4).

As shown in Figure 2.12(a) and Figure 2.12(c), significant slickensides (the polished area with white-colored patches on the fracture surfaces) can be seen on the tensile fractures SW-T1 and SW-T2 after testing, indicating that the two opposite fracture surfaces of each sample slipped past each other during injection. Several large rock chips were observed in the two tensile fractures, which are related to failure of asperities through *abrasion* (Zhao et al., 2012): the contacting asperities on fracture surfaces plough over each other to produce

relatively large-sized chips/gouge. As mentioned above, we also observed large amounts of relatively small-sized gouge (0.1 ~ 1.0 mm) on the tested samples. The small-sized gouge produced during the injection likely resulted from crushing of the large-sized chips or gouge particles (generated by *abrasion*) with the increasing shear slip. It is observed that the large rock particles were chipped off from the edges of the fractures (close to the sidewall boundary) and the fine gouge particles were produced from the interior fracture areas. These observations indicate the above explanation of the failure mode of asperity is reasonable because the interior gouge experiences a longer period of shearing/crushing.

The contours in Figure 2.12(b) and Figure 2.12(d), constructed by the 3D laser scanner, show the topography of the fracture surfaces of samples SW-T1 and SW-T2 after shearing. Note that the color scales of the two fracture surfaces in each sample no longer mate after shearing (compare with Figure 2.2). This is an indicative of the surfaces mismatch due to the asperity degradation. After sample SW-T1 was sheared, the maximum surface relief of the top and bottom fracture surfaces (the left and right contours in Figure 12(b)) were 5.21 mm and 5.92 mm, respectively. Comparison with the initial surface relief of 6.43 mm for both fracture surfaces (Figure 2.2(a)), sample SW-T1 shows 0.51-1.22 mm reduction in asperity height during fracture slip. For sample SW-T2, after shearing, the maximum surface relief was 5.56 mm for the top fracture surface (the left contour in Figure 2.12(d)), and 4.41 mm for the bottom fracture surface (the right contour in Figure 2.12(d)). This means that a maximum asperity degradation of 0.30-1.45 mm was induced on the fracture surfaces of sample SW-T2 after fracture shearing (the initial surface relief of the two fracture surfaces of sample SW-T2 are 5.96 mm, see Figure 2.2(b)). In addition, the highest degradation of asperities is located at the lower-right edge of the bottom surface (see the right contour in

Figure 2.12(d)), which matches with the location of the rock chips generated in SW-T2 (Figure 2.12(c)).

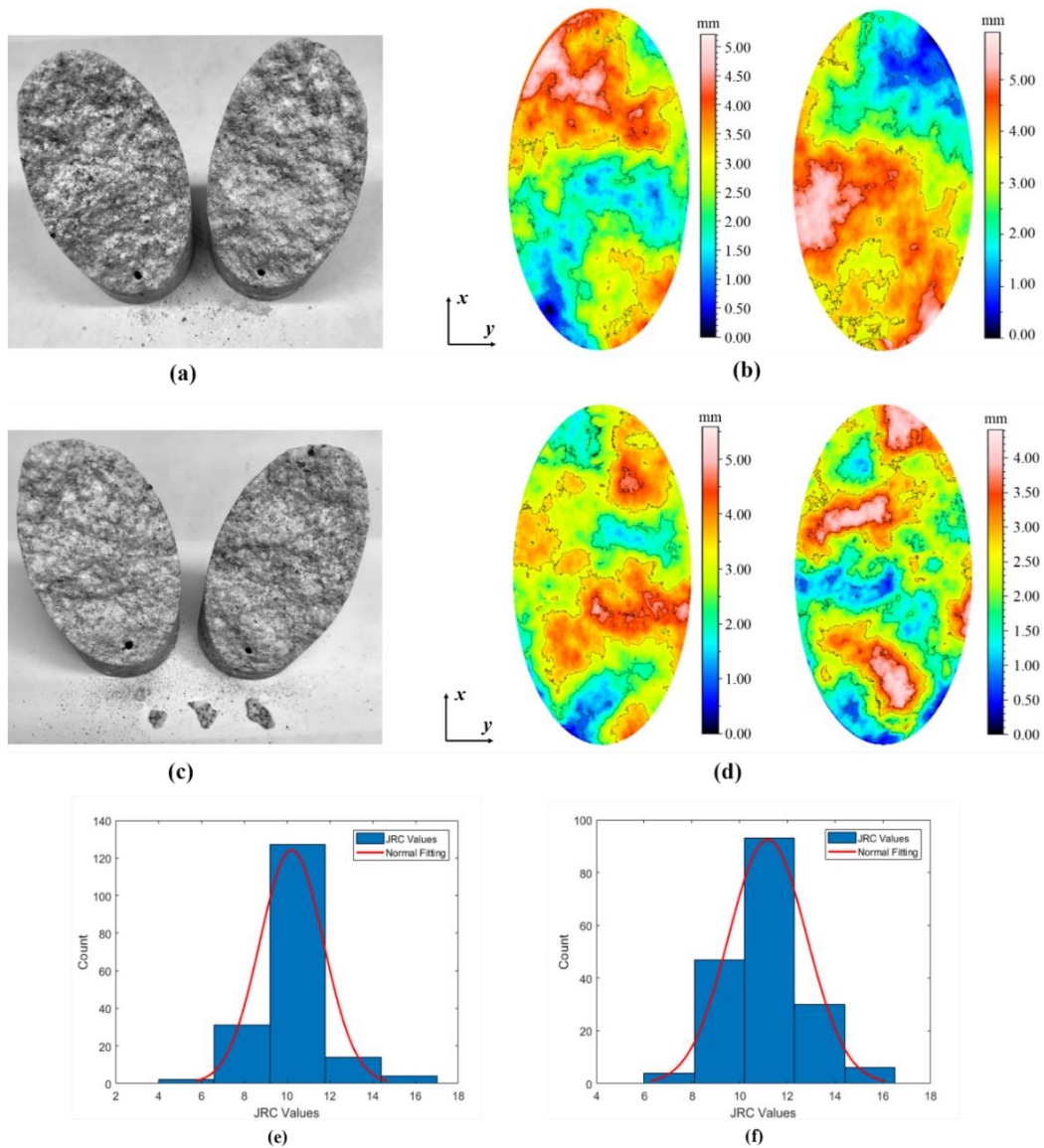


Figure 2.12: Shear-induced asperity degradation on rough tensile fractures: (a) the tested sample SW-T1; (b) the scanning contours of sample SW-T1 after testing (the left contour is for the top fracture surface; the right contour is for the bottom fracture surface); (c) the tested sample SW-T2; (d) the scanning contours of sample SW-T2 after testing (the left contour is for the top fracture surface; the right contour is for the bottom fracture surface); (e) and (f) are the JRC distribution of SW-T1 and SW-T2 after testing, respectively. Before scanning the fractures, the boreholes on fracture surfaces were filled with modeling clay carefully to avoid the influences of voids on the scanning results. Therefore, the boreholes were not located on the scanning contours.

After testing, the average JRC values are estimated from the scanning results to be 10.21 (SW-T1) and 11.27 (SW-T2), respectively. The original JRC values of these two

samples before testing were separately 15.32 and 14.63. This indicates that relatively large asperity degradation on the rough fractures was caused by shearing during the injection. The distribution of the JRC values of the tested samples SW-T1 and SW-T2 are shown in Figure 2.12(e) and Figure 2.12(f). It is clearly observed that the JRC values have a normal distribution, and the post-shear JRC values are closer to the mean of the normal distributions. This means that fracture surface(s) with a high degree of relief variability experience more degradation during shearing. Moreover, the gouge produced during shearing could plug the flow paths to further restrict fluid flow. So, in addition to the increase of the effective normal stress, this is another explanation of the fast decrease in permeability during the unloading segment of our injection tests.

2.5.5 The Effect of Loading Frame Stiffness during Fracture Shear Failure

It is well known from laboratory experiments that the post-peak failure process of a rock sample is effected by the stiffness of the loading frame (e.g., Cook, 1965). Great endeavors have been devoted to develop rock deformation testing systems with high stiffness to ensure that a stable post-peak failure behavior can be obtained (e.g., Hudson et al., 1972; Stavrogin & Tarasov, 2001).

In the above triaxial-injection tests, a fractured sample was first loaded to a near-critical stress state, and then the test was switched to a constant piston-displacement control which fixed the loading piston without further movements. Subsequently, the fracture slip was induced by increasing the injection pressure. Considering the rock specimen and the loading frame as two elastic springs each with a different stiffness, the sum of the strain energy consumed in the rock specimen (E_r) and the strain energy stored in the test frame (E_t) is equal to the mechanical energy provided by the actuator piston (E_p). The energy balance

equation of the system at the near-critical stress state before injection is (neglecting dissipation by heat and sound wave):

$$E_p = E_r + E_t \quad (2-11)$$

During the injection stage, the loading piston was fixed without any movements, and the shear failure of the pre-existing fracture was induced by the elevation of the fluid pressure. Therefore, ignoring the frictional energy loss, injection energy (the energy provided by syringe pump), and seismic energy (the energy radiated as sonic wave) during fracture shear slip, the energy balance equation for the injection-induced fracture shear slip in the laboratory test can be expressed as:

$$\Delta E_r = \Delta E_t \quad (2-12)$$

where, ΔE_r is the strain energy released from the near-critically stressed rock specimen, N·m; ΔE_t is the strain energy of the loading system released to the rock specimen during fracture shearing, N·m.

The energy released from the near-critically stressed rock specimen during the injection interval ($t_1 - t_2$) can be roughly estimated as:

$$\Delta E_r = \int_{t_1}^{t_2} F \cdot x_r \, dt \quad (2-13)$$

where, ΔF is the applied force reduced along with fracture shear slip, N; x_r is the axial shortening of the rock specimen during fracture shear slip, m.

The spring rate/stiffness (k_t) of MTS 816 system (model 3.16.02) is around 2.6×10^9 N/m (MTS, 2014). The strain energy released from the loading frame during fracture shear failure is:

$$\Delta E_t = \int_{t_1}^{t_2} \frac{1}{2} k_t x_t^2 \, dt \quad (2-14)$$

where, x_t is the axial deformation of the loading frame during the injection interval, m.

Using the test of sample SW-T1 as an example, the energy release of the rock sample during the injection interval (0-1800 s) is shown in Figure 2.13. Due to the shear failure of the fracture, the maximum energy release from the sample is 9.12 N·m, which is equal to the strain energy released from the loading system (see Eq. (2-12)).

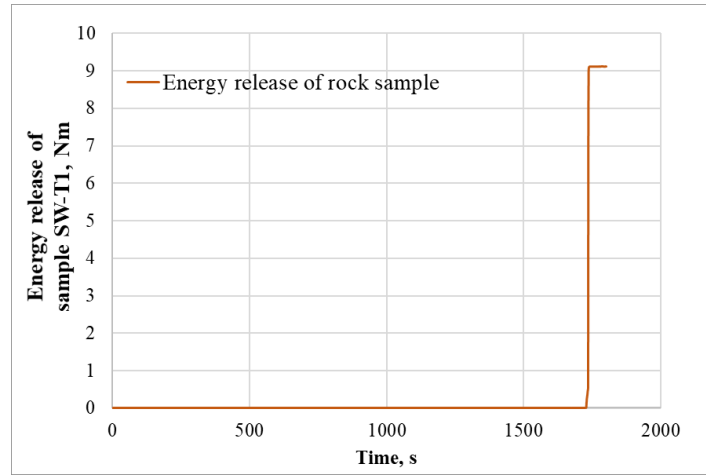


Figure 2.13: Injection-induced shear test on sample SW-T1. The energy release of rock sample during the 1800-s injection interval with fluid pressurization.

According to Eq. (2-14), the deformation of the loading system is shown in Figure 2-14. The maximum deformation of the loading system is about 0.08 mm, for a total of $\sim 3 \times 10^{-5}$ strain change. The total strain change of the sample is 3×10^{-3} . This means the system deformation is quite small compared with the sample deformation.

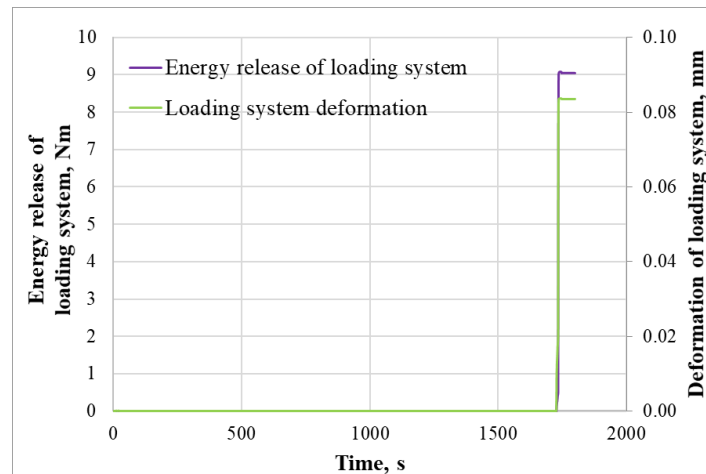


Figure 2.14: Injection-induced shear test on sample SW-T1. The energy release (purple), and the axial deformation (light-green) of the loading system during the 1800-s injection interval with fluid pressurization.

In summary, the energy released by the rock sample during fracture slip is from the strain energy stored into the loading system. The total deformation of the system (including the rock sample) doesn't (or slightly) affect the deformation of the sample during injection, since the deformation of the sample was measured by the LVDT sensors directly mounted on the sample. In addition, the deformation of the loading system is around two orders of magnitude smaller than that of the sample. However, as long as the stiffness of the loading system is finite, it has an influence on the post-peak stress-strain curve of the rock (particularly the stress-strain curve during the shear failure of the fracture in the present test).

2.6 Chapter Summary

In order to understand the dilatant fracture slip and permeability enhancement of rock fractures during shear stimulation, we conducted novel injection-induced shear experiments on four granite samples each containing a single tensile or saw-cut fracture. In the tests, both mechanical deformation (stress and displacement) and fluid flow parameters (pressure and flow rate) through the fractures were measured to investigate the coupled hydro-mechanical responses during fracture shearing. Fractures in samples SW-T1 and SW-T2 were created by mechanical splitting and are very rough, while fractures in samples SW-S3 and SW-S4 were saw-cut fractures and are relatively smoother. For the two saw-cut fractures, sample SW-S4 was further polished to simulate an *ideally* smooth fracture. The fracture surface roughness of all samples were characterized before and after testing by a 3D laser scanner. In the analysis we refer to the tensile fractures and unpolished saw-cut fracture as *rough* fractures and the polished saw-cut fracture as a *smooth* fracture.

In the injection tests, significant shear slip was induced through a stepwise increase of injection pressure. Particularly for the rough fractures (samples SW-T1, SW-T2 and SW-

S3), this resulted in a remarkable enhancement of fracture permeability. In addition, a notable hysteresis of fracture permeability during fracture shearing was observed in rough fracture tests under the loading-unloading cycle of the injection pressure. This means that production enhancement can be retained after the fracture is sheared. In contrast, only a slight permeability increase was detected in the injection test of the *ideally* smooth fracture SW-S4, and the increase was not retainable with decreasing injection pressure. Therefore, the production enhancement and its retention during fracture shearing are highly dependent on the fracture roughness.

A *stick-slip* slip mode was observed during fracture shearing by injection. At the early stage of the injection tests, the fracture tends to be in a *stick* state with a slight fracture opening controlled by the decreasing effective normal stress, resulting in a limited permeability increase and a small stress drop. The fracture reaches a *slip* state with further elevation of the injection pressure. A rapid slip with an associated large stress drop is induced, creating a much larger increase of fracture permeability. In this *slip* state, the major contributor to permeability enhancement is the irreversible normal dilation resulting from a relatively large fracture shearing. As a result of stress relaxation, the fracture slip tends to slowdown, and to finally terminate at a lower stress level.

The process of injection-induced shear slip on rough fractures can be divided into three intervals according to fracture slip characteristics: at the onset of instability, the fracture tends to slip quasi-statically with a relatively slow rate on the order of $\sim 10^{-8}$ to $\sim 10^{-6}$ m/s; as the injection continues, a faster fracture slip rate ($\sim 10^{-5}$ m/s) is induced and the fracture enters into a dynamic slip interval; and finally, the fracture slip slows down (with a slip rate of $\sim 10^{-6}$ m/s) entering into a second quasi-static slip interval because of the large

stress drop associated with the rapid fracture slip in the dynamic slip interval. It is found that fracture slip and stress relaxation are highly interconnected. The time evolution of differential stress is also a piecewise linear function of elapsed time during fracture slip. A much faster stress drop (~ 7 to ~ 20 MPa/s) is noticed in the dynamic slip interval, indicating that the process of fracture shearing is associated with a large energy release. This energy release during fracture shearing could be one of the major reasons for induced micro-seismicity in hydraulic stimulation. On the other hand, the smoothest fracture, SW-S4, displayed a much smaller slip velocity ($\sim 10^{-9}$ to $\sim 10^{-7}$ m/s), corresponding a lower stress drop rate on the order of $\sim 10^{-4}$ to $\sim 10^{-2}$ MPa/s.

Slickensides and gouge were clearly present on the tensile fractures (samples SW-T1 and SW-T2) after testing, while only minor asperity degradations with little fine gouge were observed on the tested saw-cut fractures (samples SW-S3 and SW-S4). The large-sized rock chips were observed in the tensile fractures and were related to the chip-off of contacting asperities on the fracture surfaces. Moreover, the small-sized gouge materials were also found on fracture surfaces after testing, and likely were generated by a longer period of crushing of gouge particles with the increasing shear slip.

By comparing the various observations for rough and smooth granite fractures, it is concluded that the hydro-mechanical properties of a fracture during injection-induced shearing are highly influenced by the fracture roughness. Also, the self-propping of a fracture caused by shear-induced normal dilation is a key component of the success of shear stimulation. The observations and results in this paper provide some crucial insights into the fundamental mechanisms of shear stimulation, and help improve understanding of the coupled hydro-mechanical responses during fracture shearing.

Chapter 3

Injection-Induced Shear Slip and Permeability Enhancement in Shale Fractures

In Chapter 2, the role of fracture shear slip on permeability creation in Enhanced Geothermal Systems (EGS) has been probed through injection-induced shear tests on granite fractures. In unconventional shale reservoirs, the shear reactivation of pre-existing fractures can also play a crucial role in hydraulic stimulation to enable production from low permeability shale plays. Evidence of this phenomenon are found in microseismic events induced during stimulation by hydraulic fracturing. For this chapter, laboratory triaxial-injection tests were conducted on shale fractures to reveal the fundamental mechanisms of permeability creation by fracture shear slip in shale reservoir stimulation. Also, retainable permeability increase, slip characteristics, and asperity degradation during shear slip of shale fractures are demonstrated.

3.1 Abstract

Shear reactivation of pre-existing fractures can play a crucial role in hydraulic stimulation to enable production from unconventional shale reservoirs. However, the mechanisms of permeability enhancement contributed by fracture shear slip are still poorly understood, and the existing laboratory experiments on shale fractures are insufficient. In this work, injection-induced shear tests were conducted on two reservoir shale samples (from the depth >10,000 ft.) each having a single rough fracture to characterize permeability evolution in fracture shear slip. In the tests, remarkable enhancement of flow rate/permeability have been achieved on both samples through fracture shear slip induced

by elevating injection pressure. It is shown that ~100 times increase in flow rate was induced by a ~0.1 mm of shear slip on the two cylindrical shale samples (with ~38 mm diameter). The permeability enhancement was retained on the sheared samples even with the decline of fluid pressure. This means that the permeability increase by fracture shear slip may be permanent. In addition, significant stress drops were induced by fracture shear slip in both tests, resulting in further fracture aperture/permeability enhancement. In one sample, a new fracture plane was formed during the shear slip of the original pre-existing fracture, which help generate a fracture network with high conductivity. Therefore, dilatant shear slip, stress drop, and the new fracture formation are major and often integral mechanisms of permeability enhancement contributed by pre-existing fractures during shale reservoir stimulation. The results improve the understanding of shear slip in enhancing permeability of shale fractures, and would help engineer solutions for maintaining these fractures open, reducing costs (proppant/water and additive cost savings).

3.2 Introduction

Shear slip of pre-existing fractures has been recognized as a major permeability creation mechanism in reservoir stimulation for a long time (e.g. Mayerhofer et al., 1997; Pine & Batchelor, 1984; Rutledge et al., 2004; Zoback et al., 2012). Most reservoir rocks contain abundant pre-existing fractures, some of which may be sealed with calcite or other infill minerals. Usually, these fractures are inactive and without sufficient permeability before stimulation. A number of modeling and field studies have shown that when the pre-existing natural fractures are favorably oriented with respect to the in-situ stresses, an injection or the leak-off from a hydraulic fracture (even with low fluid pressure) can cause fracture sliding and propping due to asperities. Also, the interpretations of induced

microseismic events during hydraulic injection have indicated that shear slip of pre-existing fractures around hydraulic fractures can help generate a large stimulated reservoir volume and benefit the production performance (e.g. Fisher et al., 2004; Mayerhofer et al., 2010). However, the fundamental mechanisms of permeability creation by fracture shear slip in shale reservoir stimulation are still poorly understood.

Remarkable permeability enhancement has been observed from the fracture shear tests on strong crystalline rocks (e.g. Esaki et al., 1991; Vogler et al., 2016; Ye et al., 2017a; Ye & Ghassemi, 2018), however, based on limited experimental results on shale fractures, it has been suggested that the fracture permeability tends to decrease with shear slip in shales (Fang et al., 2017; Gutierrez et al., 2000; Rutter & Mecklenburgh, 2018; Wu et al., 2017). But, in most of these shear tests in shale fractures, slip was induced by a mechanical force (Fang et al., 2017; Gutierrez et al., 2000; Wu et al. 2017), or used saw-cut fractures (Fang et al., 2017; Rutter & Mecklenburgh, 2018). In the former force-induced slip tests, the fracture likely experienced a relatively large shear displacement (~10 mm shear slip) on a small-size shale sample (cylindrical samples with 25 mm diameter or blocks with size of 85 mm × 85 mm × 30 mm), and therefore it is likely that the gouge production caused by the large shearing deformation tend to plug the fluid flow in fracture and decrease the permeability. On the other hand, the latter shear tests on saw-cut fractures yield little or no permeability increase due to the insufficient asperities on the smooth fractures. In our companion papers (Ye et al., 2017a; 2017b; Ye & Ghassemi, 2018), a number of laboratory injection tests were reported on shale or granite samples having pre-existing fracture(s), the results show shear slip can enhance fracture permeability significantly. However, in our preliminary shear tests on shale fractures (Ye et al., 2017b), the samples are not reservoir rocks but outcrops, and

the tests shown that permeability increase cannot be fully retained in sheared fracture after the decline of fluid pressure.

In this study, cylindrical samples from shale reservoirs at depth (>10,000 ft.) each containing a single rough fracture were used to conduct laboratory injection-induced shear tests under a representative triaxial stress. In the test, pressurized brine water (7% KCL) was injected into the fractured sample to induce shear slip, the measurements of sample deformation (stress, displacement) and fluid flow (injection pressure, flow rate) were all concurrently recorded. Through this work, we provide insights on several key points related to fracture shear slip in shales: (1) does shear slip of shale fractures enhance or decrease the fracture permeability; (2) how permeability evolves in response to fracture shearing by injection; (3) and what are fundamental mechanisms of permeability enhancement by fracture shear slip in shale reservoirs?

3.3 Experimental Methods

3.3.1 Sample Preparation and Characterization

The two samples used in this study are cylindrical reservoir shale rocks from depth (>10,000 ft.) with ~38.10 mm (1.5-inch) by at least 76.20 mm (3-inch). The samples were all cored perpendicular to the bedding planes, however, the bedding planes are not significantly well-defined (Figure 3.1(a) and Figure 3.2(a)). The Young's modulus and Poisson's ratio determined by triaxial compression test are around 35 GPa and 0.21, respectively. To create single fracture in each sample, a rock splitting method (described in Ye et al., 2017a) was used. First, a leading and inclined groove (3 mm in width and 3 mm in depth) was cut on the sample by a diamond saw, and then a steel wedge fitted in MTS 810 frame was used to split the shale samples (Figure 3.1(b) and Figure 3.2(b)).

A three-dimensional (3D) non-contact scanning system was used to measure the topography of fracture surface. The 3D scanning contours of the two fracture surfaces of each sample are shown in Figure 3.1(c) and Figure 3.2(c). The x (the long axis of the contour), y (the short axis of the contour) and z coordinates (the color scale of the contour) of the scanning contours are the length, width and asperity height of fracture surface, respectively. The color scale in the contour describes the values of asperity height with respect to the lowest point of the fracture surface (indicated by black color). The dark blue to light red zones represent asperity heights ranging from low to high values (with reference to the lowest point). In sample B-20V, the maximum surface relief between the highest point (peak) and lowest point (valley) on fracture plane is around 5.54 mm (Figure 3.1(c)), and the average JRC (joint roughness coefficient, Barton, 1973) value is 12.63. As shown in Figure 3.2(c), the maximum surface relief on the fracture surface of sample P-20V is 4.82 mm, and the corresponding JRC value is 10.24. Comparing with the roughness of natural fractures in our previous works (Ye et al., 2017b), the tensile fractures created by splitting and the natural fractures are with a similar roughness range. The tensile fracture is considered as a *rough* fracture. To create a flow path for fluid injection and production, two 2 mm diameter vertical boreholes (see Figure 3.3(b)), 5 mm from the sidewall, are drilled (using a diamond drill bit) from each end surface of the cylindrical sample to reach the fracture. In the test, brine water is injected into the fracture through the bottom borehole and is produced out from the top borehole. Before the shear test, the ends of each sample are generally polished by a rock surface grinder based on the ISRM standard (Kovari et al., 1983). Also, the samples were submerged into an ultrasonic bath with brine water (7% KCL) to remove the fines/grains created during rock splitting and then completely dried by a vacuum oven at 30 °C for 72

hours (see Ye & Ghassemi, 2018 for more sample preparation details). The dimensions and the fracture angle (with respect to the vertical sample axis) of the two samples after preparation are listed in Table 3.1.

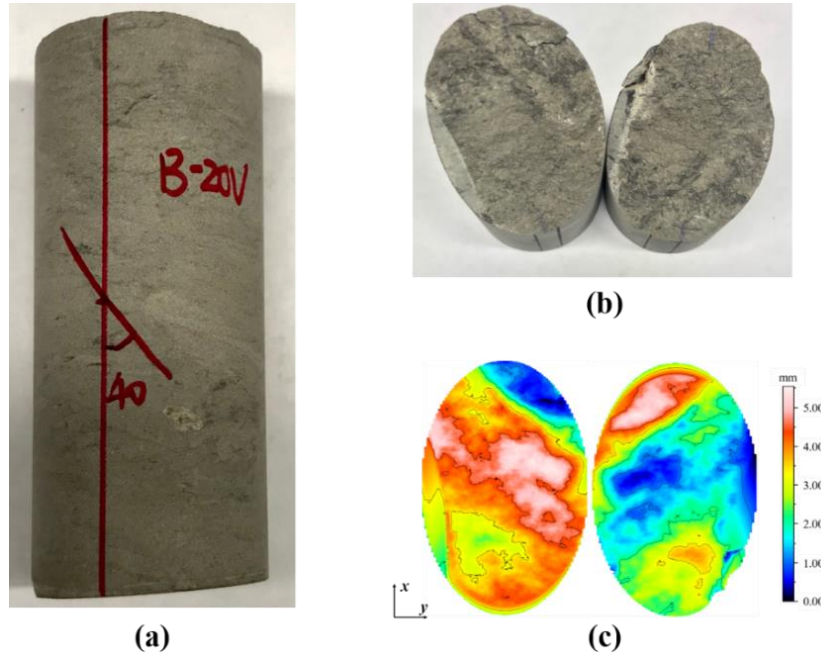


Figure 3.1: Sample preparation: (a) raw sample B-20V; (b) rough fracture created by splitting; (c) 3D laser scanning contour.

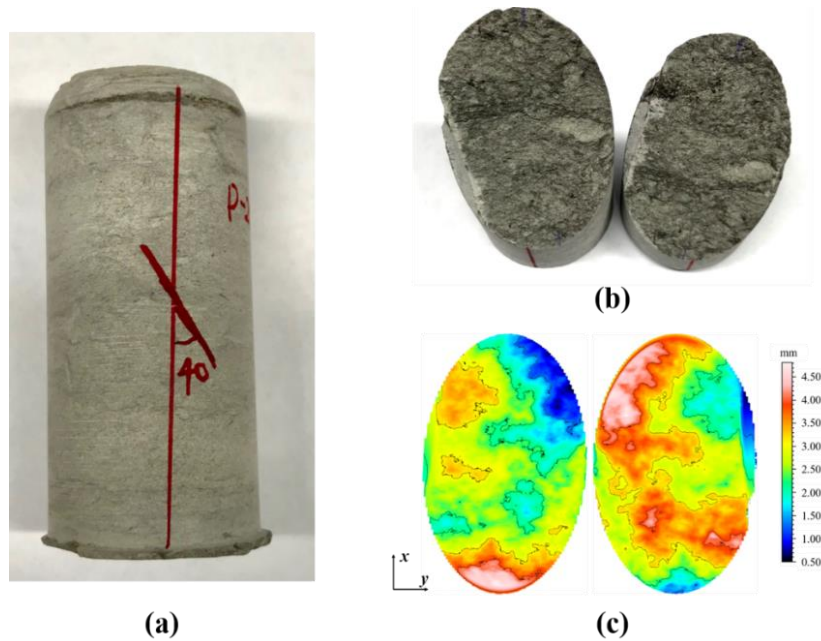


Figure 3.2: Sample preparation: (a) raw sample P-20V; (b) rough fracture created by splitting; (c) 3D laser scanning contour.

Table 3.1: Sample dimension and fracture angle of shale samples.

Sample No.	Fracture Type	Diameter (D), mm	Length (L), mm	Fracture angle* (θ), degree
B-20V	tensile	37.60	83.40	42°
P-20V	tensile	37.70	79.60	40°

* Angle measured from the long axis of sample to the fracture plane (see Figure 3.1(a) and Figure 3.2(a)).

3.3.2 Experimental Setup

An MTS 816 frame capable of achieving 1000 kN (225,000 lbs.) axial load and 138 MPa (20,000 psi) confining pressure was used to conduct the triaxial shear tests. The test data was acquired using MTS Series 793TM control software. The experimental setup is shown in Figure 3.3(a). In the test, the average axial displacement of the shale sample is measured by two Linear Variable Differential Transformer (LVDT) position sensors. Another LVDT mounted on a ring was used to record radial deformation. To keep the average error below 0.01 mm all three LVDTs were calibrated prior to testing. Two Teledyne ISCO D-Series syringe pumps (maximum 10,000 psi pressure limit and 103 mL volume capacity) controlled fluid flow and measured flow rates. An open source software “Disco” provided by Los Alamos National Laboratory was used to control the pumps and acquire flow parameters. As shown in Figure 3.3(a), during the test, water is injected from pump A through the bottom of the sample and produced from the top to pump B. The flow parameters including pressure, fluid volume, and flow rate of each pumping operation are measured.

3.3.3 Experimental Procedure

As illustrated in Figure 3.3(a), in the test, a 30 MPa confining pressure (σ_3) was first applied on the sample. After that, the production pressure of pump B (P_o) was fixed to a constant value of 4 MPa, and the injection pressure of pump A (P_i) was set to an initial value of 4 MPa and later was increased incrementally to induce fracture slip. Before elevating the injection pressure, the sample was loaded to a near-critical stress state which can be

determined from the dilation/deflection of the stress-axial strain curve (Ye & Ghassemi, 2016). This near-critical stress level should be large enough to cause fracture slip during injection, but not exceed the shear strength to induce fracture slip before injection starts. Next, the test was switched to the constant piston displacement control mode used by Ye & Ghassemi (2017a). Subsequently, the injection pressure was increased stepwise at a rate of 0.05 MPa/s from 4 MPa to 29 MPa to induce fracture slip, including five pressure steps ($P_i = 8, 12, 16, 20$ and 29 MPa). During the entire injection test, the injection pressure was at least 1 MPa smaller than the 30 MPa confining pressure. This prevents the jacket from bursting during fluid injection, and ensures that the *treatment* pressure is lower than the minimum principal stress. The stepwise elevation of the injection pressure was employed to investigate the evolution of steady-state flow rate during fracture shearing. Due to the pressure difference between the two pumps, water was circulated from pump A to pump B after starting injection. Each injection pressure step lasted 200-400 seconds depending on the increment of injection pressure, including a pressure buildup stage and a constant pressure hold stage. After a target injection pressure was achieved, the pressure was held constant for at least 100 seconds before recording the flow rate to ensure the flow rate measurement was in the steady-state flow regime. When the flow rate out of pump A was nearly identical to the flow rate into pump B (the difference of flow rates is less than 5%), we considered the fluid flow through the fracture have reached a steady-state flow regime. The injection pressure was increase in the stepwise manner described to induce fracture slip, resulting in significant displacement change, stress-drop, and flow rate increase.

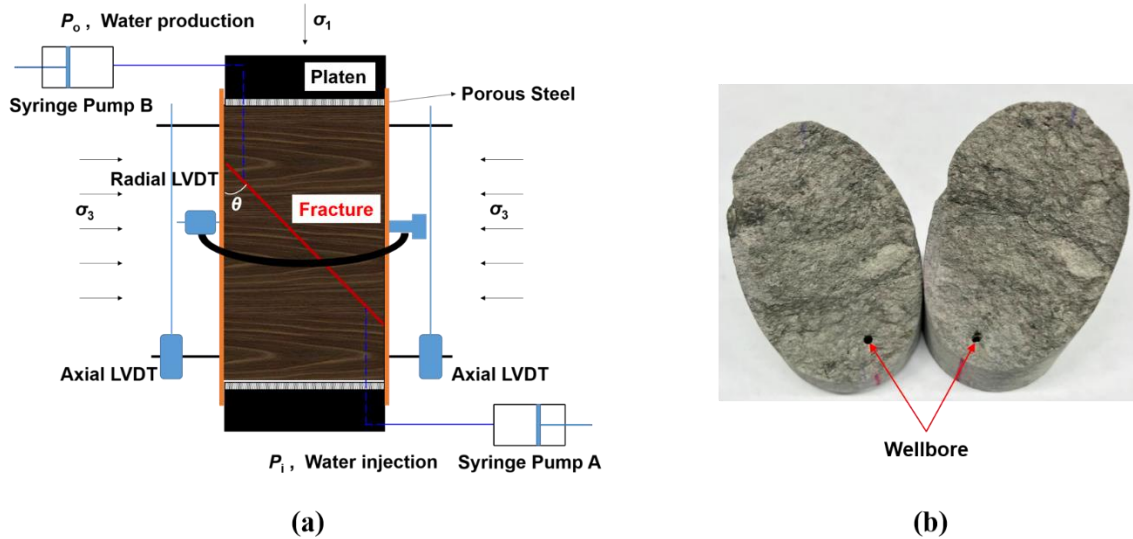


Figure 3.3: (a) The sketch of experimental setup; (b) shale fracture with boreholes for fluid flow.

To address whether the flow rate/permeability enhancement is retained in sheared fracture during the depletion of reservoir fluid pressure, a depressurization segment was subsequently performed in which the injection pressure was lowered stepwise from 29 MPa to 8 MPa using the same pressure increment after the pressurization segment. Similarly, the steady-state flow rate at each injection pressure step during depressurization segment was also measured. In the test, the time evolutions of fracture deformation and fluid flow were all recorded during the *pressurization-depressurization* cycle of injection pressure.

In the injection test, the sample is brought to a near-critical stress state, and then the piston displacement of actuator piston is fixed under the constant displacement control. Once fracture slip is initiated by elevating injection pressure, the differential stress acting on the sample decreases significantly in response to the sample shortening with the gradual sliding of the fracture. As a result, the fracture slip slows down and finally terminates when the differential stress decreases to a lower level. The assumption underlying this boundary control is that the deformation of the overburden (the piston) at a distance far from the fluid injection zone is negligible, while the energy stored into the reservoir rocks can release

through fault/fracture movement during injection. The advantage of this boundary condition is to capture the stress drop accompanying with fracture/fault reactivation in the episodes of seismicity or micro-seismicity.

3.3.4 Fracture Deformation and Permeability

In the test, the measurements of fracture deformation are with respect to the x-z coordinates rather than the local n-s coordinates of the fracture plane (Figure 3.4). To obtain the measurements of stress and displacement on local fracture plane, coordinate conversions are required. The effective normal stress and shear stress on the local n-s coordinates of the fracture plane are:

$$\sigma'_n = (\sigma_3 - P_p) + (\sigma_1 - \sigma_3)\sin^2\theta \quad (3-1)$$

$$\tau = (\sigma_1 - \sigma_3)\sin\theta\cos\theta \quad (3-2)$$

where, σ'_n and τ are the effective normal stress and shear stress on the fracture plane, respectively; θ is the fracture inclination angle with respect to the vertical axis of the sample; σ_1 is axial stress; σ_3 is confining pressure; P_p is pore pressure which can be estimated as the average of the injection pressure (P_i) and the production pressure (P_o):

$$P_p = 0.5 \times (P_i + P_o) \quad (3-3)$$

Ignoring the deformation of rock matrix, the normal dilation/fracture opening and shear slip on fracture plane can be estimated calculated as:

$$d_n = \Delta z \sin\theta - \Delta x \cos\theta \quad (3-4)$$

$$d_s = \Delta z \cos\theta + \Delta x \sin\theta \quad (3-5)$$

where, d_n and d_s are the fracture's normal dilation and shear slip, respectively; Δz is the specimen axial deformation; and Δx is the specimen radial deformation.

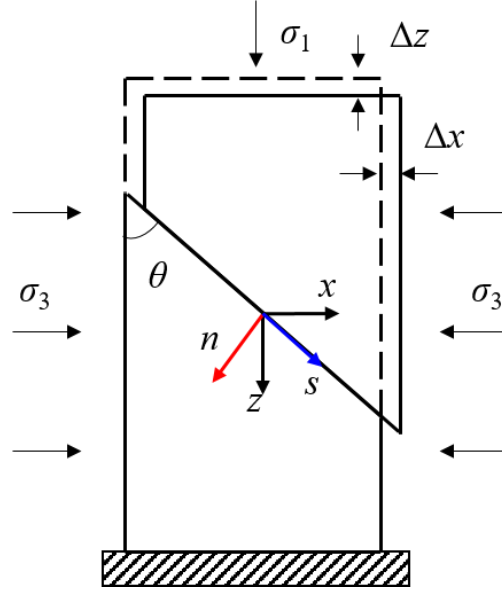


Figure 3.4: Deformation during injection-induced shear test under triaxial stress.

In the constant pressure hold stage of each step, when the injection flow rate is nearly equal to the production flow rate, the steady-state flow regime is satisfied. Using Darcy's law, the equivalent reservoir permeability of the sample can be calculated as:

$$k_e = -\frac{\mu Q}{A} \cdot \frac{L}{\Delta P} = -\frac{4\mu Q}{\pi D^2} \cdot \frac{L}{\Delta P} \quad (3-6)$$

where, Q is the flow rate in steady-state regime, estimated by averaging the injection flow rate and production flow rate, ΔP (differential pressure) is the difference between injection pressure (P_i) and production pressure (P_o); μ is the fluid viscosity (1.002×10^{-3} Pa·s at 20 °C for water); A is the cross-section area of the cylindrical shale sample ($A = \frac{1}{4} \pi D^2$); D and L are the sample diameter and sample length, respectively.

On the other hand, according to the cubic law (Witherspoon et al., 1980; Zimmerman & Bodvarsson, 1996), the fracture used in the injection test is assumed as a parallel-sided fracture with an equivalent hydraulic aperture (a_h). The fracture permeability (k_f) is further evaluated by:

$$k_f = \frac{a_h^2}{12} \quad (3-7)$$

where, k is the fracture permeability evaluated by the cubic law; a_h is the equivalent hydraulic aperture of the fracture.

Considering the matrix permeability of shale rocks are usually very small ($<10^{-18} \text{ m}^2$) and the gravity effect is negligible, the steady-state flow rate (Q) is represented using Darcy's law:

$$Q = -\frac{W a_h^3}{12\mu} \cdot \frac{\Delta P}{L} \quad (3-8)$$

where, Q is the steady-state flow rate under the constant injection pressure hold stage; ΔP is the differential pressure; μ is the fluid viscosity ($1.002 \times 10^{-3} \text{ Pa}\cdot\text{s}$ at $20 \text{ }^\circ\text{C}$ for water); W and L are the fracture width and length, respectively.

Therefore, the equivalent hydraulic aperture (a_h) of the fracture is estimated using the measurements in steady-state flow regime:

$$a_h = \left(-\frac{12\mu L Q}{W \Delta P} \right)^{1/3} \quad (3-9)$$

In the present fracture shear slip test, the two surfaces of each fracture are elliptical or near elliptical (indicated by the black ellipse in Figure 3.5), and each surface contains a borehole (the red circles in Figure 3.5). To simplify the estimation of the fracture permeability, the fluid flow region is assumed as a *rectangle* (represented by the blue rectangle in Figure 3.5). The rectangle has a same area as the elliptical fracture surface. The length (L) of the rectangle is the distance between the two boreholes on fracture surface, and the width (W) of the rectangle is equal to the area (A) of the ellipse divided by the length (L) of the rectangle (see Ye & Ghassemi, 2018 for additional details in the approximation of fracture permeability).

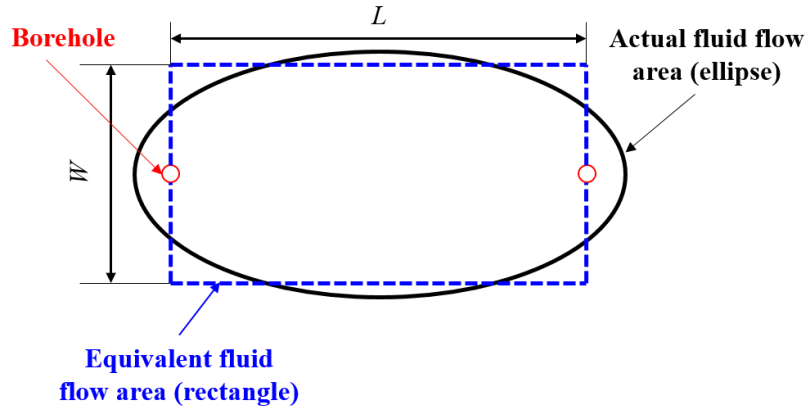


Figure 3.5: Fluid flow region for fracture permeability estimation: the ellipse is the actual fluid flow region, while the rectangular area delineated by blue dotted lines is the equivalent fluid flow region.

3.4 Experimental Results

The hydro-mechanical measurements of the two injection tests are shown in the temporal evolution plots of Figure 3.6 and Figure 3.7, respectively. The deformation properties (displacement and stress) and fluid flow parameters (flow rate and pressure) in the pre-injection stage (initial applications of confining pressure, axial loading, production pressure and injection pressure) are not shown. This means that the displacements and flow rates have been zeroed before injection. In the plots, the green curve represents the loading piston displacement of the MTS 816 frame, which was kept as constant under constant piston displacement control. The blue curve is the injection pressure which was increased stepwise from 4 MPa to 29 MPa with five injection pressure steps ($P_i = 8, 12, 16, 20$ and 29 MPa); after fracture shearing, the injection pressure was incrementally lowered to 8 MPa with the same steps as in the pressurization path of injection pressure. The constant production pressure ($P_o = 4$ MPa) is represented by the gray curve. The teal curve describes the differential stress history which shows a significant drop once the fracture slip is initiated. The computed effective normal stress and shear stress (see Eq. (3-1) and Eq. (3-2)) on the fracture plane are separately illustrated by the black and golden curves. The purple and pink

curves are the normal dilation/opening and shear slip of the fracture calculated using Eq. (3-4) and Eq. (3-5), respectively. The steady-state flow rates measured at each injection pressure hold stage are shown as the dark-blue triangles linked with the dashed dark-blue curve. The fracture permeability estimated from the steady-state flow rates (see Eq. (3-7) to Eq. (3-9)) are depicted by the dark-green dots connected by dashed dark-green curve. It is clear from the plots that the stresses, displacements, flow rates, and permeability values vary with the stepwise changes of injection pressure. The experimental data in the injection pressure hold stages for each sample, including the steady-state flow rates (Q), the normal dilation (d_n) and shear slip (d_s), the effective normal stress (σ'_n) and shear stress (τ), equivalent reservoir permeability (k_e), the hydraulic aperture (a_h), and fracture permeability (k_f), are listed in the Table 3.2.

Table 3.2: Hydro-mechanical measurements of the two injection-induced shear tests.

Sample #	P_i (MPa)	Loading Segment					Unloading Segment			
		8	12	16	20	29	20	16	12	8
B-20V	Q (mL/min)	0.0059	0.0103	0.0157	0.0214	0.5580	0.1150	0.0690	0.0370	0.0164
	d_n (mm)	0.0003	0.0010	0.0022	0.0035	0.1296	0.1084	0.1010	0.0944	0.0886
	d_s (mm)	0.0000	0.0005	0.0013	0.0026	0.4153	0.4125	0.4093	0.4065	0.4040
	σ'_n (MPa)	59.91	57.21	54.55	52.02	23.26	26.69	28.52	29.96	31.48
	τ (MPa)	39.89	39.11	38.40	37.79	10.85	9.64	9.46	8.84	8.31
	k_e ($\times 10^{-18}$ m ²)	1.85	1.61	1.64	1.68	28.00	9.02	7.21	5.80	5.14
	a_h ($\times 10^{-6}$ m)	0.64	0.61	0.62	0.62	1.58	1.09	1.01	0.94	0.90
	k_f ($\times 10^{-13}$ m ²)	0.34	0.31	0.32	0.32	2.09	0.98	0.85	0.73	0.68
P-20V	Q (mL/min)	0.0012	0.0025	0.0035	0.0046	0.1180	0.0129	0.0079	0.0044	0.0021
	d_n (mm)	0.0000	0.0000	0.0000	0.0002	0.1515	0.1427	0.1381	0.1346	0.1313
	d_s (mm)	0.0000	0.0000	0.0000	0.0003	0.1653	0.1514	0.1462	0.1428	0.1397
	σ'_n (MPa)	67.33	64.82	62.77	60.69	23.45	27.12	29.10	30.76	32.60
	τ (MPa)	43.34	42.83	42.77	42.70	9.79	9.09	8.96	8.77	8.61
	k_e ($\times 10^{-19}$ m ²)	3.57	3.75	3.51	3.39	56.22	9.60	7.80	6.52	6.25
	a_h ($\times 10^{-6}$ m)	0.38	0.38	0.37	0.37	0.94	0.52	0.49	0.46	0.45
	k_f ($\times 10^{-14}$ m ²)	1.18	1.22	1.17	1.14	7.43	2.29	1.99	1.77	1.72

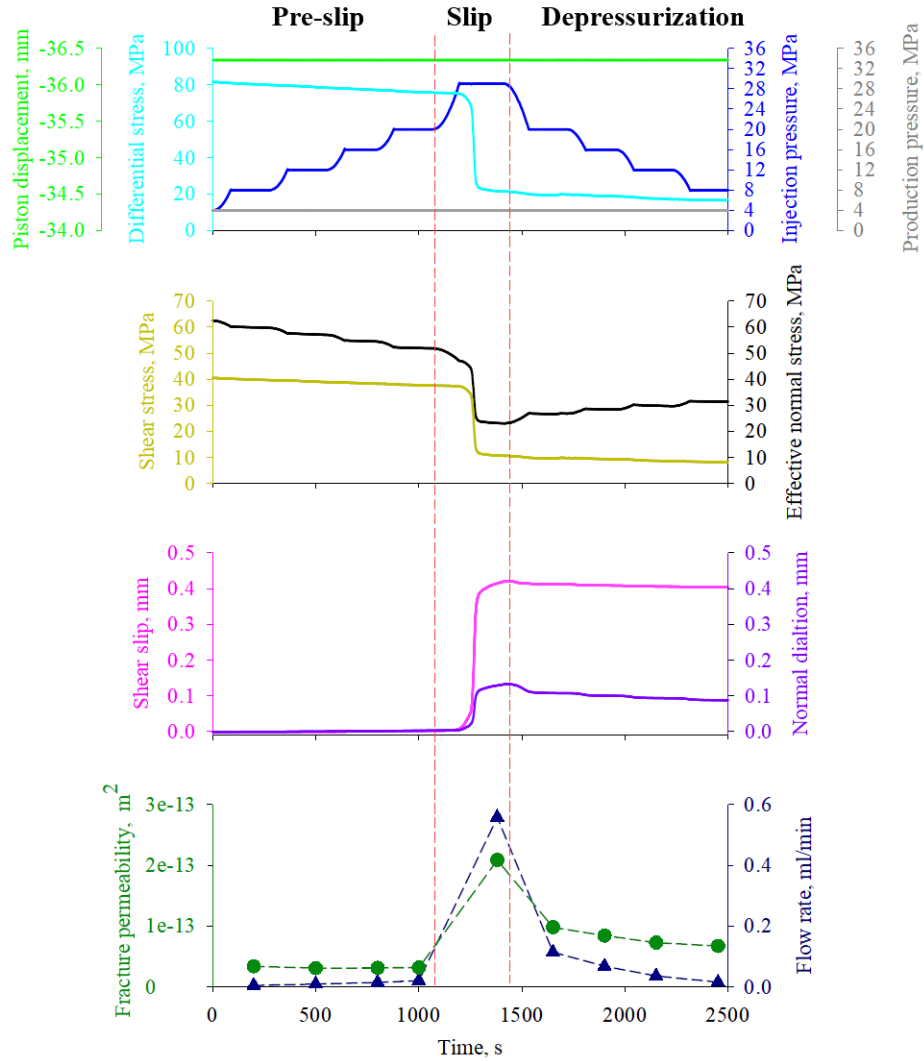


Figure 3.6: The hydro-mechanical measurements of injection-induced shear test in shale sample B-20V. The temporal evolution of the piston displacement (green), differential stress (teal), the injection pressure (blue), the production pressure (gray), the effective normal stress (black), the shear stress (golden), the normal dilation (purple), the shear slip (pink), the steady-state flow rate (dark-blue) and the fracture permeability (dark-green) during the 2500-s-long fluid injection are illustrated. The axial shortening of the sample is calculated from the measured axial displacement, since the sample length is larger than the actual gauge length (see Figure 3.3(a)).

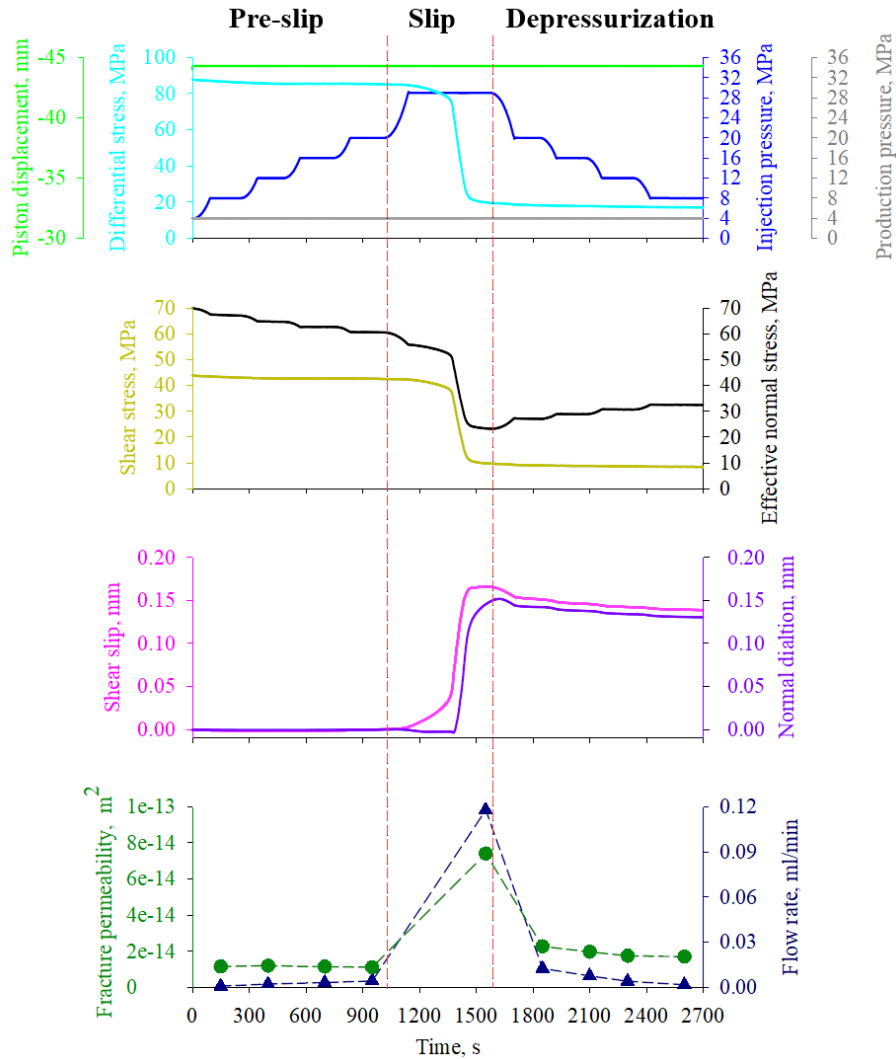


Figure 3.7: The hydro-mechanical measurements of injection-induced shear test in shale sample P-20V. The temporal evolution of the piston displacement (green), differential stress (teal), the injection pressure (blue), the production pressure (gray), the effective normal stress (black), the shear stress (golden), the normal dilation (purple), the shear slip (pink), the steady-state flow rate (dark-blue) and the fracture permeability (dark-green) during the 2700-s-long fluid injection are illustrated. The axial shortening of the sample is calculated from the measured axial displacement, since the sample length is larger than the actual gauge length (see Figure 3.3(a)).

Figure 3.6 and Figure 3.7 show the hydro-mechanical measurements of the injection tests on samples B-20V and P-20V. It is noticed that the temporal evolution of the two tests have the similar evolution pattern and each test can be roughly separated into three stages using the red-dashed line: *pre-slip* stage, *slip* stage, and *depressurization* stage. Among these three stages, the stage 1 and stage 2 are from the pressurization path of injection pressure, while stage 3 illustrates the test during the depressurization path of injection pressure.

- Stage 1. In this pre-slip stage, the injection pressure is less than 20 MPa, and the fracture is in a *stick* state with almost negligible shear slip and normal dilation. Considering three decimal places in the displacement measurements, the fracture slip and dilation are zero or close to zero in this stage (see Table 3.2). The effective normal stress gradually decreased with the elevation of pore pressure due to fluid injection. On the other hand, the shear stress declines slightly because of only minor decrease of the differential stress at this pre-shearing stage, since the shear stress only depends on the differential stress and the fracture angle but does not correlate with the pore pressure (see Eq. (3-2)). The small increase of the flow rate in this stage is related to the fracture aperture increase caused by the decrease of the effective normal stress.
- Stage 2. In this stage, the injection pressure is further increased from 20 MPa to 29 MPa, and the fracture slip is induced by pressurized fluid injection. As a result, the rapid fracture slip and dilation occurred accompanying by a significant stress drop. Moreover, the flow rate and the fracture permeability are also greatly enhanced due to the large aperture increase mainly caused by the dilatant shear slip of the fracture. The reduction of the effective normal stress also contributes to the increase of flow rate. However, the sudden and nonlinear jump in displacements (shear slip and normal dilation), flow rate, and fracture permeability clearly demonstrate that the fracture self-propping by asperities caused by dilatant fracture shear slip is major contributor. The significant drop of the differential stress can be clearly observed, resulting in a dramatic decrease of both effective normal stress and shear stress on the fractures. The large drop

of shear stress indicates that the shear failure of the fracture is satisfied. Due to the stress drop, the fracture slip slows down and appears to terminate at the end of the slip stage.

- Stage 3. In the third depressurization stage, the injection pressure is stepwise decreased from 29 MPa to 8 MPa. The goal of this stage is to check the shear-induced permeability enhancement whether can be retained during the depletion of reservoir pressure after *treatment*. The effective normal stress increases due to the decrease in fluid pressure, while the shear stress shows no significant change (the differential stress shows no notable change after the termination of fracture shear slip). Therefore, the fracture closes due to the increase in effective normal stress with continuous decline of pore pressure, resulting in a flow rate/permeability decrease. In addition, the asperity degradation and gouge production in the shearing process could also block the flow pathways, further causing the flow rate/permeability to decrease. However, the flow rate/permeability in sheared fracture is larger than which of the fracture before shearing treatment, indicating the permeability enhancement by fracture slip and dilation may be permanent.

As listed in Table 3.2, in the test of sample B-20V, a shear slip of 0.42 mm and a normal dilation of 0.13 mm were induced during the slip stage, leading to a ~95 times increase of flow rate, from the base flow rate of 0.006 ml/min to 0.558 ml/min (the base flow rate was measured at the 8 MPa injection pressure step before fracture shearing). The corresponding equivalent reservoir permeability enhanced 15 times, from the base reservoir permeability of $1.85 \times 10^{-18} \text{ m}^2$ to the enhanced reservoir permeability of $2.8 \times 10^{-17} \text{ m}^2$. Also,

the fracture permeability increased to $2.09 \times 10^{-13} \text{ m}^2$ after the shearing treatment, which is 6 times larger the base fracture permeability of $0.34 \times 10^{-13} \text{ m}^2$. In addition, the accompanying shear stress dropped from 40 MPa to 11 MPa. For sample P-20V, the flow rate increased rapidly from the base flow rate of 0.001 mL/min to a maximum steady-state flow rate of 0.118 mL/min (~98 times increase) in response to a shear slip of 0.17 mm and a normal dilation of 0.15 mm, and a shear stress drop of 33 MPa (from 43 MPa to 10 MPa). The equivalent reservoir permeability and fracture permeability enhanced 16 times and 6 times by comparing with base permeability measurements, respectively. The flow rate and permeability measurements are from the steady-state flow regimes of the injection tests.

3.5 Discussion

3.5.1 The Mechanisms of Permeability Enhancement by Fracture Shear Slip

As shown in Figure 3.6 and Figure 3.7, the irreversible normal dilation/fracture opening is induced by shear slip in both tests, resulting in a rapid and nonlinear increase of flow rate/permeability. Without fracture shear slip, the previous fluid flow tests in rock fractures (either shale or granite) have suggested that the flow rate tends to linearly increase with the elevation of injection pressure (e.g. Singh et al., 2015; Ye, et al., 2017). This means that the relatively large and nonlinear enhancement of flow rate should be contributed by the dilatant fracture slip. In our companion work (Ye & Ghassemi, 2018), the similar injection-induced shear tests were conducted on both saw-cut (smooth) and tensile-induced (rough) granite fractures. The results show that large normal dilation is induced in rough fracture, resulting in a significant flow rate/permeability increase. On the other hand, the tests on saw-cut fractures gained no or limited increase of flow rate by fracture shear slip. Therefore, the

first mechanism of permeability enhancement by fracture slip is the irreversible fracture dilation/pro-open caused by asperities during shear slip.

It is also noticed that a rapid stress drop is associated with fracture shear slip in Figure 3.6 and Figure 3.7. As a result, the effective normal stress acting on the fracture plane experienced a remarkable decrease, leading a further increase of fracture aperture/permeability. In the episodes of shear activation and seismic activities in natural faults/fractures, the accompanying stress drop/release is widely observed (Brenner et al., 2008; Gao & Crampin, 2004; Kato et al., 1997; Yang & Toksöz, 1981). Thus, the aperture increase caused by stress drop during fracture shear slip is also an important mechanism of permeability enhancement.

As shown in Figure 3.8, a new fracture was formed (~30 degree with respect to the vertical sample axis) during the injection test. Since the sample is cored perpendicular to the bedding plane, this new fracture is most likely a shear-mode fracture created by the elevation of injection pressure in a stressed sample. Therefore, the prop-opened original fracture communicated with the newly formed fracture to generate a fracture network and enhance the conductivity of the sample. It also noticed that sample B-20V has a relatively larger flow rate (0.56 ml/min) than that of sample P-20V (0.12 ml/min) after the shear treatment. In sample P-20V, there were no new fractures formed during the injection test (see Figure 3.11(b)). Considering the similar fracture roughness in both samples, the flow rate/permeability difference may be due to the newly formed fracture during shear stimulation. Similarly, in our previous shear tests on Eagle Ford shale fractures, healed fractures were reactivated by injection during the shear slip of the primary/original fracture and significantly benefit the permeability enhancement of the shale sample (Ye et al., 2017b).

In addition, it is also observed that new fractures/cracks can be propagated from the tips of the pre-existing fractures in shales during low injection pressure shear stimulation, since fracture shear slip can also cause the increase of the stress intensity around fracture tips (Ye et al., 2018). Therefore, the shear slip of pre-existing fractures in shale reservoirs can create new fractures from fracture tips, nearby natural discontinuities and rock matrix, resulting in permeability enhancement during hydraulic stimulation. However, in crystalline rocks (granite), often, the rock matrix is stronger than the fracture. The new fractures could be created at the tips of pre-existing fracture(s) or along with the nearby natural discontinuities, but seems like it is hard to form new fractures in matrix during the shear slip of pre-existing fractures.

In short, dilatant shear slip, stress drop, and new fractures formation are the three mechanisms of permeability enhancement caused by fracture shear slip during shale reservoir stimulation.

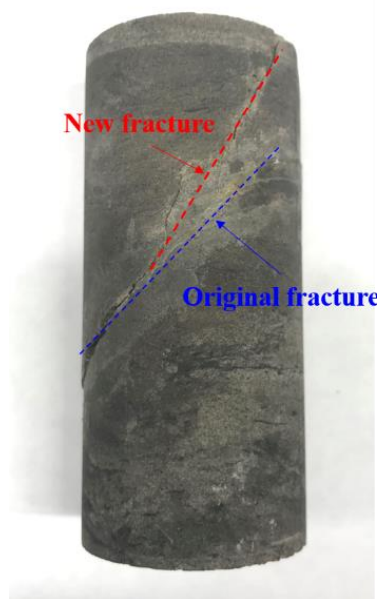


Figure 3.8: A new fracture plane was created during the shear slip of original fracture by injection in Sample B-20V. In the figure, the blue-dashed line indicates the original fracture plane, and the red-dashed line represents the newly created fracture.

3.5.2 Retainable Permeability Enhancement in Shale Fractures

Reservoir pressure depletion has been considered as a primary factor to influence the production performance in shale plays. In hydraulic fracturing by high fluid pressure injection, the hydraulic fractures (tensile-mode) tend to close significantly after pump shut-in and reservoir pressure depletion, resulting in a fast decline of reservoir permeability. Some field and laboratory research have suggested that the permeability enhancement caused by shear slip may be retainable due to the self-propping by asperities (e.g. Amann et al., 2018; Gisching & Preisig, 2015; Ye & Ghassemi, 2018). Here, to check the retention of shear-induced permeability enhancement in shale fractures, a *pressurization-depressurization* path of the injection pressure was applied in the shear test on the two shale fractures. Figure 3.9(a) - 3.9(b) are the plots of the fracture permeability vs. injection pressure. It is noticed that significant hysteresis of permeability during the loading-unloading of injection pressure, indicating that the enhancement of fracture permeability was retained in sheared fracture even the fluid pressure gets declined. Also, the hysteresis of fracture permeability is also an evidence that permeability creation by shear slip is likely permanent (at least in the present shale fracture test).

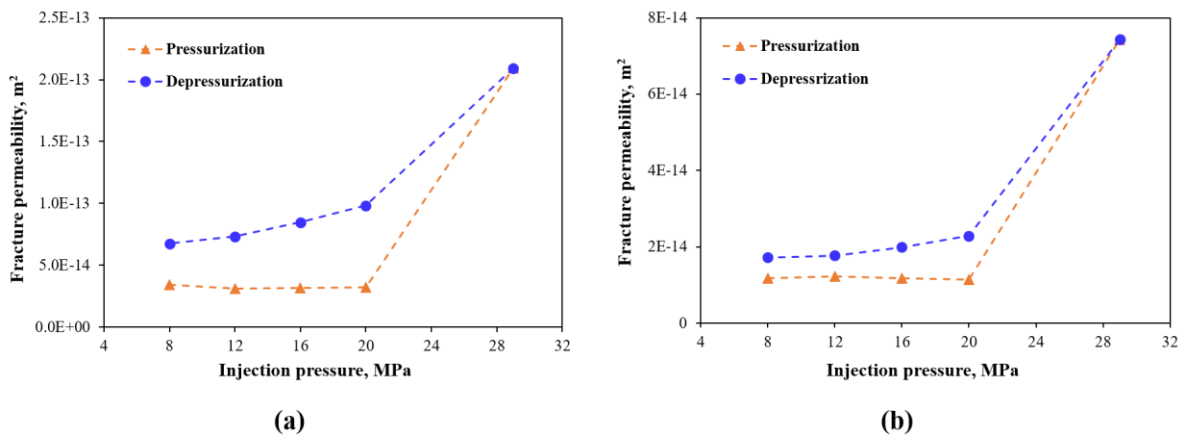


Figure 3.9: The retention of permeability enhancement during the pressurization-depressurization cycle of injection pressure in (a) sample B-20V and (b) sample P-20V.

3.5.3 Slip Characteristics and Stress Drop

In order to probe the slip characteristics and its correlation with stress drop during fracture shearing by injection, the time evolution plots of shear slip, and differential stress in the rapid slip period of each test are zoomed in Figure 3.10. It is noticed that the curves of shear slip (d_s , pink curve), and differential stress (σ_d , cyan curve) are piecewise linear functions of elapsed time during fracture slip in both tests on samples B-20V and P-20V. The plots in both tests can be roughly divided into three intervals: 1st quasi-static slip, dynamic slip, and 2nd quasi-static slip. The slip velocity ($\frac{dd_s}{dt}$) and stress-drop rate ($\frac{d\sigma_d}{dt}$, the negative sign means the decrease of differential stress) of each interval are listed in Table 3.3. In the 1st quasi-static slip, the fracture tends to slip with a relatively low rate ($\sim 10^{-7}$ m/s), and only a small stress drop is observed (<5 MPa) with a low rate (0.03 to 0.04 MPa/s). This means that the shear failure of the pre-existing fracture is approaching but not satisfied. As the continuous decrease of the differential stress, fracture slip rapidly with a high rate (1.18×10^{-5} m/s in the test of sample B-20V, and 1.64×10^{-6} m/s in the test of sample P-20V), and the test evolves into a dynamic slip interval with a shear failure. The associated stress drop is high with a fast decrease rate (40-50 MPa drop in differential stress with a drop rate in the scale of 0.1 to 1 MPa/s). Because of the large stress drop, the fracture slip tends to slow down ($\sim 10^{-8}$ to $\sim 10^{-7}$ m/s) and switches back to quasi-static slip state. The stress state on the fracture plane is not critical and the shear failure is not satisfied. In the 2nd quasi-static slip interval, the stress drop is less than 5 MPa with a decrease rate in the scale of 0.01 MPa/s. It is reasonable to expect that the fracture slip will be eventually stop once the shear stress declines to a lower level (unless the stress re-accumulates by loading or the further elevation of injection pressure). The dynamic slip interval has higher shear-slip rate and stress-drop

rate than which of the quasi-static slip interval. However, the duration of dynamic slip interval is much shorter than that of the quasi-static slip interval. Moreover, fracture slip correlates well with the associated stress relaxation: a faster fracture slip induces a quicker stress relaxation, and vice versa.

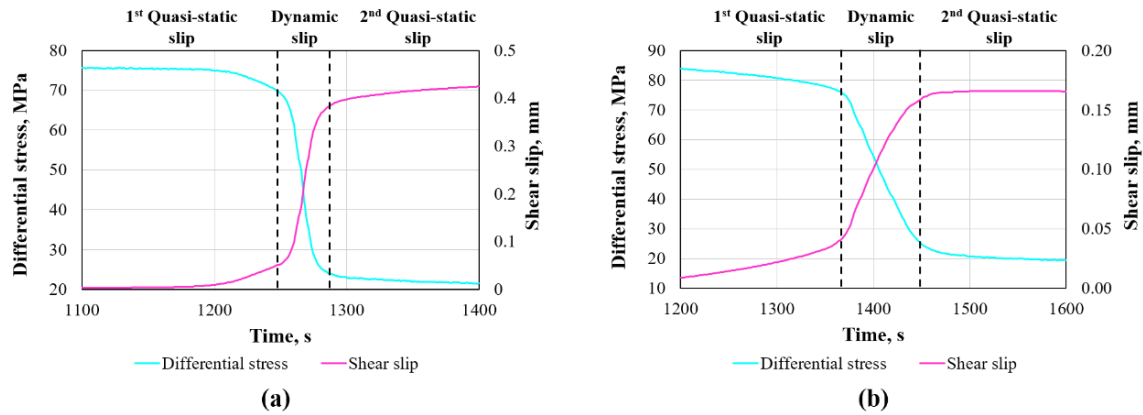


Figure 3.10: Slip characteristics and stress drop in the rapid slip period of each injection test: (a) sample B-20V; (b) sample P-20V.

Table 3.3: The values of slip rate and stress drop rate at slip period of each test.

Sample #	Slip rate ($\frac{dd_s}{dt}$), m/s			Stress relaxation rate ($\frac{d\sigma_d}{dt}$), MPa/s		
	1 st quasi-static slip	dynamic slip	2 nd quasi-static slip	1 st quasi-static slip	dynamic slip	2 nd quasi-static slip
B-20V	2.56×10^{-7}	1.18×10^{-5}	3.05×10^{-7}	-0.03	-1.62	-0.02
P-20V	1.65×10^{-7}	1.64×10^{-6}	3.19×10^{-8}	-0.04	-0.68	-0.03

3.5.4 Asperity Degradation and Gouge Production

The asperity degradation and gouge production caused by fracture shearing have been widely observed in laboratory-scale experiments and the natural fault zone. As shown in Figure 3.11, significant slickensides (the polished area with white-colored patches on the fracture surfaces) can be seen on the fracture surface of two shale samples after testing, indicating that the two opposite fracture surfaces of each sample experienced frictional shearing during injection. Also, a few large-sized rock chips and a large amount of fine gouge particles are noticed on the sheared fracture surface. In the depressurization segment of the injection tests, the fracture permeability decreased quickly with the decrease of the

injection pressure (see Figure 3.9). The possible reason is that the gouge produced during shearing could plug the flow paths to further restrict fluid flow, in addition to the increase of the effective normal stress by the decrease of injection pressure. This is also evidenced by that the many fine gouges are observed in the production wellbore (Figure 3.3) after the injection test.

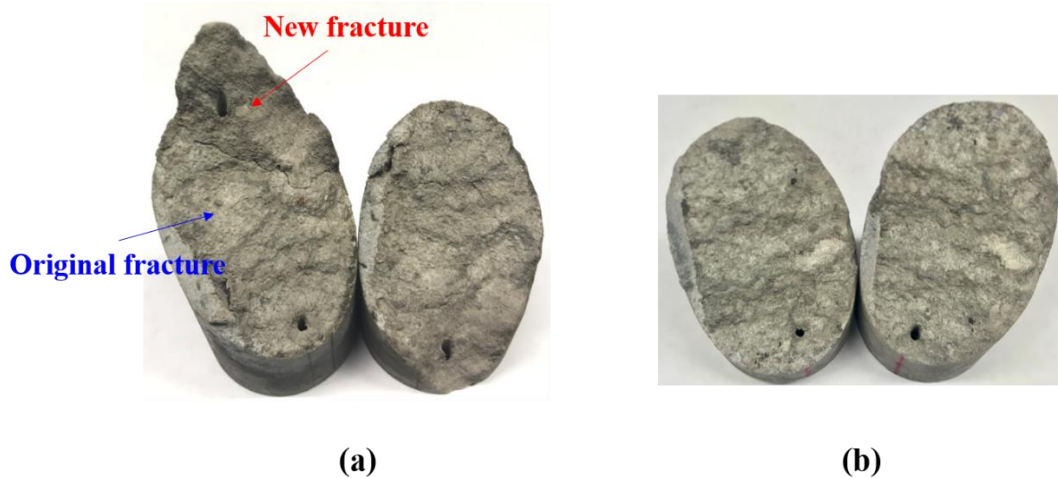


Figure 3.11: Gouge production on tested sample: (a) sample B-20V and (b) sample P-20V. In left figure, the blue-dashed line indicates the original fracture plane, and the red-dashed line represents the newly created fracture.

3.6 Chapter Summary

In this experimental study, samples from shale reservoirs from depth ($>10,000$ ft.) each containing a single rough fracture were used to conduct injection-induced shear test. In the test, a comprehensive triaxial stress was first applied on the cylindrical sample (~ 38 mm diameter) having a single rough inclined fracture. Next, pressurized brine water (7% KCl) was injected into the fracture by syringe pump from the bottom pre-drilled borehole of the sample, and then produced from the top of the sample through another pre-drilled borehole. With the stepwise elevation of injection pressure, fracture shear slip and dilation was induced. The measurements of fracture deformation (slip and dilation), stress, and fluid flow (pressure, flow rate, volume) were all concurrently recorded to characterize the hydro-mechanical

responses of shale fracture during shearing by injection. Results show that up to three orders of magnitude enhancement in flow rate was achieved by a shear slip of ~0.1 mm scale on both shale samples. In addition, significant stress drop was noticed during fracture shearing which matches well with the stress relaxation feature of natural faults/fractures shearing in reality. In addition, it is observed that the permeability enhancement was partially retained on the sheared fractures during fluid depressurization, indicating that the permeability creation caused by fracture shear slip may be also retainable (at least in a short term after the treatment) in the present shale rocks tested. However, in a similar shear test we conducted on an Eagle Ford sample (Ye et al., 2017), the permeability increase was not retained when the fluid pressure was declined to a relative low level ($\Delta P < 8$ MPa, ΔP is the pressure difference between the injection and production wellbores, see Figure 3.3 (a)). This means that the retainable permeability enhancement by fracture slip in shale may be determined by the fracture type, and the rock mineralogy composition and frictional properties. After the tests, we also observed that new fractures were created on one sheared shale samples. According to the observations and results, we conclude that three fundamental mechanisms can contribute to the permeability enhancement in shales by fracture shear reactivation: 1) shear-induced fracture prop-open by asperities; 2) the increase of fracture aperture due to stress drop accompanying with fracture slip; 3) the creation of new cracks, fractures, and interconnected fracture networks. On the other hand, the gouge produced on fracture surface during the frictional shear slip could plug the flow path and decrease fracture permeability, especially under the depletion of reservoir pressure. In addition, fracture slip correlates well with the associated stress relaxation: a faster fracture slip induces a quicker stress relaxation, and vice versa.

Chapter 4

Injection-Induced Fracture Propagation and Coalescence in Granite

The dilatant shear slip of pre-existing fractures caused by pressurized fluid injection, and its implications for enhancing permeability in reservoir stimulation for geothermal and unconventional shale resources have been demonstrated in Chapter 2 and Chapter 3. On the other hand, the creation of new cracks could be an integral part of shear stimulation as shear slip increases the stress-intensity at the tips of pre-existing fractures, potentially leading to fracture propagation and the generation of fracture networks. However, interconnected fracture network generation caused by the propagation and coalescence of pre-existing fractures during injection has been rarely studied through laboratory experiments. In this chapter, to examine permeability enhancement through the propagation and coalescence of pre-existing fracture(s), novel triaxial-injection experiments under representative crustal stress conditions were conducted on cylindrical granite samples containing one or two pre-existing fracture(s)/flaw(s).

4.1 Abstract

The dilatant shear slip of pre-existing fractures/faults by injection at pressures below the minimum in-situ stress has been recognized as an important permeability creation mechanism during reservoir stimulation. However, interconnected fracture network generation caused by the propagation and coalescence of pre-existing fractures during shear stimulation has been rarely studied through laboratory experiments. To examine permeability enhancement through the propagation and coalescence of pre-existing

fracture(s), we conducted novel triaxial-injection experiments under representative crustal stress conditions on cylindrical granite samples containing one or two pre-existing fracture(s)/flaw(s). In the sample with a single fracture, SW-1, new cracks propagated from the pre-existing fracture due to injection. In the sample with two fractures, SW-2, a highly conductive fracture network was created by the coalescence of newly formed cracks with pre-existing fractures. As a result, the equivalent permeability of the sample was enhanced by 17 to 35 times. Both tensile wing cracks, shear and/or mixed-mode secondary cracks were detected from the SEM images of the tested samples. Our results suggest that in addition to dilatant shear slip, propagation and coalescence of pre-existing fractures significantly contribute to reservoir permeability creation during low injection pressure stimulation in fractured rocks. Although the experiments focused on reservoir stimulation, the results have relevance to crustal permeability evolution and induced seismicity.

4.2 Introduction

The presence of fractures in subsurface rock masses affects their mechanical deformation and transport characteristics. Reactivation of pre-existing fractures by pressurized fluid injection has been considered as an important mechanism of reservoir stimulation and induced seismicity for a long time (Cornet & Yin, 1995; Ellsworth, 2013; Evans et al., 2005; Guglielmi et al., 2015; Kim, 2013; Majer et al., 2007; Pine & Batchelor, 1984; Willis-Richards et al., 1996; Ye & Ghassemi, 2018a; Zoback et al., 2012). Specifically, the stimulation approach to achieve economic flow rates by reactivating pre-existing fractures (so-called *shear stimulation* or *hydroshearing*) has been recognized as one of key techniques to determine the success of EGS or enhanced geothermal systems (e.g. Murphy et al., 1999; Pine & Batchelor, 1984). In contrast to hydraulic fracturing which

involves the initiation and propagation of new tensile fracture(s) under high pressure injection, shear stimulation is carried out at injection pressures below the minimum principal stress by reactivating critical or near-critical pre-existing fractures to generate highly conductive fracture networks away from the wellbore. It is also believed that the permeability created by low pressure shear stimulation is permanent, while the permeability enhanced by high pressure hydraulic fracturing is not retainable without proppant use due to significant fracture closure after pump shut-in and reservoir pressure depletion (Amann et al., 2018; Baria et al., 1999; Cheng et al., 2019; Cornet et al., 2007; Evans, 2005; Pine & Batchelor, 1984; Rahman et al., 2002; Ye, Sestey, & Ghassemi, 2018). During shear stimulation, a small reduction of effective normal stress by direct injection or the leak-off from a hydraulic fracture can be sufficient to induce the dilatant shearing of optimally oriented pre-existing fractures. A numbers of injection experiments on rock fractures have been conducted to explore permeability enhancement resulting from this process (Crawford et al., 2017; Fang et al., 2017; Gutierrez et al., 2000; Samuelson et al., 2009; Li et al., 2008; Park et al., 2013; Vogler et al., 2016; Wu et al., 2017; Zhang et al., 2013). In our companion paper (Ye & Ghassemi, 2018a), we described injection-induced shear tests on granite fractures using a more realistic boundary control, allowing us to capture the permeability evolution, slip characteristics and stress relaxation during fracture shearing. Our results also show that the permeability enhancement is retainable in sheared rough fractures due to the fracture propping by the asperities.

However, shearing of natural fractures can also lead to their propagation because of the increase in stress intensity at fracture tips (Gischig & Preisig, 2015; Horii & Nemat-Nasser, 1986; Huang et al., 2013; Jung, 2013; Min et al., 2010; Rutledge et al., 2004; Ye &

Ghassemi, 2018b; Ye, Ghassemi, & Riley, 2018). But, most studies of this phenomenon have been limited to analytical and numerical modeling (Kamali & Ghassemi, 2018; Petit & Barquins, 1988; Rao et al., 2003) and some field data interpretation (Jung, 2013). Little or no experiments have been performed to probe the propagation of pre-existing fractures at low injection pressure stimulation under realistic stress conditions, to generate a fracture network by the coalescence of propagated new cracks and pre-existing ones. A few injection tests involving pre-existing fractures are in reality *hydraulic fracturing* tests under biaxial compression or under triaxial/true triaxial compression (e.g., AlDajani et al, 2018; Gonçalves & Einstein, 2018; Morgan et al., 2017). In these tests, the new fractures/cracks were mainly tensile-mode, induced by high pressure injection (injection pressure is higher than the minimum principal stress) rather than by low pressure injection corresponding with the shear stimulation concept. In addition, most current experimental studies have induced the propagation and coalescence of pre-existing fractures via elevating the mechanical load (Bobet & Einstein, 1998; Lee & Jeon, 2011; Mirsa, et al., 2009; Sobolev, 1986; Shen et al., 1995; Wong & Einstein, 2009a, 2009b; Yin et al., 2014), instead of water injection.

In this study, we describe the results of novel triaxial-injection tests on cylindrical granite samples, each containing a single or two pre-existing fracture(s). In the test, pressurized deionized water was injected into the pre-existing fracture to initiate and propagate new cracks from the fracture tips, and to further induce the coalescence of newly propagated cracks and pre-existing fractures for fracture network generation. The analysis of the hydro-mechanical measurements during the test and SEM images from the tested samples are combined to examine the following key points: (1) the propagation and coalescence of pre-existing fracture(s) in granite under high stress, low pressure shear

stimulation; (2) the coupled hydro-mechanical response of the granite samples containing pre-existing fracture(s) during injection; (3) the generation of an interconnected fracture network through the coalescence of newly propagated cracks and pre-existing fractures; (4) permeability enhancement caused by the creation of interconnected fracture network; (5) the characteristics of the induced cracks propagated from pre-existing fracture(s), and (6) the implications of the enhanced permeability and the observed stress drop during fracture propagation.

Although the focus of this experimental study has been reservoir stimulation, it is worth noting here that the propagation/failure mechanisms of pre-existing fractures have relevance to the interpretation of Non-Double-Couple microseismicity (e.g. Julian, et al., 1998; Miller et al., 1998; Staněk & Eisner, 2017), and the accompanying permeability enhancement during fracture propagation can improve our understanding of the permeability evolution in the Earth's shallow crust (Evans, Forster, & Goddard, 1997; Ingebritsen & Manning, 2010; Rojstaczer et al., 2008).

4.3 Experimental Methods

4.3.1 Sample Preparation

The two samples used in this study are cylindrical Sierra White granites with 50.80 mm (2-inch) in diameter and 101.60 mm (4-inch) in length (see Figure 4.1(a) and Figure 4.1(d)), each containing a single or two parallel pre-existing fracture(s)/flaw(s). In the literature, different terminologies have been used to describe the discontinuities in rocks or rock-like materials created by saw-cut, waterjet-cut or other methods (molding, etc.), such as silts (e.g. Brace & Bombolakis, 1963; Nemat-Nasser & Horii, 1982), slots (e.g. Petit & Barquins, 1988; Thomas & Pollard, 1993), cracks (e.g. Ashby & Hallam, 1986; Hoek &

Bombolakis, 1965; Nemat-Nasser & Horii, 1982), flaws (e.g. Brace 1961; Lee & Jeon, 2011; Wong et al., 2009a), faults (e.g. Sobolev, 1986), joints (e.g. Liu et al., 2018; Mughieda & Karasneh, 2006), fractures (e.g. Bobet & Einstein, 1996; Misra et al., 2009; Reyes & Einstein 1991; Shen et al., 1995). In this paper, from the perspective of reservoir geomechanics, we use the term *fracture* to represent the pre-existing discontinuity in the granite sample, and use the term *crack* to indicate the new macro-fractures initiated and propagated from the pre-existing fracture(s).

The relevant geomechanical properties and mineralogy composition of this Sierra White granite were presented in Chapter 2. A commercial water-jet system was used to create the sidewall-crossed open fracture(s) in the cylindrical granite samples. Pressurized water mixed with garnet abrasive sands ejected from a 1 mm diameter nozzle was used to create the pre-existing fracture with an average 1.6 mm width/aperture. For the granite sample having a single pre-existing fracture (SW-1), the fracture length ($2a$) is 20 mm, and the inclination angle (α) from fracture to the short axis of the sample is 60° (see Figure 4.1(b)). As shown in Figure 4.1(e), in the case of granite sample containing two pre-existing fractures (SW-2), two parallel fractures (one on each side of the central axis of the sample) were created, and both fractures have 10 mm in length ($2a$) and an inclination angle (α) of 60° with respect to the short axis of the sample. The ligament length (defined as $2b$ in Figure 4.1(e), the straight-line distance between two adjacent inner tips) is also 10 mm. In addition, the ligament angle (β) is 90° with respect to the short axis of the sample. This means that the connecting line between the two inner tips is perpendicular to the short axis of the sample. The waterjet cut fracture has round tips (see Figure 4.1(c) and Figure 4.1(f)), and the tip

width at the starting point of cutting (so-called *keyhole*) is slightly wider than that at the ending point of cutting (e.g. Lee & Jeon, 2011; Miller & Einstein, 2008).

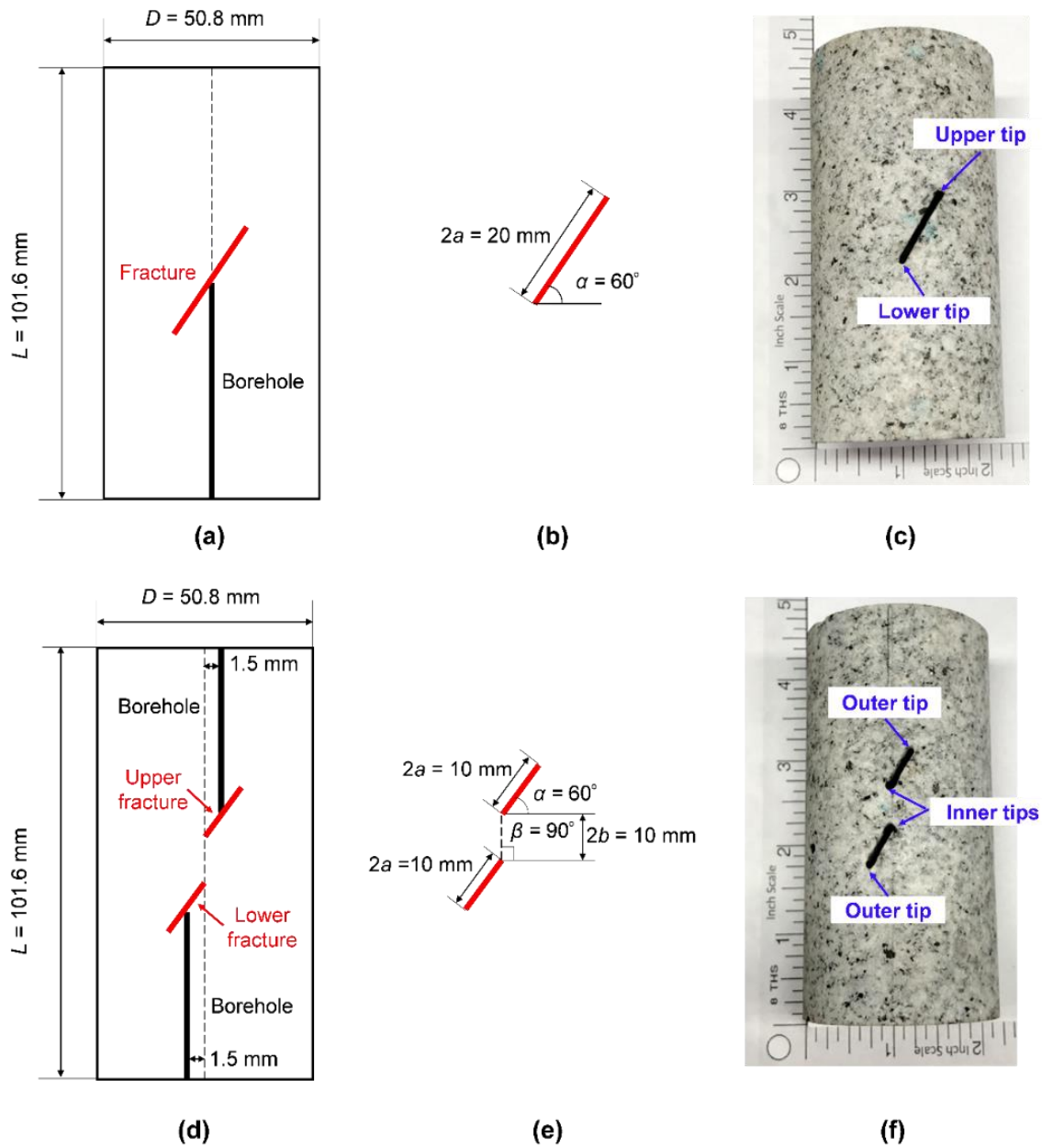


Figure 4.1: Sample preparation: (a) geometry of sample SW-1 with a single pre-existing fracture; (b) details of the pre-existing fractures; (c) side-view of sample SW-1; (d) geometry of sample SW-2 containing two pre-existing fractures; (e) details of the two pre-existing fractures and the fracture ligament; (f) side-view of sample SW-2.

To create a flow path for water injection and production, 2 mm diameter borehole was drilled to touch the pre-existing fracture(s). In sample SW-1, one injection borehole was

drilled along central axis of the sample from the bottom end to reach the fracture (Figure 4.1(a)). For sample SW-2, two boreholes, separately located each side of the sample central axis, were drilled from the sample ends to touch the upper fracture and the lower fracture, respectively (Figure 4.1(d)). The borehole only touched one surface of the fracture and did not cross it. Before testing, the ends of each sample were finely polished, and then the samples were subjected to an ultrasonic bath and subsequently dried by a vacuum oven (see Ye & Ghassemi, 2018a for additional experimental details for a similar injection test).

4.3.2 Experimental Control

Extensive experimental studies have been carried out to investigate the crack development (the process of crack initiation, propagation and coalescence) from pre-existing fracture(s) in artificial or rock materials under uniaxial/biaxial compression (e.g. Bobet and Einstein, 1998; Lee and Jeon, 2011; Spooled, 1986; Wong and Einstein, 2009a, 2009b; Yin et al., 2014). In these previous laboratory works, the propagation and coalescence of pre-existing fractures were induced via elevating the mechanical load without confining stress (in uniaxial compression) or with a low confining stress (in biaxial compression), and often, the samples were completely failed. The observations in these experiments can benefit the near-surface engineering practices such as tunnel design, rock slope stability, etc. However, the aforementioned experiments are not very representative of the rock behavior in geothermal reservoirs (~4 to 5 km, e.g. Ghassemi, 2012; Tester et al, 2006;) or the crust in general where high confining stresses prevail, and where fracture propagation is usually induced by a pressurized fluid (e.g., injection during hydraulic stimulation). In addition, stress relaxation associated with the episodes of fault/fracture reactivation and seismicity is widely observed. After the stress drop, the fault/fracture movements (either caused by

fracture slip or fracture propagation or both) should terminate at a lower stress level unless there is stress re-accumulation or the further elevation of injection pressure. Therefore, a realistic boundary control is required to simulate upper crustal conditions and capture the stress relaxation during the reactivation of pre-existing faults/fractures.

Rutter et al. (1978) conducted a *stress relaxation* test to study the mechanical behavior and rheology of geological materials (without addressing injection). In this type of triaxial test (e.g. Rutter et al., 1978; Rutter & Mainprice 1978), the elastic strain energy stored in stressed sample and the loading system can be dissipated/released by holding constant the specimen length (in ideal situation). In practice, the length of the specimen plus that of a portion of the piston is controlled as constant since it is not usually possible to hold only the length of the specimen constant in triaxial testing machines. The actuator piston moves to compensate the change of the sample length. In addition, French et al. (2016) and Rutter & Hackson (2017) performed similar triaxial-injection tests on saw-cut sandstone fractures (permeable sandstone or impermeable tight sandstone) and observed the relevant stress decrease during fracture reactivation. However, the tests were carried out under a given stress path, in which the sample was manually deformed in axial extension or in axial shortening (through adjusting the actuator piston movement) to meet with the stress path. Therefore, the observed stress drops in those tests (French et al., 2016; Rutter & Hackson, 2017) was controlled/determined by the stress path, and cannot represent an evolving energy release during fracture shearing in response to injection. To provide a realistic boundary condition during the hydraulic stimulation in naturally fractured reservoirs, we proposed a triaxial-injection test with a constant piston-displacement control to probe the permeability enhancement caused by dilatant fracture slip in cylindrical granite samples (see Chapter 2).

Under the constant piston-displacement control, the actuator piston is fixed without movement, but the fracture slip/deformation is not restricted. As a result, stress drop occurs due to the compression acted on the sample by actuator piston drops in response to fracture slip, and the fracture slips slows down and finally ends at a lower stress level. Later, Passelègue et al. (2018) also used a similar constant piston-displacement control to study the distribution of pressure and effective stress in a fracture.

Here, the triaxial-injection test (using a constant piston-displacement control mode, see Chapter 2) was further adopted to investigate the propagation and coalescence of pre-existing fractures in granite during shear stimulation. During the fracture propagation test, a confining pressure (employed by confining oil) and an initial/reference differential stress (exerted by the actuator piston of the test system) are first applied on the cylindrical sample. Next, the test is switched to the constant piston-displacement control to keep the piston displacement constant. This means that no further movement of the piston and no further increase of the differential stress. However, the sample shortening in axial direction and the sample expansion in lateral direction are without any restrictions. Subsequently, the pressurized water is injected into the pre-existing fracture through the drilled borehole (see Figure 4.1) to induce crack propagation. At the onset of the crack propagation, the differential stress/compression exerted on the sample by the piston drops significantly in response to the sample shortening with the gradual propagation of the pre-existing fracture. As a result, without further increase of the injection pressure, the crack propagation slows down and finally terminates when the differential stress decreases to a lower level. The assumption of this experimental control is that the deformation of the overburden (the piston) at a distance far from the fluid injection zone is negligible, while the energy stored into the

reservoir rocks can release during fault/fracture reactivation. To our knowledge, the triaxial-injection test we proposed with constant piston-displacement control is the first experiment which can reveal an evolving stress drop during fault/fracture reactivation, and can be used for the corresponding acoustic emission (seismicity) interpretation.

4.3.3 Experimental Setup and Procedure

The tests were conducted at room temperature (25 °C) using an MTS 816 Rock Mechanics Test System. Silicone oil was employed as confining medium, and deionized water was used as injection fluid to provide fluid pressure. A copper sheet, rubber ring, and epoxy were used to seal the pre-cut fracture, preventing the injected water flowing out from the inside of fracture through the sidewalls during injection. Further, to isolate the sample from the silicone oil, the sample was jacketed by Viton heat-shrink tubing with 0.75 mm thickness. The average axial deformation of the rock sample was measured by two Linear Variable Differential Transformer (LVDT) position sensors mounted on the sample, while the lateral deformation of the sample was evaluated by another LVDT sensor attached on a radial ring (see Figure 4.2(a) and Figure 4.2(b)). A load-cell located inside of the triaxial pressure vessel was used to measure the axial force. In addition, Teledyne ISCO 100DM syringe pump was used to control fluid flow and record the relevant parameters (pressure, flow rate and pump volume). More details of the test system, the sensors and the syringe pump can be found in our previous paper (Ye & Ghassemi, 2018a).

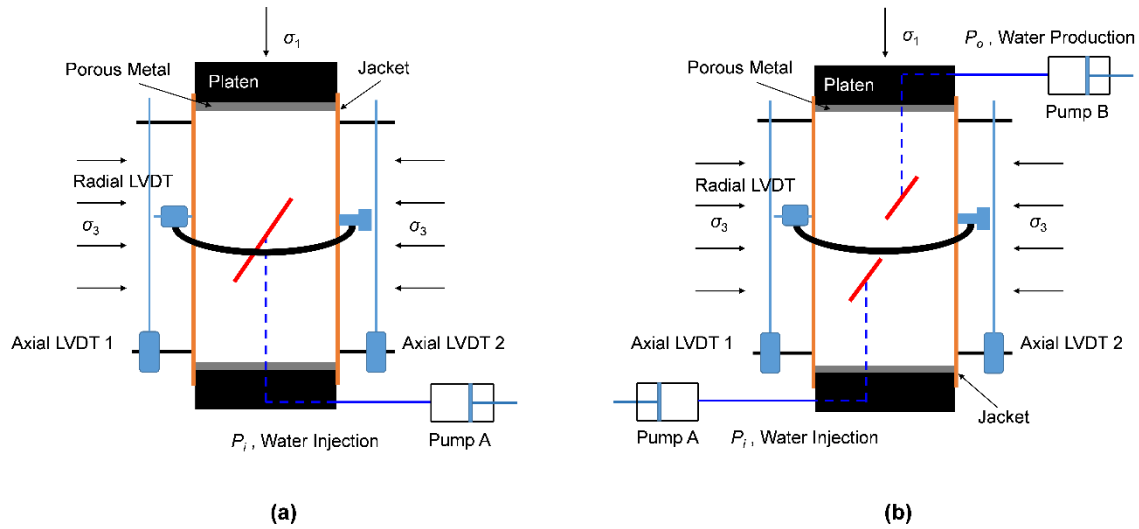


Figure 4.2: The sketches of experimental setup: (a) sample SW-1 containing a single pre-existing fracture; (b) sample SW-2 having two pre-existing fractures. LVDT = linear variable differential transformer.

The overall experimental procedure is quite similar to the injection-induced triaxial shear test we proposed in our companion paper (Ye & Ghassemi, 2018a). For the test of sample SW-1, after applying a 30 MPa (σ_3) confining pressure to the sample, the initial injection pressure (P_i , connected to the pre-existing fracture through the borehole) was set to 5 MPa (see Figure 4.2(a)). The sample was then loaded to an initial/reference differential stress ($\sigma_d = \sigma_1 - \sigma_3$) of ~110 MPa, which is ~80% of the average compressive strength determined by regular triaxial tests (with 30 MPa confining pressure) on several Sierra White samples with same geometry as sample SW-1. It was observed that the stress-strain curve of sample SW-1 was perfectly linear during loading (except for the initial seating part), without any dilation/deflection under this reference stress level (see Figure 4.3(a)). This means that there were no macro-cracks induced and propagated from the pre-existing fracture before the start of injection. However, a few micro-cracks or white patches may have developed at the tips in response to the loading (Wong & Einstein, 2009b; Yin et al., 2014). Subsequently, the test was switched to constant piston-displacement control, and the injection pressure was continuously increased from 5 MPa to 29 MPa at a constant rate of 0.15 MPa/s to facilitate

propagation of new cracks from the pre-existing fracture. The injection pressure was kept lower than the confining pressure to replicate the concept of low-pressure shear stimulation (injection pressure is lower than minimal principal stress). The relatively large range of fluid pressurization used (from 5 MPa to 29 MPa) in the test was intended to induce fracture propagation under a relatively low stress level (~80% of rock strength) in a short time (less than 500 s).

Similarly, for sample SW-2, the same confining pressure ($\sigma_3 = 30$ MPa) and the initial injection pressure (applied by pump A, $P_i = 5$ MPa) were applied, while the production pressure (P_o) maintained by pump B was set to 5 MPa during the entire test period (see Figure 4.2(b)). Next, an initial/reference differential stress (σ_d) of ~135 MPa was applied to the sample. Subsequently, under the constant piston-displacement control, the injection pressure was gradually elevated at a rate of 0.15 MPa/s (from 5 MPa to 29 MPa) to induce the propagation and coalescence of pre-existing fractures. The remaining steps are the same as those applied to the sample SW-1.

4.4 Results and Discussions

The purpose of the injection test on sample SW-1 is to illustrate that the stressed pre-existing fracture can be propagated at injection pressure lower than the minimum applied stress. While the test of sample SW-2 is used to explore the permeability (or flow rate) enhancement upon the formation of an interconnected fracture network in response to the propagation and coalescence of pre-existing fractures by low pressure injection.

4.4.1 Hydro-Mechanical Coupled Measurements

Figure 4.3 shows the test results for sample SW-1, including the full stress-strain curve during the entire test (see Figure 4.3(a)), and the hydro-mechanical measurements

during injection (see Figure 4.3(b)). The sample was first loaded to a reference stress level (from point A to point B, see Figure 4.3(a)), and then the test was switched to constant piston-displacement control at point B (the peak-stress point). As a result, the actuator piston was suddenly fixed with no further movements, and the stress-strain curve evolved into point C. A small decrease of differential stress (~ 3 MPa) is observed from point B to point C which resulted from the system's servo-control lag. Subsequently, the sample deformation (in both axial and radial directions) and the time were zeroed, and the stress-strain curve reached point D. The reason that we zeroed the sample deformation at point C is to conveniently monitor the temporal evolution of hydro-mechanical measurements during injection, since the sample deformation in the initial stage (setting of the confining pressure, injection pressure and differential stress) are much larger than that in the injection segment (from point D to point E). The hydro-mechanical measurements corresponding with the interval from point D to point E (on the stress-strain curve in Figure 4.3(a)) is illustrated in Figure 4.3(b).

In Figure 4.3(b), the green curve is the piston displacement during the test, which was kept constant using the constant piston-displacement control. The blue curve is the injection pressure which was elevated gradually from 5 MPa to 29 MPa to induce fracture propagation. The differential stress is described by the black curve which dropped significantly once fracture propagation was initiated. The red and pink curves represent the axial shortening and radial expansion of the sample, respectively. The brown curve is the fluid volume of the injection pump, while the flow rate of the injection pump is represented by the purple curve. As shown in Figure 4.3(b), the temporal evolution of the test on sample SW-1 can be separated into three stages using the black vertical dashed-lines, corresponding

with the change in the injection pressure. The major aspects of each stage with different hydro-mechanical response are discussed below:

- Stage 1. The injection pressure was held constant as 5 MPa for ~70 s. In this stage, sample SW-1 was in a *static* state with almost negligible axial shortening and radial expansion. The corresponding changes of injection flow rate and pump volume were zero or almost zero. This means that no water flowed into or leaked-off from the pre-existing fracture after the injection pressure was stabilized as 5 MPa. It is also an evidence that both the sample and the pre-existing fracture had a good sealing. Hence, it is reasonable to conclude that no macro-cracks were emanated from the pre-existing fracture at this stage. Furthermore, the slight decrease of differential stress (<0.5 MPa) was related to the elastic energy stored in the sample during axial loading which is released in a creeping manner under the constant piston-displacement control.
- Stage 2. The injection pressure was elevated from 5 MPa to 29 MPa at a constant rate of 0.15 MPa/s. This injection pressure buildup stage lasted from ~70 s to ~240 s. The hydro-mechanical plots of this stage can be roughly divided into two segments. In the first segment (from ~70 s to ~120 s), the flow rate increased with the elevation of the injection pressure, and the flow rate curve is relatively smooth without any significant fluctuations. The pump volume decreased 0.13 ml. Slight changes of axial and radial displacements (both are less 0.01 mm), corresponding with a limited stress drop (0.32 MPa) are also evident. This indicates that significant macro-cracking had not started during this early segment of the injection pressure buildup stage. The small sample deformation

can be contributed mainly to the expansion of the pre-existing fracture caused by the increased water pressure. After the injection pressure reached above ~8 MPa, the test entered into the second segment (from ~120 s to ~240 s), where the injection pressure was continuously elevated to 29 MPa. Major initiation and propagation of cracks from the pre-existing fracture occurred in this segment. This is indicated by the significant increase in displacements (0.03 mm in axial shortening, and 0.15 mm in radial expansion) and a rapid decrease of differential stress (~11 MPa stress drop). The injection pressure was prescribed to elevate at a constant rate, so the flow rate was automatically adjusted by the pump to keep the constant pressure rate during the injection. Therefore, the flow rate fluctuates significantly (purple curve in Figure 4.3(b)) during the second segment providing evidence for the initiation and propagation of new cracks from the pre-existing fracture. In addition, another 1.38 ml deionized water was further consumed in this segment of injection, which is >10 times the volume injection in the first segment. This means that the water leaked off from the pre-existing fracture and flowed into the propagated new cracks.

- Stage 3. After the injection pressure reached the target of 29 MPa, the injection pressure was held constant for another ~200 s (from ~240 s to ~440 s at the time evaluation axis in Figure 4.3(b)). In this stage, the fracture propagation slowed down as indicated by the decreased rates of sample deformation and stress-drop. The curves (displacements, differential stress, flow rate and pump volume) all tend to become flat and show a gradual decrease in slope. The explanation is that the injection pressure was not increased further and the differential stress

experienced a significant decrease in Stage 2, limiting further crack propagation. However, it is likely that a few localized crack propagation events occurred during this constant injection pressure stage as indicated by several small fluctuations in the flow rate curve from ~290 to ~310 s (see Figure 4.3(b)).

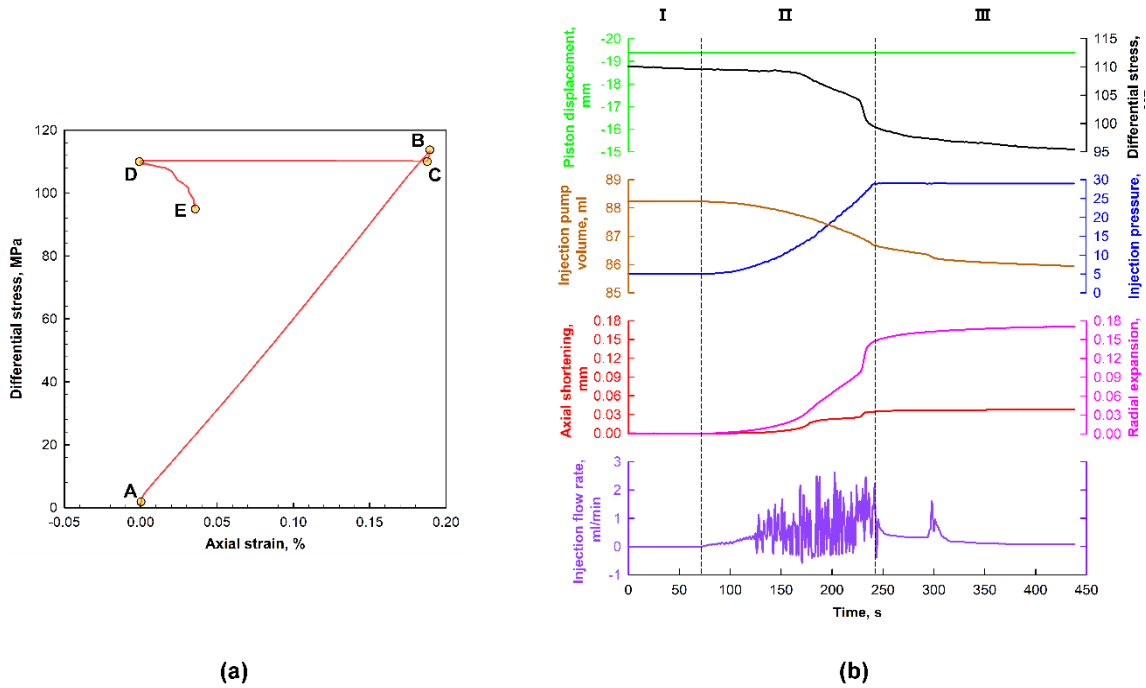


Figure 4.3: Test results for sample SW-1 (having a single pre-existing fracture): (a) the full stress-strain curve, in which points A, B, C, D and E describe the multi-step experimental procedure; (b) the hydro-mechanical measurements over time during injection (corresponding with the interval from point D to point E in the stress-strain curve), in which the temporal evolution of the piston displacement (green), differential stress (black), the injection pressure (blue), the injection pump volume (brown), the axial shortening (red), the radial expansion (pink), and the injection flow rate (purple) during the 440 s long fluid injection are illustrated. The axial shortening of the sample is calculated from the measured axial displacement, since the sample length is larger than the actual gauge length (see Figure 4.2(a)).

The full stress-strain curve and the hydro-mechanical measurements (in the injection segment) of sample SW-2 are shown in Figure 4.4(a) and Figure 4.4(b), respectively. The signature of the stress-strain curve of sample SW-2 is quite similar to that of sample SW-1. It is also observed that the stress-strain curve of sample SW-2 is perfectly linear (except for the initial seating part) without dilation/deflection during the loading interval (from point A

to point B in Figure 4.4(a)). This means that no macro-cracks or macro-damage was induced before the start of the injection. In the temporal evolution plots of Figure 4.4(b) (corresponding with the interval from point D to point E in Figure 4.4(a)), a color schemes the same as in the previous test on sample SW-1 is used. Three extra curves recording the fluid flow properties of production pump B are added into Figure 4.4(b): the gray curve describes the fluid pressure in production pump B, which was kept constant ($P_o = 5$ MPa) during the test; the gold curve indicates the flow rate of production pump, which increased significantly once the communication of the lower and the upper fractures was achieved through fracture propagation; the teal curve is the fluid volume/production of pump B, which shown a remarkable increase trend after the coalescence of the two pre-existing fractures. Similarly, the hydro-mechanical plots during injection of sample SW-2 can be divided into three stages:

- Stage 1. In this stage, the injection pressure was kept constant at 5 MPa for ~70 s. The rock deformation and stress-drop are negligible. The flow rates of pump A (injection pump) and pump B (production pump) are almost zero, corresponding with the slight changes of pump volumes. This means that both the lower fracture and the upper fracture were all in the *static* state, and the test assembly was perfectly sealed.

Stage 2. The injection pressure was increased from 5 MPa to 29 MPa. According to the hydro-mechanical response, this stage can be separated into three segments. The first segment lasted from ~70 s to ~140 s and shows small changes in the sample deformation, differential stress, and injection pump volume in response to the injection pressure increase. The injection flow rate was stably increased

and the curve of injection flow rate is quite smooth without any significant fluctuations, while the production flow rate remained at zero. This means that no new cracks emanated from the two pre-existing fractures. The lower fracture deformed a little bit due to the elevation of the fluid pressure inside of it, while the upper fracture was still in a *static* state. As the injection pressure continued to increase above ~9 MPa, noticeable rock deformation (0.01 mm axial shortening and 0.02 mm radial expansion) and stress relaxation (1.30 MPa stress drop) were induced during the second segment (time interval of ~140 s to ~200 s in Figure 4.4(b)). The fluctuations of the injection flow rate curve and the noticeable decrease of the injection pump volume (0.62 ml water loss from injection pump A) demonstrate the initiation and propagation of new cracks from the lower fracture. On the other hand, the production flow rate was still zero and the volume of production pump B did not show any gain, indicating that no hydraulic interactions occurred between the two pre-existing fractures. In the third segment of stage 2 with the injection pressure above 18 MPa (from ~200 s to ~240 s in Figure 4.4(b)), the rock deformation and stress drop were further induced in response to the continuous elevation of injection pressure. The flow rate of the pump B gradually increased from zero, indicating that the upper fracture communicated with the lower fracture by coalescence of propagated new cracks with the two pre-existing fractures. As a result, water flowed from the lower fracture to the upper fracture due to the pressure difference between the two pumps (pump A and pump B). However, the injection flow rate was still much larger than the production flow rate, and showed fluctuations. This can be

explained by incomplete connection of two pre-existing fractures by new cracks, and the propagation of other *non-connecting* cracks (i.e., the cracks did not coalesce with the dominant fracture network) consumed some amount of injection fluid (see SEM images).

- Stage 3. The injection pressure was increased to 29 MPa and was kept constant for another ~240 s. The production flow rate continuously increased with further fracture propagation and coalescence, and the production rate was almost equal to the injection rate at the end of stage 3. This means that a dominant crack/fracture network controlling fluid flow was completely formed and a steady-state fluid flow was reached at this stage. As a result, further propagation of the *non-connecting* cracks was restricted because all the water injected by pump A was produced by pump B at the end of this stage.

The sample SW-1 having a single pre-existing fracture experienced an axial shortening of 0.04 mm and a radial expansion of 0.17 mm during the entire injection test, along with a differential stress drop of 14 MPa (~12% of the peak differential stress). A total 2.28 ml (net volume) of water was injected into sample, and most of the water was stored in the induced new cracks considering the ultra-low permeability of the rock matrix. The sample SW-2 having two pre-existing fractures experienced an axial shortening of 0.03 mm and a radial expansion of 0.05 mm along with a differential stress drop of 6 MPa (~4% of the peak differential stress). The production flow rate gradually increased and was almost equal to the injection flow rate at the end of the test (the injection flow rate is 0.51 ml/min, while the production flow rate is 0.48 ml/min) when communication between the two pre-existing fractures was established. The total water loss of injection pump A was 3.61 ml,

while the total water gain of production pump B was 1.62 ml. This means that around 1.99 ml of water (net volume) was stored into the newly induced cracks (no more water can be stored into the fully-saturated pre-existing fractures considering the low compressibility of water). Moreover, the differential stress drops caused by fracture propagation were relatively small in both two tests, and the samples did not completely fail due to insufficient energy provided by the final injection rates.

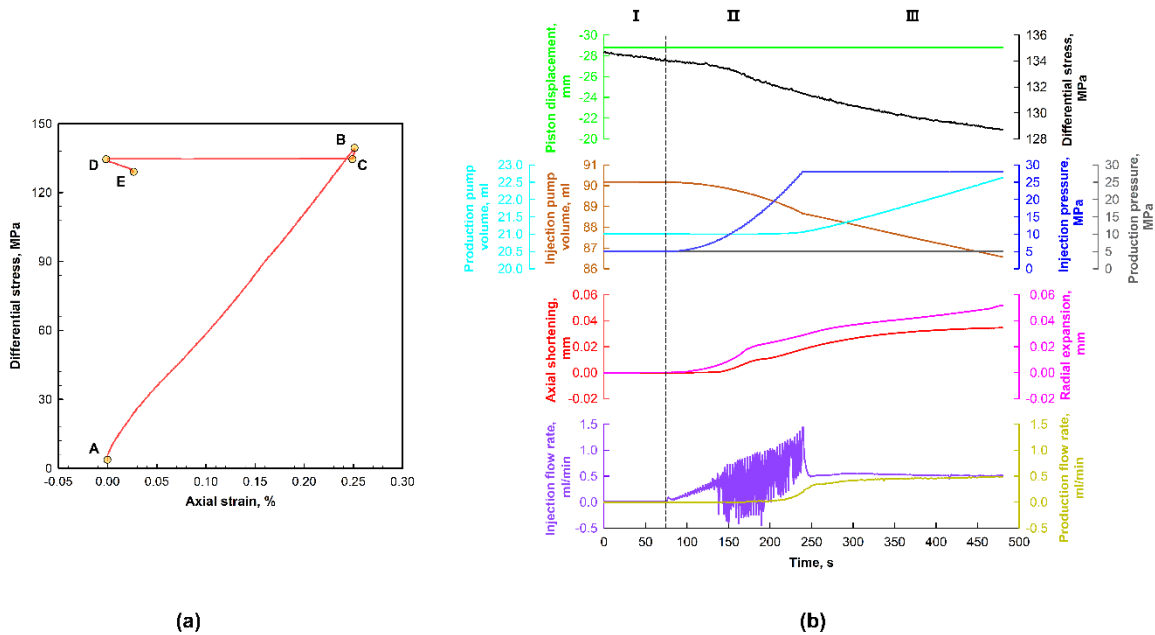


Figure 4.4: Test results for sample SW-2 (having two pre-existing fractures): (a) the full stress-strain curve, in which points A, B, C, D and E indicate the multi-step experimental procedure; (b) the hydro-mechanical measurements over time during the injection (corresponding with the interval from point D to point E in the stress-strain curve), in which the temporal evolution of the piston displacement (green), the differential stress (black), the injection pressure (blue), the injection pump volume (brown), the production pressure (gray), the production pump volume (teal), the axial shortening (red), the radial expansion (pink), the injection flow rate (purple), and the production flow rate (gold) during the 480 s long fluid injection are illustrated. Here, the axial shortening of the sample is calculated from the measured axial displacement, since the sample length is larger than the actual gauge length (see Figure 4.2(b)).

4.4.2 Crack Characteristics

The results of previous fracture propagation and coalescence experiments reported in the literature have demonstrated that as one would expect, the characteristics of pre-existing fracture(s) are highly influenced by the rock matrix texture and fracture geometry.

In addition, various crack types and different coalescence patterns have been reported in previous experimental works (e.g., Bobet & Einstein, 1998; Wong & Einstein, 2009a, 2009b, Yin et al., 2014). In our study, we used SEM (scanning electron microscope) images of the tested samples to demonstrate the characteristics of the newly propagated cracks, and to interpret their possible types and formation modes. However, a comprehensive study on cracking mechanisms and coalescence patterns is out of the scope of this paper.

After the tests, the two granite samples (SW-1 and SW-2) were cut axially in two halves, and then the central-cut surface of one half of each sample were gently polished by a rock surface grinder and used for SEM scanning. The SEM image assemblages of the two samples are shown in Figures 4.5 and 4.6, respectively. The pre-existing fracture(s) are identifiable as the dark-void groove(s) on the SEM images. Moreover, due to the surface-relief difference between the intact rock surface and the induced cracks, the occurrence of the induced cracks made them appear black in SEM images while the intact rock surface is light-gray.

Two types of cracks are usually observed in crack propagation tests: wing cracks (or primary cracks) originating from high tensile stress zone, which are usually found to be initiated at the tips of the pre-existing fracture; secondary cracks originating from the high compressive stress zone, which may or may not initiate from the fracture tips but propagate in the opposite direction from the wing cracks (e.g., Bobet & Einstein, 1998; Wong & Einstein, 2009a).

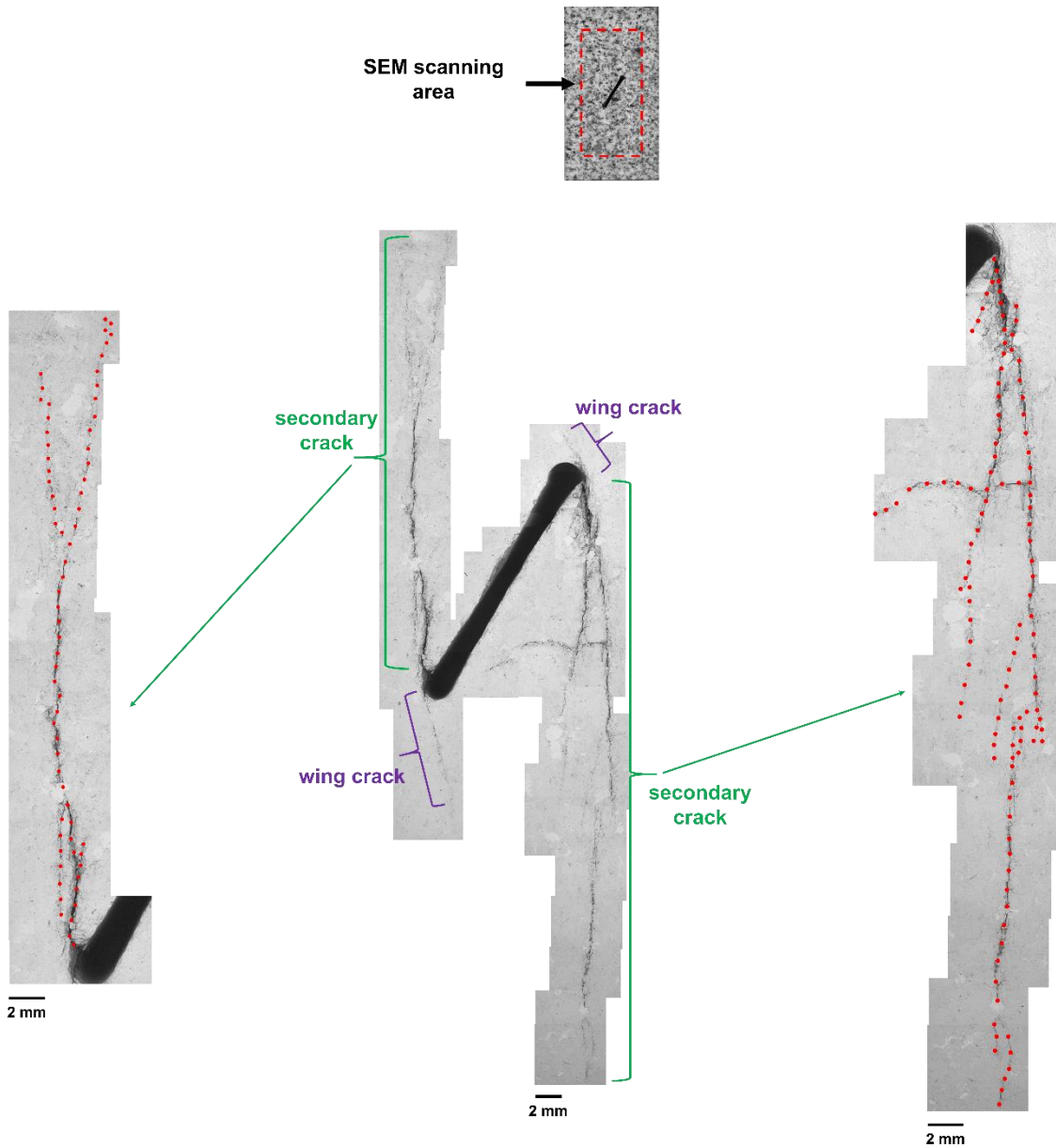


Figure 4.5: Assemblage of SEM images from sample SW-1 (containing a single pre-existing fracture). Center: image of the entire induced cracks that propagated from the pre-existing fracture; the tensile wing cracks are indicated by purple brackets, and the secondary cracks are marked by green brackets. Left: the enlarged image of the secondary cracks from the lower tip of the fracture. Right: the enlarged image of the secondary cracks from the upper tip of the fracture. The crack paths in the enlarged images are indicated by the red dots.

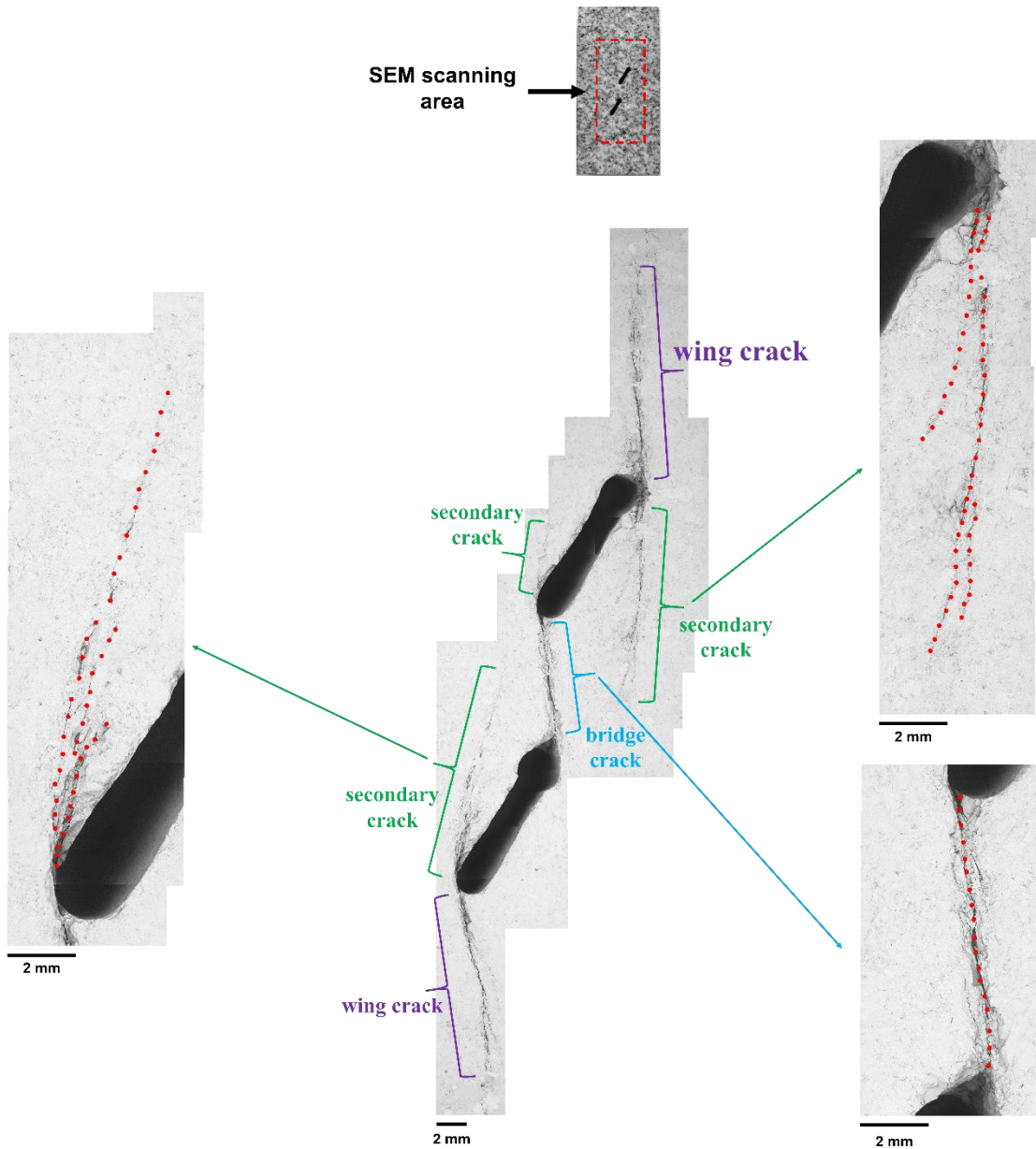


Figure 4.6: SEM image assemblages of sample SW-2 (containing two pre-existing fracture). Center: image of the entire induced cracks that propagated from the two parallel pre-existing fractures; the tensile wing cracks are indicated by purple brackets, the secondary cracks are marked by green brackets, and the bridge crack is represented by the blue bracket. Left: the enlarged image of the secondary cracks from the outer tip of the lower fracture. Right: the bridge crack (bottom), and the secondary cracks from the outer tip of the upper fracture (top). The crack paths in the enlarged images are indicated by the red dots.

In the case of sample SW-1 having a single pre-existing fracture, two pairs of major-cracks (emanating at or near the fracture tips) can be detected (Figure 4.5). Considering the initiation region and the curvilinear path, a pair of wing cracks (marked by purple brackets) appear to have initiated from the fracture tips. On the other hand, another pair of cracks

(indicated by the green brackets) propagated in the direction opposite to the wing cracks are also observed on the SEM image, which suggest they are secondary cracks. Unlike the wing cracks, the secondary cracks were initiated at a distance away from the tips of the pre-existing fracture. Similar to the observations in previous studies, significant material protrusion/spalling from surface with a large amount of crushed grains and failed grain boundaries can be observed at the initiation area of the secondary cracks. This suggests that the secondary cracks were initiated through shear-mode from a compressive stress field at least on a meso- and macro-scale. However, the initiation of the secondary cracks could be from the growth and coalescence of micro-tensile-cracks (Hori & Nemat-Nasser, 1986; Petit & Barquins 1988;). Unlike the traditional coplanar and oblique secondary cracks observed in nearly homogenous rocks or rock-like materials, the secondary cracks in granite of this test tend to form a *cluster* containing multiple sub-cracks with various crack widths and orientations. One or a few crack *trunks* (or host cracks) in each secondary crack combined with a number of crack *branches* to form a *horsetail* zone (see Figure 4.5). To our knowledge, the horsetail feature observed in our tests has not been reported in previous crack propagation experiments even through it is widely observed in natural fault zones (e.g., Cruikshank et al., 1991; Granier 1985; Petit & Barquins, 1988). In the secondary crack cluster, there are some curvilinear sub-cracks which appear as wing cracks but propagate in the direction opposite to the classical wing cracks (so-called *anti-wing cracks*, which normally propagate in mixed mode, see Yin et al, 2014). In addition, a few horizontal or near-horizontal sub-cracks appear in the secondary crack cluster that are nearly perpendicular to the maximum principal stress, which suggests the occurrence of shear-mode propagation. The appearance of material protrusion/spalling (the features of shear cracks), horizontal cracks (shear-mode feature),

anti-wing cracks (mixed-mode feature) and horsetail zone (mixed-mode features) in the secondary cracks indicate the propagation to be of a mixed-mode nature on the meso- and macro-scales. The secondary cracks are much longer and much wider than the wing cracks: the lengths of the wing cracks are ~2 mm to ~6 mm, while the lengths of the secondary cracks are ~32 mm to ~45 mm; the maximum width of the secondary cracks is ~400 μm , while the maximum width of the wing cracks is less than 40 μm . The reasonable interpretation is that the high confining stress in the test (30 MPa) suppressed significant growth of the wing cracks (e.g., Kamali & Ghassemi, 2018; Misra et al., 2009; Petit & Barquins, 1988), and the dominant secondary cracks took more fluid flow and further restricted the propagation of the wing cracks.

For sample SW-2 containing two pre-existing fractures, three types of major-cracks can be detected on the SEM images (Figure 4.6): wing cracks (indicated by purple brackets), secondary cracks (marked by green brackets) and bridge crack (depicted by light-blue bracket). It is noticed that two wing cracks (with the length of ~12 mm to ~16 mm) separately emanated from the outer tips of the lower and upper pre-existing fractures. A bridge crack (with ~ 10 mm in length) was induced in the ligament area, directly connecting the two inner tips of the two pre-existing fractures, providing a flow path for water circulation from the lower fracture to the upper fracture. Considering the fracture geometry, the direct crack coalescence pattern, and the existence of a high tensile stress zone in the ligament area, the bridge crack should be a tensile-mode crack and was formed by the coalescence of the wing cracks emanating from the inner tips of the two pre-existing fractures (Bobet & Einstein, 1998; Yin et al., 2014). Similarly, secondary cracks (propagating in a direction opposite to the wing crack) with the features of surface spalling, anti-wing cracks, and horsetail zones

also are present on the SEM images of sample SW-2 (see Figure 4.6). This means that, aside from the tensile-mode crack propagation (in wing cracks), shear and/or mixed-mode crack propagation also occurred. The secondary crack emanating from the outer tip of the lower fracture (with ~15 mm in length) propagated upward and attempted to coalesce with the inner tip of the upper fracture and the bridge crack. On the other hand, the secondary crack growing from the outer tip of the upper fracture (with ~17 mm in length) propagated downward and attempted to connect with the inner tip of the low fracture and the bridge crack. The horsetails of these two secondary cracks with their multiple branches, very likely have partially coalesced with the bridge crack and the pre-existing fractures to yield a fracture network. A third secondary crack with only ~3 mm in length is observed to have emanated from the inner tip of the upper fracture. The propagation direction of this secondary crack is opposite to the bridge crack. This is further evidence that the bridge crack formed in the tensile mode. Unlike the case of sample SW-1, the width of the tensile-mode cracks (including the wing cracks and the bridge crack) are even larger (or at least not smaller) than the width of the secondary cracks. The reason is that high tensile stress at the ligament area can benefit the growth of the wing crack, while suppressing the propagation of the secondary cracks which initiated from the compressive stress zone. After the coalescence of the two preexisting fractures, the bridge crack dominated the fluid flow and restrained the further growth of the secondary cracks.

The observations from SEM images show that the crack development from pre-existing fractures induced by injection is complex, and the cracks can form in tensile mode, shear mode and/or mixed-mode. The specific crack characteristics observed in this work

indicate that the crack propagation and coalescence could be strongly influenced by confining stress, pressurized fluid injection and material heterogeneity.

4.4.3 Fluid Flow/Permeability Enhancement

Another question we wanted to address in this study is whether reservoir permeability/fluid-flow can be enhanced in response to the propagation and coalescence of pre-existing fractures. We found that a significant flow rate increase occurred in the test of sample SW-1 in response to fracture propagation (see Figure 4.3(b)). Moreover, in the injection test of sample SW-2, a fracture network was generated through the coalescence of the propagated new cracks and the pre-existing fractures. As a result, the production flow rate was gradually increased and was almost equal to the injection flow rate at the end of stage 3 (see Figure 4.4(b)). In addition, in the last part of the Stage 3, the injection pressure and the production pressure were constant and the fluid volume changes in the two pumps were linear. This means that a steady-state fluid flow was reached. Therefore, the equivalent permeability of the sample SW-2 can be calculated by using Darcy's law:

$$k_e = -\frac{\mu Q}{A} \cdot \frac{L}{\Delta P} = -\frac{4\mu Q}{\pi D^2} \cdot \frac{L}{\Delta P} \quad (4-1)$$

where, Q is the flow rate in steady-state regime ($Q = 0.50$ ml/min), estimated by averaging the injection flow rate ($Q_i = 0.51$ ml/min) and production flow rate ($Q_o = 0.48$ ml/min); ΔP (differential pressure, $\Delta P = 24$ MPa) is the difference between injection pressure ($P_i = 29$ MPa) and production pressure ($P_o = 5$ MPa); μ is the fluid viscosity (1.002×10^{-3} Pa·s at 20 °C for water); A is the cross-section area of the sample ($A = \frac{1}{4}\pi D^2$); D and L are the sample diameter ($D = 50.80$ mm) and sample length ($L = 101.60$ mm), respectively.

The calculated equivalent permeability is 1.74×10^{-17} m², while the matrix permeability of Sierra White granite is around 5×10^{-19} m² to 1×10^{-18} m². This means that

the permeability of the sample was enhanced about 17 to 35 times, after the formation of the fracture network due to the propagation and coalescence of the two pre-existing fractures. Therefore, fracture shear slip, and the propagation and coalescence of pre-existing fracture(s) in response to low pressure injection are key and often concomitant mechanisms for permeability enhancement during shear stimulation. Moreover, the creation of a highly conductive fracture network far away from the injection well can be achieved by fault/fracture reactivation through low pressure shear stimulation.

4.4.4 Relation to Crustal Permeability and Induced Seismicity

The focus of this experimental study has been reservoir stimulation, however, the results do have relevance to crustal permeability evolution and induced seismicity. Crustal permeability is not constant in time and space. In fact, it has been suggested by Rojstaczer et al. (2008) that crustal-scale permeability is a “dynamically self-adjusting” property responding to various driving forces. According to Ingebritsen and Manning (2010) the dynamic or transient nature permeability is supported by hydrothermal-flow transients at various time scales. Such transience in the shallow, brittle crust can be attributed to forces that promote permeability creation (such as natural fracture slip and fracture propagation by fluid pressurization) competing with permeability degradation forces of depressurization, healing, and compaction. The enhanced permeability in active fault zones has been attributed to the creation of new flow paths through formation of new fractures and/or re-opening of pre-existing fractures in response to hydraulic pressurization and earthquakes (Caine et al., 1996; Gudmundsson, 2000; Guglielmi et al., 2015; Ingebritsen & Manning, 2010; Rojstaczer et al., 1995). In our companion paper (Ye & Ghassemi, 2018a), we demonstrated that the dilatant shear slip of pre-existing fracture caused by shear stimulation (with relatively low

injection pressure) can induce a remarkable enhancement in fluid flow in a fault/fracture zone (~100 times increase in flow rate). While in the present study, the contribution of fracture network creation (through the coalescence of induced new cracks and pre-existing fractures) on permeability increase in crystalline basement rocks during low fluid pressure injection is clearly revealed. The suggestion is that dilatant shear slip, and as well as the propagation and coalescence of pre-existing fractures are major and often integral mechanisms of fault/fracture reactivation and permeability dynamics in the shallow crust. Large-scale field injection practices also clearly have shown that the reactivation of pre-existing fractures induced by relatively low pressures have resulted in significant permeability creation. For instance, in the geothermal project (hot-dry-rock site) at the Soultz, France, a differential pressure of 15-20 % above hydrostatic by injection caused a 200-fold increase in the transmissivity of an injection zone at ~3.5 km depth (Evans et al., 2005; Rojstaczer et al., 2008).

The significant stress drop accompanying fracture propagation in the experiments presented herein indicates that mechanisms other than slip can contribute to energy release and possible seismicity or microseismicity. Usually, it has been assumed that microseismicity is directly caused by the shear motion on pre-existing faults and fractures (Double-Couple or DC model). However, many well-recorded seismic data have revealed the existence of Non-Double-Couple (Non-DC) source mechanisms. The motion normal to fault/fracture surfaces (tensile faulting) or the mixed-mode failure mechanisms (tensile and shear faulting) have been considered as the reasons of Non-DC seismic activities (e.g. Julian, et al., 1998; Miller et al., 1998; Staněk & Eisner, 2017). Although acoustic emission monitoring and the associated focal mechanism analysis were not recorded in our tests, the

propagation of pre-existing fractures via tensile cracks or mixed-mode secondary cracks in response to inflow of fluid is consistent with the failure mechanisms involved in Non-DC seismicity. It is suggested that a further experimental study on injection-induced fault/fracture reactivation coupled with concurrent acoustic emission monitoring would benefit our understanding of the role of mixed-mode fracture on Non-DC mechanisms in induced seismicity.

4.5 Chapter Summary

In this study, the propagation and coalescence of pre-existing fracture(s) in granite was induced by water injection under a realistic upper crustal condition of stress to simulate the low-pressure shear stimulation in enhanced geothermal systems (EGS). The results indicate that stressed pre-existing fracture(s) can be propagated as tensile, shear and/or mixed mode at injection pressures below the minimum principal stress. Also, fracture networks and a dominant flow path can be formed by the coalescence of newly propagated cracks and pre-existing fractures, resulting in remarkable enhancement of permeability/fluid flow. This indicates that dilatant shear slip, tensile and shear propagation, and coalescence of pre-existing fractures can be the integral mechanisms for permeability enhancement in fault/fracture reactivation by injection. Detailed field-scale geomechanical characterization and analysis of injection related seismicity by Cornet et al. (2007) has suggested the important role of these mechanisms in rock mass failure localization during stimulation at depth. Our experimental study further confirms those observations, and supports the findings of numerical modeling (Kamali & Ghassemi, 2018) showing that in deep subsurface conditions, the secondary shear cracks can often be the dominant contributor to fracture network generation and reservoir stimulation. Observations and results in this study also

provide some insights on the contribution mechanisms to permeability evolution in the shallow crust. Furthermore, the mixed-mode crack propagation and the accompanying stress relaxation observed in our tests shed lights on the mixed nature of source mechanisms in induced seismicity during reservoir stimulation and saltwater disposal activities.

Chapter 5

Injection-Induced Fracture Propagation and Coalescence in Shale

In this Chapter, the propagation and coalescence of pre-existing fractures in shale is probed through a similar laboratory triaxial-injection test method described in Chapter 4. Also, the potential of fracture network creation and permeability enhancement through fracture propagation and coalescence is explored. Combined with Chapter 3, the goal of the present work is to fundamentally understand the mechanisms of permeability creation through reactivation of pre-existing fractures in shales during reservoir stimulation.

5.1 Abstract

Shear stimulation has been recognized as an important factor in enhancing unconventional reservoir permeability during hydraulic fracturing or re-fracturing jobs. The process of shear slip stimulation is believed to reactivate critical or near critical pre-existing fractures causing them to slip and dilate and further propagate to generate a fracture network at treatment pressure below minimum principal stress, resulting in enhanced flow rate. However, the fundamental mechanisms and their contributions to surface area generation and permeability increase are not well understood. In our previous study, we have shown the potential of flow enhancement through dilatant fracture slip on Eagle Ford shales. In this paper, we present the results to another novel experiment on injection-induced fracture propagation and coalescence on pre-flawed shale samples. The cylindrical Eagle Ford shales with dimensions of 1.5-inch diameter by 3-inch length, containing two pre-existing fractures/flaws, are used to conduct the injection tests under triaxial condition. For a given

confining pressure and overburden stress, salt water (7% KCL) was injected into the fractures to induce fracture propagation and coalescence to generate fracture network. Results of the injection test show that flow rate can be significantly enhanced through the propagation and coalescence of pre-existing fractures at treatment pressure below the minimum principal stress. A pair of tensile cracks emanated from the fracture tips is induced during water injection. These observations show that shear stimulation involves both shear slip and fracture propagation and contribute to the permeability creation during shale reservoir stimulation.

5.2 Introduction

Unconventional shale oil/gas reservoirs require stimulation to achieve economic production rates. The standard hydraulic fracturing in petroleum industry involves massive fluid injections to induce and propagate new tensile fractures at treatment pressures much higher than the minimum principal stress. Proppant is then used to support the new and conductive fractures. However, fracture conductivity and increased reservoir permeability can also result from shear stimulation (Pine and Batchelor 1984, Willis-Richards et al. 1996, Gutierrez et al. 2000, Ghassemi and Zhou 2011, Reece et al. 2014, Weng et al. 2015, Crandall et al. 2017, Fang et al. 2017, Ye et al. 2017, Ye et al. 2018). In contrast to conventional hydraulic fracturing, shear stimulation reactivates pre-existing critical or near critical fractures causing them to slip and prop-open (Pine and Batchelor 1984, Willis-Richards et al. 1996, Baria et al. 1999, Rahman et al. 2002, Nygren and Ghassemi 2005, Cheng & Ghassemi, 2016) and possibly propagate new fractures to generate a high conductivity fracture network (Rutledge et al. 2004, Ye and Ghassemi 2018). A relatively small reduction of normal stress by injection can cause reactivation of critically or near-

critically stressed pre-existing fractures at treatment pressures below the minimum principal stress causing them to dilate. Also, leak-off from a major hydraulic fracture can lead to propagation of natural fractures (Sesetty and Ghassemi 2017, Ye et al. 2018) in the rock resulting in a large stimulated reservoir volume (SRV).

In Chapter 2 and Chapter 3, I have presented the results of dilatant fracture shear slip and the associated permeability enhancement during shear stimulation in granite and shale fractures under triaxial condition. Results showed that on a cylindrical granite/shale sample having a single rough fracture, two or three orders of magnitude enhancement in flow rate/permeability can be achieved by injection-induced fracture shear slip. Moreover, the permeability enhancement was retained in sheared fracture even reservoir/fluid pressure get declined. The observations also indicate that the irreversible normal dilation caused by fracture shear slip is the main means to make fracture prop-open permanently.

In Chapter 4, the propagation and coalescence of pre-existing fractures by pressurized fluid injection in granite samples with embedded fracture(s)/flaw(s) has been discussed. Here, the generation of interconnected fracture networks through fracture propagation and coalescence in shales is further discussed. The initiation and propagation of new cracks from pre-existing fractures in shale reservoir stimulation can be an integral part of shear stimulation mechanism as shear slip increases the stress-intensity at the fracture tips, potentially leading to fracture propagation. Until recently, this process had not been clearly demonstrated in laboratory scale experiments.

The previous experimental studies involved with fracture propagation and coalescence in shales have been *hydraulic fracturing* tests under uniaxial/biaxial compression (AlDajani et al., 2018; Morgan et al. 2017; Li & Einstein, 2019) or under

triaxial compression (Gu et al. 2012; Olson et al. 2012; Zhou et al. 2008). The newly created fractures/cracks are mainly tensile-mode, since the injection pressure is significantly higher than the minimum principal stress. To our knowledge, no experiments have been completed that directly induce fracture propagation and coalescence by injection at pressures below the confining pressure under triaxial stress conditions to simulate the process of shear stimulation.

In this novel study, injection-induced fracture propagation test has been conducted on a cylindrical Eagle Ford shale samples (1.5-inch diameter by 3-inch length) containing two pre-existing fractures/flaws. In the test, both mechanical properties (stress, axial and radial sample deformation) and fluid flow parameters (flow rate, pressure and volume) were currently measured to characterize the hydro-mechanical responses of the shale sample during injection. Moreover, the images of scanning electric microscope from the tested sample is used to crack characteristics. The goals of this work are to examine the generation of interconnected fracture network through the propagation and coalescence of pre-existing fractures in shear stimulation, and to explore the possibility of the associated permeability enhancement during fracture propagation.

5.3 Experimental Methods

5.3.1 Sample Materials

The samples used in this study are Eagle Ford shale outcrops (Del Rio region, Texas) acquired from a commercial outlet. Some mechanical properties of this shale (or mudstone) including density, matrix permeability, TOC, Young's modulus, Poisson's ratio, and tensile strength are given in Table 5.1. The data of matrix permeability and TOC are provided by the commercial outlet. Whereas, the Young's modulus and Poisson's ratio of the same type

of Eagle Ford shale were measured through a triaxial compressive test on an intact plug, and as well as the tensile strength of this shale was obtained through a Brazilian test on a shale disc (1-inch diameter by 0.5-inch thickness). The mineralogy composition was determined by powder X-ray diffraction analysis (XRD) at Texray Laboratory Services (Argyle, Texas). As listed in Table 5.2, the mineral contents of this Eagle Ford shale is dominated by calcite (52.2 wt.%), quartz (35 wt.%), and kaolinite/clay (7.4 wt.%).

Table 5.1: Some geomechanical parameters of the Eagle Ford shale.

Density (ρ), g/cm ³	Matrix Permeability (k), Nano-Darcy	TOC, wt.%	Young's Modulus (E), GPa	Poisson's Ratio (ν)	Tensile Strength (σ_t), MPa
2.40	1.98×10^{-4}	2.02	25.52	0.29	9.40

Table 5.2: Mineralogy composition of Eagle Ford shale.

Calcite, wt.%	Quartz, wt.%	Kaolinite, wt.%	Gypsum, wt.%	Calzirtite, wt.%	Pyrite, wt.%
52.2	35.0	7.4	2.3	3.0	0.1

5.3.2 Sample Preparation

Similar as Chapter 4, from the perspective of reservoir stimulation, the term *fracture* is used to represent the pre-existing discontinuity in the shale sample, and the term *crack* is used to indicate the new macro-fractures initiated and propagated from the pre-existing fracture(s).

The geometry of the cylindrical sample with a pair of pre-existing fractures is shown in Figure 5.1(a). The two fractures have an inclination angle of 60° with respect to the short axis of the sample, and are 12 mm long. The bridge length between the two parallel fractures is 16 mm. In addition, for water injection and production during the test, two wellbores with 2 mm diameter are drilled from the two sample ends to meet the upper fracture and the lower

fracture, respectively. The wellbore only touches with one surface of the pre-existing fracture and does not cross them. The wellbores are situated 2 mm from the central axis of the sample. To create the pre-existing fractures on shale samples, we use the similar procedure described in (Morgan 2015, AlDajani et al. 2017). As shown in Figure 5.1(b), 2 mm diamond twist drill bit attached on a drilling machine was first used to drill two holes (the inner tips in Figure 5.1(b)) on the central axis of the sample, the hole size could be a little larger than 2 mm due to the slight movement of the drill bit during drilling. After that, a scroll saw containing 120 grit diamond-coated wire blade with 1.14 mm diameter was used to cut the two embedded fractures. The pre-cut fractures have around 1.4 mm width and are not perfect straight due to the slight vibration of the cutting system during the cutting. It is observed that the pre-existing fractures have round tips, and the inner tip is larger than outer tip due to the size of drill bit is larger than the size of wire saw.

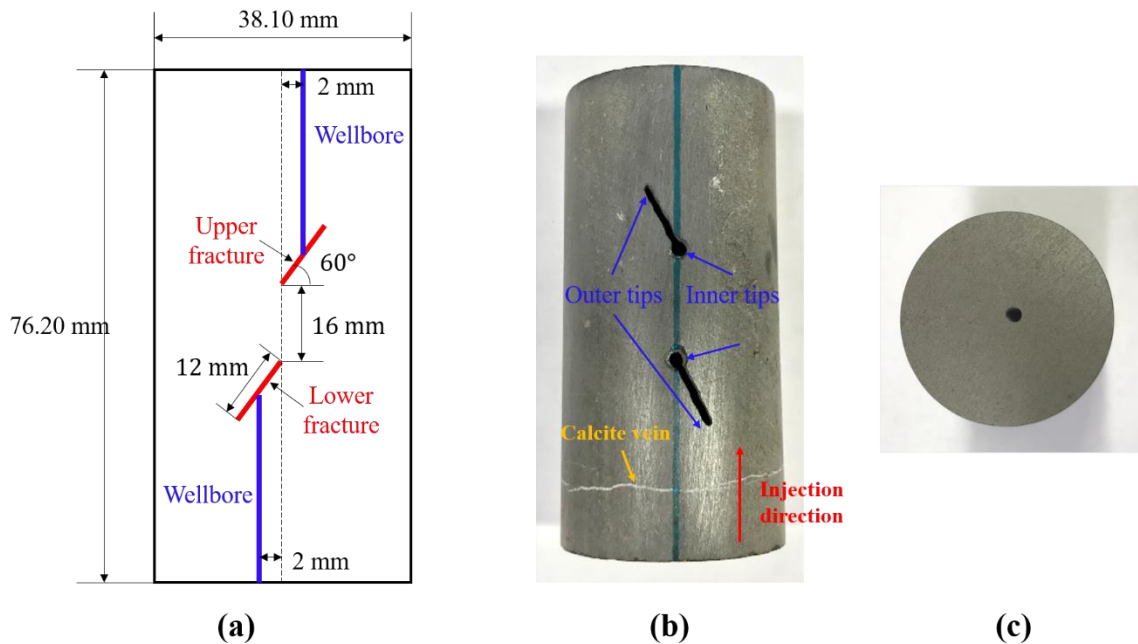


Figure 5.1: Sample preparation of the double-flawed Eagle Ford shale: (a) the sketch of sample geometry; (b) the Eagle Ford shale with two pre-existing fractures; (c) injection/production wellbore on one sample end.

At last, two wellbores were drilled using the same drill machine and diamond drill bit (see Figure 5.1(c)) for fluid injection and production. The red arrow on the sample picture in Figure 5.1(b) indicates the injection direction (salt water was injected from bottom to up). In addition, it is noticed that a white calcite vein perpendicularly crosses the sample with respect to the long axis of the sample. Before testing, the two sample ends were finely polished by a rock surface grinder with 200-grit gridding wheel based on ISRM standard (Kovari et al., 1983).

5.3.3 Experimental Setup and Procedure

The injection-induced fracture propagation test is carried out using an MTS 816 frame, which has a maximum 1000 kN axial load and includes a triaxial cell with 138 MPa (20,000 psi) confining pressure capacity. Control and data acquisition were performed using MTS Series 793TM Control software. The setup of the test with pre-existing fractures is sketched in Figure 5.2. During the injection tests, the average axial displacement of the rock sample is measured by two Linear Variable Differential Transformer (LVDT) position sensors. Another LVDT attached on a radial ring is used to record transverse displacement. Two Teledyne ISCO 100DM syringe pumps (68.95 MPa pressure limit, 25 ml/min flowrate limit and 103 mL volume capacity) are used to inject/produce water and measure the related flow parameters (pressure, flow rate and pump volume). As shown in Figure 5.2, salt water (7% KCL) is injected into the lower fracture from the bottom wellbore by pump A to initiate and propagate new cracks. Once the lower fracture coalesces with the upper fracture through the crack propagation, salt water is produced from the top wellbore to pump B due to the pressure difference of the two pumps.

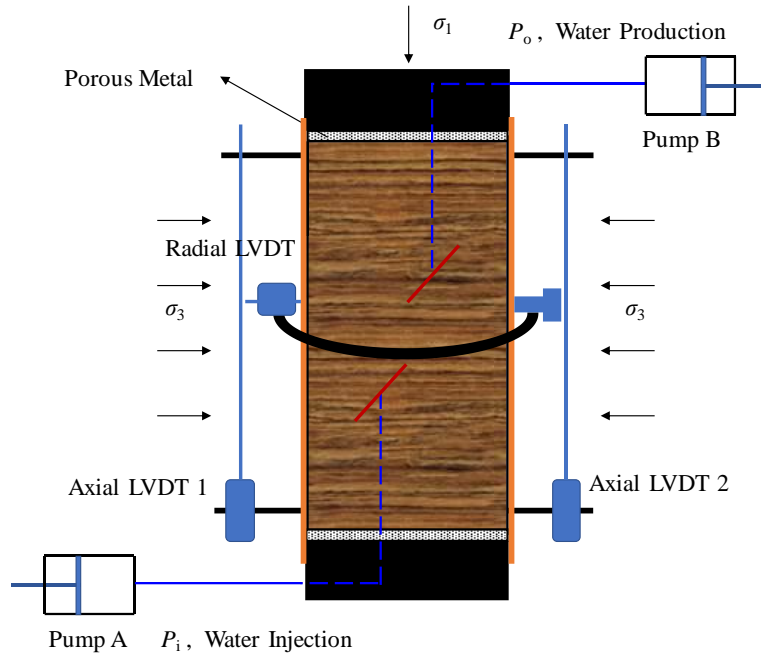


Figure 5.2: Experimental setup of the injection-induced fracture propagation test on Eagle Ford sample.

The experimental procedure is quite similar as the injection test conducted on granite samples having pre-existing fracture(s) in Chapter 4. As shown in the Figure 5.2, in the triaxial-injection test of the Eagle Ford shale sample, we initially applied a 20 MPa confining pressure on the sample. The production pressure of pump B was set to a constant value of 5 MPa, while the injection pressure of pump A was set to an initial value of 5 MPa and later was raised to induce fracture propagation and coalescence. Then, the sample was loaded to a reference differential stress level (80MPa) and system control was switched to a constant displacement control mode (see Chapter 2). Next, the injection pressure was continually raised to 19 MPa with a constant rate of 0.15 MPa/s to induce fracture propagation and coalescence. The mechanical properties and fluid-flow parameters were concurrently recorded during the entire test. To investigating the hydro-mechanical process under different operation conditions, an injection scenario was designed including a pressure buildup stage

which required ~140 seconds, a constant pressure hold stage which lasted another ~200 seconds, and a pump shut-in stage with a duration of ~160 seconds.

5.4 Experimental Results

5.4.1 Hydro-Mechanical Coupled Measurements

The measurements of hydro-mechanical properties during injection of the Eagle Ford shale are shown in Figure 5.3, the deformation properties and fluid flow parameters during confining pressure increase and axial loading on the sample in the pre-injection stage are not shown in this graph. This means that the displacements and flow rates are zeros before injection (see Chapter 4). In Figure 5.3, the green curve represents the loading piston displacement of the MTS 816 frame, which was kept as constant under a constant displacement control mode during the injection process; the differential stress is plotted using the black curve, which significantly drops with fracture propagation (because the compression exerted on the sample decreases with gradual propagation of the fracture); the blue curve shows the injection pressure and consists of a pressure buildup stage where the injection pressure is continuously increased at constant rate, a pressure hold stage where the pressure is kept as constant, and a pump shut-in stage; the brown curve represents the production pump pressure, which was initially kept constant and later increased during the pump shut-in stage; the purple and teal curves are separately show the injection flow rate and production flow rate; the axial displacement and radial displacement are illustrated by the red and pink curves, respectively.

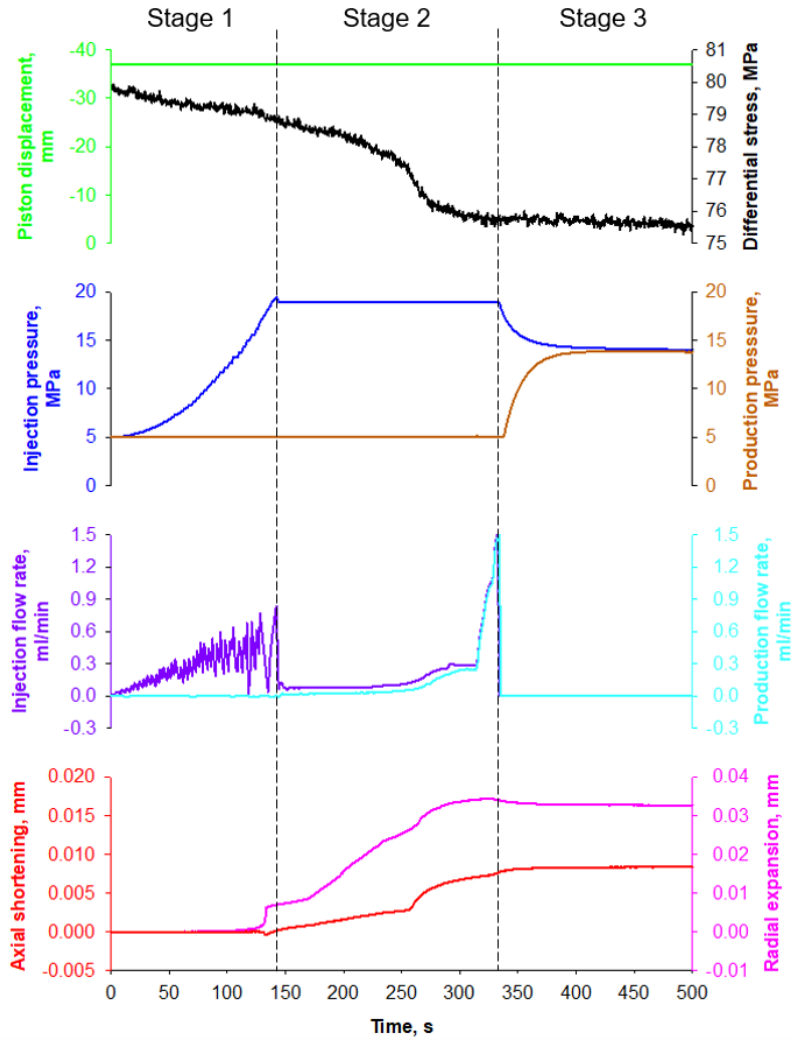


Figure 5.3: Hydro-mechanical measurements of the double-flawed Eagle Ford shale during injection-induced fracture propagation test.

As illustrated in Figure 5.3, the hydro-mechanical measurements can be separated into three stages, according to the changes of the injection pressure (blue curve): pressure buildup stage, constant pressure stage, and pump shut-in stage.

In the first stage (pressure buildup stage), the injection pressure was gradually increased from 5 MPa to 19 MPa with a constant rate (0.15 MPa/s) and the production pressure was kept constant at 5 MPa. Because we control the injection pressure in the test, the injection flow rate (purple curve) fluctuates during the pressure buildup stage. During most of the 1st stage of the test (0 to ~130 seconds in Figure 5.3), a slight decrease of

differential stress is noticed along with a small increase of the radial expansion and axial shortening. This deformation record indicates significant macro-cracking had not started during this early segment of the injection pressure buildup stage. However, a few micro-cracks may have developed around the tips of the pre-existing fractures. The small sample deformation can be contributed mainly to the expansion of the pre-existing fracture caused by the increased water pressure.

Near the end of the 1st stage and the early part of the 2nd stage (~130 to ~240 seconds in Figure 5.3), both displacements (axial shortening and radial expansion) and differential stress display significant changes, which correspond to the propagation of new cracks from the pre-existing fractures. However, the lower fracture and the upper fracture did not coalesce with each other, since the production flow rate of pump B was still zero. The latter part of the 2nd stage (240 to 340 seconds in Figure 5.3) reflects the fracture coalescence where the flow rate of the pump B (brown curve in Figure 5.3) shows a continuous increase, and much larger deformations and stress drops are observed. In this zone, the two pre-existing fractures have coalesced through the newly propagated cracks allowing the injected water to flow from the lower fracture to the upper fracture. At the end of this zone, the flow rate of pump B is near identical to that of pump A, indicating that all water injected by pump A was produced by pump B. This observation is similar with which is reported in the triaxial-injection test of the granite sample having two pre-existing fractures (SW-2 in Chapter 4).

In the last stage (340 to 500 seconds in Figure 5.3), the two pumps (injection pump A and production pump B) were both shut-in. This means that no fluid flew in and out of the sample from the pumps. The pressure in the upper fracture gradually increased along as the pressure in the lower fracture decreased, both finally merging to the same value. This is also

an evidence that an interconnected fracture work has been created in the injection test. In this shut-in stage, any fracture propagation tends to cease as the pressure potential between the two pumps is zero.

5.4.2 Crack Characteristics

To characterize crack characteristics after testing, the side wall of the cylindrical Eagle Ford shale was polished using a fine-mesh grinder to achieve two flat surfaces (see Figure 5.4). The side views and the views of sample ends are shown in Figure 5.4. During the injection test, salt water was injected from the bottom to propagate new cracks from the lower fracture, and water was produced once the two pre-existing fractures were hydraulically communicated. As shown in Figure 5.4(a) and Figure 5.4(b), It is observed a pair of wing cracks separately emanating from the two tips of the lower fracture. The wing crack initiated from the inner tip of the lower fracture was to propagate upwardly and bridged with the inner tip of the upper fracture, and then an interconnected fracture network was generated to produce water on the top of the sample. On the other hand, the wing crack emanated from the outer tip of the lower fracture was to propagate downwardly and touch with the bottom sample end. The lower wing crack axially cut the wellbore of injection hole on the bottom end of the sample (Figure 5.4(d)). In addition, it is noticed that no cracks were propagated from the outer tip of the upper fracture on side views (Figure 5.4(a) and Figure 5.4(b)) and the view of top sample end (Figure 5.4(c)). In addition, the crack characteristics in front side (Figure 5.4(a)) and which of in back side (Figure 5.4(b)) are similar but not identical, which could be related to the heterogeneous of rock or stress field.

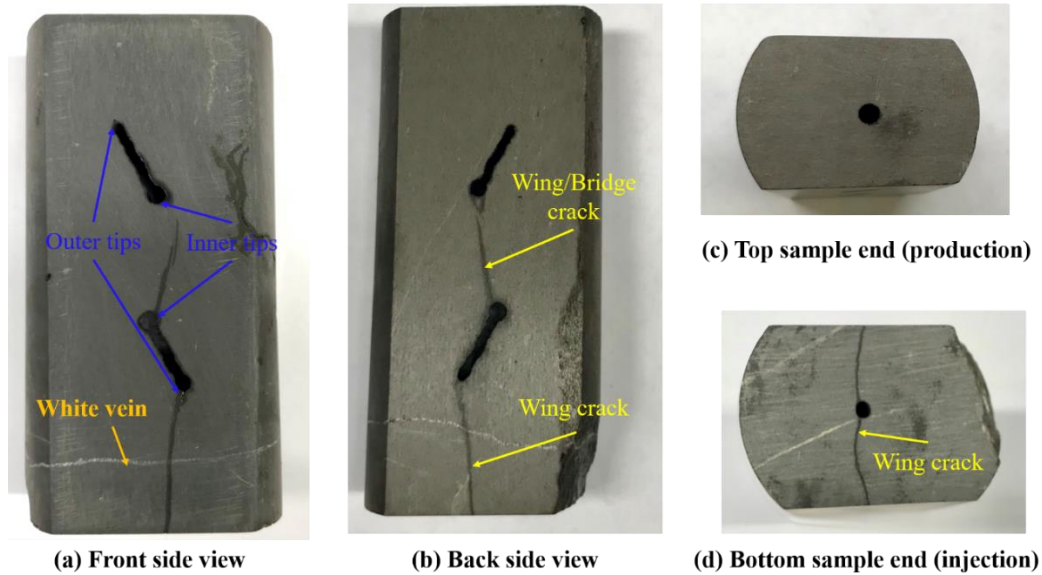
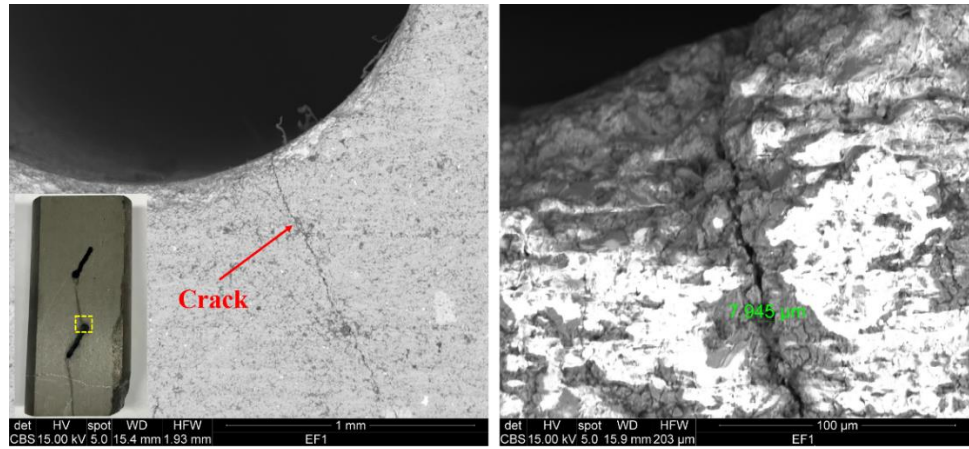


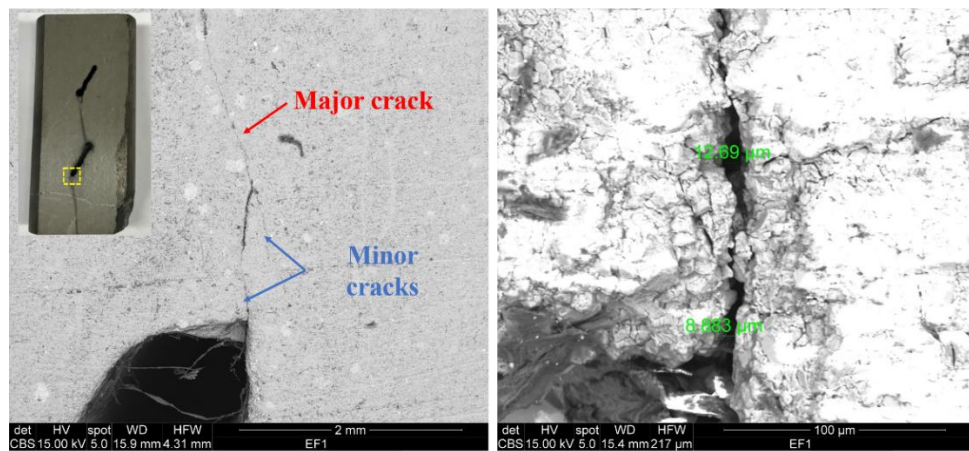
Figure 5.4: The propagation and coalescence of pre-existing fractures on Eagle Ford shale: (a) front view; (b) back view; (c) the view of the sample end (production); (d) the view of the sample end (injection).

The crack characteristics at the fracture tips, the bridge area, and the interaction of the wing cracks with the calcite vein are also demonstrated using Scanning Electron Microscope (SEM) images (Figure 5.5 - Figure 5.7). In each SEM image, the yellow square on sample picture marks the location of the SEM scanning area, and the SEM image is axially reversed with respect to the sample picture. Two scales of observation on fracture tips are shown in Figure 5.5 and Figure 5.6; the left picture has a scanning scale of 1-mm, while the right picture has a scanning scale of 100- μ m. Whereas the two images in Figure 5.7 are all with the scanning scale of 1mm.

In Figure 5.5(a), a single crack has emanated from the inner tip of the lower flaw and has a width of $\sim 8 \mu\text{m}$. Considering the curvilinear path (wing shape) and the initiation area (high tensile stress zone), the crack is a tensile wing crack. Whereas, two minor cracks appear to have initiated from the outer tip of the lower fracture (see Figure 5.5(b)) and later joined to form a single well-defined wing crack with a width of ~ 8 to $\sim 13 \mu\text{m}$. Considering



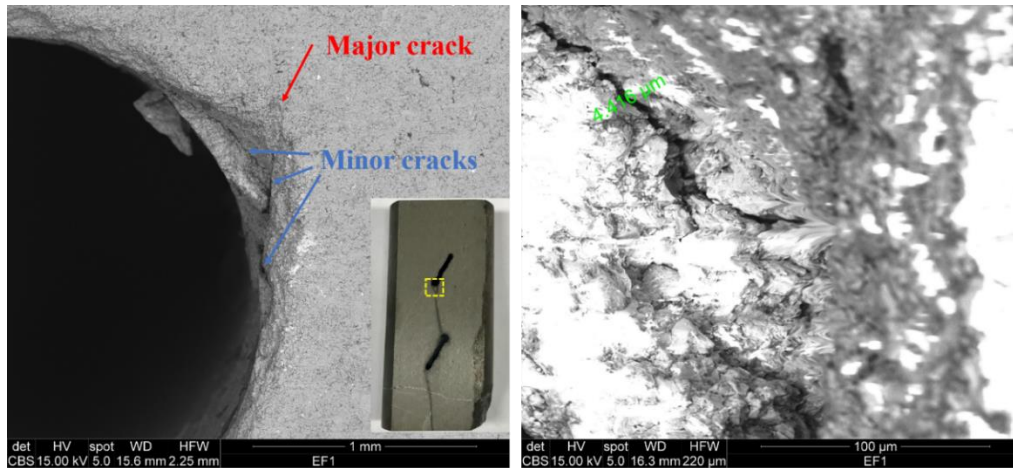
(a)



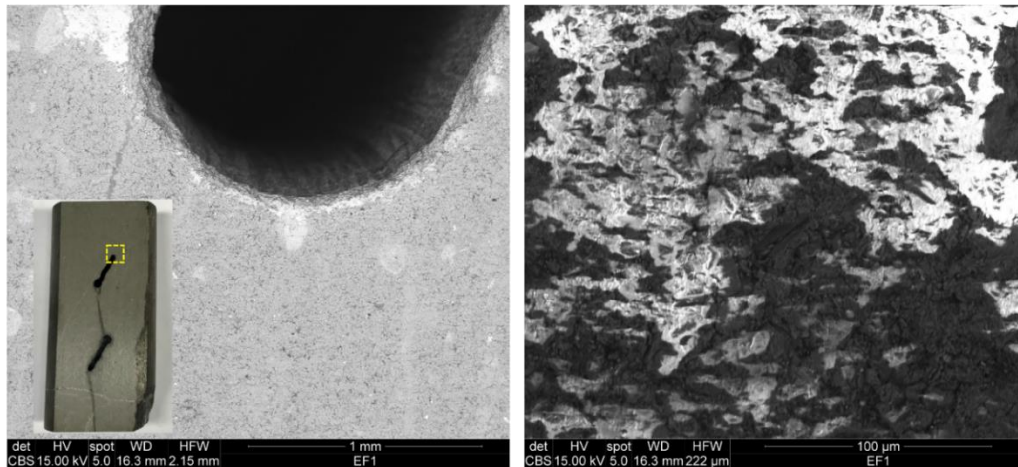
(b)

Figure 5.5: SEM images of the cracks propagated from the lower fracture: (a) the inner tip of the lower fracture; (b) the outer tip of the lower fracture. The left picture in each figure is with 1-mm scale, while the right picture is with 100- μm scale.

The SEM images of the upper fracture are shown in Figure 5.6. A major crack and multiple minor cracks are found at the inner tip of the upper flaw (Figure 5.6(a)). The larger crack has a width of $\sim 4 \mu\text{m}$ which is smaller than the width of the cracks that emanated from the lower fracture. This is likely because water was injected from lower fracture to upper fracture. No cracks formed from the outer tip of the upper fracture even at micron scale of observation (Figure 5.6b).



(a)



(b)

Figure 5.6: SEM images of the cracks propagated from the upper fracture: (a) the inner tip of the upper fracture; (b) the outer tip of the upper fracture. The left picture in each figure is with 1-mm scale, while the right picture is with 100- μ m scale.

The SEM images of the cracking behavior of the bridge area and the area containing a white vein are shown in Figure 5.7. A single bridge crack (tensile mode, Figure 5.7(a)) can be seen to connect the two pre-existing flaws and further to form an interconnected fracture network. Due to the existence of high tensile stress concentration in the ligament area, the bridge crack is likely a tensile-mode. This is similar to the tensile bridge crack described in Chapter 4. In Figure 5.7(b), it is clear that the propagated crack crossed the calcite vein (based on mineralogical analysis during SEM scanning). The width of the vein is around $\sim 266 \mu\text{m}$,

while the width of newly propagated crack near the vein is $\sim 89 \mu\text{m}$ (wider than the cracks propagated in the rock matrix). This could be related to the larger grain size in vein area.

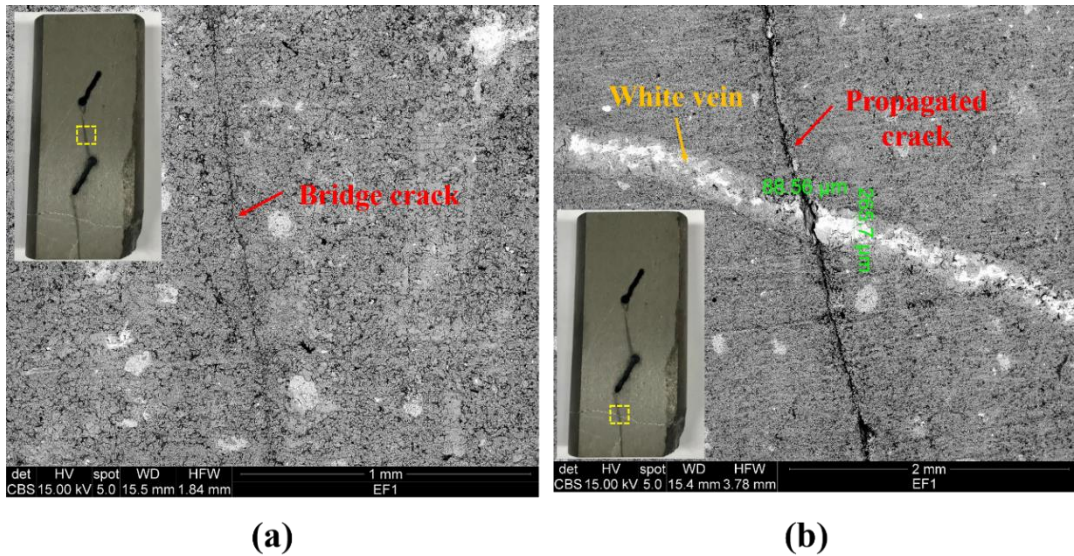


Figure 5.7: SEM images in (a) the ligament area and (b) the interaction area of the newly propagated crack and the calcite vein.

Unlike the injection-induced fracture propagation test presented in Chapter 4, the secondary cracks were not induced on the test of the double-flawed Eagle Ford shale sample (Figure 5.3). Some previous works have reported that the crack propagation on glass, CR39 (Columbia resin), and PMMA (polymethylmethacrylate) in compression are mainly through wing cracks (Bobet, 2000; Hoek & Bieniawski, 1964; Horii & Nemat-Nasser, 1986). Therefore, the reason that secondary cracks were not generated on the pre-flawed Eagle Ford shale sample could be related to its fine grain size, since macroscopic shear cracks are caused by the interactive growth of tensile cracks at suitable set of micro-flaws (e.g., grain boundaries, Horii & Nemat-Nasser, 1986).

5.4.3 Permeability Enhancement

In Figure 5.3, the production flow rate in pump B was always zero before the hydraulically interaction of the two pre-existing fractures, while the production increased

significantly once the fracture network formed by the coalescence of the newly propagated cracks and the pre-existing ones. At the end of the stage 2, the bridge crack dominated the fluid flow, and the production flow rate (0.27 ml/min) is almost equal to the injection flow rate (0.29 ml/min). Here, the flow rates are the average and steady-state values, estimated separately as the slopes of temporal evolution of injection pump (pump A in Figure 5.2) volume and production pump (pump B in Figure 5.2) volume (the estimation method can be referred from Chapter 2).

Using the Darcy's Law, the equivalent permeability of the Eagle Ford sample SW-2 can be calculated by using Darcy's law:

$$k_e = -\frac{\mu Q}{A} \cdot \frac{L}{\Delta P} = -\frac{4\mu Q}{\pi D^2} \cdot \frac{L}{\Delta P} \quad (5-1)$$

where, Q is the flow rate in steady-state regime ($Q = 0.28$ ml/min), estimated by averaging the injection flow rate ($Q_i = 0.29$ ml/min) and production flow rate ($Q_o = 0.27$ ml/min); ΔP (differential pressure, $\Delta P = 14$ MPa) is the difference between injection pressure ($P_i = 19$ MPa) and production pressure ($P_o = 5$ MPa); μ is the fluid viscosity (1.002×10^{-3} Pa·s at 20 °C for water); A is the cross-section area of the sample ($A = \frac{1}{4}\pi D^2$); D and L are the sample diameter ($D = 38.10$ mm) and sample length ($L = 76.20$ mm), respectively.

The equivalent permeability of the shale sample after injection is 2.23×10^{-17} m². This means the shale permeability increased more than 100 times, comparing with the ultra-low matrix permeability of 1.98×10^{-19} m². This means that the propagation and coalescence of pre-existing fractures by injection can be an important contributor for permeability creation in shale reservoir stimulation.

5.5 Chapter Summary

In this research, we performed laboratory-scale injection tests on a double-flawed shale sample (Eagle Ford shale). In the test, the pre-existing fractures successfully propagated and coalesced to generate a fracture network during water injection at injection pressure below the confining pressure, resulting in a significant permeability increase and eventually all water injected was extracted from the production well. In addition, corresponding changes in deformation properties (axial and radial displacements, stress) and fluid flow parameters (flow rate, pressure, pump volume) have been definitely observed during the injection-induced fracture propagation and coalescence. A pair of tensile wing cracks emanated from the tips of pre-existing fracture(s) is detected on the tested sample. Scanning Electron Microscope (SEM) images are used to analyze the cracking characteristics in micro-scale. Moreover, the cracking behavior correlates well with the measurements of deformation properties and flow parameters, explaining the development of fracture propagation and coalescence. Generally, several steps during the propagation and coalescence of fractures emanating from the pre-existing fractures in response to water injection: micro-cracks nucleation, onset of fractures propagation, stable propagation of fractures, and fractures coalescences. These observations resulting from this work, combined with our previous injection-induced shear slip tests on shales, clearly indicate that both dilatant shear slip and fracture propagation are two fundamental and integral mechanisms for permeability enhancement contributed by pre-existing fractures during injection, and also prove that shear stimulation is a potential and effective stimulation method for unconventional shale reservoirs.

Chapter 6

Injection-induced Fracture slip and Microseismicity in Granite

Microseismic events caused by fluid injection are frequently observed during reservoir development and disposal well operations. Characterization and understanding of the induced micro-seismicity can be an important tool in seismicity risk assessment and reservoir performance forecasting. Several issues pertaining to the evolution of fracture response to injection and the evolution of micro-seismicity remain poorly understood and are the subject of continued scientific discourse. In particular, the occurrence of aseismic and seismic slip and their relation to the fault constitutive behavior (slip weakening vs slip strengthening) and the role of pore pressure and fracture surface heterogeneity have been the subject of several field and modeling investigations. However, although highly valuable, field investigations are costly and provide significant challenges to monitoring and measurement of parameters of interest. Successful measurement can still be subject to large uncertainty and multiple plausible hypotheses. Laboratory-scale experiments are an alternative setting for closer examination of the phenomena of interest in a controlled environment. In this work, I present data and analysis from laboratory injection tests into a rough fracture and examine the relationships between fracture slip, microseismicity and its spatio-temporal evolution, and permeability dynamics. The triaxial-injection experiment was conducted under a realistic stress boundary condition on a granite sample having a single rough fracture. The measurements of fracture deformation, fluid flow and acoustic emissions

(AE) were concurrently recorded to probe the slip-seismicity-permeability evolution in granite fracture during shear slip by pressurized fluid injection.

6.1 Abstract

It is well-known that faults/fractures slip caused by fluid injection can induce seismicity. However, some fundamental questions regarding the spatial and temporal distributions of seismicity resulting from fault/fracture pressurization have remained. Specifically, the nature of the relation between aseismic and seismic slip and the role of fault heterogeneity, and fluid pressure on micro-seismicity need more direct examination. In this work, we present fully coupled seismo-hydro-mechanical results from a laboratory injection-induced shear test on a rough granite fracture with concurrent acoustic emission monitoring. The stressed fracture is subjected to pressure increase by injection via a borehole. The test reveals a transitional fracture shear deformation response namely, aseismic (or creeping) slip to seismic slip to aseismic slip during fluid injection. In the two creeping or aseismic intervals, the fracture sheared at a low rate of $\sim 10^{-8}$ m/s, and very few or no acoustic emission events were triggered concomitant with small decline of the shear stress and slight enhancement of flow rate into the fracture. A significant number of acoustic emission events were detected in the second slip interval containing a quasi-static slip stage with a $\sim 10^{-7}$ m/s slip rate, and a dynamic slip stage with $\sim 10^{-4}$ m/s slip rate. The shear failure of the fracture occurred in the dynamic slip stage, and was accompanied by a large stress drop and a dramatic fluid flow rate increase. The observed aseismic slip along with minimal dilatancy is consistent with previous findings from field experiments and supports the notion that slip strengthening is causal to aseismic slip. However, our results further show the transition from aseismic/creeping slip to seismic slip and strength weakening, and finally a return to

the creeping slip state. The spatio-temporal evolution of acoustic emission hypocenters demonstrates the existence of slip heterogeneity on the fracture plane and supports the notion that the accumulation of local asperity failure ultimately results in the global failure of entire fracture. Comparing AE distribution with the fracture surface topography shows that the integrated effect of fault/fracture surface roughness, and pressurized fluid injection on promoting slip heterogeneity during fault/fracture reactivation by injection.

6.2 Introduction

Significant high-grade geothermal reservoirs are deficient in water and permeability, so called *hot-dry* rocks. Hydraulic stimulation treatments are required to achieve economical flow rates from these low permeability geothermal reservoirs, which has led to the concept of Enhanced or Engineered Geothermal Systems (EGS). In an EGS project, an injection well is first drilled into the geothermal reservoir (typical the host rocks are crystalline rocks) containing open and sealed pre-existing fractures. Next, water is injected at sufficient pressure to create a highly conductivity fracture network by reactivating pre-existing fractures and inducing man-made fractures. Two or more production wells are further drilled into the stimulated fracture network to form flow paths for water circulation. As a result, the production of geothermal energy can be achieved by injecting cold water into the stimulated EGS reservoir through the injection well and producing hot water/steam from the production wells. Due to proppant uses in the development of geothermal reservoirs are rare, the shear stimulation has been considered as the main approach of permeability creation by reactivating pre-existing fractures to slip and self-propping by injection in EGS (e.g., Baria et al., 1999; Cheng, Wang & Ghassemi, 2019; Pine & Batchelor, 1984; Willis-Richards et al., 1996). One of issues accompanying with the development of geothermal reservoirs is microseismic or

seismic events caused by pressurized fluid injection. To date, although none of these events have resulted in loss of life or significant properties damage, but several EGS projects have been delayed or cancelled in worldwide, such as Basel EGS at Switzerland (Deichmann & Giardini, 2009; Ellsworth, 2013) and Pohang EGS at South Korea (Kim et al., 2018), etc. On the other hand, the induced microseismicity during hydraulic stimulation can be used to characterize fracture properties and fluid migration (e.g., Rutledge et al., 2004; Maxwell, et al., 2010).

The microseismic events accompanying with reservoir stimulation can be caused by the creation of new fractures or the reactivation of pre-existing fractures. However, it is found that the typical microseismic events induced by the creation of new fractures (tensile-mode) are with low moment magnitudes (less than 0) and hard to be detected. While the shear slip of pre-existing fractures is usually the dominant source mechanism of induced seismicity during hydraulic fracturing (e.g., Clarke et al., 2014; Maxwell et al., 2010). In addition, some field observations have shown that a large stimulated reservoir volume (mapped from the microseismic motoring) results in a better production performance (Fisher et al., 2004; Mayerhofer et al., 2010). The possible interpretation is that microseismic events are mostly caused by the shear slip of pre-existing fractures, and fracture slip can break the seals of the pre-existing fractures and cause fracture dilation/opening to enhance production performance. However, the relationships of fracture shear slip, induced microseismicity, and permeability are still poorly understood.

In addition, the heterogeneity of fault/facture slip and seismicity distribution in the episodes of fault reactivation and earthquake rupture has been widely discussed through field observations, geophysical inverse studies, and numerical models. These previous works

have suggested that slip heterogeneity may be related to the heterogeneity of fault/fracture surface roughness (e.g., Resor & Meer, 2009; Tinti et al., 2016; Zielke et al., 2017). However, geophysical inverse studies and numerical models are usually with large uncertainties, while the direct observations on fault zone geometry are from exhumed fault zones but not from the seismic faults at depth. To date, there are a few reliable studies directly link fracture surface roughness and slip heterogeneity. Moreover, the possible effect of pressurized fluid injection on slip heterogeneity have not been explored. We hypothesize that the heterogeneous fluid flow of pressurized fluid in a rough fault/fracture locally changes the effective normal stress of contacted asperities, promoting the further slip heterogeneity.

In the laboratory, some experiments induced the shear slip of pre-existing fracture by fluid injection but without concurrent acoustic emission (AE) monitoring (e.g. French et al., 2016; Nemoto et al., 2008; Rutter & Hackson, 2017; Scuderi et al., 2017; Ye & Ghassemi, 2018). On the other hand, some experiments studied the signature of acoustic emissions during fracture shearing, however, the fracture slip was not produced by pressurized fluid injection but through elevating the differential stress (e.g. Goebel et al., 2013; Grzegorz et al., 2014; McLaskey & Lockner, 2016; Thompson et al., 2009; Zhao et al., 2018). The observations in these laboratory studies have improved our understandings on fracture slip mechanics (the former injection-induced shear tests) and the related microseismic signature during fracture shear slip (the latter shear test with acoustic emission). However, most of these previous laboratory studies have not incorporated the full seismo-hydro-mechanical coupling, and the injection-induced fracture shear experiments with concurrent AE monitoring are rare.

In this work, laboratory injection test was conducted on a granite sample (having a single rough fracture) under relevant triaxial stress. The measurements of fracture deformation (stress, fracture slip and dilation), fluid flow (flow rate and pressure) and acoustic emission (hits and events) were concurrently monitored to characterize the seismo-hydro-mechanical response of the granite fracture during pressurized fluid injection. The fracture surface roughness was described by a 3D laser scanner and linked with the slip characteristics and the microseismic signature. Through this work, we try to address several key questions related to the reactivation of pre-existing fractures and induced seismicity in EGS development: (1) the relationships of fracture slip, microseismicity, and permeability; (2) microseismic signature of granite fracture during the shear failure of pre-existing fractures by injection; (3) the slip heterogeneity promoted by fracture surface roughness and pressurized fluid injection.

6.3 Experimental Methods

6.3.1 Sample Preparation and Characterization

The rock material used in this study is Sierra White granite. Several relevant mechanical properties of the granite measured through regular laboratory experiments are: Young's modulus ($E=67$ GPa), Poisson's ratio ($\nu=0.32$), uniaxial compressive strength ($UCS=150$ MPa), and tensile strength ($T=11$ MPa). The P-wave velocity of the granite is relatively isotropic in different directions with an average value as 3700 m/s. This Sierra White granite has an ultralow matrix permeability in the range of $5 \times 10^{-19} \text{ m}^2$ to $1 \times 10^{-18} \text{ m}^2$.

A cuboidal granite brick (with dimensions of 75mm×75mm×150mm) was used to create a cylindrical sample containing a single rough fracture. Firstly, an inclined groove (5 mm in width and 5 mm in depth) was cut at a 35-degree angle with respect to the long axis

of the cuboidal granite brick. After that, a V-shaped steel blade fitted in MTS 810 Materials Testing System (manufactured by MTS Systems Corporation) was used to induce a tensile fracture by splitting the grooved granite brick (based on a Brazilian test technique). Subsequently, a diamond coring system was used to obtain a pre-fractured cylindrical sample from the granite brick (Ye & Ghassemi, 2018). The two end surfaces of the cylindrical granite sample (hereinafter SW-1) were finely polished using a rock surface grinder with a 200-grit grinding wheel. The prepared granite sample (SW-1) is with a diameter of 50 mm and a length of 106 mm, having a single rough fracture with a $\sim 36^\circ$ angle with respect to the long sample axis (see Figure 6.1(a)). To enable fluid injection into the fracture, one ~ 3.5 mm diameter borehole was drilled along central axis of the sample from the bottom end to reach the fracture (Figure 6.1(b)).

A three-dimensional (3D) laser scanning system was used to measure fracture surfaces' topography. The surface scanning contour is shown in Figure 6.1(c). The color scale in the contour describes the values of surface relief (or asperity height) with respect to the lowest point of the fracture surface (indicated by black color). The dark blue to light red zones represent surface reliefs ranging from low to high values (with reference to the lowest point). The two fracture surfaces have a perfect fracture matching, and a convex on one fracture surface corresponds to a concave on the other. Hence, we only show one fracture surface of the sample SW-1. As shown in the scanning contour, the maximum surface relief between the highest point (peak) and lowest point (valley) of the fracture surfaces is 6.08 mm. The average Joint Roughness Coefficient (JRC, Barton, 1973) values of the fracture surface is 14.38 (Ye & Ghassemi, 2018).

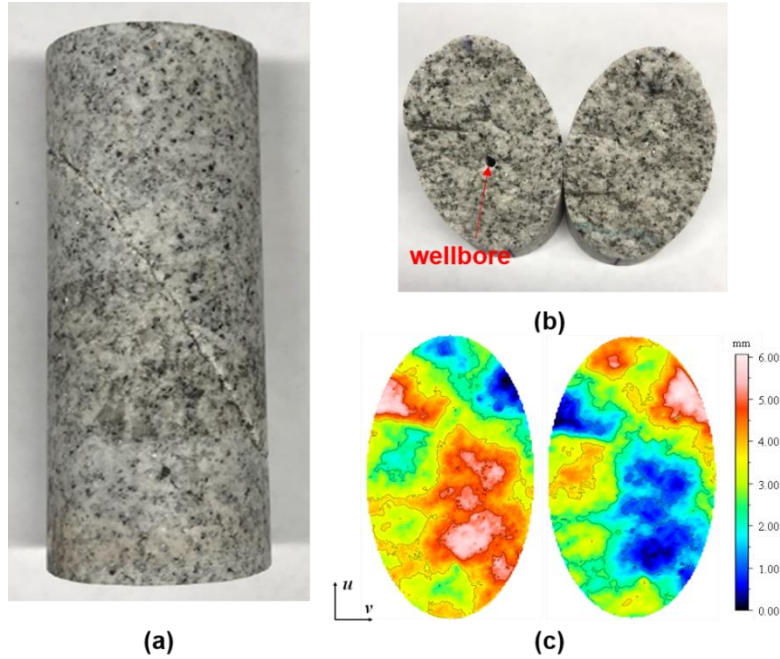


Figure 6.1: Sample preparation: (a) cylindrical Sierra White granite (SW-A1) having a single rough fracture; (b) fracture surfaces, and one borehole was drilled on one part of the sample for water injection; (c) 3D surface scanning contour, the u (the long axis of the contour), v (the short axis of the contour) and w coordinates (the color scale of the contour) are the length, width and asperity height of fracture surface, respectively.

6.3.2 Experimental Setup

The injection-induced fracture slip test with concurrent acoustic emission (hereinafter AE) was conducted at room temperature (25 °C) using MTS 816 Rock Mechanics Test System (manufactured by MTS Systems Corporation). The apparatus used for triaxial test ($\sigma_1 > \sigma_2 = \sigma_3$) has a maximum axial load capacity of 1000 kN and includes a triaxial pressure vessel with a limit of 140 MPa confining pressure. The silicone oil was employed as confining medium, and the confining pressure was provided and measured by an MTS 286.20 confining fluid intensifier, with a pressure measurement resolution of 0.02 MPa. The axial stress (σ_1) was servo-controlled by the axial loading actuator of MTS 816 system, and the applied axial force was measured by a load-cell located inside of the triaxial pressure vessel with maximum 1 kN loading error. In the test, as shown in Figure 6.2(a), the average axial displacement of the rock sample was measured by two Linear Variable

Differential Transformer (LVDT) position sensors mounted on the sample. Another LVDT sensor attached on a radial ring was used to record the transverse displacement of the sample. The associated error of the LVDT sensor is $\pm 0.05\%$. The mechanical parameters (stress and displacement) of the sample was acquired by MTS Series 793 software.

A Teledyne ISCO 100DM syringe pump connected with the fracture (through the pre-drilled borehole) was used to inject pressurized fluid (deionized water) to induce fracture shear slip. The corresponding fluid flow parameters (pressure, flow rate and pump volume) were concurrently measured during the injection test by a LabVIEW based software provided by Teledyne ISCO. The ISCO D-series pump has a $\pm 0.5\%$ pressure error and a $\pm 0.3\%$ flow rate error.

The granite sample was jacketed by a copper sheet with thickness of 1.27 mm, and then was subjected to a triaxial compression with 30 MPa confining pressure and 10 MPa differential stress in the pressure vessel of MTS 816 frame. The purpose to this step is to close the fracture and set the copper jacket tightly against the sample (to make a good coupling between the sample and the attached AE sensors). Afterwards, 8 piezoelectric transducers of diameter 5 mm and 1 MHz resonant frequency were bonded to the copper jacket with conductive epoxy in the arrangement shown in Figure 6.2(b). The AE instrument used for data acquisition in this study is Express-8 AE system (supplied by MISTRAS Group Inc.) with a 16-bit A/D converter on each channel. In the test, the radiated wave signals received by the piezoelectric transducers were amplified by 40 dB using PAC 2/4/6 preamplifiers (Physical Acoustics Corporation) and passed through an analog filter. After the filter, each of the signals (voltages) was then measured if above a threshold level of 45 dB with a 10 MSPS sampling rate. The main AE data obtained in this work includes: (1) AE

events and event rates; (2) relative AE event magnitudes estimated from the maximum amplitude data; (3) b-values calculated from the magnitude-frequency relationship; (4) AE hypocenters determined from AE first arrivals using a Powell's method with an isotropic velocity structure (the estimated accuracy of AE location is ± 2 mm); (5) AE source types (in tensile, shear and collapse) obtained from the polarity analysis of AE first arrivals.

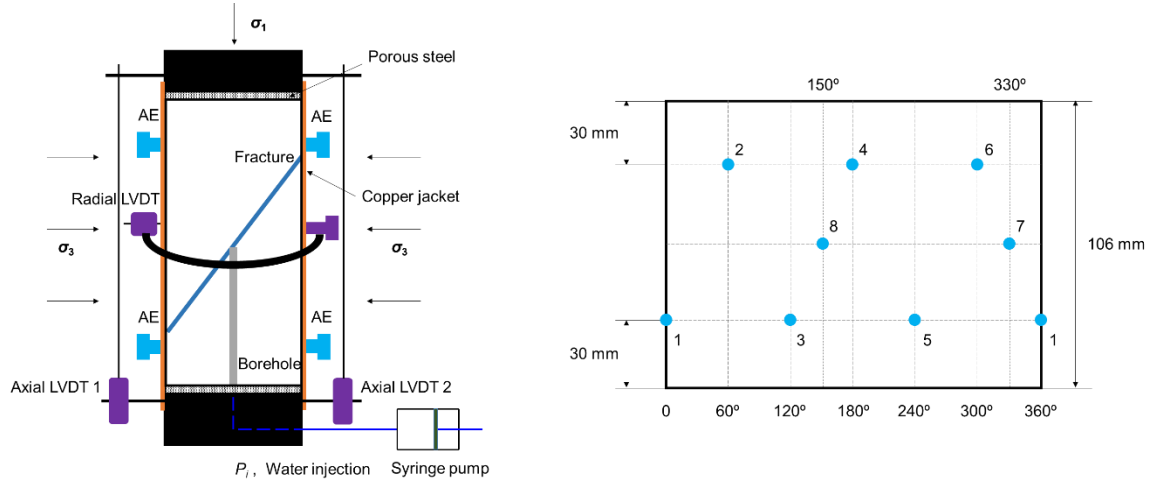


Figure 6.2: Experimental setup: (a) sketch of sample configuration; (b) projected sample surface showing the location of 8 piezoelectric crystal transducers for AE monitoring (the blue circles indicate the transducers). The red line in the left plot represents the fracture. AE=Acoustic Emission, LVDT= Linear Variable Differential Transformer.

6.3.3 Pencil Lead Break Test

In order to ensure the good performance and sensitivity of AE sensors, a Pencil Lead Break (PLB, ASTM standard, 2015) test were conducted on the sample after it was installed in the pressure vessel of MTS 816 (before closing the lid of the pressure vessel). Also, the PLB test also can provide important information of the signal waveforms to determine related parameters for acoustic emission. Here, based on the ASTM standard E976 (2015), a PLB test was conducted on sample SW-A1 and the waveforms of all 8 crystal sensors were recorded (Figure 6.3). The waveforms in Figure 6.3 clearly indicate that all 8 sensors had good performance and were sensitive to the energy source released from the sample. Since the PLB signal was triggered close to sensor 7 (see Figure 6.2(b)), waveforms received by

sensors 1 and 7 have relatively higher AE amplitude than the others. On the other hand, sensor 8 has relatively lower AE amplitude, because it is farther from sensor 7 and separated from sensor 7 by the fracture. In addition, the sign of the first motion amplitudes of most sensors are positive, which is likely related to more compressive waves produced by the PLB test. Through the PLB test, several AE timing parameters, such as PDT (Peak Definition Time), HDT (Hit Definition Time) and HLT (Hit Lockout Time), were determined for later acoustic emission monitoring during injection.

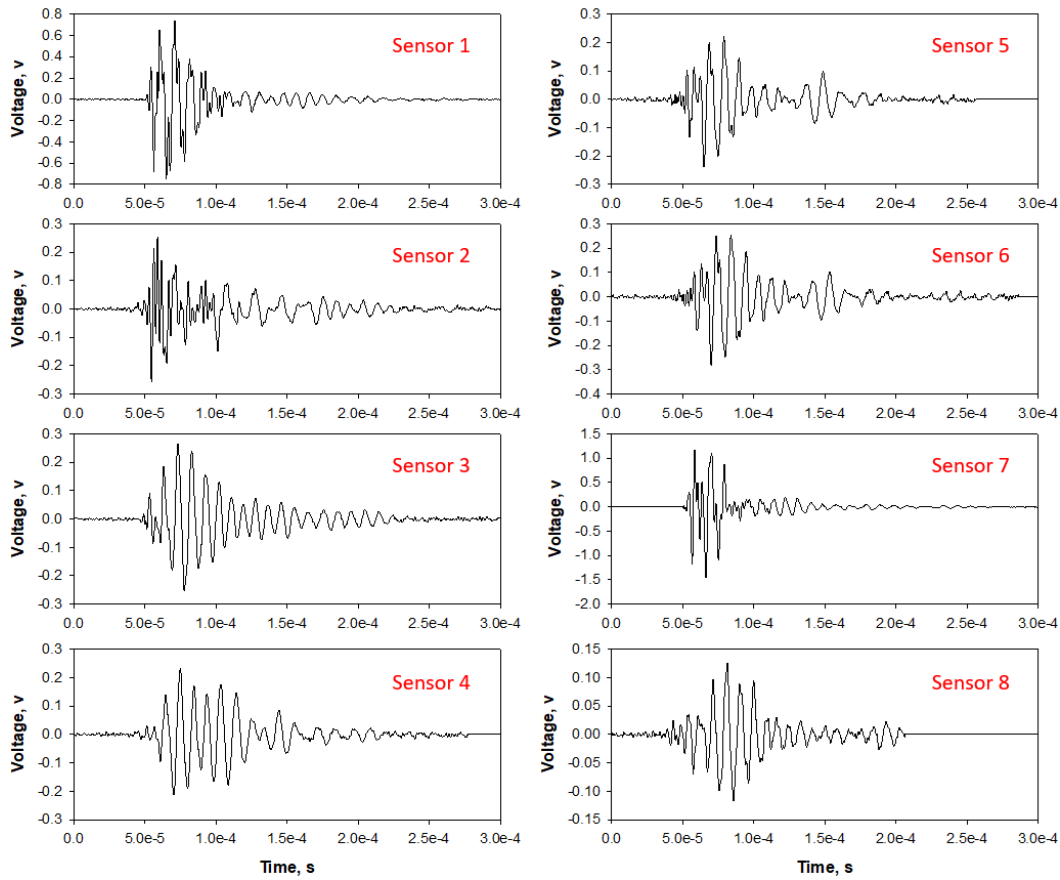


Figure 6.3: Waveforms of the 8 crystal sensors in a PLB test on the granite sample SW-A1. PLB=Pencil Lead Break.

6.3.4 Experimental Procedure

The prepared sample was installed into the pressure vessel of MTS 816 system. The displacement sensors, AE transducers and hydraulic line were then connected with the three

sub-systems (MTS 816 system, syringe pump system, and Express-8 AE system), respectively. Before running the experiment, the time settings in the three sub-systems were finely synchronized to ensure the simultaneous data acquisition of the seismo-hydro-mechanical measurements during test. The experimental procedure includes three major steps:

Step 1: Initial Condition Setting. As illustrated in Figure 6.2(a), during the test, a 30 MPa confining pressure (σ_3) was first applied on the fractured sample SW-1. The confining pressure was held constant during the entire test. After that, the injection pressure of pump (P_i) connected with the fracture was set to an initial value of 4 MPa by injection deionized water. The purpose of providing an initial fluid pressure is to completely saturate the fracture and to reduce transient flow effect during elevating injection pressure. To diminish the plastic deformation caused by the initial seating between fractures, porous metal discs and platens, five loading-unloading cycles of differential stress (to a relatively low differential stress level of 20 MPa) were performed on the sample assembly by loading the axial actuator piston with a displacement rate of 0.01 mm/s. The sample was then loaded using a same displacement rate to an initial differential stress level ($\sigma_d = \sigma_1 - \sigma_3$) as 145 MPa, which was a near critical stress state exerted on sample SW-1 roughly determined from the stress-strain curves. The near critical stress state is also evidenced by the detection of A few AE events at the later part of the axial loading.

Step 2: Boundary Condition Setting. After the axial loading terminated at the initial differential stress level, the test was switched to a constant piston-displacement control mode to keep the loading piston displacement constant. This means that the actuator piston was locked without further movement until the end of the test. However, the motion of the

fracture was without any restrictions. Hence, once the fracture slip was initiated, the differential stress/compression exerted on the sample by the piston dropped significantly in response to the sample shortening with the gradual shear slip of the pre-existing fracture. The assumption of this experimental control is that the deformation of the overburden (the piston) at a distance far from the fluid injection zone is negligible, while the stored elastic strain energy can release along with earthquake rupture during fault/fracture reactivation.

Step 3: Pressurized Fluid Injection. The stressed sample was permitted to relax for at least 20 minutes, ensuring that no new AE events were induced and the fluid flow was stabilized in the fracture (with almost zero flow rate reading on the pump) before elevating injection pressure. During the switch of control mode and the relaxation time, the differential stress decreased ~ 5 MPa. Next, the sample deformation (in both axial and radial directions), the AE monitoring, and the time were zeroed. The reason that we zeroed the sample deformation and the corresponding AE monitoring is to conveniently characterize the temporal evolution of the hydro-mechanical measurements and the corresponding AE activities during pressurized fluid injection, since the sample deformation in the initial loading stage (setting of the initial differential stress) are much larger than that in the injection stage. Subsequently, after the injection pressure was gradually increased at a rate of 0.1 MPa/s from 4 MPa to 28 MPa to induce fracture slip. During the entire test, the injection pressure was at least 2 MPa smaller than the 30 MPa confining pressure. This prevents the jacket from bursting by fluid pressure. Once the injection pressure reached the target of 28 MPa, the injection pressure was held constant for another couple minutes.

6.4 Experimental Results

The seismo-hydro-mechanical response of fractured granite sample SW-A1 during the injection test is shown in Figure 6.4. In the plots, the rock deformation and fluid flow in the pre-injection stages (initial applications of confining pressure, axial loading, and injection pressure) are not shown. This means that the displacements and flow rates were zeroed before elevating the injection pressure. Also, the corresponding acoustic emission activities in the pre-injection stage was not accounted into Figure 6.4. During the test, a total of 11 parameters were concurrently measured in response to fluid injection. As shown in Figure 6.4, the green curve represents the loading piston displacement of the MTS 816 frame, which was kept as constant under a constant piston-displacement control. The black curve describes the differential stress history which shows a significant drop once the fracture slip is induced. The computed effective normal stress and shear stress (see Eq. (2-3) and Eq. (2-4)) on the fracture plane are separately illustrated by the dark-red and teal curves. The blue curve is the injection pressure which was increased gradually from 4 MPa to 28 MPa at a rate of 0.1 MPa/s. The accompanying pump volume (pump A, see Figure 6-2(a)) is represented by the orange curve. The red and pink curves are the normal dilation and shear slip of the fracture calculated using Eq. (2-6) and Eq. (2-7), respectively. The light-blue curve is injection flow rate in syringe pump A. The cumulative AE events and hits are illustrated by the purple curve and the gold curve, respectively. It is noticed from the plots that the stresses, displacements, flow rates, and AE signals vary with the changes of fracture shear slip.

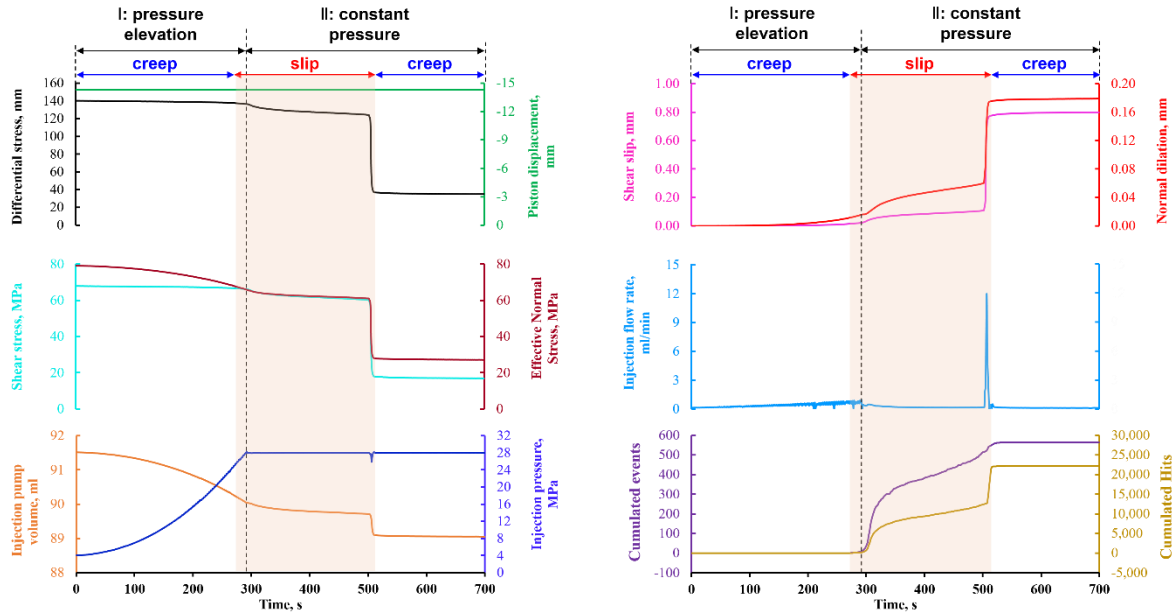


Figure 6.4: The seismo-hydro-mechanical response of granite sample SW-A1 during injection-induced shear test: temporal evolution of the piston displacement (green), the differential stress (black), the shear stress (teal), the effective normal stress (dark-red), the injection pressure (blue), the pump volume (orange), the fracture shear slip (pink), the fracture normal dilation (red), the injection flow rate (light-blue), the cumulated AE hits (gold), and the cumulated AE events (purple) during the 700-s-long fluid injection.

As can be seen in Figure 6.4, generally, the injection process contains two stages: a pressure elevation stage in which the injection pressure is gradually increased; and a constant pressure stage in which the injection pressure is held as constant after it reaches the target of 28 MPa. In the test, the injection pressure was continuously increased from 4 MPa to 28 MPa at a constant rate. As a result, the effective normal stress (σ'_n) and the corresponding critical shear stress (τ_c) gradually decrease as the fluid pressure is elevated. The pre-existing fracture slips (fails in shear) when the critical shear stress (τ_c) is reduced to the shear stress (τ) along the fracture plane. As a result, the strain energy stored in sample and in the loading frame is released along with the fracture slip, triggering acoustic emission/microseismic events. According to the evolution of slip characteristics, the test can be divided into three intervals each with a different seismo-hydro-mechanical response.

- 1st aseismic/creep interval:** In the *post-seismic* interval (from 0 s to ~270 s), the fracture slip shows a creeping manner with a low velocity of 4×10^{-8} m/s and accumulates a slip displacement of 0.017 mm. The effective normal stress gradually decreases with continuous elevation of fluid pressure, while the shear stress shows no significant change. This means that the shear failure of the pre-existing fracture is not satisfied at this creep interval. No AE events were detected, which corresponds with a limited numbers of AE hits. The sample was in a *pre-seismic* or *aseismic* state. The accompanying normal dilation is 0.013 mm, which mainly caused by the decrease of effective normal stress during the increase of injection pressure. The injection flow rate increased almost linearly with regular pump oscillations. A few rapid fluctuations observed on the flow rate curve (light-blue curve in Figure 6.4) may be caused by the dilatant shear failure of some local asperities. The failure of local asperities is also evidenced by the existence of a few AE hits.
- Seismic slip interval:** After the injection pressure reached above ~24 MPa, the fracture slip evolved into a seismic slip interval with a duration of ~240 s (from ~270 s to ~510 s, the interval lasts from the end of 1st pressure elevation stage to the half of 2nd constant pressure stage). A quasi-static/stable fracture shear slip can be noticed from ~270 s to ~500 s, following by a dynamic/unstable slip from ~500 s to ~510 s. The quasi-static slip stage has an average slip rate as $\sim 3 \times 10^{-7}$ m/s (with an accumulated slip of 0.09 mm), while the dynamic slip stage has a much faster slip rate of $\sim 1 \times 10^{-4}$ m/s (with an accumulated slip of 0.66 mm). The shear stress starts to decrease after the initiation of fracture shear slip: in the

quasi-static slip stage with 230 s duration, a total ~6.26 MPa decrease in shear stress (having a stress-drop rate of ~0.02 MPa/s) was induced; while in the dynamic slip interval, in 10 seconds the shear stress dropped ~42 MPa with a rapid drop-rate of ~6 MPa/s. The drop of shear stress is an evidence that the fracture shear failure is satisfied. Upon the large stress drop, a huge number of AE events and hits were detected in this seismic slip interval. It is found that the AE signals correlate well with the shear stress drop and fracture slip. Due to the suddenly increase of fracture normal dilation (~0.16 mm dilation) caused by fracture shear slip, a significant increase of injection flow rate (in transient flow regime) can be observed in the flow rate curve (light-blue curve in Figure 6.4).

- **2nd aseismic/creep interval:** In this post-slip interval from ~510 s to 700 s, the injection pressure was kept as constant 28 MPa, and the fracture slip slowed down and switched back to a creeping manner with a velocity of $\sim 8 \times 10^{-8}$ m/s and accumulated a slip displacement of 0.03 mm. Due to the significant stress drop occurred in the previous seismic slip interval, the stress state in the fracture was no longer in a critical state. Also, the injection pressure was kept constant. As a result, the fracture slip decelerated to a creep behavior. In this interval, only a few AE events were detected in ~510 s to ~530 s (the transition zone from slip to creep), there were no AE events detected in the later creep interval (from ~530 s to 700 s). This means that the fault/fracture tends to be aseismic after the large stress drop (or energy release) during seismic slip, until the stress is re-accumulated in next slip cycle. In addition, since there was no further increase of fracture dilation, fracture storage became stable and as a result, the fluid flow

evolved in to steady-state flow regime and the injection flow rate dropped back to a lower value. As mentioned in our previous works (Ye et al., 2017), the steady-state flow rate is much smaller than the flow rate in transient flow regime.

6.5 Discussion

6.5.1 The Slip-Seismicity-Permeability Relationship

As illustrated in Figure 6.4, sample SW-A1 (containing a pre-existing fracture) experienced a creep-slip-creep cycle during the injection test, and each part of the cycle has a different slip behavior. In the test, a total shear displacement of 0.80 mm has been induced by pressurized fluid injection. The seismic slip interval accumulated a shear displacement of 0.75 mm (94% of the total shear displacement), and only 0.05 mm shear displacement (6% of the total shear displacement) was accumulated in the two creep intervals. The total normal displacement during the entire test is 0.18 mm, including a 0.16 mm displacement accumulation (90% of the total normal displacement) in the seismic slip interval and a 0.02 mm displacement accumulation (10% of the total normal displacement) caused by fracture creep. In addition, the majority of shear stress drop also occurred in the seismic slip interval (48 MPa, 94% of the total shear stress drop). As a result, a total 509 AE events (97% of the total AE events) was induced in the seismic slip interval, excepting to the 17 AE events induced in the transition zone of slip-creep from 510 s to 530 s. It is also noticed that a remarkable flow rate increase indicating by a rapid fluctuation on the flow rate curve was caused the fracture slip. Moreover, a total 1.16 ml fluid was injected into the fracture during the seismic-slip interval due to the normal dilation caused by fracture slip. Therefore, all these observations demonstrate that the microseismic events, fluid flow and fracture slip correlate well with each other in the injection test: the generation of microseismicity and the

enhancement of flow rate/permeability are directly caused by the shear slip of the pre-existing fracture.

6.5.2 Acoustic Emission/Microseismic Signature

To obtain a better acoustic emission (AE) location, we applied an energy filter to remove some low energy events. The location maps of the filtered AE events in x - z plane and y - z plane are illustrated in Figure 6.5(a) and Figure 6.5(b), respectively. It is noticed that a total of 662 events with different amplitudes from 55 dB to 97 dB were detected into the slip interval and the two transition zones in the creep-slip-creep cycle (from 270 s to 530 s). There were no AE events detected in the 1st creep zone (0 - 270 s) and 2nd creep zone (530 - 700 s). As shown in the Figure 6.5(a), the AE events locate in an area near the inclined fracture plane (sketched by the black line). Also, in Figure 6.5(b), it is clear that almost all events occurred in the fracture plane (almost all AE events are located in the ellipse depicted in Figure 6.5(b)). These observations support the notion that induced microseismicity during hydraulic injection is mainly related to the shear failure of the pre-existing fracture. In addition, the onset of microseismicity starts at the near wellbore region, further demonstrating that the fracture shear slip was directly induced by fluid injection.

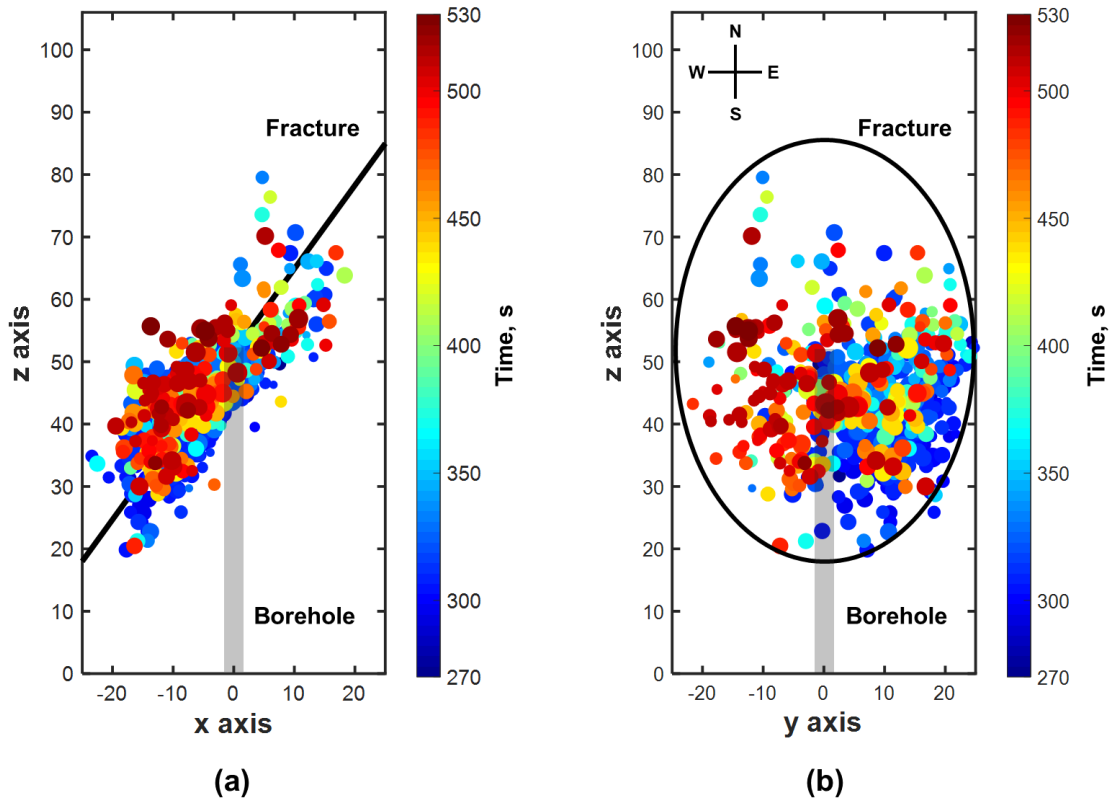


Figure 6.5: The location of acoustic emission events in: (a) x - z plane; and (b) y - z plane. The black line in the x - z plane (left) and the black ellipse in y - z plane (right) are the projection of the pre-existing fracture onto the two planes, respectively. The pre-drilled borehole for fluid injection is represented by the light-gray pillar. In the two plots, the dots with different sizes indicate the AE events with different amplitudes (from 55 dB to 97 dB), while the color scheme is used to represent the elapsed time from 270 s to 530 s.

Figure 6.6 shows the spatio-temporal evolution of microseismicity/AE activities in x - z plane (top) and y - z plane (bottom). In general, the AE events initiated at 270 s after elevating injection pressure. We observed 598 events in the quasi-static slip interval (from 270 s to 500 s), 42 events in the dynamic slip zone (from 500 s to 510 s), and 22 events in the aftershocks (510 s to 530s). This means that 90% of the AE events are induced in the quasi-static slip zone. It is found that the AE events tend to spread from the central injection zone to the southeast quadrant of the fracture plane (see the AE location in y - z plane of Figure 6.6) in the first 40 s (from 270 s to 310 s) after the onset of AE events. Also, the slip tends to migrate downward in the first 40 s after the AE initiation, indicating the spatial

evolution of AE hypocenters in x - z plane (the top plots in Figure 6.6). We noticed 197 events in the first 40 s with the density of ~ 5 event/s. Among the 197 AE events, there are more than 180 events are mainly located in southeast quadrant of the fracture plane, indicating a large number of local asperity-slip initiated and accumulated in this quadrant. AE hypocenters starts to expand into the other three quadrants of the fracture plane since 310 s. More AE events accumulated in most area of the fracture plane with the elapse of the time. This means that the local shear slip of asperities accumulates and evolves toward the global shear failure of the fracture plane. The final shear failure of the pre-existing fracture occurred at the interval between 500 s to 510 s, which is evidenced by the appearance of AE hypocenters in most area in y - z plane at $t = 500$ s and $t = 530$ s (Figure 6.6). After the final shear failure of the fracture, a few numbers of AE events (22 events) were detected in the transition zone of slip-creep (from 510 s to 530 s). Subsequently, the fracture evolved into another *aseismic* creep stage. The spatio-temporal evolution of AE hypocenter location in our test provides an important insight that the existence of slip heterogeneity during the shear reactivation of faults/fractures by injection. To our best knowledge, the slip heterogeneity observed in our injection-induced shear test has not been directly reported in previous experimental study even through it is widely discussed in the field observations of natural fault-slip or numerical modeling study (e.g., Resor & Meer, 2009; Tinti et al., 2016; Zielke et al., 2017).

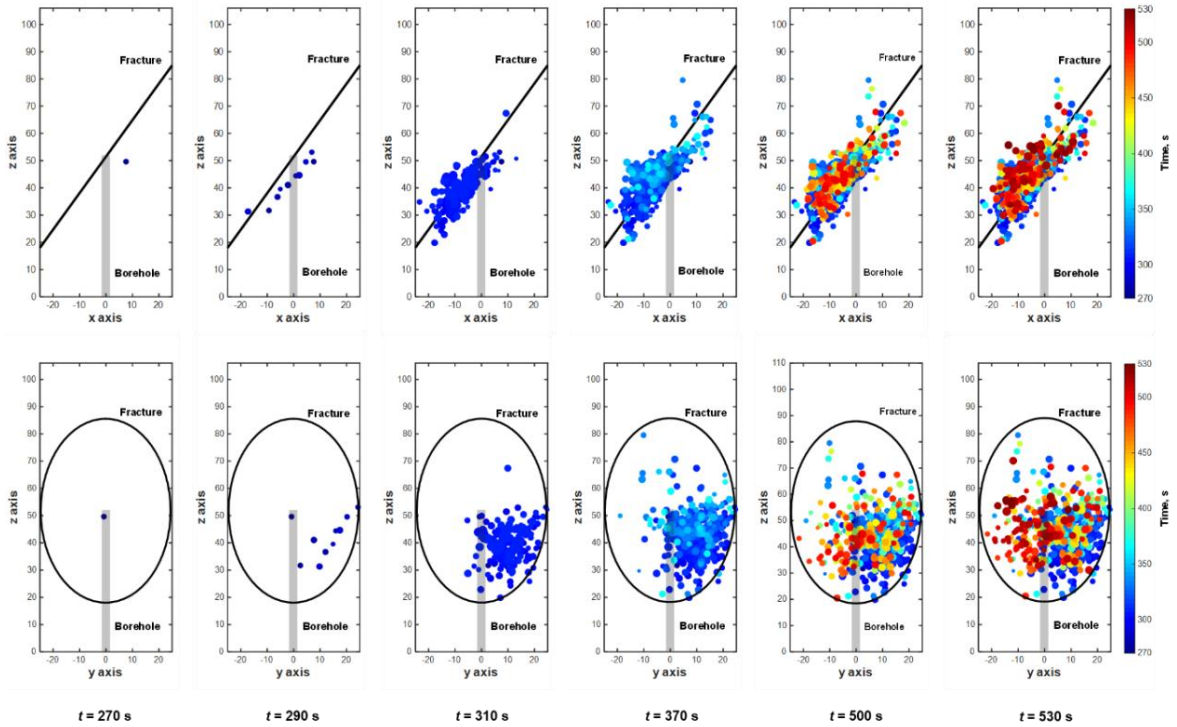


Figure 6.6: The spatio-temporal evolution profiles of acoustic emission events in x - z plane (top) and y - z plane (bottom) at $t = 270, 290, 310, 370, 500,$ and 530 s. The black line in the x - z plane (top) and the black ellipse in y - z plane (bottom) are the projection sketches of the pre-existing fracture onto the two planes, respectively. The pre-drilled borehole for fluid injection is represented by the light-gray pillar. In the plots, the dots with different sizes indicate the AE events with different amplitudes (from 55 dB to 97 dB), while the color scheme is used to represent the elapsed time from 270 s to 530 s.

6.5.3 The Effect of Fracture Surface Roughness

As demonstrated in Figure 6.6, the AE hypocenters mainly distribute in the southeast quadrant (see Figure 6.5(b)) of the fracture plane in our test on the rough granite fracture, indicating a strong slip heterogeneity during the shear activation of the pre-existing fracture by injection. Several laboratory experiments conducted on saw-cut fractures reported that a relatively even distribution of AE hypocenters on the smooth fracture surface is usually generated by fracture slip (e.g., Kwiatek et al., 2014; Goebel et al., 2013). This means that the slip heterogeneity could be related to the nonplanarity of rough fracture surface. However, although the fracture surface roughness has been considered as the possible reason inducing the slip heterogeneity during fault/fracture shear slip, most of the previous

interpretation on the link of fracture surface roughness and the heterogeneity of slip or microseismicity distribution have been based on numerical modeling (e.g., Tinti et al., 2016; Zielke et al., 2017) and field observations (e.g. Resor & Meer, 2009).

Figure 6.7 shows the projections of AE hypocenters on the scanning contours of the fracture surface. In the Figure 6.7(a), it is observed that most AE events initiated and accumulated in southeast quadrant of the fracture plane in the first 40 s of the quasi-static slip interval (from 270 s to 310 s), corresponding with the area with largest variation of asperity height (or so-called the *rough* area in the fracture surface). The fracture surface with largest surface relief tends to have the highest density of AE hypocenters distribution. As more AE events spreading from the southeast quadrant, the accumulation of local asperity failure ultimately led to the shear failure/dynamic instability of the pre-existing fracture (Figure 6.7(b)). Also, the AE hypocenters locally covered the almost full rough area before the final dynamic failure of the entire fracture. This means that the damage of the *rough* area controls the failure of the fracture. The proper interpretation is that the *rough* area in fracture surface has more asperity contacts, and the stress tends to locally concentrate in these contacts.

Therefore, with the elevation of fluid pressure, these stress-concentrated asperities in *rough* area tends to fail before the asperities with less stress concentration in the *smooth* area. With the growth of local asperity failure, the contact area in fracture plane increases, while the shear resistance of the fracture decreases. As a result, the stress redistributes on the fracture surface, and finally triggers the dynamic failure of the entire fracture. On the other hand, the local shearing of contacted asperities induces an irreversible normal dilation, resulting in a flow path with a higher permeability around the sheared asperities.

Consequently, the pressurized fluid permits the further local shearing/failure of near-by asperities. This is supported by the observation that the *rough* area has a highest distribution density of AE events. In short, the integrated effect of fracture surface roughness and pressurized fluid injection promotes the slip heterogeneity during fault/fracture reactivation by injection.

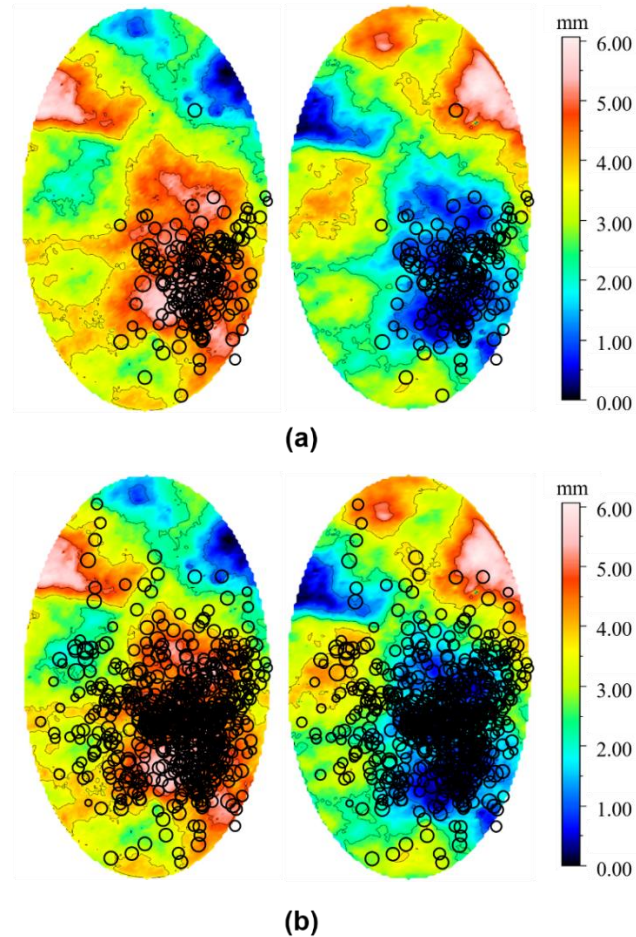


Figure 6.7: The projection of AE hypocenter locations on the scanning contours of fracture surfaces (left is the bottom surface): (a) the distribution of AE location at $t=310$ s; (b) the distribution of AE location at $t=530$ s. In the scanning contour, the color scheme indicates the asperity height. The black circles indicate the AE hypocenters with different magnitudes from 55 dB to 97 dB.

6.6 Chapter Summary

The presented study reveals the fully coupled seismo-hydro-mechanical response of a granite fracture during shear slip by pressurized fluid injection. In the 700-s-long injection

test, a creep-slip-creep manner of fracture shearing during injection was detected, correlating well with the evolution of stress drop and acoustic emission activities. The creep interval has a slow slip rate of $\sim 10^{-8}$ m/s, while the slip interval contains a quasi-static slip stage with a $\sim 10^{-7}$ m/s slip rate and a dynamic slip stage with a $\sim 10^{-4}$ m/s slip rate. The final shear failure of the pre-existing fracture occurred at the dynamic slip stage, which analogs the earthquake instability during natural fault reactivation. We observed 598 events in the quasi-static slip interval (from 270 s to 500 s), 42 events in the dynamic slip zone (from 500 s to 510 s), and 22 events in the aftershocks (510 s to 530 s). On the other hand, the 1st creep interval (0 - 270 s) and most part of the 2nd creep interval, the fracture tends to be *aseismic*. In the two creep intervals, the total shear stress drop is less than 3 MPa, while the total shear stress drop in seismic slip interval is 49 MPa (including 7 MPa drop in quasi-static slip stage and 43 MPa drop in dynamic slip stage). This means that the microseismic events and the coseismic stress drop strongly link with the slip behavior of the pre-existing fractures during hydraulic injection.

The spatio-temporal evolution of acoustic emission hypocenters reveals the accumulation and evolution of the local asperity shearing/failure. The results indicate the existence of slip heterogeneity on fracture plane and support the notion that the global fracture failure/instability is caused by the accumulation of local asperity failure. By comparing with fracture surface topography, we found that acoustic emission activities tend to initiate at the *rough* area of the fracture surface with high surface relief. Also, the *rough* area has the highest distribution density of AE hypocenters. This indicates that the failure of the *rough* area controls the global instability of the fracture. On the other hand, the local shearing of contacted asperities induces an irreversible normal dilation, resulting in a flow

path with a higher permeability around the sheared asperities, permitting the further local shearing/failure of near-by asperities. We conclude that the integrated effect of facture surface roughness and pressurized fluid injection promotes the slip heterogeneity during fault/fracture reactivation by injection.

Chapter 7

Injection-induced Fracture slip and Microseismicity in Shale

In Chapter 6, the microseismic signature of granite fracture during injection has been demonstrated. The results shown that microseismic events correlates well with fracture shear slip. In this chapter, the experimental results of injection-induced shear slip test on shale fracture with concurrent acoustic emission (AE) monitoring are presented to explore the evolution of microseismicity and permeability in shale reservoir stimulation. It is found that the induced microseismic signature of shale fracture is different with that of granite fracture. The various frictional characteristics in response to fracture shearing in shale fracture and in granite fracture may be the reason.

7.1 Abstract

Shear slip of pre-existing fractures can play a crucial role in hydraulic stimulation to enable production from unconventional shale reservoirs. Evidence of the phenomenon is found in microseismic/seismic events induced during stimulation by hydraulic fracturing. However, induced seismicity and permeability evolution in response to fracture shear reactivation by injection has not been extensively studied in laboratory tests under relevant conditions. In this work, a cylindrical Eagle Ford shale sample having a single fracture (tensile fracture) was used to perform laboratory injection test with concurrent acoustic emission (AE) monitoring. In the test, shear slip was induced on the fracture at near critical stress state by injecting pressurized brine water (7% KCL). Sample deformation (stress, displacement), fluid flow (injection pressure, flow rate) and AE signals (hits, events) were all recorded. The data was then used to characterize the fractures' fully coupled seismo-

hydro-mechanical response during shearing. Results shown that the induced AE/microseismic events correlate well with the fracture slip and the permeability evolution. Most of the recorded AE hits and events were detected during the seismic slip interval corresponding a rapid fracture slip and a quick stress drop. As a result of dilatant shear slip, a remarkable enhancement of fracture permeability was achieved. Prior to this seismic interval, an aseismic slip interval was evident during the tests, where the fracture slip, the associated stress relaxation, and the permeability increase were limited. The test results and analyses clearly demonstrate the role of shear slip in permeability enhancement and induced seismicity by hydraulic stimulation for unconventional shale reservoirs.

7.2 Introduction

Shear slip of pre-existing fractures has been recognized as a major permeability creation and micro-seismicity mechanism of reservoir stimulation for a long time (e.g., Mayerhofer et al., 1997; Pine & Batchelor, 1984; Rutledge, Phillips, & Mayerhofer, 2004; Zoback et al., 2012). Most reservoir rocks contain abundant pre-existing fractures, some of which may be sealed with calcite or other infill minerals. Usually, these fractures are inactive and without sufficient permeability before stimulation. A number of modeling and field studies have shown that when the pre-existing natural fractures are favorably oriented with respect to the in-situ stresses, an injection or the leak-off from a hydraulic fracture (even with low fluid pressure) can cause the fractures sliding and propping due to asperities (e.g., Rutledge et al., 2004; Ye & Ghassemi, 2018). This mechanism of permeability increase is often called *shear stimulation* or *hydroshearing*. The shear slip mode is evident in the microseismic signature during hydraulic fracturing (e.g., Clarke et al., 2014; Maxwell et al., 2010).

During pressurized fluid injection into the subsurface (e.g., hydraulic fracturing, wastewater disposal, etc.), the effective normal stress (σ'_n) acting on pre-existing fracture(s) is gradually decreased with the elevation of the pore pressure, leading to the reduction of the critical shear stress ($\tau_c = \mu\sigma'_n$; μ is the sliding friction coefficient). Fracture slip occurs when the critical shear stress (τ_c) is reduced to the shear stress (τ) along the fracture plane. As a result, microseismic can be generated as the strain energy stored in surrounding rock mass is released (e.g., Majer et al., 2007). In the petroleum industry, the monitoring of microseismic activity induced by hydraulic fracturing is generally used a tool for reservoir characterization (e.g., Rutledge et al., 2004; Maxwell, et al., 2010). Some field observations have shown that a large stimulated reservoir volume (mapped from the microseismic monitoring) results in a better production (Fisher et al., 2004; Mayerhofer et al., 2010), which is likely caused by fracture dilation/opening due to shearing. However, fundamental investigations through laboratory experiments under relevant stress and boundary conditions have not been carried out.

Remarkable permeability enhancement has been observed from the fracture shear tests on strong crystalline rocks (e.g. Esaki et al., 1991; Vogler et al., 2018; Ye, Janis, & Ghassemi, 2017; Ye & Ghassemi, 2018), however, based on a few experiments on shale fractures, it has been suggested that fracture permeability tends to decrease with shear slip (Fang et al., 2017; Gutierrez, Øino, & Nygaard, 2000; Rutter & Mecklenburgh, 2018; Wu et al., 2017). In these shear tests, slip was mechanically forced (Fang et al., 2017; Gutierrez et al., 2000; Wu et al., 2017), or saw-cut shale fractures (Fang et al., 2017; Rutter & Mecklenburgh, 2018) were used. In the former set of force-induced slip experiments, the fracture likely experienced a relatively large shear displacement (~0.4-inch shear slip) on a

small-size shale sample (1-inch diameter cylindrical samples or 3-inch by 3-inch by 1-inch shale blocks), and therefore it is highly likely that asperity degradation and gouge production caused by the large shearing deformation plugged flow paths in the fracture, decreasing its permeability. On the other hand, shear tests on saw-cut fractures yield little permeability increase because of insufficient asperities on the smooth fractures. In our companion papers (Ye, Ghassemi, & Riley, 2018; Ye et al., 2017), a number of laboratory injection tests were reported on shale samples having pre-existing fracture(s), the results show shear slip can enhance fracture permeability. Moreover, our works suggest that in addition to dilatant shear slip, the propagation and coalescence of pre-existing fractures can also contribute to the permeability enhancement during shale reservoir stimulation (Ye, Ghassemi, & Riley, 2018; Ye & Ghassemi, 2019). However, these previous works did not study the occurrence of microseismicity during injection-induced fracture slip.

In this study, an injection-induced shear test with concurrent acoustic emission monitoring was carried out using an Eagle Ford shale sample with a rough tensile fracture under triaxial stress. In the test, pressurized brine water (7% KCL) was injected into the fractured cylindrical sample to induce shear slip, the measurements of sample deformation (stress, displacement), fluid flow (injection pressure, flow rate) and AE signals (hits, events) were all concurrently recorded to characterize the seismo-hydro-mechanical responses of shale fracture during pressurized fluid injection. Through this work, we provide insights on several key questions related to the reactivation of pre-existing fractures in shale reservoir stimulation: (1) does shear slip of shale fractures enhance or decrease the fracture permeability; (2) how does permeability evolve in response to fracture shear slip by injection;

(3) and what is the microseismic signature during injection-induced fracture shear reactivation.

7.3 Experimental Methods

7.3.1 Sample Preparation and Characterization

The specimen used in this test was a cylindrical Eagle Ford shale (from Del Rio region, Texas) with 38.10 mm diameter and 80 mm length (hereinafter EF #1). The sample was cored parallel to the bedding planes from a shale outcrop acquired from a commercial outlet, however, the bedding planes are not significantly well-define (Figure 7.1). The powder X-ray diffraction analysis has shown that calcite and quartz, 52% and 35% (in weight fraction), dominate the mineral contents of this Eagle Ford shale. The TOC and matrix permeability of this shale are 2.02% (in weight fraction) and 1.98×10^{-4} mDarcy, respectively. The Young's modulus and Poisson's ratio determined by regular triaxial compression test are separately 3.70×10^6 psi (25.5 GPa) and 0.29. A Brazilian test was used to measure the tensile strength of the Eagle Ford as 1362 psi (9.40 MPa).

To ensure the accurate detection of AE events during the test, wave propagation velocities of the rock are needed. It is found that rock anisotropy affects the determination of wave arrival time and propagation velocity (e.g. Moradian et al., 2015). To minimize the complications associated with influence of wave-velocity anisotropy, the selected Eagle Ford sample, which is fine-grained, and relatively isotropic. Before creating a fracture in the sample, its velocity anisotropy was evaluated by ultrasonic wave measurements. The P-wave velocities in x, y and z direction were measured at ambient conditions using a pair of piezoelectric crystal transducers. One transducer served as a trigger to generate a sine waveform, and the other transducer played as a receiver. The received waveform was then

amplified by a low-noise preamplifier type 2/4/6/ from PAC (Physical Acoustics Corporation) set at 40 dB and displayed on an oscilloscope (made by Tektronix). Through the oscilloscope, the P-wave arrival time was determined and used to calculate the wave velocity. The P-wave velocity in z- axis (parallel to bedding planes) was 5664 m/s (1.86×10^4 ft./s), while the wave velocities in x-axis (perpendicular to bedding planes) and y-axis were 5259 m/s (1.72×10^4 ft./s) and 5393 m/s (1.77×10^4 ft./s), respectively. The results show the velocity anisotropy to be quite small, and only with a variability (variability=range/average) of 5% ~ 8%.

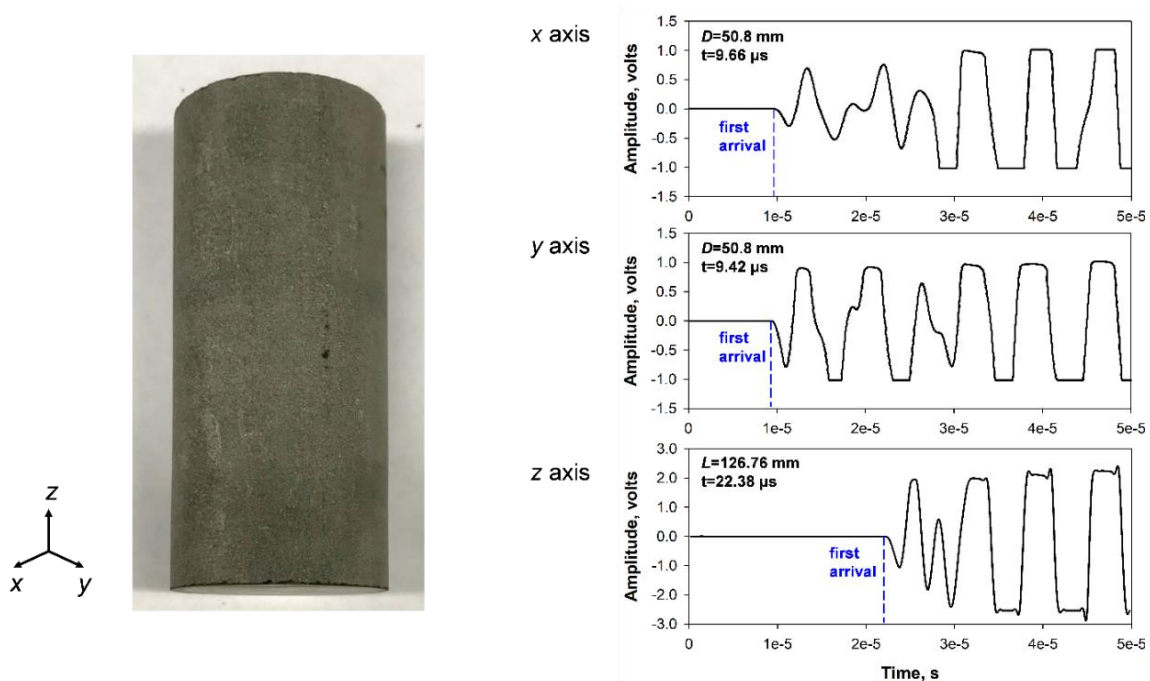


Figure 7.1: Anisotropy evaluation of P-wave velocity: the small velocity differences in three directions indicate that this Eagle Ford shale is without significant velocity anisotropy. In the plot, D is the sample diameter, L is the sample length, and t represent the arrival time of P-Wave.

A single tensile fracture was then created in the sample. An inclined groove (40-degrees with respect to the vertical axis of the sample) was first cut by a diamond saw on the sample, and then a tensile fracture having rough fracture surface was created through rock splitting using a steel wedge (Figures 7.2(a) and 7.2(b)). A three-dimensional (3D) non-

contact scanning system was used to measure fracture surfaces' topography. As shown in the resulting contour plot (Figure 7.2(c)), the maximum surface relief is 4.93 mm (see the color scale in Figure 7.2(c)) and the average JRC (Joint Roughness Coefficient, Barton 1973) value is around 9.0. To enable injection into the fracture, two ~2.5 mm diameter boreholes were drilled (5 mm from the sidewall) from each end of the sample to reach the fracture (see Figure 7.2(b)).

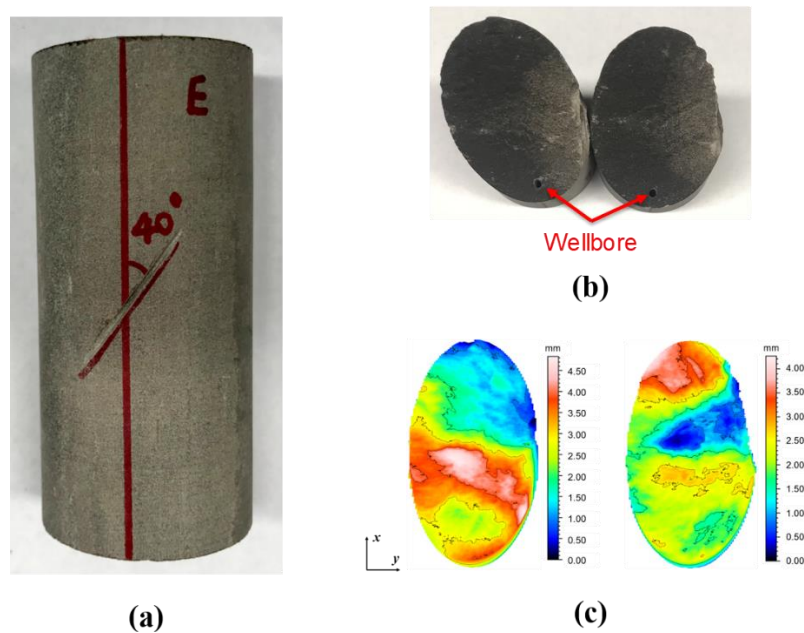


Figure 7.2: Sample preparation: (a) Eagle Ford shale having an inclined groove; (b) fracture surfaces, and two boreholes were drilled for water injection/fluid flow; (c) 3D surface scanning contour, the x (the long axis of the contour), y (the short axis of the contour) and z coordinates (the color scale of the contour) are the length, width and asperity height of fracture surface, respectively

7.3.2 Experimental Setup and Procedure

The injection test with acoustic emission of sample EF #1 was carried out using the MTS 816 frame. As shown in Figure 7.3(a), the rock deformation in axial and radial directions were measured by two axial LVDT (Linear Variable Differential Transformer) sensors and one radial LVDT sensor, respectively. The associated error of this type of LVDT is $\pm 0.05\%$. The history of stress change during the test was recorded by a load-cell located inside of the triaxial pressure vessel, with maximum 1 KN loading error. A Teledyne ISCO

100DM syringe pump connected with the bottom borehole of the sample was used to inject brine water (7% KCL, deionized water solution) to induce fracture shear slip, and another syringe pump connected with the top borehole was used to produce water. The corresponding fluid flow parameters (pressure, flow rate and pump volume) were concurrently measured during the injection test. The ISCO pump has a $\pm 0.5\%$ pressure error and a $\pm 0.3\%$ flow rate error. In addition, two porous metal discs (38.10 mm diameter by 3.2 mm thickness) with a pore size of 60 microns were placed on each end of the sample to provide an even fluid flow distribution (see Figure 7.3(a)). The measurements of mechanical parameters (displacement and stress) and fluid flow parameters (pressure and flow rate) are used to characterize the hydro-mechanical coupled responses of the fracture in the shearing process.

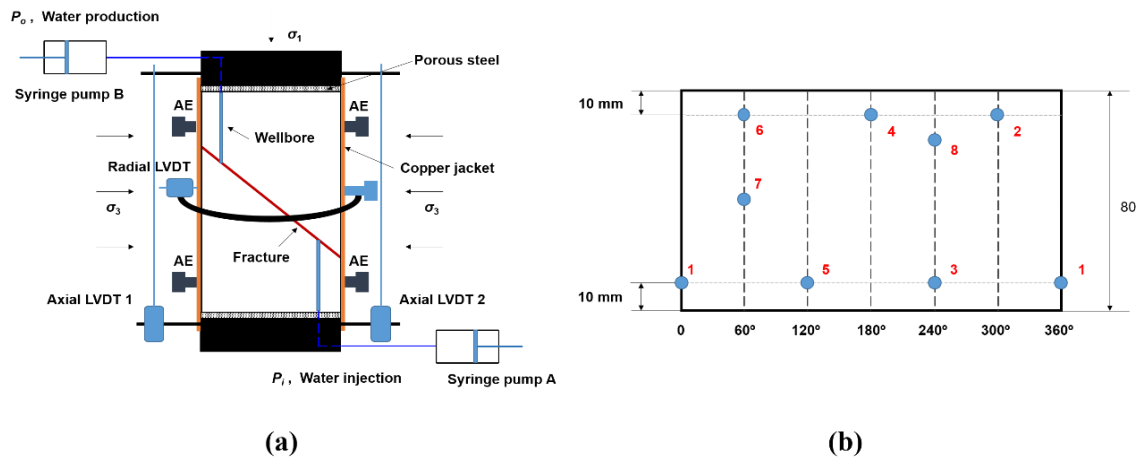


Figure 7.3: Experimental setup: (a) sketch of sample configuration; (b) projected sample surface showing the location of 8 piezoelectric crystal transducers for AE monitoring (the blue circles indicate the transducers). The red line in the left plot represents the fracture. AE=Acoustic Emission, LVDT= Linear Variable Differential Transformer.

Sample EF #1 was jacketed by a copper sheet with thickness of 1.27 mm (0.05-inch), and then was subjected to a triaxial compression with 20 MPa (2900 psi) confining pressure and 10 MPa (1450 psi) differential stress in the pressure vessel of MTS 816 frame. The purpose to this step is to close the fracture and set the copper jacket tightly against the sample.

Afterwards, 8 piezoelectric crystal transducers, with 1 MHz resonant frequency, were bonded to the jacketed sample with glue in the arrangement shown in Figure 7.3(b). The AE (acoustic emission) instrument used in this study is an Express-8 AE system supplied by PAC. The AE test setup consists of crystal transducers, 2/4/6 preamplifiers, processing instrumentation, and AE win software. During the test, the electrical signals from each of the crystal transducers were amplified by the 2/4/6 preamplifiers and passed through an analog filter operating between 5 kHz and 400 kHz. After the filter, each of the signals (voltages) then was measured if above a threshold level of 45 dB with a 10 MSPS sampling rate (high sampling rate).

To control the quality of the injection test with acoustic emission, the present experiment contains two steps. The procedure and purpose of each step are discussed below:

- Step 1: In order to determine the frequency range, waveform shape and relative parameters for acoustic emission, a pencil lead break (PLB, ASTM standard, 2015) test was conducted on the sample after it was installed in the pressure vessel of MTS 816 (before closing the lid of the pressure vessel). Through the PLB test, several important AE timing parameters can be determined, such as PDT (peak definition time), HDT (hit definition time), etc.
- Step 2: After the PLB test, the sample was first subjected to a 20 MPa confining pressure in the closed pressure vessel. To eject out air bubbles in the sample assembly and completely saturate the fracture, brine water (7% KCL, deionized water solution) was circulated from the bottom borehole to the upper borehole through the fracture for 10 minutes (under a 5 MPa pressure difference between the two syringe pumps). After that, the production pressure in pump B was set to

4 MPa and kept constant during entire injection test. The initial injection pressure provided by pump A was 4 MPa, but later was gradually elevated to induce fracture slip. Next, the sample with loaded to a near-critical state with 70 MPa differential stress. The test system was then switch to a constant piston displacement control. Upon this control mode, the actuator piston was fixed without any movement during injection test, and the stress drop in response to fracture shearing can be captured (Ye & Ghassemi, 2018). Subsequently, the injection pressure was continuously elevated at a rate of 4 MPa/min from 4 MPa to 19 MPa to induce fracture slip. Once the injection pressure reached the target of 19 MPa, the injection pressure was held constant for another couple minutes. During the test, the coupled hydro-mechanical properties and the concurrent acoustic emission signals of the Eagle ford shale fracture in response to injection were all recorded.

7.4 Experimental Results

7.4.1 Pencil Lead Break (PLB) Test

The pencil lead break (PLB) test is widely used to test the performance of acoustic emission sensors, which also can provide important information of the signal waveforms to determine related parameters for acoustic emission. Here, based on the ASTM standard E976 (2015), a PLB test was conducted on sample EF #1 and the waveforms of all 8 crystal sensors were recorded (Figure 7.4). The waveforms in Figure 7.4 clearly indicate that all 8 sensors had good performance and were sensitive to the energy source released from the sample. Since the PLB signal was triggered close to sensor 7, waveforms received by sensors 5, 6 and 7 have relatively higher AE amplitude than the others. On the other hand, sensors 4 and

8 have relatively lower AE amplitude, because they are farther from sensor 7. In addition, the sign of the first motion amplitudes of most sensors are positive, which is likely related to more compressive waves produced by the PLB test. Through the PLB test, several AE timing parameters, such as PDT (Peak Definition Time), HDT (Hit Definition Time) and HLT (Hit Lockout Time), were determined for later acoustic emission monitoring during injection.

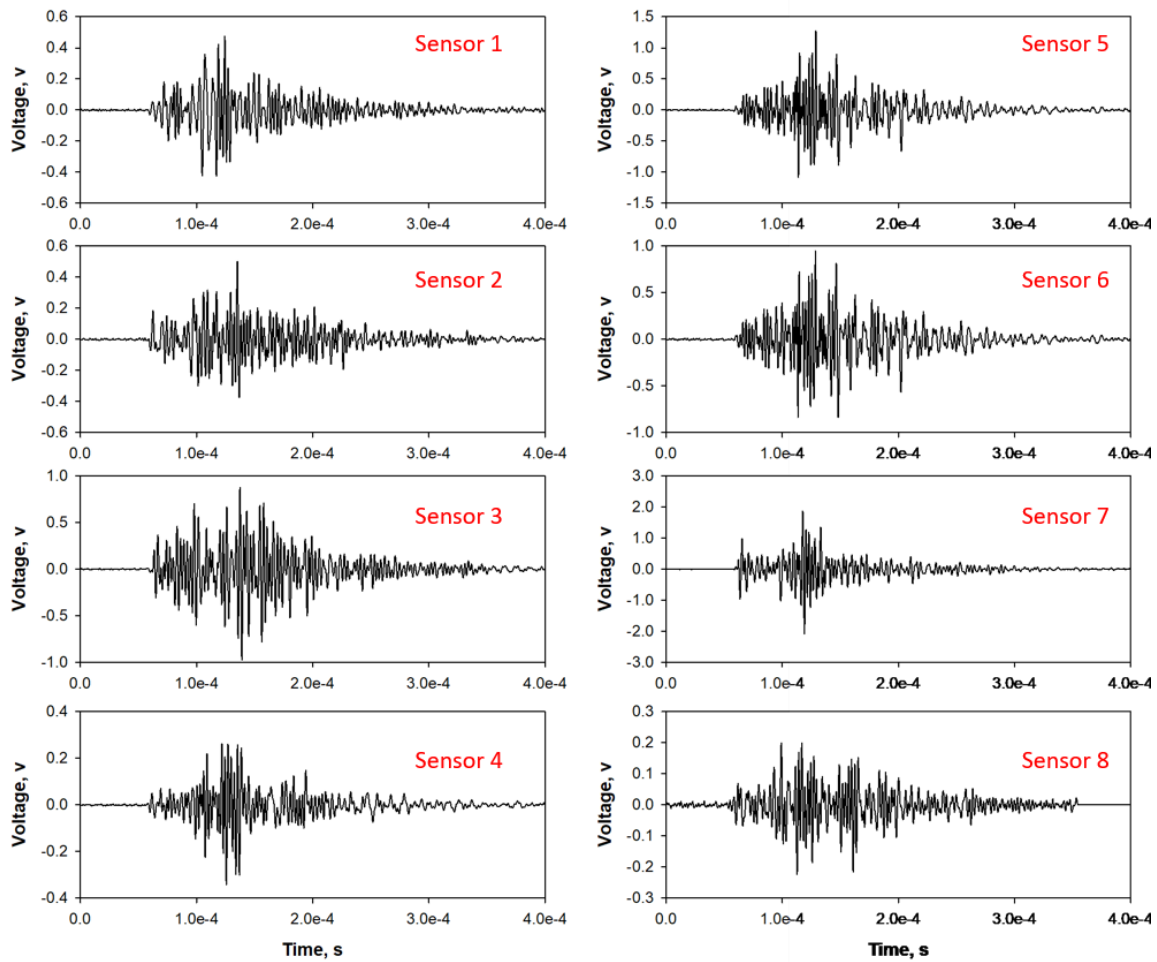


Figure 7.4: Waveforms of the 8 crystal sensors in a PLB test on the shale sample EF #1. PLB=Pencil Lead Break. (check)

7.4.2 The Seismo-Hydro-Mechanical Measurements

The seismo-hydro-mechanical response of sample EF #1 during the injection test is shown in Figure 7.5. In the plots, the rock deformation and fluid flow in the pre-injection

stages (initial applications of confining pressure, axial loading, and injection pressure) are not shown. This means that the displacements and flow rates were zeroed before elevating the injection pressure. Also, the corresponding acoustic emission activities in the pre-injection stage was not accounted into Figure 6.4. During the test, a total of 12 parameters were concurrently measured in response to fluid injection. As shown in Figure 7.5, the green curve represents the loading piston displacement of the MTS 816 frame, which was kept as constant under a constant piston displacement control. The black curve describes the differential stress history which shows a significant drop once the fracture slip is initiated. The computed effective normal stress and shear stress (see Eq. (2-3) and Eq. (2-4)) on the fracture plane are separately illustrated by the dark-blue and teal curves. The blue curve is the injection pressure which was increased gradually from 4 MPa to 19 MPa at a rate of 4 MPa/min. The constant production pressure ($P_o = 4$ MPa) is represented by the orange curve. The red and pink curves are the normal dilation and shear slip of the fracture calculated using Eq. (2-6) and Eq. (2-7), respectively. The dark-red curve is the injection flow rate recorded by syringe pump A, and the light-blue curve is production flow rate in syringe pump B. The cumulated AE events and hits are illustrated by the purple curve and the gold curve, respectively. It is noticed from the plots that the stresses, displacements, flow rates, and AE signals vary with the changes of fracture shear slip.

As can be seen in Figure 7.5, generally, the injection process contains two stages: a pressure elevation stage in which the injection pressure is gradually increased; and a constant pressure stage in which the injection pressure is held as constant after it reaches the target. The different seismo-hydro-mechanical responses of each stage are discussed below:

- **Pressure elevation stage:** In this fluid pressurization stage, the injection pressure was continuously increased. As a result, the effective normal stress (σ'_n) and the corresponding critical shear stress (τ_c) gradually decrease as the fluid pressure is elevated. The pre-existing fracture slips (fails in shear) when the critical shear stress (τ_c) is reduced to the shear stress (τ) along the fracture plane. As a result, the strain energy stored in sample and the loading frame is released with the fracture slip, triggering acoustic emission/microseismic events. According to the onset of AE events, this stage can be divided into two intervals. In the aseismic interval (from 0 s to 220 s), the effective normal stress gradually decreases with continuous elevation of fluid pressure, while the shear stress shows no significant change. The variations of fracture slip and fracture opening are quite small. No AE events was detected, which corresponding with a few numbers of AE hits. This means that the energy release was too small and the generated acoustic/seismic signals cannot be detected by AE sensors. The injection flow rate increased stably and linearly with regular pump oscillations in response to the elevation of injection pressure. Also, the production flow rate linearly increased with a stable manner due to the pressure difference between the two pumps. It is noticed that the injection flow rate is larger than the production flow rate. This is attributed to the storage of some of the injected fluid in the fracture due to the gradual increase of the fracture opening. After the injection pressure reached above ~15 MPa, the fracture slip evolved into a seismic slip interval (from ~220 s to ~260 s, from the end of 1st pressure elevation stage to the beginning of 2nd constant pressure stage). The shear stress shows a significant

drop in response to the rapid fracture slip, and the effective normal stress is further decreased. Upon the large stress drop, more AE events and hits were detected. It is found that the AE signals correlate well with the shear stress drop and fracture slip. Due to the fracture opening/normal dilation caused by fracture shear slip, the nonlinear and remarkable flow rate enhancements are noticed on both the injection flow rate curve and the production flow rate curve.

- **Constant pressure stage:** Once the injection pressure reached the target of 19 MPa, the injection pressure was kept constant for another ~240 s. In this stage, the fracture slip and dilation decreased because the injection pressure was not increased further and the differential stress on the sample had dropped in the previous stage. Due to the significant stress drop corresponding to the fracture slip, the fracture was no longer in a critical state since without further elevation of injection pressure. In this stage, the shear stress and the effective normal stress show no significant changes, and the fracture slip and opening represent a slight change (<0.01 mm and can be ignored). No AE events and AE hits were generated in this stage, indicating the test evolved into the second aseismic interval. This means that the fault/fracture tends to be aseismic after the large stress drop/energy release during seismic slip, until the stress is re-accumulated in next seismic cycle. In addition, since there was no further increase of fracture dilation, fracture storage became stable and as a result, the production flow rate equaled the injection flow rate and the flow evolved in to steady-state flow regime.

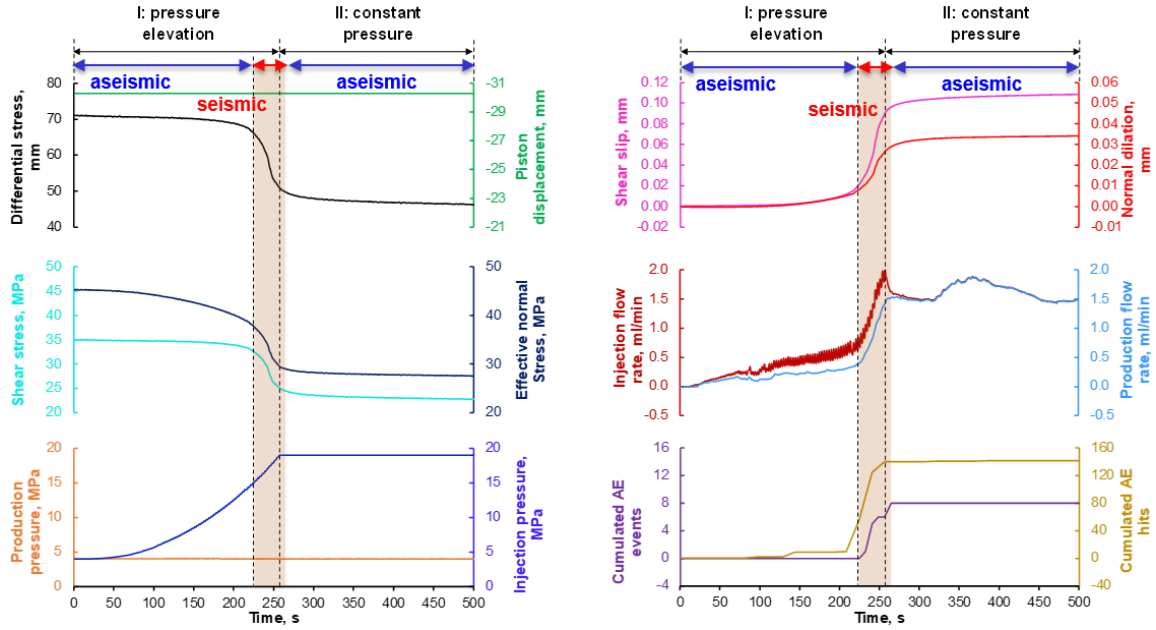


Figure 7.5: The seismo-hydro-mechanical response of sample EF #1 during injection-induced shear test: temporal evolution of the piston displacement (green), the effective normal stress (black), the shear stress (teal), the effective normal stress (dark-blue), the injection pressure (blue), the production pressure (orange), the fracture shear slip (pink), the fracture opening/normal dilation (red), the injection flow rate (dark-red), the production flow rate (light-blue), the cumulated AE hits (gold), and the cumulated AE events (purple) during the 500-s-long fluid injection.

In the injection test, the Eagle Ford shale sample experienced a fracture slip of 0.11 mm and a fracture dilation of 0.04 mm in the pressurization stage, corresponding with ~23 MPa relaxation in differential stress. Due to the dilatant fracture slip and propping by the asperities, a significant enhancement of flow rate was resulted. During the fracture shearing phase, 142 AE hits and 8 AE events were detected. As shown in Figure 7.6(b), the amplitudes of AE events are in the range of 53 dB to 72 dB. After filtering out some low energy events (Figure 7.6(a)), it is noticed that the microseismic events locate in a zone near the fracture plane. The AE events with higher amplitudes locate in the lower middle part of the sample, which is likely related to the area's high surface relief (see Figure 7.2(c)). These observations support the notion that the induced microseismicity is related to the energy release caused by the cut-off/abrasion of contacting asperities during fracture shearing by injection.

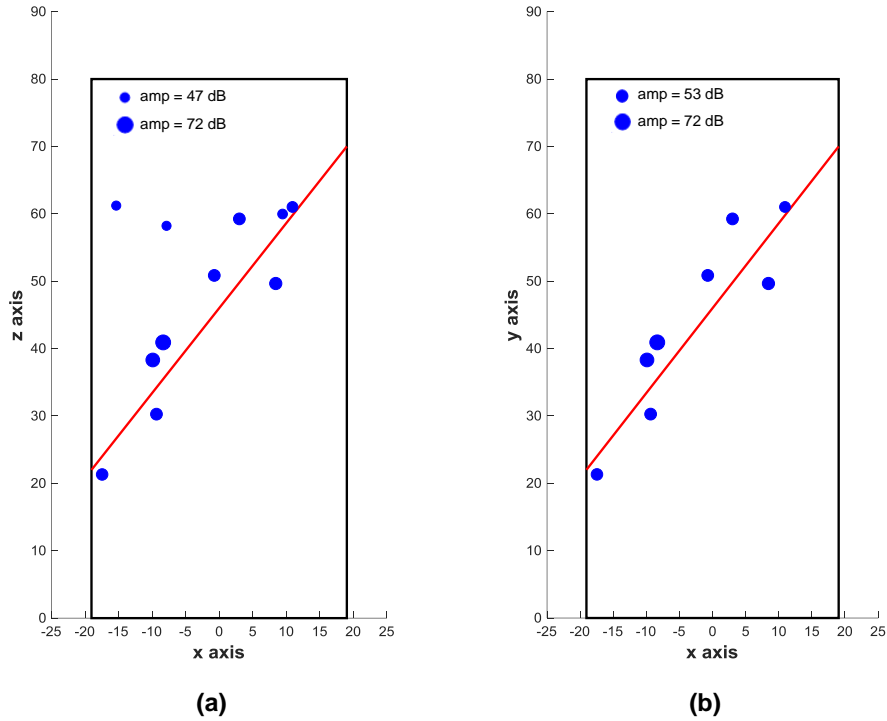


Figure 7.6: AE Location map: (a) before applying an AE amplitude filter; (b) after applying an AE amplitude filter. In the plots, the blue dots indicate the AE events (with different magnitudes), and the red line represents the pre-existing fracture. AE = Acoustic Emission.

7.5 Discussion

7.5.1 Permeability Enhancement by Dilatant Fracture Slip

In the shear test, we induced shear slip on a rough shale fracture by injection under a constant-piston displacement control. In this control mode, the differential stress can decrease in response to fracture slip during injection. The stress drop (frequently occurring in real fault/fracture reactivation) possibility in the test ensures the fracture shear displacement is in a reliable range when compared with the slow slip in shale reservoirs. Therefore, as can be seen in Figure 7.5, a small fracture slip (0.11 mm) on the rough shale fracture (sample EF #1) induced a significant flow rate enhancement. As demonstrated by the previous fluid flow tests on rock fractures (either shale or granite), without fracture shearing the flow rate would tend to linearly increase with the elevation of injection pressure

(e.g., Singh, Singh, & Ranjith, 2015; Ye, Janis, & Ghassemi, 2017). Therefore, the flow rate enhancement of sample EF #1 during fluid pressurization can be attributed to two factors: the increase of fracture aperture due to the decrease of the effective normal stress (resulting in the linear enhancement of flow rate); the rapid increase of the fracture aperture caused by the dilatant fracture slip (leading to nonlinear enhancement of flow rate).

In a meso-scale injection test on a 66-ft. long shale fault, Guglielmi et al. (2015) demonstrated that the hydraulic diffusivity of the fault was enhanced from $\sim 2 \times 10^{-8}$ to $\sim 10^{-4}$ ft²/s after a small shear slip (on the order of $\sim 10^{-4}$ ft.). Also, a nonlinear enhancement of flow rate along with the fault slip and dilation was observed. It is understood that shale fractures usually have small-size asperities and low asperity strength, and may not significantly support the fracture as in the granite fractures. However, observations in our laboratory experiments and also field tests (Guglielmi, Cappa, et al., 2015; Guglielmi, Elsworth, et al., 2015) provide a strong evidence that the dilatant shear slip of rough pre-existing fractures or newly-created tensile and mixed-mode fractures (Ye & Ghassemi, 2019). can enhance the permeability of unconventional shale reservoirs during hydraulic stimulation

7.5.2 Stress Control on Fracture Slip and Microseismicity

Mohr-Coulomb theory or Amontons' law of friction ($\tau = \mu \sigma'_n$, μ is the friction coefficient on the fracture plane) is widely used to determine the shear failure of pre-existing fractures/faults. According to this friction law, shear failure of pre-existing fracture(s) starts when the effective normal stress drops or the fluid pressure increases sufficiently to make the failure function ($CFF = \tau - \mu \sigma'_n$) approaching zero. During injection, the effective normal stress (σ'_n) and the corresponding critical shear stress $\tau_c = \mu \sigma'_n$ progressively decrease with the pore pressure elevation. Often, shear failure of pre-existing fractures/faults

is considered to be the sources of seismicity or microseismicity. To explore the control of stress/friction law on fracture slip and microseismicity in our test, measurements of shear stress (teal), injection pressure (blue), fracture shear slip (pink), cumulated AE hits (gold), AE rates (orange) and the production flow rate (dark-green) are plotted in Figure 7.7.

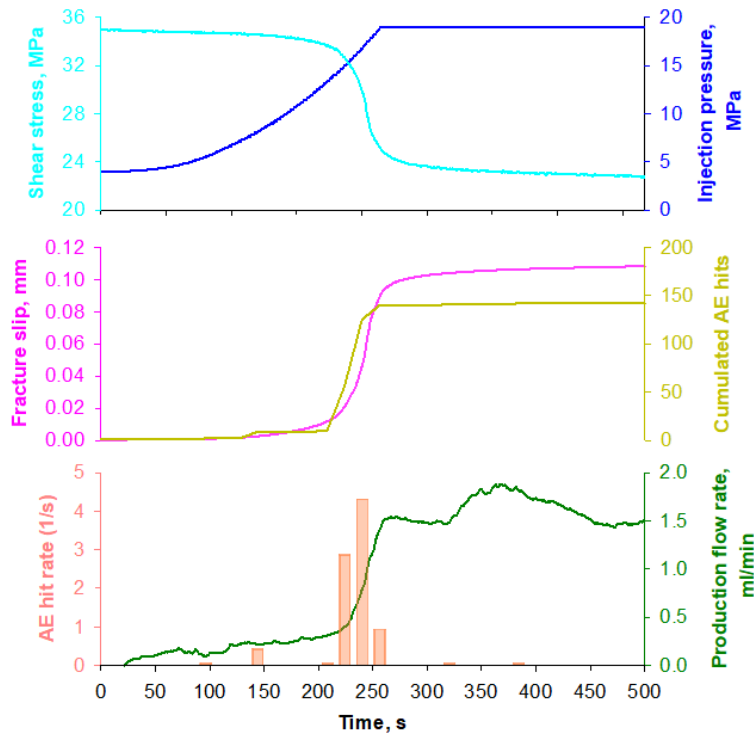


Figure 7.7: The temporal evolution plots of shear stress (teal), injection pressure (blue), fracture shear slip (pink), cumulated AE hits (gold), AE rates (orange) and the production flow rate (dark-green).

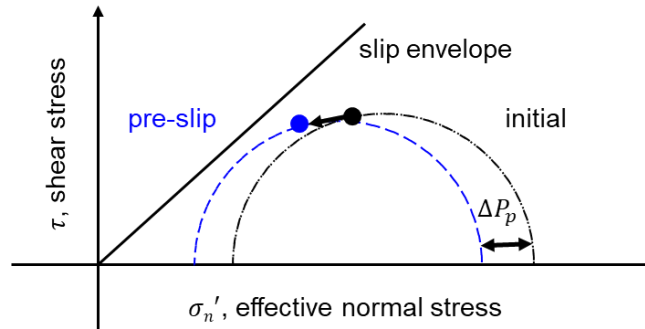
The profiles of shear stress, fracture shear slip and AE hits, the injection test can be divided into three stages each having a different stress state. In the first stage (pre-slip stage, from 0 to ~220 s in the Figure 7.7), the injection pressure was increased from 4 MPa to ~12 MPa, only a slight fracture shear motion was induced, corresponding a very small drop of shear stress. As a result, only a few AE events were detected. This could be related to the failure of a few secondary asperities and/or the increased contact area caused by the slight fracture motion. The linear and small flow rate increase is mainly caused by the fracture aperture increase in response to the lowering of the effective normal stress by injection. As

shown in Figure 7.8(a), after injection the Mohr circle moves leftward, and the diameter of the Mohr circle gradually decreases (at a small rate) in response to the elevation of the injection pressure. However, the circle does not touch the slip envelope yet. Therefore, significant fracture slip is not induced, and the slight motion on the fracture is aseismic.

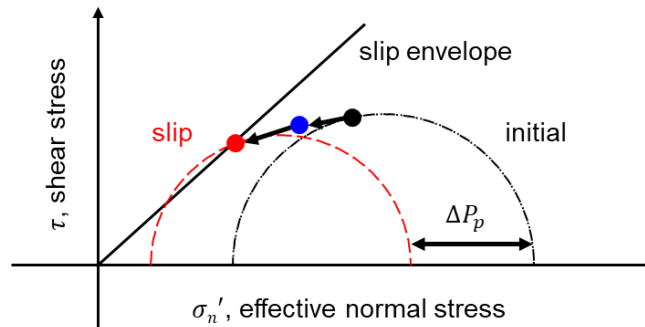
With further elevation of injection pressure, the test entered the seismic slip stage (at the interval from ~220 s to ~260 s in Figure 7.7) indicating by rapid increases of fracture slip, stress drop and AE hits. As a result of the large fracture slip, remarkable nonlinear increase of the production flow rate was induced. The stress stage of the seismic-slip stage also can be demonstrated by the Mohr-Coulomb theory (Figure 7.8(b)). The Mohr circle continually moved leftward with further increase of the injection pressure, fracture slip starts when Mohr circle touches the frictional slip. This means that the critical shear stress (τ_c) was reduced to the shear stress (τ) along the fracture plane by injection and CFR approached 0. Due to the large fracture slip, significant drop of shear stress was induced, indicating that the release of the strain energy stored in the fracture. Therefore, the AE hits increased a lot with high AE rates, and the fracture shear motion is seismic.

At the third stage of post slip (from ~260 s to 500 s in Figure 7.7), the injection pressure was kept as constant. Also, it is noticed that a large drop of shear stress caused by the rapid fracture slip in the seismic slip stage. Therefore, the stress state on fracture plane was not critical any more in the third, fracture slip slowed down and finally terminated at a lower stress level. Since, there was no more drop of shear stress, the fractured became *silent* again indicating by no more AE hits were triggered. The stress state of the post slip stage is demonstrated in Figure 7.8(c). Due to the large stress drop, the diameter of the Mohr circle decreases a lot, and the circle does not touch the frictional slip envelope. This means that

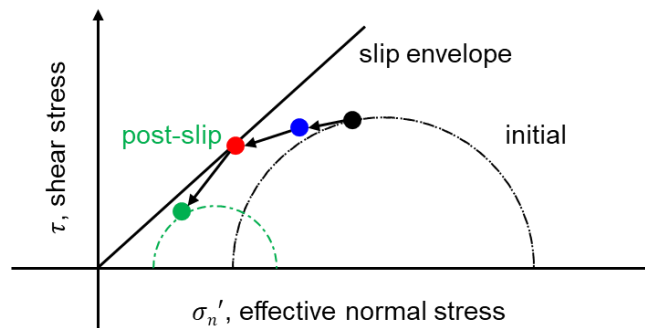
CFR is not close to 0 and the shear failure of the pre-existing fracture is not satisfied. Therefore, the fracture is in aseismic again unless there is stress re-accumulation or the further elevation of injection pressure.



(a)



(b)



(c)

Figure 7.8: Stress state on the fracture plane during injection: (a) pre-slip stage; (b) slip stage; (c) post-slip stage. In the figure, the black circle indicates the initial stress state, the blue circle indicates the stress state at pre-slip stage, the red circle indicates the stress state at slip stage, and the green circle indicates the stress state at post-slip stage.

7.5.3 The Slip-Seismicity-Permeability Relationship

During hydraulic stimulation in shale reservoirs, it is suggested that the microseismic cloud structure can be approximately related to the stimulated reservoir volume (SRV), i.e., where the rock mass may have failed in shear in response to pore pressure increase and/or stress perturbations around a hydraulic fracture (Rutledge & Phillips, 2003; Warpinski et al., 2004). Using the microseismic mapping data, it is also found that a larger SRV normally result in a better production performance (Fisher et al., 2004; Mayerhofer et al., 2010). The implication is that more microseismic activity probably indicates a higher permeability enhancement (caused by injection-induced fracture slip). However, the slip-seismicity-permeability evolution in fracture slip by injection is not well understood either in field studies or laboratory investigations. To our knowledge, no laboratory experiments have been conducted to directly explore the relationships of fracture slip and microseismicity, and permeability.

Figure 7.9(a) shows a plot of cumulated AE hits vs. fracture shear slip from the present injection test. The plot demonstrates that more AE hits are induced with the increase of fracture slip. Considering the microseismic activity is the result of a sudden energy release stored in the stressed sample, the positive correlation of microseismicity and fracture slip is reasonable because of the stress drop/energy release is directly resulted from fracture shear slip. Moreover, in Figure 7.9(b), it is also noticed that a similar positive-linear trend exists in the plot of fluid production vs. fracture shear slip: large fracture slip results in more production. The reason is that the increase of fracture aperture/normal dilation is mainly caused by the fracture shear slip. Figure 7.9(c) illustrates the relationship of production flow rate vs. cumulated AE events in the test. As can be expected, more AE hits indicate a better

production performance (higher production flow rate). In all three plots, the extremely high R-squared value represents a good linear fit of each group data. Therefore, the interpretation that more microseismicity induced by hydraulic fracturing generally indicates that a better production performance (or a high reservoir permeability) is reasonable.

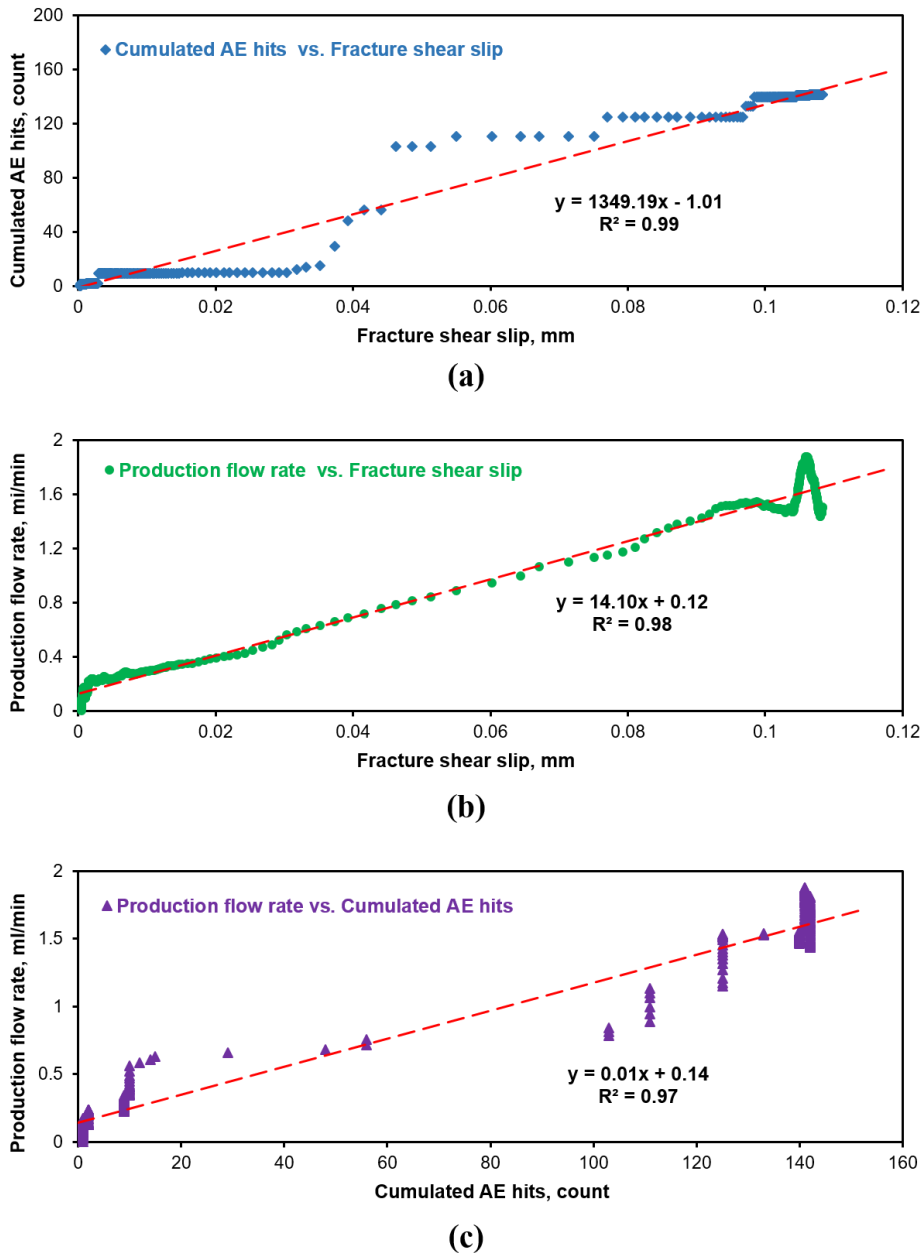


Figure 7.9: The relationships of fracture shear slip, cumulated AE hits, and production flow rate. (a) Cumulated AE hits vs. Fracture shear slip; (b) Production flow rate vs. Fracture shear slip; (c) Production flow rate vs. Cumulated AE hits. AE = Acoustic Emission.

7.5.4 Acoustic Emission/Microseismic Signature

As shown in Figure 7.5 and Figure 7.7, the fracture slip appears to have initiated at ~150 s, and the initiation of AE hits also occurred at ~150 s. On the other hand, the onset of micro-seismicity/AE events was started at ~220 s. This means that the early stage of the fracture slip may be aseismic. Considering the sample EF #1 had been loaded to a near-critical condition, the fracture slip should start shortly after the elevation of injection pressure, and the interpretation of aseismic slip occurrence prior to seismic slip is reasonable. The average slip rate in the aseismic interval is in the order of ~0.1 $\mu\text{m/s}$, while the slip rate in the seismic slip interval is up to ~5 $\mu\text{m/s}$. In another field injection test on a ~1600-ft. long carbonate fault, Guglielmi et al. (2015) observed that the onset of seismic slip was ~700 s later than the initiation of fault slip. They also note that an aseismic slip with a rate of 4 $\mu\text{m/s}$, while in the seismic slip interval the average slip rate was 23 $\mu\text{m/s}$. These observations suggest that there is a transition period from the aseismic slip to seismic slip during injection, and the transition is most likely controlled by the slip rate. In our previous work (Ye & Ghassemi, 2018), the results of fracture shear tests indicate that the stress-drop rate correlates well with the slip velocity: a faster fracture slip induces a quicker stress drop. Generally, seismic events with large magnitude have a high stress drop. Therefore, the interpretation that the transition of aseismic slip to seismic slip is accompanied by a transition of slip velocity /stress-drop rate is reasonable.

In the present test on the Eagle Ford shale fracture (sample EF #1), only a limited number of AE events (8 events) and hits (142 hits) were detected. While in a similar injection test we carried out on a Sierra White granite sample containing a rough tensile fracture, more than 500 AE events with high energy were monitored during injection-induced fracture

shearing. The evolution of friction coefficient with shear displacement in the shale test and in the granite test are illustrated in Figure 7.10, respectively. As can be seen, the Eagle Ford shale fracture shows a slip-strengthening behavior in which the friction coefficient increases from 0.85 to 0.94 during fracture slip, while the Sierra White granite fracture shows a slip-weakening behavior with friction coefficient decreases from 0.87 to 0.62 after fracture slip. This means that the Eagle Ford shale fracture experienced a stable slip during pressurization by fluid injection, while an unstable slip occurred on the Sierra White granite fracture. In general, unstable fracture slip likely leads to seismic fracture slip. The different features of the friction change during slip could explain why the fracture shearing in the shale sample was relatively “silent”.

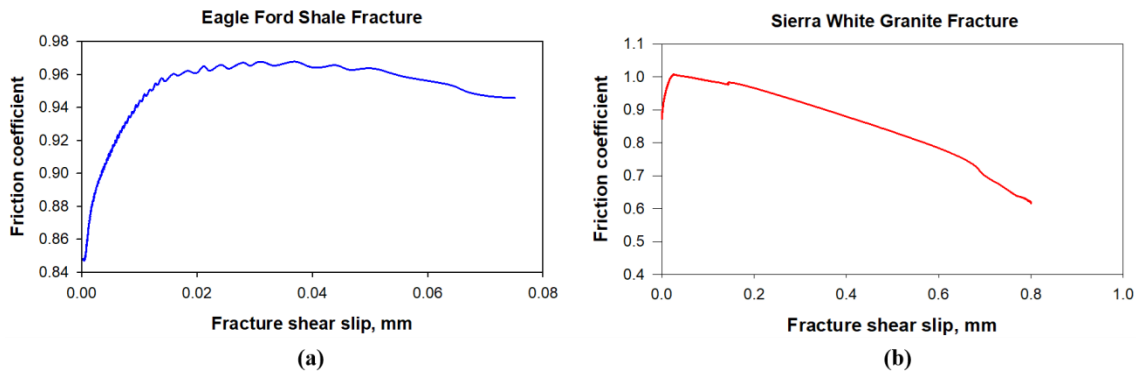


Figure 7.10: The evolution of friction coefficient with fracture shear slip in: (a) Eagle Ford shale having a rough tensile fracture (sample EF #1); (b) a Sierra White granite sample containing a rough tensile fracture.

7.6 Chapter Summary

Laboratory triaxial test with concurrent acoustic emission monitoring was conducted on a cylindrical Eagle Ford shale sample (having a single rough fracture, JRC=9.0) to characterize its seismo-hydro-mechanical response during fracture shearing by injection. Under a near-critical stress condition, a fracture slip of 0.11 mm (with a corresponding 0.04 mm fracture dilation) was induced on the 38.10 mm (1.5 in.) diameter shale sample by

elevating the injection pressure. As a result, a significant flow rate enhancement was achieved through the dilatant fracture slip. Rapid stress relaxation was noticed in response to the fracture slip, which indicates the energy release during the shear reactivation of the fracture. Meanwhile, it was found that the acoustic emission/microseismicity correlates well the fracture slip and the permeability evolution. In the aseismic interval, the fracture moved with a low slip rate (on the order of $\sim 0.1 \mu\text{m/s}$), and the corresponding stress relaxation and flow rate increase were limited. Due to the low stress relaxation, no AE events was detected in this interval. With the continuous elevation of the injection pressure, the fracture slip evolved into a seismic interval with a high slip rate (up to $\sim 5 \mu\text{m/s}$), resulting in rapid stress relaxation and a remarkable flow rate increase. The variations of slip rate in aseismic and seismic interval suggest that the aseismic/seismic transition may be related to the transition of fracture slip velocity. In addition, comparing with the microseismic signature in granite fractures, the fracture reactivation in the shales are relatively “silent”. This is likely related to the slip-strengthening of frictional properties during fracture shearing in shales.

Chapter 8

Conclusions

8.1 Conclusions of The Present Work

This dissertation presented a systematic experimental study to reveal the role of pre-existing fractures in reservoir stimulation and induced seismicity. Triaxial-injection shear tests with realistic stress and boundary conditions were conducted on granite fractures (Chapter 2) and shale fractures (Chapter 3). The results shown that retainable permeability increase caused by the irreversible dilation during fracture shearing can be achieved on both granite and shale fractures. In Chapter 4 and Chapter 5, the propagation and coalescence of pre-existing fractures due to fluid injection was probed as another important contributor of permeability enhancement during reservoir stimulation. The experimental results of injection-induced fracture slip test with concurrent acoustic emission monitoring in granite and shale were respectively described in Chapter 6 and Chapter 7. Based on the observations and results of these studies, the following conclusions were made.

Significant permeability increase caused by the irreversible dilation during fracture shearing can be achieved on both granite and shale fractures. In rough fracture tests, the enhanced permeability was retained on sheared fracture even during the depletion of fluid/reservoir pressure. While in smooth fracture tests, no or very little the enhanced permeability was retained after the depressurization of fluid pressure. This indicates that the self-propping of a fracture caused by shear-induced normal dilation is a key component of the success of shear stimulation. A *stick-slip* phenomenon was noticed during fracture shearing by injection. At early stage of pressurized fluid injection, the fracture tends to be in

a *stick* state with a slight fracture opening controlled by the decreasing effective normal stress, resulting in a limited permeability increase and a small stress drop. The fracture reaches a *slip* state with further elevation of the injection pressure. A rapid slip with an associated large stress drop is induced, creating a much larger enhancement of fracture permeability which is mainly caused by shear-induced normal dilation. Moreover, fracture slip correlates well with the associated stress relaxation: a faster fracture slip induces a quicker stress relaxation, and vice versa.

The propagation and coalescence of pre-existing fracture(s) was induced by pressurized fluid injection under a realistic stress condition. The results show that stressed pre-existing fracture(s) can be propagated as tensile, shear and/or mixed mode at injection pressures below the minimum principal stress. Stress conditions and rock heterogeneity are critical to the dominant form of the new fracture. Also, fracture networks and dominant flow paths can be formed by the coalescence of newly propagated cracks and pre-existing fractures, resulting in remarkable enhancement of permeability/fluid flow. This indicates that dilatant shear slip, tensile and shear propagation, and coalescence of pre-existing fractures are key and often concomitant mechanisms for permeability enhancement in fault/fracture reactivation by injection. In the granite test, the appearance of *horsetail* fracture demonstrates the creation of shear/mixed-mode secondary cracks. However, the secondary cracks were not induced on the test of the double-flawed Eagle Ford shale sample. The possible reason is that the granite with large grain size promotes the generation of shear-mode cracks, since macroscopic shear cracks are caused by the interactive growth of tensile cracks at suitable set of micro-flaws (e.g., grain boundaries). In addition, it is found that high confining stress tends to suppress the growth of the tensile wing cracks. Furthermore,

observations and results in this study also provide some insights on the contribution mechanisms to permeability evolution in the shallow crust.

Laboratory triaxial tests with concurrent acoustic emission monitoring were conducted on cylindrical granite and shale samples (each having a single rough fracture) to characterize their seismo-hydro-mechanical response during fracture shearing by injection. The tests reveal a transitional response during fracture shear slip namely, aseismic (or creeping) slip to seismic slip to aseismic slip during fluid injection. In the two creeping or aseismic intervals, the fracture sheared at a relatively low rate ($\sim 10^{-8}$ to 10^{-7} m/s), and very few or no acoustic emission events were triggered concomitant with small decline of the shear stress and slight enhancement of flow rate into the fracture. A significant number of acoustic emission events were detected in the seismic slip interval with a high slip rate (up to 10^{-4} m/s). The shear failure of the fracture occurred in the seismic slip stage, and was accompanied by a large stress drop and a dramatic fluid flow rate increase. In granite fracture test, a large number of AE events were detected corresponding with a frictional weakening during the dynamic slip interval (an analog of the earthquake instability). The spatio-temporal evolution of acoustic emission hypocenters demonstrates the existence of slip heterogeneity on the fracture plane and supports the notion that the accumulation of local asperity failure ultimately results in the global failure of entire fracture. Comparing AE distribution with the fracture surface topography shows that the integrated effect of fault/fracture surface roughness, and pressurized fluid injection on promoting slip heterogeneity during fault/fracture reactivation by injection. On the other hand, the fracture reactivation in the shales are relatively “silent” with a limited number of AE events, which

is likely related to the slip-strengthening of frictional properties during fracture shearing in shales.

8.2 Original Contributions

In this dissertation, I focused on revealing the role of pre-existing fractures in reservoir stimulation and induced seismicity through novel experimental investigation. The original contributions of this dissertation research are briefly summarized as:

1. To capture the stress drop relaxation associated with the episodes of fault/fracture reactivation and seismicity, a constant piston-displacement control mode is proposed. In which the actuator piston is fixed without movement during fluid injection, but the fracture slip/deformation is not restricted. As a result, stress drop occurs because the compression on the sample by actuator piston drops in response to fracture motion (either caused by fracture slip or fracture propagation or both), and the fracture motion slows down and finally ends at a lower stress level. The assumption of this experimental control is that the deformation of the overburden (the piston) at a distance far from the fluid injection zone is negligible, while the energy stored into the reservoir rocks can release during fault/fracture reactivation. To our knowledge, the constant piston-displacement control is the first realistic boundary control in triaxial test which can reveal an evolving stress drop during fault/fracture reactivation, and can be used for the corresponding AE (seismicity) interpretation.
2. Most previous laboratory shear-flow tests on rock fractures have focused on force-driven fracture slip or have manually displaced the fractured specimen to represent fracture slip. In this research, a novel triaxial shear test was proposed

to induce fracture shear slip by elevating injection pressure. Moreover, a step-wise injection scenario was used to evaluate the steady-flow fluid flow in the rough-walled rock fracture. In the test, the fully coupled hydro-mechanical properties of rock fracture in response to fluid injection were characterized to probe permeability evolution and slip characteristics during fracture shearing.

3. Since Griffith's theory in brittle fracture, extensive experimental studies have been carried out to investigate the cracking development (the process of crack initiation, propagation and coalescence) of pre-existing fracture(s) in artificial or rock materials. However, almost all these experimental studies were carried out under uniaxial/biaxial compression, without addressing the effect of fluid injection on the propagation of pre-existing fractures. Also, in these tests, the propagation and coalescence of pre-existing fractures were induced via elevating the mechanical load without confining stress (in uniaxial compression) or with a low confining stress (in biaxial compression). Although the observations in these experiments can benefit the near-surface engineering practices (e.g. tunnel design, rock slope stability, etc.), they are not representative for subsurface rock mass at depth where confining stresses prevail and where fracture propagation is usually induced by pressurized fluid injection. This dissertation presented an injection-induced fracture test to induce the propagation and coalescence of pre-existing fractures by injection under a realistic triaxial stress loading. The results demonstrated that pre-existing fracture can be propagated as tensile, shear or mixed-mode by fluid injection.

4. Injection-induced fracture slip can trigger microseismicity. But, the mechanisms underlying induced seismicity are poorly understood. In the laboratory, some experiments induced the shear slip of pre-existing fracture by fluid injection but without concurrent acoustic emission (AE) monitoring. On the other hand, some experiments studied the signature of acoustic emission/microseismicity during fracture shearing, however, the fracture slip was not produced by pressurized fluid injection but through elevating the differential stress. Yet, most of these previous laboratory studies have not incorporated the full seismo-hydro-mechanical coupling, and the injection-induced fracture shear experiments with concurrent AE monitoring are rare. In this dissertation, the injection-induced fracture slip test with concurrent acoustic emission monitoring was conducted on granite or shale fractures. The fully coupled seismo-hydro-mechanical measurements were achieved to explore the microseismic signature along with fracture slip during injection.
5. The injection tests in this dissertation demonstrate a transitional response during fracture shear slip namely, aseismic (or creeping) slip to seismic slip to aseismic slip during fluid injection. The aseismic-seismic slip transition is accompanied by a slip acceleration from creeping slip to seismic slip. The dynamic slip in the experiment controlled by friction weakening is similar to natural earthquake instability.

8.3 Suggestions for Future Research

For subsurface engineering practices, many issues related to the deformation, failure, fluid transport, and seismic response of naturally fractured reservoirs still remain enigmatic.

Extensions of this Ph.D. dissertation research may include the following aspects:

1. The mechanical response of sealed fractures (e.g. filled fractures, foliations, veins) and their permeability change during hydraulic injection.
2. The influence of fluid viscosity on the propagation and coalescence of pre-existing fracture(s) at low injection pressure stimulation.
3. Crack devolvement from pre-existing fracture(s) under true-triaxial stress.

REFERENCES

- AlDajani, O. A., Morgan, S. P., Germaine, J. T. et al. 2017. Vaca Muerta Shale – Basic Properties, Specimen Preparation, and Fracture Processes. Presented at the 51st US Rock Mechanics/Geomechanics Symposium, San Francisco, California, USA.
- Amann, F., Gischig, V., Evans, K., Doetsch, J., Jalali, R., Valley, B., . . . Brixel, B. (2018). The seismo-hydronechanical behavior during deep geothermal reservoir stimulations: open questions tackled in a decameter-scale in situ stimulation experiment. *Solid Earth*, 9(1), 115.
- Ashby, M. F., & Hallam, S. D. (1986). The failure of brittle solids containing small cracks under compressive stress states. *Acta Metallurgica*, 34(3), 497-510. doi:[https://doi.org/10.1016/0001-6160\(86\)90086-6](https://doi.org/10.1016/0001-6160(86)90086-6)
- ASTM, A. (2015). *standard guide for determining the reproducibility of acoustic emission sensor response, 1994*. Paper presented at the American society for testing and materials.
- Bakshi, R., Halvaei, M. E., & Ghassemi, A. (2016). *Injection Experiments on Basaltic Tuffs under Triaxial and Heated Conditions with Acoustic Emissions Monitoring*. Paper presented at the 50th U.S. Rock Mechanics/Geomechanics Symposium, Houston, Texas, USA.
- Baria, R., Baumgärtner, J., Rummel, F., Pine, R. J., & Sato, Y. (1999). HDR/HWR reservoirs: concepts, understanding and creation. *Geothermics*, 28(4–5), 533-552, doi:10.1016/S0375-6505(99)00045-0.
- Barton, N. (1973). Review of a new shear-strength criterion for rock joints. *Engineering Geology*, 7(4), 287-332, doi: 10.1016/0013-7952(73)90013-6.
- Bauer, S. J., Huang, K., Chen, Q., Ghassemi, A., & Barrow, P. (2016). *Experimental and Numerical Investigation of Hydro-Thermally Induced Shear Stimulation*. Paper presented at the 50th U.S. Rock Mechanics/Geomechanics Symposium, Houston, Texas, USA.
- Beugelsdijk, L. J. L., de Pater, C. J., and Sato, K. 2000. Experimental Hydraulic Fracture Propagation in a Multi-Fractured Medium. Presented at the SPE Asia Pacific Conference on Integrated Modelling for Asset Management, Yokohama, Japan.
- Blanpied, M. L., Lockner, D. A., & Byerlee, J. D. (1995). Frictional slip of granite at hydrothermal conditions. *Journal of Geophysical Research: Solid Earth*, 100(B7), 13045-13064, doi:10.1029/95JB00862.
- Bobet, A., & Einstein, H. H. (1998). Fracture coalescence in rock-type materials under uniaxial and biaxial compression. *International Journal of Rock Mechanics and Mining Sciences*, 35(7), 863-888. [https://doi.org/10.1016/S0148-9062\(98\)00005-9](https://doi.org/10.1016/S0148-9062(98)00005-9)

- Brace, W. F. (1961). *Dependence of Fracture Strength of Rocks on Grain Size*. Paper presented at the 4th U.S. Symposium on Rock Mechanics (USRMS), University Park, Pennsylvania, USA.
- Brace, W. F., & Bombolakis, E. G. (1963). A note on brittle crack growth in compression. *Journal of Geophysical Research*, 68(12), 3709-3713. doi:10.1029/JZ068i012p03709
- Brenguier, F., Campillo, M., Hadziioannou, C., Shapiro, N. M., Nadeau, R. M., & Larose, E. (2008). Postseismic Relaxation Along the San Andreas Fault at Parkfield from Continuous Seismological Observations. *Science*, 321(5895), 1478-1481. doi:10.1126/science.1160943
- Caine, J. S., Evans, J. P., & Forster, C. B. (1996). Fault zone architecture and permeability structure. *Geology*, 24(11), 1025-1028. doi:10.1130/0091-7613(1996)024<1025:fzaaps>2.3.co;2
- Chen, Z., Narayan, S., Yang, Z., & Rahman, S. (2000). An experimental investigation of hydraulic behaviour of fractures and joints in granitic rock. *International Journal of Rock Mechanics and Mining Sciences*, 37(7), 1061-1071, doi:10.1016/S1365-1609(00)00039-3.
- Cheng, Q., & Ghassemi, A. (2016). *Numerical Modeling of Newberry EGS Stimulation*. Paper presented at the 50th U.S. Rock Mechanics/Geomechanics Symposium, Houston, Texas, USA.
- Cheng, Q., Wang, X., & Ghassemi, A. (2019). Numerical simulation of reservoir stimulation with reference to the Newberry EGS. *Geothermics*, 77, 327-343. doi:https://doi.org/10.1016/j.geothermics.2018.09.011
- Clarke, H., Eisner, L., Styles, P., & Turner, P. (2014). Felt seismicity associated with shale gas hydraulic fracturing: The first documented example in Europe. *Geophysical Research Letters*, 41(23), 8308-8314. doi:10.1002/2014gl062047
- Cook, N. G. W., & Hojem, J. P. M. (1966). A rigid 50-ton compression and tension testing machine. *Journal of the Southern African Institute of Mining and Metallurgy*, 1, 89-92.
- Cornet, F. H., & Yin, J. (1995). Analysis of induced seismicity for stress field determination and pore pressure mapping. *pure and applied geophysics*, 145(3), 677-700, doi:10.1007/bf00879595.
- Cornet, F., Bérard, T., & Bourouis, S. (2007). How close to failure is a granite rock mass at a 5 km depth? *International Journal of Rock Mechanics and Mining Sciences*, 44(1), 47-66. https://doi.org/10.1016/j.ijrmms.2006.04.008

- Crandall, Dustin, Moore, Johnathan, Gill, Magdalena et al. 2017. CT scanning and flow measurements of shale fractures after multiple shearing events. *International Journal of Rock Mechanics and Mining Sciences* 100: 177-187.
- Crawford, B. R., Tsenn, M. C., Homburg, J. M., Stehle, R. C., Freysteinson, J. A., & Reese, W. C. (2017). Incorporating Scale-Dependent Fracture Stiffness for Improved Reservoir Performance Prediction. *Rock Mechanics and Rock Engineering*, 50(12), 3349-3359, doi:10.1007/s00603-017-1314-z.
- Cruikshank, K. M., Zhao, G., & Johnson, A. M. (1991). Analysis of minor fractures associated with joints and faulted joints. *Journal of Structural Geology*, 13(8), 865-886. [https://doi.org/10.1016/0191-8141\(91\)90083-U](https://doi.org/10.1016/0191-8141(91)90083-U)
- Deichmann, N., & Giardini, D. (2009). Earthquakes Induced by the Stimulation of an Enhanced Geothermal System below Basel (Switzerland). *Seismological Research Letters*, 80(5), 784-798. doi:10.1785/gssrl.80.5.784
- Durham, W. B., & Bonner, B. P. (1994). Self-propping and fluid flow in slightly offset joints at high effective pressures. *Journal of Geophysical Research: Solid Earth*, 99(B5), 9391-9399, doi:10.1029/94JB00242.
- Ellsworth, W. L. (2013). Injection-Induced Earthquakes. *Science*, 341(6142). <https://doi.org/10.1126/science.1225942>
- Esaki, T., Du, S., Mitani, Y., Ikusada, K., & Jing, L. (1999). Development of a shear-flow test apparatus and determination of coupled properties for a single rock joint. *International Journal of Rock Mechanics and Mining Sciences*, 36(5), 641-650, doi:10.1016/S0148-9062(99)00044-3.
- Esaki, T., Hojo, H., Kimura, T., & Kameda, N. (1991). *Shear-flow coupling test on rock joints*. Paper presented at the 7th ISRM Congress, Aachen, Germany.
- Evans, J. P., Forster, C. B., & Goddard, J. V. (1997). Permeability of fault-related rocks, and implications for hydraulic structure of fault zones. *Journal of Structural Geology*, 19(11), 1393-1404. [https://doi.org/10.1016/S0191-8141\(97\)00057-6](https://doi.org/10.1016/S0191-8141(97)00057-6)
- Evans, K. F. (2005). Permeability creation and damage due to massive fluid injections into granite at 3.5 km at Soultz: 2. Critical stress and fracture strength. *Journal of Geophysical Research: Solid Earth*, 110(B4). <https://doi.org/10.1029/2004JB003169>
- Evans, K. F., Genter, A., & Sausse, J. (2005). Permeability creation and damage due to massive fluid injections into granite at 3.5 km at Soultz: 1. Borehole observations. *Journal of Geophysical Research: Solid Earth*, 110(B4), doi:10.1029/2004JB003168.

- Fang, Y., Elsworth, D., Wang, C., Ishibashi, T., & Fitts, J. P. (2017). Frictional stability-permeability relationships for fractures in shales. *Journal of Geophysical Research: Solid Earth*, 122(3), 1760-1776, doi:10.1002/2016JB013435.
- Farmahini-Farahani, M., & Ghassemi, A. (2016). Simulation of micro-seismicity in response to injection/production in large-scale fracture networks using the fast multipole displacement discontinuity method (FMDDM). *Engineering Analysis with Boundary Elements*, 71, 179-189, doi:10.1016/j.enganabound.2016.07.004.
- Fisher, M. K., Heinze, J. R., Harris, C. D., Davidson, B. M., Wright, C. A., & Dunn, K. P. (2004). *Optimizing Horizontal Completion Techniques in the Barnett Shale Using Microseismic Fracture Mapping*. Paper presented at the SPE Annual Technical Conference and Exhibition, Houston, Texas. <https://doi.org/10.2118/90051-MS>
- French, M. E., Wenlu, Z., & Jeremy, B. (2016). Fault slip controlled by stress path and fluid pressurization rate. *Geophysical Research Letters*, 43(9), 4330-4339. doi:doi:10.1002/2016GL068893
- Gao, Y., & Crampin, S. (2004). Observations of stress relaxation before earthquakes. *Geophysical Journal International*, 157(2), 578-582, doi: 10.1111/j.1365-246X.2004.02207.x.
- Ghassemi, A. (2012). A Review of Some Rock Mechanics Issues in Geothermal Reservoir Development. *Geotechnical and Geological Engineering*, 30(3), 647-664, doi:10.1007/s10706-012-9508-3.
- Ghassemi, A. and Zhou, X. (2011). A three-dimensional thermo-poroelastic model for fracture response to injection/extraction in enhanced geothermal systems. *Geothermics* 40 (1): 39-49.
- Ghassemi, A., Zhou, X. X., & Rawal, C. (2013). A three-dimensional poroelastic analysis of rock failure around a hydraulic fracture. *Journal of Petroleum Science and Engineering*, 108, 118-127. <https://doi.org/10.1016/j.petrol.2013.06.005>
- Gischig, V. S., & Preisig, G. (2015). *Hydro-Fracturing Versus Hydro-Shearing: A Critical Assessment of Two Distinct Reservoir Stimulation Mechanisms*. Paper presented at the 13th ISRM International Congress of Rock Mechanics, Montreal, Canada.
- Goebel, T. H. W., Becker, T. W., Schorlemmer, D., Stanchits, S., Sammis, C., Rybacki, E., & Dresen, G. (2012). Identifying fault heterogeneity through mapping spatial anomalies in acoustic emission statistics. *Journal of Geophysical Research: Solid Earth*, 117(B3), doi:10.1029/2011JB008763.
- Goebel, T., Candela, T., Sammis, C., Becker, T., Dresen, G., & Schorlemmer, D. (2013). Seismic event distributions and off-fault damage during frictional sliding of saw-cut surfaces with pre-defined roughness. *Geophysical Journal International*, 196(1), 612-625.

- Gonçalves da Silva, B., & Einstein, H. (2018). Physical processes involved in the laboratory hydraulic fracturing of granite: Visual observations and interpretation. *Engineering Fracture Mechanics*, 191, 125-142. <https://doi.org/10.1016/j.engfracmech.2018.01.011>
- Goncalves da Silva, B., Li, B. Q., Moradian, Z. et al. (2015). Development of a Test Setup Capable of Producing Hydraulic Fracturing in the Laboratory with Image and Acoustic Emission Monitoring. Presented at the 49th US Rock Mechanics/Geomechanics Symposium, San Francisco, California, USA.
- Granier, T. (1985). Origin, damping, and pattern of development of faults in granite. *Tectonics*, 4(7), 721-737. <https://doi.org/10.1029/TC004i007p00721>
- Gu, Hongren, Weng, Xiaowei, Lund, Jeffrey B et al. (2012). Hydraulic fracture crossing natural fracture at nonorthogonal angles: a criterion and its validation. *SPE Production & Operations* 27 (01): 20-26.
- Gudmundsson, A. (2000). Active fault zones and groundwater flow. *Geophysical Research Letters*, 27(18), 2993-2996.
- Guglielmi, Y., Cappa, F., Avouac, J.-P., Henry, P., & Elsworth, D. (2015a). Seismicity triggered by fluid injection–induced aseismic slip. *Science*, 348(6240), 1224-1226, doi: 10.1126/science.aab0476.
- Guglielmi, Y., Elsworth, D., Cappa, F., Henry, P., Gout, C., Dick, P., & Durand, J. (2015b). In situ observations on the coupling between hydraulic diffusivity and displacements during fault reactivation in shales. *Journal of Geophysical Research: Solid Earth*, 120(11), 7729-7748, doi:10.1002/2015JB012158.
- Gutierrez, M, Øino, LE, and Nygaard, Runar. 2000. Stress-dependent permeability of a de-mineralised fracture in shale. *Marine and Petroleum Geology* 17 (8): 895-907.
- Hoek, E., & Bieniawski, Z. T. (1965). Brittle fracture propagation in rock under compression. *International Journal of Fracture Mechanics*, 1(3), 137-155. doi:10.1007/bf00186851
- Hofmann, H., Blöcher, G., Milsch, H., Babadagli, T., & Zimmermann, G. (2016). Transmissivity of aligned and displaced tensile fractures in granitic rocks during cyclic loading. *International Journal of Rock Mechanics and Mining Sciences*, 87, 69-84, doi:10.1016/j.ijrmms.2016.05.011.
- Homand, F., Belem, T., & Souley, M. (2001). Friction and degradation of rock joint surfaces under shear loads. *International Journal for Numerical and Analytical Methods in Geomechanics*, 25(10), 973-999, doi:10.1002/nag.163.
- Horii, H., & Nemat-Nasser, S. (1986). Brittle failure in compression: splitting faulting and brittle-ductile transition. *Phil. Trans. R. Soc. Lond. A*, 319(1549), 337-374. <https://doi.org/10.1098/rsta.1986.0101>

- Hu, L., Ghassemi, A., Pritchett, J. et al. (2016). *Laboratory Scale Investigation of Enhanced Geothermal Reservoir Stimulation. Proc., 50th US Rock Mechanics/Geomechanics Symposium*, Houston, Texas, USA.
- Huang, K., Zhang, Z., & Ghassemi, A. (2013). Modeling three-dimensional hydraulic fracture propagation using virtual multidimensional internal bonds. *International Journal for Numerical and Analytical Methods in Geomechanics*, 37(13), 2021-2038, doi:10.1002/nag.2119.
- Huang, K., Zhang, Z., & Ghassemi, A. (2013). Modeling three-dimensional hydraulic fracture propagation using virtual multidimensional internal bonds. *International Journal for Numerical and Analytical Methods in Geomechanics*, 37(13), 2021-2038. <https://doi.org/10.1002/nag.2119>
- Huang, X., Haimson, B. C., Plesha, M. E., & Qiu, X. (1993). An investigation of the mechanics of rock joints—Part I. Laboratory investigation. *International Journal of Rock Mechanics and Mining Sciences & Geomechanics Abstracts*, 30(3), 257-269, doi:10.1016/0148-9062(93)92729-A.
- Hudson, J. A., Crouch, S. L., & Fairhurst, C. (1972). Soft, stiff and servo-controlled testing machines: a review with reference to rock failure. *Engineering Geology*, 6(3), 155-189. [https://doi.org/10.1016/0013-7952\(72\)90001-4](https://doi.org/10.1016/0013-7952(72)90001-4)
- Hutson, R. W., & Dowding, C. H. (1990). Joint asperity degradation during cyclic shear. *International Journal of Rock Mechanics and Mining Sciences & Geomechanics Abstracts*, 27(2), 109-119, doi: 10.1016/0148-9062(90)94859-R.
- Ingebritsen, S. E., & Manning, C. E. (2010). Permeability of the continental crust: dynamic variations inferred from seismicity and metamorphism. *Geofluids*, 10(1-2), 193-205. doi:10.1111/j.1468-8123.2010.00278.x
- Ishibashi, T., Asanuma, H., Fang, Y., Wang, C., & Elsworth, D. (2016). *Exploring the Link between Permeability and Strength Evolution during Fracture Shearing*. Paper presented at the 50th U.S. Rock Mechanics/Geomechanics Symposium, Houston, Texas, USA.
- Jang, H.-S., Kang, S.-S., & Jang, B.-A. (2014). Determination of joint roughness coefficients using roughness parameters. *Rock Mechanics and Rock Engineering*, 47(6), 2061-2073, doi:10.1007/s00603-013-0535-z.
- Javadi, M., Sharifzadeh, M., Shahriar, K., & Mitani, Y. (2014). Critical Reynolds number for nonlinear flow through rough-walled fractures: The role of shear processes. *Water Resources Research*, 50(2), 1789-1804, doi:10.1002/2013WR014610.
- Julian, B. R., Miller, A. D., & Foulger, G. R. (1998). Non-double-couple earthquakes 1. Theory. *Reviews of Geophysics*, 36(4), 525-549. <https://doi.org/10.1029/98RG00716>

- Jung, R. (2013). EGS — Goodbye or Back to the Future 95. In A. P. Bunger, J. McLennan, & R. Jeffrey (Eds.), *Effective and Sustainable Hydraulic Fracturing* (pp. Ch. 05). Rijeka: InTech.
- Kamali, A., & Ghassemi, A. (2018). Analysis of injection-induced shear slip and fracture propagation in geothermal reservoir stimulation. *Geothermics*, 76, 93-105. <https://doi.org/10.1016/j.geothermics.2018.07.002>
- Kato, N., Ohtake, M., & Hirasawa, T. (1997). Possible mechanism of precursory seismic quiescence: Regional stress relaxation due to preseismic sliding. *pure and applied geophysics*, 150(2), 249-267, doi:10.1007/s000240050075.
- Kato, N., Ohtake, M., & Hirasawa, T. (1997). Possible Mechanism of Precursory Seismic Quiescence: Regional Stress Relaxation due to Preseismic Sliding. *pure and applied geophysics*, 150(2), 249-267. doi:10.1007/s000240050075
- Keranen, K. M., Weingarten, M., Abers, G. A., Bekins, B. A., & Ge, S. (2014). Sharp increase in central Oklahoma seismicity since 2008 induced by massive wastewater injection. *Science*, 345(6195), 448-451, doi:10.1126/science.1255802.
- Kim, K.-H., Ree, J.-H., Kim, Y., Kim, S., Kang, S. Y., & Seo, W. (2018). Assessing whether the 2017 Mw 5.4 Pohang earthquake in South Korea was an induced event. *Science*, eaat6081. doi:10.1126/science.aat6081
- Kim, W.-Y. (2013). Induced seismicity associated with fluid injection into a deep well in Youngstown, Ohio. *Journal of Geophysical Research: Solid Earth*, 118(7), 3506-3518, doi:10.1002/jgrb.50247.
- Kovari, K., Tisa, A., Einstein, H., & Franklin, J. (1983). Suggested methods for determining the strength of rock materials in triaxial compression: revised version. *Intl J of Rock Mech & Mining Sci & Geomechanics*, 20(6), doi:10.1016/0148-9062(83)90598-3.
- Kwiatek, G., Goebel, T. H. W., & Dresen, G. (2014). Seismic moment tensor and b value variations over successive seismic cycles in laboratory stick-slip experiments. *Geophysical Research Letters*, 41(16), 5838-5846. doi:doi:10.1002/2014GL060159
- Lee, H. S., Park, Y. J., Cho, T. F., & You, K. H. (2001). Influence of asperity degradation on the mechanical behavior of rough rock joints under cyclic shear loading. *International Journal of Rock Mechanics and Mining Sciences*, 38(7), 967-980, doi:10.1016/S1365-1609(01)00060-0.
- Lee, H., & Jeon, S. (2011). An experimental and numerical study of fracture coalescence in pre-cracked specimens under uniaxial compression. *International Journal of Solids and Structures*, 48(6), 979-999. <https://doi.org/10.1016/j.ijsolstr.2010.12.001>.

- Lei, X., Li, S., & Liu, L. (2018). Seismic b-Value for Foreshock AE Events Preceding Repeated Stick-Slips of Pre-Cut Faults in Granite. *Applied Sciences*, 8(12), 2361. <https://doi.org/10.3390/app8122361>.
- Li, B., Jiang, Y., Koyama, T., Jing, L., & Tanabashi, Y. (2008). Experimental study of the hydro-mechanical behavior of rock joints using a parallel-plate model containing contact areas and artificial fractures. *International Journal of Rock Mechanics and Mining Sciences*, 45(3), 362-375, doi:10.1016/j.ijrmms.2007.06.004.
- Li, B. Q., & Einstein, H. H. (2019). Direct and Microseismic Observations of Hydraulic Fracturing in Barre Granite and Opalinus Clayshale. *Journal of Geophysical Research: Solid Earth*. doi:10.1029/2019jb018376
- Li, Y., Wang, J., Jung, W., & Ghassemi, A. (2012). Mechanical properties of intact rock and fractures in welded tuff from Newberry Volcano. In *Proceedings of 37th Workshop on Geothermal Reservoir Engineering, Stanford, CA* (Vol. 30).
- Liu, Y., Dai, F., Dong, L., Xu, N., & Feng, P. (2018). Experimental Investigation on the Fatigue Mechanical Properties of Intermittently Jointed Rock Models Under Cyclic Uniaxial Compression with Different Loading Parameters. *Rock Mechanics and Rock Engineering*, 51(1), 47-68. doi:10.1007/s00603-017-1327-7
- Lockner, D. A., & Byerlee, J. D. (1994). Dilatancy in hydraulically isolated faults and the suppression of instability. *Geophysical Research Letters*, 21(22), 2353-2356, doi:10.1029/94GL02366.
- Majer, E. L., Baria, R., Stark, M., Oates, S., Bommer, J., Smith, B., & Asanuma, H. (2007). Induced seismicity associated with Enhanced Geothermal Systems. *Geothermics*, 36(3), 185-222, doi: 10.1016/j.geothermics.2007.03.003.
- Maxwell, S. C., Rutledge, J., Jones, R., & Fehler, M. (2010). Petroleum reservoir characterization using downhole microseismic monitoring. *Geophysics*, 75(5), 75A129-175A137. doi:10.1190/1.3477966
- Mayerhofer, M. J., Lolon, E., Warpinski, N. R., Cipolla, C. L., Walser, D. W., & Rightmire, C. M. (2010). What Is Stimulated Reservoir Volume? *SPE Production & Operations*, 25(01), 89-98. doi:10.2118/119890-PA
- Mayerhofer, M., Richardson, M., Walker Jr, R., Meehan, D., Oehler, M., & Browning Jr, R. (1997). *Proppants? We don't need no proppants*. Paper presented at the SPE Annual Technical Conference and Exhibition.
- McLaskey, G. C., & Lockner, D. A. (2016). Calibrated Acoustic Emission System Records M -3.5 to M -8 Events Generated on a Saw-Cut Granite Sample. *Rock Mechanics and Rock Engineering*, 49(11), 4527-4536. doi:10.1007/s00603-016-1082-1

- Miller, A. D., Foulger, G., & Julian, B. R. (1998). Non-double-couple earthquakes 2. Observations. *Reviews of Geophysics*, 36(4), 551-568. <https://doi.org/10.1029/98RG00717>
- Miller, J. T., & Einstein, H. H. (2008). *Crack Coalescence Tests on Granite*. Paper presented at the The 42nd U.S. Rock Mechanics Symposium (USRMS), San Francisco, California, USA.
- Min, K. S., Zhang, Z., & Ghassemi, A. (2010). *Numerical Analysis of Multiple Fracture Propagation In Heterogeneous Rock*. Paper presented at the 44th U.S. Rock Mechanics Symposium and 5th U.S.-Canada Rock Mechanics Symposium, Salt Lake City, Utah, USA.
- Misra, S., Mandal, N., Dhar, R., & Chakraborty C. (2009). Mechanisms of deformation localization at the tips of shear fractures: Findings from analogue experiments and field evidence. *Journal of Geophysical Research: Solid Earth*, 114(B4). <https://doi.org/10.1029/2008JB005737>
- Moradian, Z., Li, Q., Morgan, S., da Silva, G., Germaine, J., & Einstein, H. (2015). *Acoustic emission characteristics of shale*. Paper presented at the 13th ISRM International Congress of Rock Mechanics.
- Morgan, S., Li, B., & Einstein, H. (2017). *Effect of Injection Rate on Hydraulic Fracturing of Opalinus Clay Shale*. Paper presented at the 51st US Rock Mechanics/Geomechanics Symposium, San Francisco, California, USA.
- Morgan, S.. 2015. *An experimental and numerical study on the fracturing processes in Opalinus shale*, Massachusetts Institute of Technology, Department of Civil and Environmental Engineering.
- Mughieda, O., & Karasneh, I. (2006). Coalescence of offset rock joints under biaxial loading. *Geotechnical & Geological Engineering*, 24(4), 985. doi:10.1007/s10706-005-8352-0
- Murphy, H., Brown, D., Jung, R., Matsunaga, I., & Parker, R. (1999). Hydraulics and well testing of engineered geothermal reservoirs. *Geothermics*, 28(4-5), 491-506. [https://doi.org/10.1016/S0375-6505\(99\)00025-5](https://doi.org/10.1016/S0375-6505(99)00025-5)
- Nemat-Nasser, S., & Horii, H. (1982). Compression-induced nonplanar crack extension with application to splitting, exfoliation, and rockburst. *Journal of Geophysical Research: Solid Earth*, 87(B8), 6805-6821. doi:10.1029/JB087iB08p06805
- Nemoto, K., Moriya, H., Niitsuma, H., & Tsuchiya, N. (2008). Mechanical and hydraulic coupling of injection-induced slip along pre-existing fractures. *Geothermics*, 37(2), 157-172, doi: 10.1016/j.geothermics.2007.11.001.

- Nygren, A., & Ghassemi, A. (2005). *Influence of cold water injection on critically stressed fractures in Coso geothermal field, CA*. Paper presented at the Alaska Rocks 2005, The 40th U.S. Symposium on Rock Mechanics (USRMS), Anchorage, Alaska, USA.
- Olson, J., Ben, B., and Holder, J. (2012). *Examining Hydraulic Fracture: Natural Fracture Interaction in Hydrostone Block Experiments*. Presented at the SPE Hydraulic Fracturing Technology Conference, The Woodlands, Texas, USA.
- Olsson, R., & Barton, N. (2001). An improved model for hydromechanical coupling during shearing of rock joints. *International Journal of Rock Mechanics and Mining Sciences*, 38(3), 317-329, doi:10.1016/S1365-1609(00)00079-4.
- Olsson, W. A., & Brown, S. R. (1993). Hydromechanical response of a fracture undergoing compression and shear. *International Journal of Rock Mechanics and Mining Sciences & Geomechanics Abstracts*, 30(7), 845-851, doi: 10.1016/0148-9062(93)90034-B.
- Park, H., Osada, M., Matsushita, T., Takahashi, M., & Ito, K. (2013). Development of coupled shear-flow-visualization apparatus and data analysis. *International Journal of Rock Mechanics and Mining Sciences*, 63, 72-81, doi:10.1016/j.ijrmms.2013.06.003.
- Passelègue, F. X., Brantut, N., & Mitchell, T. M. (2018). Fault Reactivation by Fluid Injection: Controls From Stress State and Injection Rate. *Geophysical Research Letters*, 45(23), 12,837-812,846. doi:10.1029/2018gl080470
- Petit, J. P., & Barquins, M. (1988). Can natural faults propagate under mode II conditions? *Tectonics*, 7(6), 1243-1256. <https://doi.org/10.1029/TC007i006p01243>
- Pine, R. J., & Batchelor, A. S. (1984). Downward migration of shearing in jointed rock during hydraulic injections. *International Journal of Rock Mechanics and Mining Sciences & Geomechanics Abstracts*, 21(5), 249-263, doi: 10.1016/0148-9062(84)92681-0.
- Rahman, M., Hossain, M., & Rahman, S. (2002). A shear-dilation-based model for evaluation of hydraulically stimulated naturally fractured reservoirs. *International Journal for Numerical and Analytical Methods in Geomechanics*, 26(5), 469-497. <https://doi.org/10.1002/nag.208>
- Ranjith, P., & Viete, D. (2011). Applicability of the ‘cubic law’ for non-Darcian fracture flow. *Journal of Petroleum Science and Engineering*, 78(2), 321-327, doi: 10.1016/j.petrol.2011.07.015.
- Rao, Q., Sun, Z., Stephansson, O., Li, C., & Stillborg, B. (2003). Shear fracture (Mode II) of brittle rock. *International Journal of Rock Mechanics and Mining Sciences*, 40(3), 355-375. [https://doi.org/10.1016/S1365-1609\(03\)00003-0](https://doi.org/10.1016/S1365-1609(03)00003-0)

- Reece, JS, Zoback, MD, and Kohli, AH. 2014. Effect of Shear Slip on Fault Permeability in Shale Reservoir Rocks. *Proc.*, AGU Fall Meeting Abstracts.
- Resor, P. G., & Meer, V. E. (2009). Slip heterogeneity on a corrugated fault. *Earth and Planetary Science Letters*, 288(3), 483-491. doi:https://doi.org/10.1016/j.epsl.2009.10.010
- Reyes, O., & Einstein, H. H. (1991). *Failure Mechanisms of Fractured Rock - A Fracture Coalescence Model*. Paper presented at the 7th ISRM Congress, Aachen, Germany.
- Rojstaczer, S. A., Ingebritsen, S. E., & Hayba, D. O. (2008). Permeability of continental crust influenced by internal and external forcing. *Geofluids*, 8(2), 128-139. doi:10.1111/j.1468-8123.2008.00211.x
- Rojstaczer, S., Wolf, S., & Michel, R. (1995). Permeability enhancement in the shallow crust as a cause of earthquake-induced hydrological changes. *Nature*, 373(6511), 237-239. doi:10.1038/373237a0
- Rutledge, J. T., Phillips, W. S., & Mayerhofer, M. (2004). Faulting induced by forced fluid injection and fluid flow forced by faulting: An interpretation of hydraulic-fracture microseismicity, Carthage Cotton Valley gas field, Texas. *Bulletin of the Seismological Society of America*, 94(5), 1817-1830.
- Rutqvist, J., Birkholzer, J., Cappa, F., & Tsang, C. F. (2007). Estimating maximum sustainable injection pressure during geological sequestration of CO₂ using coupled fluid flow and geomechanical fault-slip analysis. *Energy Conversion and Management*, 48(6), 1798-1807, doi:10.1016/j.enconman.2007.01.021.
- Rutter, E. H., & Mecklenburgh, J. (2018). Influence of normal and shear stress on the hydraulic transmissivity of thin cracks in a tight quartz sandstone, a granite and a shale. *Journal of Geophysical Research: Solid Earth*, n/a-n/a. doi:10.1002/2017JB014858
- Rutter, E., & Hackston, A. (2017). On the effective stress law for rock-on-rock frictional sliding, and fault slip triggered by means of fluid injection. *Philosophical Transactions. Series A, Mathematical, Physical, and Engineering Sciences*, 375(2103), 20160001, doi:10.1098/rsta.2016.0001.
- Rutter, E., & Mainprice, D. (1978). The effect of water on stress relaxation of faulted and unfaulted sandstone *Rock Friction and Earthquake Prediction* (pp. 634-654): Springer.
- Rutter, E., Atkinson, B., & Mainprice, D. (1978). On the use of the stress relaxation testing method in studies of the mechanical behaviour of geological materials. *Geophysical Journal International*, 55(1), 155-170.

- Safari, R., & Ghassemi, A. (2015). 3D thermo-poroelastic analysis of fracture network deformation and induced micro-seismicity in enhanced geothermal systems. *Geothermics*, 58, 1-14, doi:10.1016/j.geothermics.2015.06.010.
- Samuelson, J., Elsworth, D., & Marone, C. (2009). Shear-induced dilatancy of fluid-saturated faults: Experiment and theory. *Journal of Geophysical Research: Solid Earth*, 114(B12), n/a-n/a, doi:10.1029/2008JB006273.
- Scuderi, M. M., Collettini, C., & Marone, C. (2017). Frictional stability and earthquake triggering during fluid pressure stimulation of an experimental fault. *Earth and Planetary Science Letters*, 477, 84-96. doi:<https://doi.org/10.1016/j.epsl.2017.08.009>
- Sesetty, V and Ghassemi, A. 2017. Complex Fracture Network Model for Stimulation of Unconventional Reservoirs. *Proc.*, 51st US Rock Mechanics/Geomechanics Symposium.
- Shapiro, S. (2011). *Microseismic monitoring: a tool for reservoir characterization*. Paper presented at the AGU Fall Meeting Abstracts.
- Shen, B., Stephansson, O., Einstein, H. H., & Ghahreman, B. (1995). Coalescence of fractures under shear stresses in experiments. *Journal of Geophysical Research: Solid Earth*, 100(B4), 5975-5990. <https://doi.org/10.1029/95JB00040>
- Singh, K., Singh, D., & Ranjith, P. (2015). Laboratory simulation of flow through single fractured granite. *Rock Mechanics and Rock Engineering*, 48(3), 987-1000, doi:10.1007/s00603-014-0630-9.
- Sobolev, G. A. (1986). The study of barrier fracture in relation to earthquake and rockburst prediction. *pure and applied geophysics*, 124(4), 811-824. <https://doi.org/10.1007/bf00879612>
- Stanchits, S., Vinciguerra, S., & Dresen, G. (2006). Ultrasonic velocities, acoustic emission characteristics and crack damage of basalt and granite. *pure and applied geophysics*, 163(5-6), 975-994, doi:10.1007/s00024-006-0059-5.
- Staněk, F., & Eisner, L. (2017). Seismicity Induced by Hydraulic Fracturing in Shales: A Bedding Plane Slip Model. *Journal of Geophysical Research: Solid Earth*, 122(10), 7912-7926. <https://doi.org/10.1002/2017JB014213>
- Stavrogin, A. N., & Tarasov, B. G. (Eds.). (2001). *Experimental physics and rock mechanics*. CRC Press.
- Su, K., & Ghoreychi, M. (1999). *Experimental Study of Hydro-mechanical Behaviour of Closed Fractures In a Granite*. Paper presented at the 9th ISRM Congress, Paris, France.

- Tatone, B. S., & Grasselli, G. (2012). Quantitative measurements of fracture aperture and directional roughness from rock cores. *Rock Mechanics and Rock Engineering*, 45(4), 619-629, doi: 10.1007/s00603-011-0219-5.
- Tester, J. W., Anderson, B. J., Batchelor, A. S., & Blackwell, D. D. (2006). The Future of Geothermal Energy: Impact of Enhanced Geothermal Systems (EGS) on the United States in the 21st Century. *Massachusetts Institute of Technology*, 209.
- Thomas, A. L., & Pollard, D. D. (1993). The geometry of echelon fractures in rock: implications from laboratory and numerical experiments. *Journal of Structural Geology*, 15(3), 323-334. doi:[https://doi.org/10.1016/0191-8141\(93\)90129-X](https://doi.org/10.1016/0191-8141(93)90129-X)
- Thompson, B. D., Young, R. P., & Lockner, D. A. (2009). Premonitory acoustic emissions and stick-slip in natural and smooth-faulted Westerly granite. *Journal of Geophysical Research: Solid Earth*, 114(B2). doi:10.1029/2008jb005753
- Tinti, E., Scognamiglio, L., Michelini, A., & Cocco, M. (2016). Slip heterogeneity and directivity of the ML 6.0, 2016, Amatrice earthquake estimated with rapid finite-fault inversion. *Geophysical Research Letters*, 43(20), 10,745-710,752. doi:10.1002/2016gl071263
- Tse, R., & Cruden, D. M. (1979). Estimating joint roughness coefficients. *International Journal of Rock Mechanics and Mining Sciences & Geomechanics Abstracts*, 16(5), 303-307, doi:10.1016/0148-9062(79)90241-9.
- Vogler, D., Amann, F., Bayer, P., & Elsworth, D. (2016). Permeability Evolution in Natural Fractures Subject to Cyclic Loading and Gouge Formation. *Rock Mechanics and Rock Engineering*, 49(9), 3463-3479, doi:10.1007/s00603-016-1022-0.
- Vogler, D., Settgest, R. R., Annavarapu, C., Madonna, C., Bayer, P., & Amann, F. (2018). Experiments and Simulations of Fully Hydro-Mechanically Coupled Response of Rough Fractures Exposed to High-Pressure Fluid Injection. *Journal of Geophysical Research: Solid Earth*, 123(2), 1186-1200. doi:10.1002/2017jb015057
- Warpinski, N. R., Wolhart, S. L., & Wright, C. A. (2004). Analysis and Prediction of Microseismicity Induced by Hydraulic Fracturing. *SPE Journal*, 9(01), 24-33. doi:10.2118/87673-PA
- Weng, X., Sestetty, V., and Kresse, O. (2015). *Investigation of Shear-Induced Permeability in Unconventional Reservoirs*. Presented at the 49th US Rock Mechanics/Geomechanics Symposium, San Francisco, California.
- Willis-Richards, J., Watanabe, K., & Takahashi, H. (1996). Progress toward a stochastic rock mechanics model of engineered geothermal systems. *Journal of Geophysical Research: Solid Earth*, 101(B8), 17481-17496. <https://doi.org/10.1029/96JB00882>

- Witherspoon, P. A., Wang, J. S. Y., Iwai, K., & Gale, J. E. (1980). Validity of Cubic Law for fluid flow in a deformable rock fracture. *Water Resources Research*, 16(6), 1016-1024, doi:10.1029/WR016i006p01016.
- Wong, L. N. Y., & Einstein, H. H. (2009a). Systematic evaluation of cracking behavior in specimens containing single flaws under uniaxial compression. *International Journal of Rock Mechanics and Mining Sciences*, 46(2), 239-249. <https://doi.org/10.1016/j.ijrmms.2008.03.006>
- Wong, L. N. Y., & Einstein, H. H. (2009b). Crack Coalescence in Molded Gypsum and Carrara Marble: Part 1. Macroscopic Observations and Interpretation. *Rock Mechanics and Rock Engineering*, 42(3), 475-511. <https://doi.org/10.1007/s00603-008-0002-4>
- Wu, W., Reece, J. S., Gensterblum, Y., & Zoback, M. D. (2017). Permeability Evolution of Slowly Slipping Faults in Shale Reservoirs. *Geophysical Research Letters*, 44(22), 11,368-311,375, doi:10.1002/2017GL075506.
- Yang, M., & Toksöz, M. N. (1981). Time-dependent deformation and stress relaxation after strike slip earthquakes. *Journal of Geophysical Research: Solid Earth*, 86(B4), 2889-2901. doi:10.1029/JB086iB04p02889
- Yang, Z. Y., Lo, S. C., & Di, C. C. (2001). Reassessing the joint roughness coefficient (JRC) estimation using Z2. *Rock Mechanics and Rock Engineering*, 34(3), 243-251, doi:10.1007/s006030170012.
- Ye, Z., & Ghassemi, A. (2016). *Deformation Properties of Saw-Cut Fractures in Barnett, Mancos and Pierre Shales*. Paper presented at the 50th US Rock Mechanics/Geomechanics Symposium.
- Ye, Z., & Ghassemi, A. (2018a). Injection-Induced Shear Slip and Permeability Enhancement in Granite Fractures. *Journal of Geophysical Research: Solid Earth*, 123(10), 9009-9032. <https://doi.org/10.1029/2018JB016045>
- Ye, Z., & Ghassemi, A. (2018b). *Experimental Study on Injection-induced Fracture Propagation and Coalescence for EGS Stimulation*. Paper presented at the 43rd Workshop on Geothermal Reservoir Engineering, Stanford, California, USA.
- Ye, Z., & Ghassemi, A. (2018c). *Injection-induced Fracture Propagation and Coalescence Under Triaxial Loading*. Paper presented at the 52nd U.S. Rock Mechanics / Geomechanics Symposium, Seattle, Washington, USA.
- Ye, Z., & Ghassemi, A. (2019). Injection-Induced Propagation and Coalescence of Preexisting Fractures in Granite Under Triaxial Stress. *Journal of Geophysical Research: Solid Earth*, 124. c

- Ye, Z., Ghassemi, A., & Riley, S. (2018). *Stimulation Mechanisms in Unconventional Reservoirs*. Paper presented at the Unconventional Resources Technology Conference (URTeC), Houston, Texas, USA.
- Ye, Z., Janis, M., & Ghassemi, A. (2017). *Experimental Investigation of Injection-driven Shear Slip and Permeability Evolution in Granite for EGS Stimulation*. Paper presented at the 42nd Workshop On Geothermal Reservoir Engineering, California, USA.
- Ye, Z., Janis, M., Ghassemi, A., & Bauer, S. (2017). *Experimental Investigation of Injection-driven Shear Slip and Permeability Evolution in Granite for EGS Stimulation*. Paper presented at the 42nd Workshop On Geothermal Reservoir Engineering, Stanford, California, USA.
- Ye, Z., Janis, M., Ghassemi, A., & Riley, S. (2017). *Laboratory Investigation of Fluid Flow and Permeability Evolution through Shale Fractures*. Paper presented at the Unconventional Resources Technology Conference (URTeC), Austin, Texas, USA.
- Ye, Z., Sesetty, V., & Ghassemi, A. (2018). *Experimental and Numerical Investigation of Shear Stimulation and Permeability Evolution in Shales*. Paper presented at the SPE Hydraulic Fracturing Technology Conference and Exhibition, Woodlands, Texas, USA.
- Yeo, I. W., De Freitas, M. H., & Zimmerman, R. W. (1998). Effect of shear displacement on the aperture and permeability of a rock fracture. *International Journal of Rock Mechanics and Mining Sciences*, 35(8), 1051-1070, doi:10.1016/S0148-9062(98)00165-X.
- Yin, P., Wong, R. H. C., & Chau, K. T. (2014). Coalescence of two parallel pre-existing surface cracks in granite. *International Journal of Rock Mechanics and Mining Sciences*, 68, 66-84. <https://doi.org/10.1016/j.ijrmms.2014.02.011>
- Yu, X., & Vayssade, B. (1991). Joint profiles and their roughness parameters. *International Journal of Rock Mechanics and Mining Sciences & Geomechanics Abstracts*, 28(4), 333-336, doi:10.1016/0148-9062(91)90598-G.
- Zhao, Q., Tisato, N., Kovaleva, O., & Grasselli, G. (2018). Direct observation of faulting by means of rotary shear tests under X-ray micro-computed Tomography. *Journal of Geophysical Research: Solid Earth*, 123(9), 7389-7403.
- Zhang, Z., Nemcik, J., & Ma, S. (2013). Micro- and macro-behaviour of fluid flow through rock fractures: an experimental study. *Hydrogeology Journal*, 21(8), 1717-1729. <https://doi.org/10.1007/s10040-013-1033-9>
- Zhao, J. (1997a). Joint surface matching and shear strength part A: joint matching coefficient (JMC). *International Journal of Rock Mechanics and Mining Sciences*, 34(2), 173-178, doi:10.1016/S0148-9062(96)00062-9.

- Zhao, J. (1997b). Joint surface matching and shear strength part B: JRC-JMC shear strength criterion. *International Journal of Rock Mechanics and Mining Sciences*, 34(2), 179-185, doi: 10.1016/S0148-9062(96)00063-0.
- Zhao, Z., Jing, L., & Neretnieks, I. (2012). Particle mechanics model for the effects of shear on solute retardation coefficient in rock fractures. *International Journal of Rock Mechanics and Mining Sciences*, 52, 92-102, doi:10.1016/j.ijrmms.2012.03.001.
- Zhou, J., Chen, M., Jin, Y., et al. (2008). Analysis of fracture propagation behavior and fracture geometry using a tri-axial fracturing system in naturally fractured reservoirs. *International Journal of Rock Mechanics and Mining Sciences* 45 (7): 1143-1152.
- Zhu, H., Deng, J., Jin, X. et al. (2015). *journal article*. Hydraulic Fracture Initiation and Propagation from Wellbore with Oriented Perforation. *Rock Mechanics and Rock Engineering* 48 (2): 585-601.
- Zielke, O., Galis, M., & Mai, P. M. (2017). Fault roughness and strength heterogeneity control earthquake size and stress drop. *Geophysical Research Letters*, 44(2), 777-783. doi:10.1002/2016gl071700
- Zimmerman, R. W., & Bodvarsson, G. S. (1996). Hydraulic conductivity of rock fractures. *Transport in Porous Media*, 23(1), 1-30, doi:10.1007/bf00145263.
- Zoback, M. D., Kohli, A., Das, I., & McClure, M. W. (2012). *The Importance of Slow Slip on Faults During Hydraulic Fracturing Stimulation of Shale Gas Reservoirs*. Paper presented at the SPE Americas Unconventional Resources Conference, Pittsburgh, Pennsylvania USA.